UNCLASSIFIED

MARTIN MARIETTA ENERGY SYSTEMS LIBRARIES

3 4456 0050692 2

ORNL-2081
Progress

5

APPLIED NUCLEAR PHYSICS DIVISION ANNUAL REPORT

FOR PERIOD ENDING SEPTEMBER 10, 1956

CENTRAL RESEARCH LIBRARY
DOCUMENT COLLECTION

LIBRARY LOAN COPY

DO NOT TRANSFER TO ANOTHER PERSON

If you wish someone else to see this document, send in name with document and the library will arrange a loan.

OAK RIDGE NATIONAL LABORATORY
OPERATED BY
UNION CARBIDE NUCLEAR COMPANY
A Division of Union Carbide and Carbon Corporation
UCC
POST OFFICE BOX X • OAK RIDGE, TENNESSEE

UNCLASSIFIED

Printed in USA. Price 1.25 cents. Available from the

Office of Technical Services
U. S. Department of Commerce
Washington 25, D. C.

LEGAL NOTICE

This report was prepared as an account of Government sponsored work. Neither the United States, nor the Commission, nor any person acting on behalf of the Commission:

A. Makes any warranty or representation, express or implied, with respect to the accuracy, completeness, or usefulness of the information contained in this report, or that the use of any information, apparatus, method, or process disclosed in this report may not infringe privately owned rights; or

B. Assumes any liabilities with respect to the use of, or for damages resulting from the use of any information, apparatus, method, or process disclosed in this report.

As used in the above, "person acting on behalf of the Commission" includes any employee or contractor of the Commission to the extent that such employee or contractor prepares, handles or distributes, or provides access to, any information pursuant to his employment or contract with the Commission.

UNCLASSIFIED

ORNL-2081

Contract No. W-7405-eng-26

APPLIED NUCLEAR PHYSICS DIVISION ANNUAL REPORT

for Period Ending September 10, 1956

E. P. Blizard, Director
A. Simon, Associate Director

A. D. Callihan, Leader, Critical Experiments Facility
C. E. Clifford, Leader, Tower Shielding Facility
F. C. Maienschein, Leader, Bulk Shielding Facility
R. W. Peelle, Leader, Lid Tank Shielding Facility

DATE ISSUED

NOV 5 1956

OAK RIDGE NATIONAL LABORATORY
Operated by
UNION CARBIDE NUCLEAR COMPANY
A Division of Union Carbide and Carbon Corporation
Post Office Box X
Oak Ridge, Tennessee

MARTIN MARIETTA ENERGY SYSTEMS LIBRARIES

3 4456 0050692 2

UNCLASSIFIED

ORNL-2081
Progress

INTERNAL DISTRIBUTION

1. C. E. Center
2. Biology Library
3. Health Physics Library
4–6. Central Research Library
7. Reactor Experimental Engineering Library
8–27. Laboratory Records Department
28. Laboratory Records, ORNL R.C.
29. A. M. Weinberg
30. L. B. Emlet (K-25)
31. J. P. Murray (Y-12)
32. J. A. Swartout
33. E. H. Taylor
34. E. D. Shipley
35. A. H. Snell
36. W. H. Jordan
37. S. J. Cromer
38. G. E. Boyd
39. R. A. Charpie
40. S. C. Lind
41. F. L. Culler
42. A. Hollaender
43. J. H. Frye, Jr.
44. M. T. Kelley
45. R. S. Livingston
46. K. Z. Morgan
47. E. J. Murphy
48. A. S. Householder
49. C. P. Keim
50. C. S. Harrill
51. C. E. Winters
52. D. S. Billington
53. D. W. Cardwell
54. E. M. King
55. A. J. Miller
56. D. D. Cowen
57. W. M. Breazeale (consultant)
58. M. J. Skinner
59. R. R. Dickison
60. P. M. Reyling
61. G. C. Williams
62. L. S. Abbott
63. S. Auslender
64–88. E. P. Blizard
89. T. V. Blosser
90. A. D. Callihan
91. G. T. Chapman
92. C. E. Clifford
93. R. R. Coveyou
94. G. deSaussure
95. L. Dresner
96. J. K. Fox
97. L. W. Gilley
98. E. Guth
99. R. Gwin
100. K. M. Henry
101. L. B. Holland
102. E. B. Johnson
103. F. L. Keller
104. W. E. Kinney
105. M. E. LaVerne
106. T. A. Love
107–109. F. C. Maienschein
110. J. H. Marable
111. J. M. Miller
112. F. J. Muckenthaler
113. R. B. Murray
114. M. L. Nelson
115. D. R. Otis
116. R. W. Peelle
117. A. B. Reynolds
118. E. G. Silver
119. A. Simon
120. J. Smolen
121. J. G. Sullivan
122. J. T. Thomas
123. D. K. Trubey
124. T. A. Welton
125. C. D. Zerby
126. W. Zobel
127. Francis L. Friedman (consultant)
128. Herbert Goldstein (consultant)
129. Henry Hurwitz, Jr. (consultant)
130. L. W. Nordheim (consultant)
131. Robert R. Wilson (consultant)

EXTERNAL DISTRIBUTION

132. R. F. Bacher, California Institute of Technology
133. Division of Research and Development, AEC, ORO
134–730. Given distribution as shown in TID-4500 (12th ed.) under Physics category (200 copies – OTS)

DISTRIBUTION PAGE TO BE REMOVED IF REPORT IS GIVEN PUBLIC DISTRIBUTION

PREFACE

On July 1, 1955, those parts of the Physics Division primarily concerned with critical experiments and reactor shielding were combined with a theoretical reactor physics group in the Director's Division to form the new Applied Nuclear Physics Division. The change has not altered the work assignments of its new members significantly but has, rather, brought together in a single professional division a group of scientists with common interests, namely, the generation and ordering of information basic to the nuclear physics aspects of reactors.

In the studies of critical arrays of fissionable and moderating materials at the Critical Experiments Facility, either of two criteria are accepted for undertaking work. One is that the array being studied experimentally be sufficiently simple that it be amenable to a parallel calculation, enabling an understanding of the phenomena that are observed. The other is that the array mock up as nearly as possible a configuration which is of interest because it is to be built, either as an operating reactor or as a part of a chemical processing plant. Two experimental bays are currently being used for various experiments, primarily with thermal reactors. A third is planned for studying reactors operating in an intermediate energy region (1 to 10 kev).

Shielding research accepts the same two criteria. The Lid Tank Shielding Facility, which operates with a large (28-in.-dia) uranium converter plate as a source, is utilized for slab-type experiments with materials of interest to shielding. The Tower Shielding Facility, consisting of a reactor which can be elevated 200 ft above the ground, is used for those shielding experiments in which ground scattering is to be avoided and air scattering is to be studied.

The Bulk Shielding Facility encompasses work of several types. First, shield mockups can be inserted in the pool of water in which the reactor operates, and the penetration can then be measured. Second, the facility affords a strong controlled source of radiation for physics experiments, which deal largely with studies of the fission process itself. Examples are studies of the fission-neutron spectra of various isotopes. Third, the reactor itself is studied. This installation is the prototype for many research and educational reactors, such as the one used at the Atoms for Peace Conference in Geneva, and the onus of obtaining as much information as possible about the operation and possibilities of the Bulk Shielding Reactor falls on the Laboratory. Thus the temperature coefficient of reactivity, effect of poisoning, neutron spectra, as well as many engineering features, have been studied here.

The Reactor Theory Group is concerned with both analytical and numerical methods of calculating the properties of reactors. The analytical work, currently, is on problems of resonance escape and capture cross sections. Current nuclear models are used whenever possible to obtain simple estimates of these quantities. The numerical work is dedicated to making the greatest use of the ORNL high-speed digital computer, known as the Oracle. To this end, various codes are under development, either to calculate reactor criticality and complete distributions of fluxes or fissions, or to calculate auxiliary parameters such as the Fermi age in

various media. A general cross-section tape for use with the various routines is near completion, as is a "Compiler" routine for constructing reactor codes from subroutines already existent. The end result, when proved by comparison with critical experiments (ORNL and others), should be a considerable versatility in reactor calculational ability.

In addition to the foregoing, it is intended that special experiments be undertaken in the reactor physics field. Typical of these is one now under way to measure diffusion coefficients in various materials at various temperatures, using a time-varying source of neutrons. Another is the measurement of various cross sections of particular reactor interest, such as the fission cross sections of the more unusual fissile elements. These experiments may utilize the BSR, the ORNL Graphite Reactor, or an accelerator which will be purchased.

About half the division's work is not now declassifiable and hence does not appear in this document. That work is reported, however, in the periodic reports of the several classified projects such as Aircraft Nuclear Propulsion Project and Project Sherwood (a study of controlled thermonuclear reactors).

TABLE OF CONTENTS AND SUMMARY

I. RESEARCH FOR LIGHT-WATER-MODERATED REACTORS

1. CRITICAL EXPERIMENTS AT THE BSF
K. M. Henry, E. B. Johnson, and J. Kington 3

Critical experiments were performed at the BSF with the 20%-enriched elements for the swimming-pool-type Aquarium Reactor prior to their shipment to Geneva. The total amount of U^{235} in the critical loading was 3660.9 g, but the excess reactivity was not determined. Similar experiments were performed with the highly enriched (~89%) elements for the Pennsylvania State University Reactor. The reactor was critical with 2914 g of U^{235} and an excess reactivity of ~1%. In addition, several critical experiments were performed by ORSORT students as part of their laboratory class. The effect on the reactivity of slowly flooding a large air-filled void adjacent to the BSR was investigated; the largest change observed was +2.62% $\Delta k/k$. A series of experiments to determine the effect of introducing voids within the core was also performed.

2. EFFECT OF THE REFLECTOR ON THE NEUTRON FLUX IN AN ORR BEAM HOLE MOCKUP
K. M. Henry, E. B. Johnson, and J. D. Kington 12

An experiment with the BSR has shown that the thermal-neutron flux leakage into a beam tube adjacent to the reactor could be appreciably increased by substituting heavy water for the light-water reflector immediately surrounding the beam tube. The experiment was motivated by the interest in increasing the flux in beam holes adjacent to the Oak Ridge Research Reactor, and several configurations were tested.

3. SENSORY INSTRUMENTATION STUDIES FOR THE BSR
K. M. Henry and J. N. Anno 21

A series of experiments has been performed to check the saturation properties and linearity of response of the ionization chambers which supply the basic signals for control and power-level indication of the BSR. It was found that the saturation properties of the log N chamber, which actuates the log reactor power indicator, recorder, period meter, and period scram circuit, have changed no more than about 0.4% since its initial installation. The investigation of the response of the fission chamber and galvanometer chamber indicates that for power demands of 100 kw, 500 kw, and 1 Mw the actual power sags approximately 2, 10, and 16%, respectively.

4. TEMPERATURE DISTRIBUTION IN THE BSR UNDER NATURAL CONVECTION COOLING
K. M. Henry and J. N. Anno 25

Measurements of the temperature distribution on the surface and in the core of BSR fuel plates have been made to provide information on (1) the rate of temperature rise within the core, the knowledge of which will facilitate the design of similar reactors, and (2) the power at which boiling would first occur. The measurements also provide experimental evidence for heat transfer and nuclear calculations. Extrapolation of the data from the surface measurements indicates that boiling would first occur in the reactor at a power of approximately 2100 kw.

5. WATER PURIFICATION AND CIRCULATION SYSTEMS AT THE BSF
J. D. Flynn 32

Two water purifying loops for the demineralized water of the reactor pool have been installed at the BSF. One system removes suspended particles from the water, and another system maintains a 250,000- to 350,000-ohm/cm specific resistance of the pool water. A set of jets has also been installed above the BSR in order to diffuse the activated water for a sufficient length of time to suppress the N^{16} activity at the pool surface. With the jets in operation and the reactor at a power of 1 Mw, the radiation $19\frac{1}{2}$ in. above the $17\frac{1}{2}$ ft of water directly over the reactor is reduced from 800 mr/hr to 32 mr/hr.

6. *AIR ACTIVITY PRODUCED BY THE BSR*
W. R. Champion 35

Since the air-borne gamma-ray activity measured 40 ft from the BSR was an appreciable fraction of the tolerance level, an experiment was performed to determine the origin of the activity. Sources of activity were collected from the air above the pool surface and from the pool water 6 in. above the reactor, and an examination was made of their energy spectra and the time-decay characteristics. The half lives of several prominent peaks were observed, but comparison with published data has failed to result in any definite assignments other than N^{16}.

7. *MEASUREMENTS OF THE THE THERMAL-NEUTRON FLUX FROM THE BSF THERMAL COLUMN*
E. G. Silver 39

A thermal column with a geometrically uniform neutron beam is needed for numerous experiments. A thermal column which consists of a stack of graphite against which the reactor can be positioned has been built at the BSF. A 10-in.-thick lead shield between the graphite and the reactor serves to attenuate the gamma-ray flux from the reactor. Foil measurements of the flux at the radiation port indicated that a uniform flux is available in an area of 4π in.^{2}.

8. *CALCULATION OF THE EFFECT ON REACTIVITY WHEN HEAVY WATER IS ADDED TO A LIGHT-WATER-MODERATED REACTOR*
E. G. Silver 43

A calculation of the effect on the reactivity of adding D_2O in various proportions to the moderator of H_2O-moderated reactors has been made. Plots of $k_{(H_2O+D_2O)}/k_{H_2O}$ as a function of the volume fraction of D_2O in the moderator are presented for all combinations of several values of the macroscopic total absorption cross section of the uranium in the core (Σ_a^{fuel}), the ratio of the volume fraction of metal in the core to the volume fraction of the moderator (M/W), and the buckling (B^2). The values used were Σ_a^{fuel} = 0.03, 0.052, and 0.07 cm^{-1}, M/W = 0.5, 0.733, and 1.0, and B^2 = 0.01, 0.007, 0.004, and 0.001.

9. *COMPARISON OF CALCULATED CRITICAL MASS OF THE BSR WITH EXPERIMENT*
E. G. Silver 47

The critical masses of three swimming-pool-type reactors have been computed and compared with corresponding experimental critical masses for the specified loadings in the BSR. Two reactor codes were employed in the calculations: the UNIVAC Eyewash 30-group code using three concentric spherical regions (control rod, fuel, and reflector), and the Oracle three-group, three-region code. The latter was used both as a two-region and as a three-region problem for a cylindrical or spherical reactor. The calculations with the best assumptions gave results that were within 1% of the experimental critical mass and within 0.4% of the reactivity.

II. CRITICAL EXPERIMENTS

10. *CRITICAL EXPERIMENTS WITH AQUEOUS SOLUTIONS OF U^{235}*
J. K. Fox and L. W. Gilley 61

A number of experiments have been performed to determine the critical conditions for vessels containing highly enriched (~90%) uranium in water solutions of UO_2F_2. It was found that, for solutions contained in cylinders, 8.76 in. is very near the diameter of an infinitely high, unreflected aluminum cylinder; 8.5 to 9 in. is the corresponding diameter for stainless steel cylinders.

The effect of interacting arrays of 6- and 8-in.-dia cylinders containing a solution with an $H:U^{235}$ atomic ratio of 44.3 was also investigated for various reflector conditions and edge-to-edge spacings. The critical height of water-reflected arrays of 6-in.-dia cylinders approaches the value of a single cylinder at an edge-to-edge spacing of about 15 in. When the cylinders are wrapped in cadmium sheets, the infinite critical height would be for a spacing of 2 in. The critical height of water-reflected arrays of 8-in.-dia

cylinders approaches the value of a single cylinder at an edge-to-edge spacing of approximately 9 in. A single cadmium-wrapped 8-in.-dia water-reflected cylinder becomes critical, and the values of the critical heights of arrays of cadmium-wrapped 8-in.-dia cylinders approach the value for the single cylinder. Three unreflected 8-in.-dia cylinders would become critical with infinite height at about a 9-in. edge-to-edge spacing, while seven cylinders would require an 18-in. spacing.

The relative effects of water, furfural, concrete, graphite, and firebrick as neutron reflectors for solutions contained in aluminum cylinders were also investigated.

11. TWO BERYLLIUM-MODERATED CRITICAL ASSEMBLIES
E. L. Zimmerman 69

Two unreflected beryllium-moderated critical assemblies have been built in a simple geometry in order to check the critical parameters predicted for them by multigroup reactor calculational methods. The assemblies, designated as CA-1 and CA-18, had regular lattices of 10-mil-thick enriched uranium metal fuel disks separated by 1- and 4-in. blocks of beryllium metal, respectively. Assembly CA-1 had outside dimensions of 21 × 21 × 23.2 in. and was critical with a U^{235} mass of 18.08 kg; the withdrawal of one control rod was equal to 0.0054 in reactivity. Assembly CA-18 had outside dimensions of 24 × 28.4 × 24.1 in. and was critical with 7.65 kg of U^{235}; the control-rod withdrawal was equal to 0.0020 in reactivity. Only the experimental data are presented, the correlation with theory having been published elsewhere.

12. LIMITING CRITICAL CONCENTRATIONS OF AQUEOUS SOLUTIONS OF FISSILE ISOTOPES
J. T. Thomas 78

Calculations are made of the concentration of fissile isotopes which will not be critical even in very large quantities. For U^{233}, U^{235}, and Pu^{239}, the values are 10.92, 11.59, and 7.27 g of fissile isotope per gram of aqueous solution, respectively. Calculations are extended to the case in which some conversion from one fissile element to another has taken place, giving mixtures of fissile elements.

13. PARAMETERS FOR TWO-GROUP ANALYSIS OF CRITICAL EXPERIMENTS WITH WATER-REFLECTED SPHERES OF UO_2F_2 AQUEOUS SOLUTIONS
J. T. Thomas 81

From four critical measurements on spheres of three sizes containing aqueous uranium solutions are obtained a set of parameters from which various other critical spheres are calculated. These include a determination of minimum critical volume (6.291 liters for a U^{235} concentration of 537.86 g/liter) and minimum critical mass (0.790 kg of U^{235} for a U^{235} concentration of 58.81 g/liter). The parameters are not satisfactory for calculations on slabs and infinite cylinders, probably because the measured cadmium fraction varies with geometry.

14. DETERMINATION OF REACTOR PARAMETERS FROM PERIOD MEASUREMENTS
R. Gwin 84

Measurements of a static critical mass as well as reactor period for off-critical conditions can be used to determine the effective delayed neutron fraction, and from this the age of prompt and delayed neutrons can be estimated by age theory. From data on a dilute aqueous solution of U^{235} in a cylindrical container the age of prompt neutrons has been estimated to be 25.4 cm^2. For delayed neutrons the age was estimated to be 14.1 cm^2, the effective delayed neutron fraction being 0.0096. Probable errors for these values have not been estimated.

15. COMPARISON OF ONE-DIMENSIONAL CRITICAL MASS COMPUTATIONS WITH EXPERIMENTS FOR COMPLETELY REFLECTED REACTORS
F. G. Prohammer 86

Critical-mass calculations for completely reflected cylindrical reactors would be greatly facilitated if a one-dimensional computational program used for spherical reactors could be applied. A comparison

of cylindrical and spherical reactors has shown that the cylindrical reactors can be converted to equivalent spheres by a relationship which assumes that the buckling of a sphere is equal to that of the cylinder, making allowance for reflector savings δ. The relationship is expressed as

$$\frac{\pi}{R + \delta} = \left[\left(\frac{2.4048}{r + \delta}\right)^2 + \left(\frac{\pi}{h + 2\delta}\right)^2\right]^{1/2},$$

where R and r are the radii of the sphere and cylinder, respectively, and h is the cylinder height.

III. FISSION PHYSICS

16. MEASUREMENT OF THE SPECTRUM OF SHORT-LIVED FISSION-PRODUCT DECAY GAMMA RAYS EMITTED FROM A ROTATING FUEL BELT
R. W. Peelle, W. Zobel, and T. A. Love 91

By means of a rotating belt containing U^{235}, the short-lived fission-product gamma rays have been measured with a three-crystal spectrometer. Rotation times as short as 1 sec have been used. A value for the total gamma-ray energy of 4.8 Mev for the 0.36- to 5.8-Mev photon energy interval was observed.

17. TIME AND ENERGY SPECTRA OF FISSION-PRODUCT GAMMA RAYS MEASURED AT SHORT TIMES AFTER URANIUM SAMPLE IRRADIATIONS
W. Zobel and T. A. Love 95

The fast pneumatic tube at the ORNL Graphite Reactor has been used in conjunction with the three-crystal spectrometer to measure short-lived fission-product gamma rays for times after fission from 1.25 to 1600 sec. The total energy of photons in the interval 0.28 to 5.0 Mev was found to be 3.23 Mev $\pm$25%. Spectra for various times after fission are given, from which it is anticipated that individual emitters can be identified.

18. THERMAL-NEUTRON FISSION CROSS SECTIONS OF Pu^{239} AND Pu^{240}
W. W. Pratt, F. J. Muckenthaler, and E. G. Silver 102

By use of neutrons coming from a hole in the shield and moderator of the ORNL Graphite Reactor, measurements have been made of the relative fission cross sections of Pu^{239} and Pu^{240} compared with the cross section of U^{235}. The results, after correction for the neutron spectrum to give cross sections for neutrons of 2200 m/sec, are $\sigma_f^{49} = 715 \pm 15$ barns and $\sigma_f^{40} = 3.7 \pm 8$ barns. A value of $\sigma_f^{25} = 580 \pm 8$ barns was used to determine the results.

19. NUMBER OF NEUTRONS RELEASED PER THERMAL FISSION OF Pu^{241}
G. deSaussure and E. G. Silver 105

By measuring fast neutrons in coincidence with fissions induced by thermal neutrons from the ORNL Graphite Reactor, the relative neutron yields of Pu^{241} and U^{235} have been determined. The results give a value of 3.17 $\pm$ 0.12 neutrons per thermal fission of Pu^{241}, assuming a value of 2.46 $\pm$0.03 for U^{235}. The results of this experiment are compared with those reported by other investigators.

20. FISSION NEUTRON SPECTRUM OF U^{233}
K. M. Henry and M. P. Haydon 108

The fission neutron spectrum of U^{233} was measured at the BSF with nuclear photographic plates under the same experimental conditions as those of earlier measurements with a proton-recoil neutron spectrometer. The shapes of the resulting spectra agreed within the combined limits of error.

21. FAST-NEUTRON SPECTRUM OF A 117-CURIE Po-Be SOURCE
K. M. Henry 110

Since Po-Be sources are used to calibrate fast-neutron dosimeters, the fast-neutron spectrum of such sources should be known. Recently, the availability of a source of larger physical size and intensity

prompted a further measurement with the BSF proton-recoil spectrometer. The resulting spectrum agrees within statistical error with the spectra previously determined.

IV. REACTOR THEORY

22. *REFLECTOR SAVINGS METHOD FOR ESTIMATING FLUXES IN A FULLY REFLECTED REACTOR*
M. L. Nelson 115

The group equations for a fully reflected reactor have not been satisfactorily solved, except in one dimension, owing to the nonseparability of the flux. An iterative scheme is described which converges to what is presumed to be a good approximation to the criticality and flux in the reflected reactor. This scheme has been programed for use with the Oracle three-group, three-region code and may be applied to a fully reflected cylinder or parallelepiped.

23. *ESTIMATION OF RESONANCE INTEGRALS*
L. Dresner 116

Resonance parameters are known for quite a large number of nuclei. These parameters exhibit regular behavior throughout the periodic table. Based on this information a systematics of resonance integrals has been constructed; estimated resonance integrals are compared with experimentally determined values.

24. *HOMOGENEOUS EFFECTIVE RESONANCE INTEGRALS OF U^{238} AND Th^{232}*
L. Dresner 121

Numerical calculations performed on the Oracle have made possible exact inclusion of the effect of Doppler broadening of resonance lines in the calculation of homogeneous resonance absorption integrals. The effective resonance integrals of U^{238} and Th^{232} have been calculated as functions of the scattering cross section per absorbing nucleus for 0 and 300°K, using the theory of Wigner *et al.* Agreement of the calculated (300°K) and experimental resonance integrals is excellent for U^{238} and good for Th^{232}, except for pure ThO_2, where a discrepancy is noted. The temperature coefficients for the metals have also been calculated, and a comparison with experiment is given. Finally, the effect of multiple scatterings in the lowest resonances has been investigated for pure U^{238} metal and has been found to be important.

25. *EFFECT OF GEOMETRY ON RESONANCE NEUTRON ABSORPTION*
L. Dresner 128

By use of the theory of Wigner *et al.*, an expression has been derived, for the geometric dependence of the effective resonance integral of lumps, which is *independent* of the details of resonance structure (widths, resonance energies). This expression has been compared with experimentally determined geometric variations for U^{238} and Th^{232} and is found to overestimate the ratio of surface-to-volume absorption by about 40%. The cause of this overestimate is obscure, but its amount should be the same in all materials.

26. *CALCULATION OF NEUTRON RADIATIVE CAPTURE CROSS SECTIONS*
L. Dresner 130

Several methods of calculating radiative capture cross sections are compared, and numerical results are given for U^{238}. The importance of neutron angular momenta higher than zero is found to be large at quite low energies.

27. *THE ORACLE THREE-GROUP, THREE-REGION REACTOR CODE*
W. E. Kinney and G. Heilborn 132

Improvements have been made in the Oracle three-group, three-region reactor code. Some of these take advantage of new features of the Oracle, such as the curve plotter.

28. MULTIGROUP CALCULATIONS FOR A MULTIREGION REACTOR
W. E. Kinney, R. R. Coveyou, J. G. Sullivan, and B. J. Garrick 133

A multigroup, multiregion reactor code known as "Corn Pone" is under development. Equations resulting from a consistent P_1 approximation to the Boltzmann equation are incorporated in the code. Hydrogen slowing down is treated exactly, while a variety of approximate slowing-down kernels for the heavier elements are available.

29. ORACLE MASTER CROSS-SECTION TAPE
R. R. Bate, J. H. Marable, and J. W. Niestle 140

A master cross-section tape is being prepared for use with the various reactor programs on the Oracle. Cross sections which have not been experimentally determined will be estimated by use of current nuclear models. Auxiliary routines for this purpose are being prepared.

30. MONTE CARLO MASTER CROSS-SECTION TAPE
R. R. Bate, J. H. Marable, and J. W. Niestle 140

This Monte Carlo tape has greater cross-section detail for a lesser number of elements than the master cross-section tape. It is specifically tailored with regard to fast access and rapid use in Monte Carlo problems.

31. A PROGRAM COMPILER FOR THE ORACLE
R. R. Bate and M. E. LaVerne 141

The "Compiler" is an Oracle routine which is capable of integrating standard subroutines into a more general code. A routine of this sort has proved to be a valuable aid to programmers. A brief description of the Compiler is presented.

32. MONTE CARLO CALCULATION OF NEUTRON AGE IN WATER
R. R. Coveyou 144

A Monte Carlo code has been prepared for the Oracle to compute neutron ages in mixtures. The age of fission neutrons to indium resonance in water has been computed to be 25.17 ± 0.27 cm^2, which is in agreement with previous calculations and in the usual disagreement with experiment.

33. NUMERICAL INTEGRATION OF THE ONE-VELOCITY BOLTZMANN EQUATION
J. H. Marable 146

A program for solution of the one-velocity transport equation has been coded for the Oracle. Numerical integrations are performed over an arbitrary number of space points and up to 20 regions of solid angle as determined by the neutron direction. The code, at present, applies only to a single region.

34. SOME REMARKS ON THE SLOWING DOWN OF NEUTRONS IN HYDROGEN
T. A. Welton and L. C. Biedenharn 146

The predictions of the Goertzel-Selengut theory for the age in pure hydrogen are compared with the exact values obtained from the P_1 equations. These results are obtained for both the second moment of the flux density and the second moment of the slowing-down density. Numerical results are given for constant cross sections and for the experimental value of Σ_H.

35. NEUTRON SLOWING DOWN BY HYDROGEN IN THE CONSISTENT P_1 APPROXIMATION
A. Simon 147

Two analytical solutions for the flux, slowing-down density, and age are derived in the consistent P_1 approximation to the Boltzmann equation. One solution is for pure, nonabsorbing hydrogen with a $1/v$ scattering cross section. The other is for all cross sections constant, with the heavy elements assumed to have infinite mass. These results are compared with the corresponding predictions of the Goertzel-Selengut theory, and a tentative explanation of the gross behavior is advanced.

V. SHIELDING RESEARCH

36. ATTENUATION BY WATER OF THE FAST-NEUTRON DOSE RATE FROM THE BSR
T. V. Blosser 151

The fast-neutron dose rate in water at distances up to 180 cm from the BSR has been measured.

37. STUDY OF NUCLEAR AND PHYSICAL PROPERTIES OF THE ORNL GRAPHITE REACTOR SHIELD
T. V. Blosser, G. W. Bond, L. A. Lee, D. T. Morgan, J. F. Nichols, T. O. P. Speidel, D. W. Vroom, M. A. Welt, R. C. Reid, and A. B. Reynolds 155

The structural and nuclear durability of the 7-ft-thick concrete shield around the ORNL Graphite Reactor has been investigated. The results of the gamma-ray and neutron attenuation measurements are presented.

38. RADIATION ATTENUATION CHARACTERISTICS OF STRUCTURAL CONCRETE
J. M. Miller 157

Since the shields of many stationary reactors will probably be made of concrete, a series of experiments has been initiated at the LTSF to measure the attenuation by concrete of radiation from a fission source. A fast-neutron removal attenuation coefficient (Σ_R/ρ) of 3.7×10^{-2} cm^2/g was calculated and was in good agreement with a value of $(3.6 \pm 0.2) \times 10^{-2}$ cm^2/g obtained by taking the sum of the products of the per cent by weight of each element (obtained by chemical analysis) and the mass attenuation coefficient of the element.

39. NEW LID TANK SHIELDING FACILITY SOURCE PLATE
D. R. Otis 163

The source at the LTSF consists of a plate containing U^{235}, which absorbs thermal neutrons that issue from a hole in the ORNL Graphite Reactor shield. In September 1955, a new source plate (SP-2) that has several advantages over the old one (SP-1) was installed. The power of SP-2 is 5.18 ± 0.26 w, with a unit source strength of 1.30×10^{-2} w/cm^2.

40. DETERMINATION OF THE EFFECTIVE POWER OF THE OLD LID TANK SOURCE PLATE (SP-1)
J. Smolen 164

After installation of the new source plate (SP-2) at the LTSF, the power of the old source plate (SP-1) was determined by multiplying the power of SP-2 by a neutron leakage factor and dividing by an effective power ratio of the two plates. The results indicated a power of 1.7 w $\pm$11%.

41. EFFECTIVE NEUTRON REMOVAL CROSS SECTIONS OF CARBON AND OXYGEN IN CONTINUOUS MEDIA
D. K. Trubey and G. T. Chapman 167

Thermal-neutron flux measurements at the LTSF in media of water, oil, and a sugar-water solution have been used to calculate the neutron removal cross sections of carbon and oxygen distributed in continuous media. The values were 0.72 ± 0.05 barn for carbon and 0.92 ± 0.05 barn for oxygen.

42. THEORY OF THE $C^{13}(\gamma,n)C^{12}$ REACTION
E. Guth and G. deSaussure 167

A theoretical investigation of the $C^{13}(\gamma,n)C^{12}$ reaction has led to the conclusion that, in contrast with the $Be^9(\gamma,n)Be^8$ reaction, there is no evidence of resonance right above the threshold. This causes the $C^{13}(\gamma,n)C^{12}$ cross section to become much smaller (by about a factor of 10) than the corresponding $Be^9(\gamma,n)Be^8$ cross section.

43. ESTIMATION OF PHOTONEUTRONS FROM C^{13}
D. K. Trubey 168

LTSF measurements of thermal-neutron flux in the presence of high-energy gamma rays in liquid media containing hydrogen, or carbon and hydrogen, indicate that photoneutrons comprise a large fraction of the total thermal-neutron flux at large distances from the neutron source. This is attributed chiefly to the (γ,n) reaction in C^{13}. Measurements in an oil medium with and without a bismuth slab to reduce the gamma rays, and consequently the photoneutrons which they produced, agreed with calculated fluxes.

44. ENERGY AND ANGULAR DISTRIBUTION OF GAMMA RADIATION FROM A Co^{60} SOURCE AFTER DIFFUSION THROUGH MANY MEAN FREE PATHS OF WATER
R. W. Peelle, F. C. Maienschein, and T. A. Love 170

Measurements have been made of the energy and angle spectra of the photon energy flux resulting from 1.17- and 1.33-Mev gamma rays from a point source after diffusion in an infinite water medium. The two sources used had strengths of 100 curies and 195 mc, respectively. Spectral measurements were made with a Compton spectrometer having a peak-to-total ratio of 0.7 and a resolution of 14% (full width at half maximum) for 1.12-Mev photons. The resulting energy and angle spectra of the energy flux are compared, after integration over angle, with calculated results which have been obtained by the "moments method."

45. ENERGY AND ANGULAR DISTRIBUTION OF AIR-SCATTERED NEUTRONS FROM A MONOENERGETIC SOURCE
C. D. Zerby 180

A calculation of the energy and angular flux distribution of air-scattered neutrons is being made by using the Monte Carlo method. The source of neutrons can be taken as an isotropic point source, or a unit surface source, located in a sphere. The coding for calculation on the Oracle is near completion.

46. ENERGY ABSORPTION RESULTING FROM GAMMA RADIATION INCIDENT ON A MULTIREGION SHIELD WITH SLAB GEOMETRY
S. Auslender 180

The code of a Monte Carlo calculation of energy penetration and deposition resulting from transport gamma radiation in a shield of slab geometry has been used in a parametric study of a two-region lead-water shield. For the study the radiation was 1-Mev gamma rays incident on the slab at 0°, 60°, $70^\circ\,32'$, and $75^\circ\,31'$. Results of the calculation are presented.

47. MONTE CARLO STUDY OF THE GAMMA-RAY ENERGY FLUX, DOSE RATE, AND BUILDUP FACTORS IN A LEAD-WATER SLAB SHIELD OF FINITE THICKNESS
S. Auslender 184

The gamma-ray energy flux, dose rate, and buildup factors in a lead-water shield of finite thickness have been calculated by a Monte Carlo method for 1-, 3-, and 6-Mev photons incident on the slab both along a normal and at an angle of 60 deg. The results are compared with those obtained by use of the "moments method" for monoenergetic, plane monodirectional sources normally incident upon a semi-infinite, homogeneous medium. The calculations for lead agree reasonably well for the first few relaxation lengths, where the effects stemming from the dissimilarity of the slabs should be least.

VI. RADIATION DETECTOR DEVELOPMENT

48. FAST-NEUTRON SPECTROMETER DEVELOPMENT
R. B. Murray 191

A program is in progress that is aimed toward developing a fast-neutron spectrometer with a greater sensitivity than has been available heretofore. The types of spectrometers being considered are (1) proton-recoil spectrometers and (2) those in which the total energy released in a neutron-induced nuclear reaction is measured. For the latter the $Li^6(n,\alpha)H^3$ reaction (Q = 4.78 Mev) is being utilized.

49. INVESTIGATION OF THE HORNYAK BUTTON AS A FAST-NEUTRON DOSIMETER
F. J. Muckenthaler 199

In the interest of developing an improved fast-neutron dosimeter, an investigation of the Hornyak button as a dosimeter has been initiated. The button consists of a homogeneous mixture of fine Lucite and ZnS powder mounted on a phototube. The neutrons impinging upon the crystal collide with the protons present, and the recoiling protons excite the ZnS centers. These, in turn, emit photons that are detected by the photomultiplier tube. The response of the button to neutrons from Po-Be sources, the BSR, the TSR, and the Van de Graaff are presented.

50. INSTRUMENTATION FOR A GAMMA-RAY SPECTROMETER
T. A. Love, R. W. Peelle, and W. Zobel 208

In order to measure the time and energy spectra of short-lived fission-product gamma rays, it was necessary to modify the instrumentation for the BSF multicrystal gamma-ray scintillation spectrometer. The modifications in the existing equipment, and the new equipment added to the system are described.

51. PULSE-HEIGHT DISTRIBUTION FROM AN NaI(Tl) CRYSTAL
C. D. Zerby 214

A calculation of the relation between incident gamma-ray energy spectra and the pulse-height distribution from an NaI(Tl) crystal used as a gamma-ray spectrometer has been started.

VII. PROJECT SHERWOOD

52. DIFFUSION OF IONS IN A PLASMA ACROSS A MAGNETIC FIELD
A. Simon 217

The diffusion rate of ions across a magnetic field has been investigated both experimentally and theoretically. The resultant diffusion coefficient is found to vary inversely as the square of the magnetic field strength, in accord with the usual collision-diffusion theory. The magnitude of the coefficient is much larger (x 700) than the coefficient predicted by the usual ambipolar diffusion theory. This discrepancy is resolved by showing that diffusion across a magnetic field is *not* ambipolar in character in most arc experiments. The final experimental and theoretical values are in good agreement, and it is unnecessary to postulate any additional diffusion mechanisms, such as plasma oscillations.

53. DIFFUSION OF LIKE PARTICLES ACROSS A MAGNETIC FIELD
A. Simon 217

The diffusion rate across a magnetic field due to collision of like charged particles is derivable from the macroscopic equations of the plasma. However, it is necessary to include the off-diagonal terms in the stress tensor. The resultant diffusion rate does not obey Fick's law and is proportional to the inverse fourth power of magnetic field strength.

Part I

RESEARCH FOR

LIGHT-WATER-MODERATED REACTORS

1. CRITICAL EXPERIMENTS AT THE BSF

K. M. Henry E. B. Johnson J. D. Kington

Several critical experiments with the fuel elements for swimming-pool-type reactors being constructed elsewhere have been performed at the Bulk Shielding Facility (BSF). The first set of elements tested were those from the Aquarium Reactor, which was demonstrated by Oak Ridge National Laboratory at the Atoms-for-Peace Conference at Geneva in August 1955, and in a second experiment the criticality of the fuel elements of the Pennsylvania State University Reactor (PSUR) was tested. A series of critical experiments with the Bulk Shielding Reactor (BSR) elements has been performed by the 1955 class of the Oak Ridge School of Reactor Technology (ORSORT), and the effect on reactivity of voids adjacent to, and within, the BSR was investigated.

AQUARIUM REACTOR CRITICAL TESTS

The critical tests for the Aquarium Reactor were carried out in four steps: (1) the evaluation in terms of reactivity of a single Aquarium fuel element in a BSR lattice; (2) a preliminary critical test in the grid of the BSR, using Aquarium fuel elements except for those containing the control rods, which were BSR components; (3) the installation in the Aquarium grid of BSR elements in a known critical assembly to check instrumentation; and (4) the final (in this country) critical test, using the entire Aquarium Reactor assembly.

The elements for the Aquarium Reactor were of the MTR type, with UO_2 as the core material. The enrichment was 20%, each full element containing about 170 g of U^{235}. The rod elements contained approximately half this amount of material, or 85 g of U^{235}. Since these elements were the first pool-type reactor elements containing such a low fuel enrichment, the BSF measurements served to demonstrate the small effect of the lower enrichment on the critical mass.

Test Using Single Aquarium Element in BSR

A single Aquarium fuel element (No. G-1) was placed at various positions in the BSR lattice, and its effect on the reactivity was compared with that of a regular BSR element (No. B-106) in the same positions. The basic configuration was a cold[1] loading designated as ORSORT 18 (Fig. 1.1), which was a 5 by 5 fuel-element array with two additional elements, one on the east center line and the other on the west. Throughout the tests the two safety rods were completely withdrawn, and the position of the regulating rod at a low stable power level was observed. The change in reactivity resulting from the substitution of the Aquarium element for the standard BSR element was obtained from the calibration curve of the regulating rod. The results (Table 1.1) indicated that the Aquarium element contributed considerably more reactivity than did the BSR element.

Tests Using Aquarium Elements in the BSR Grid

Twenty full (170-g) Aquarium fuel elements were placed in the grid of the BSR and made critical with BSR instrumentation and the three BSR rod elements. The first loading (Fig. 1.2), which was the result of an attempt to find the minimum critical

[1]The term "cold" is used to designate loadings that consist of fuel elements that have not previously been operated at powers higher than 1 mw.

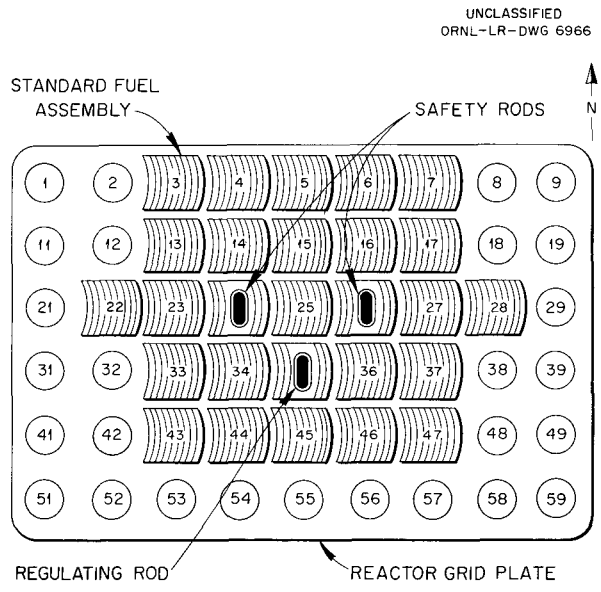

Fig. 1.1. BSR Reactor Loading (ORSORT 18) Used for Tests of Single Aquarium Element.

mass, was essentially a 5 by 5 fuel-element array with the two back corners missing. The total U^{235} content was 3615 g. The excess reactivity indicated by the regulating rod position was about 0.4%.

TABLE 1.1. EFFECT OF AN AQUARIUM ELEMENT IN THE BSR ON THE REACTIVITY

Lattice Position	Element	Distance Regulating Rod is Withdrawn (cm)	Change in Reactivity (% $\Delta k/k$)
3	BSR	44.7	+0.10
	Aquarium	40.2	
4	BSR	46.7	+0.14
	Aquarium	40.3	
5	BSR	44.4	+0.15
	Aquarium	37.6	
15	BSR	50.6	+0.18
	Aquarium	41.5	
25	BSR	53.3	+0.23
	Aquarium	41.0	

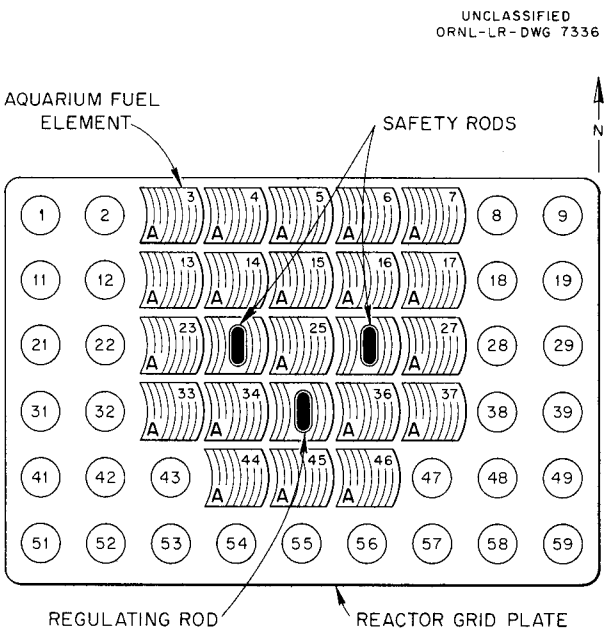

Fig. 1.2. Aquarium Loading No. 1 in BSR Grid.

The second Aquarium loading (Fig. 1.3) was the result of an attempt to mock up the Aquarium control rod and source element positioning and at the same time to approximate the 5 by 6 element BSR loading. In addition to the BSR control-rod elements, this configuration contained two other BSR partial elements – one in lattice position 15 and the other in lattice position 45. The U^{235} content of this loading was 3792.6 g, and the excess reactivity was about 0.5%. It was presumed from the test with the single Aquarium element that the substitution of Aquarium elements for the remaining BSR elements in either of these loadings would increase the excess reactivity of the loading.

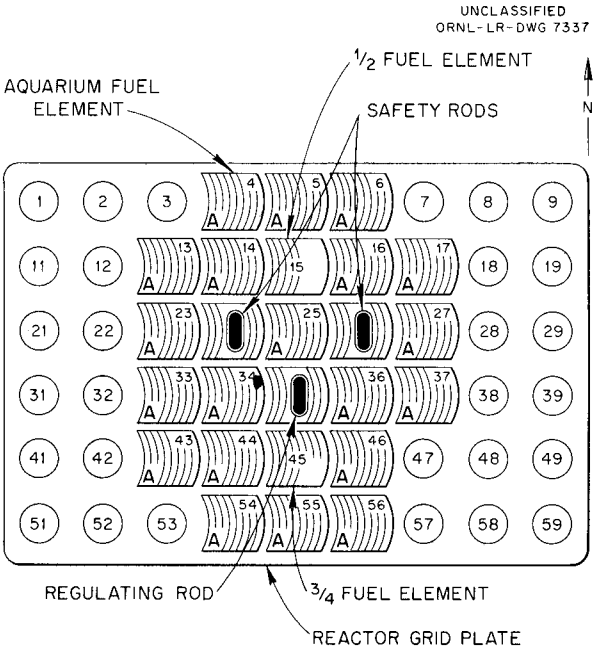

Fig. 1.3. Aquarium Loading No. 2 in BSR Grid.

Because of the stringent time schedule for the construction of the Aquarium Reactor no calculations of the critical mass were performed prior to the critical experiments. A comparison can be made with BSR loading No. 33, however, which contains 3636 g of U^{235}, with an excess reactivity of about 0.66%. This comparison shows that the design of the Aquarium elements was very conservative with respect to achieving criticality in a 6 by 5 element lattice.

Check of Aquarium Instrumentation

In order to provide a final check on the instrumentation and controls of the Aquarium Reactor,

the regular BSR "hot" elements were installed in the Aquarium grid and operated at power levels up to 100 kw. Since the Aquarium elements were to be shipped to Geneva, it was not possible to operate them at appreciable power levels.

Tests Using Aquarium Elements in Aquarium Grid

The final loading of the Aquarium elements in the Aquarium grid resulted in the same configuration as shown in Fig. 1.2, except that Aquarium rod elements were used rather than BSR rod elements. The total amount of U^{235} in this lattice was 3660.9 g. The excess reactivity could not be measured, since the Aquarium rods were not calibrated.

The results of the Aquarium Reactor experiments have been published elsewhere.[2]

PENNSYLVANIA STATE UNIVERSITY REACTOR CRITICAL TESTS

Critical tests were performed in the grid of the BSR with PSUR fuel elements, which contained highly enriched (~89%) fuel but had a lower metal-to-water ratio than BSR- or MTR-type elements and thus permitted a lower critical mass. Since the metal-to-water ratio was reduced by reducing the number of plates, the heat transfer potentialities of the elements were also reduced. A total of three configurations was assembled, each of which was completely reflected by water. In each loading the proposed positions of the four control-rod elements were simulated.

The fuel elements were modified MTR-type elements with the same outside dimensions as the BSR elements. A full element consisted of ten curved fuel-bearing plates brazed into flat aluminum side plates in such a way that cooling water could flow freely between the individual plates. Each fuel plate was of sandwich-type construction with a 28-mil-thick core of enriched uranium–aluminum alloy and a 20-mil-thick aluminum cladding on each side. Each full fuel element contained approximately 165 g of U^{235}. The elements through which the control rods moved consisted of seven fuel-bearing plates, giving a total of about 131 g of U^{235} in each element. There was one partial element which contained only five fuel plates and therefore had only about half the amount of U^{235} (~82 g) as a full element.

The first configuration (Fig. 1.4) consisted of 13 full fuel elements and the four control-rod elements. The total U^{235} content of this loading was 2666 g, and the excess reactivity[3] was about 0.5%.

A second configuration (Fig. 1.5) was a result of an attempt to fill the three vacant corners (see Fig. 1.4) by placing the partial element in a high flux region (position 15) and inserting a full fuel element into one of the corners. The resulting loading was symmetrical around the north-south center line but was not a perfect rectangle. It contained 13 full fuel elements, one partial fuel element, and four rod elements. The total amount of U^{235} in this lattice was 2749 g, and the excess reactivity[3] was about 0.7%.

[2] E. B. Johnson and K. M. Henry, *Reactivity Measurements with a Single Aquarium Fuel Element*, ORNL CF-55-5-118 (May 19, 1955); K. M. Henry, E. B. Johnson, and F. C. Maienschein, *Preliminary Critical Tests Using Aquarium Fuel Elements in the BSR Grid*, ORNL CF-55-5-189 (May 31, 1955).

[3] The amount of excess reactivity in each loading was determined from the position of the rods at criticality. The values quoted are a lower limit because they are based on the calibration of the pertinent rods in a larger loading and in a different rod configuration. It is known that these rods are more effective in smaller lattices, but the magnitude of the difference is not readily determined.

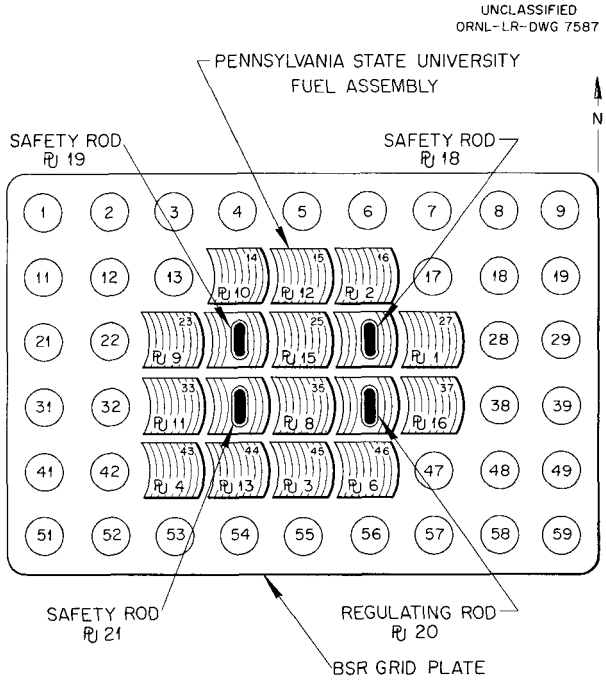

Fig. 1.4. Pennsylvania State University Reactor Critical Test No. 1.

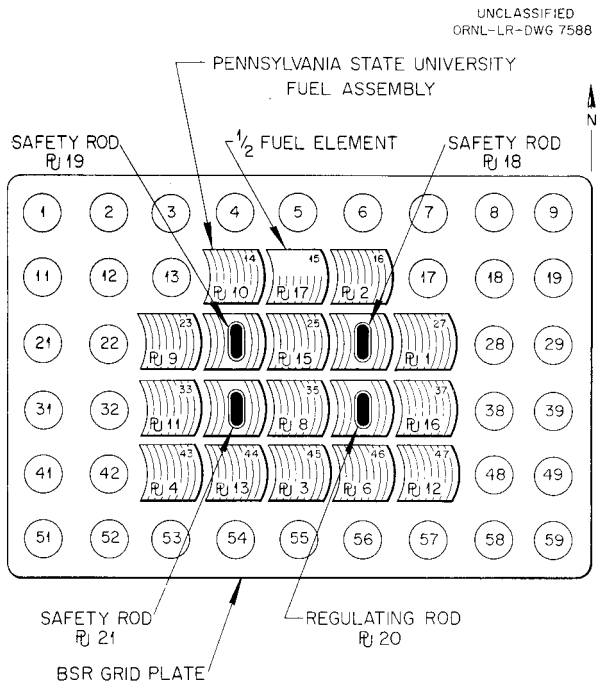

Fig. 1.5. Pennsylvania State University Reactor Critical Test No. 2.

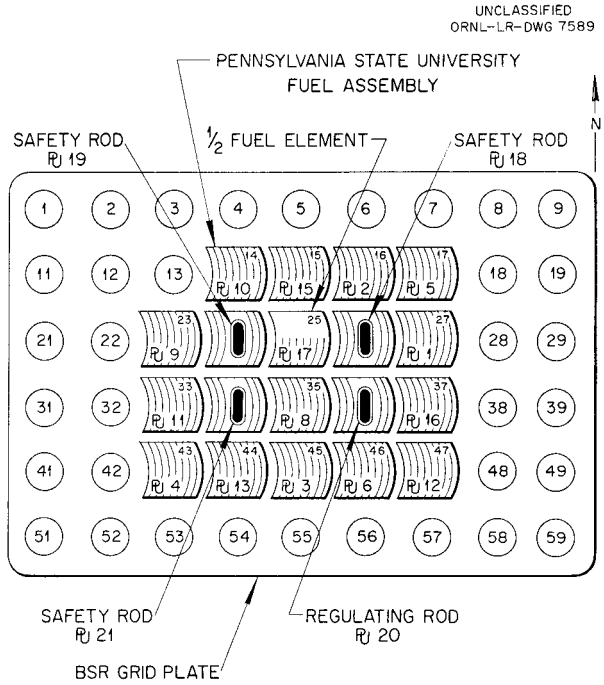

Fig. 1.6. Pennsylvania State University Reactor Critical Test No. 3.

In a third arrangement (Fig. 1.6) the partial element was moved from position 15 to position 25 (between two of the safety rods). The reactor was almost critical before a full fuel element was placed in the corner (position 17). With 14 full fuel elements, one partial element, and four rod elements the total amount of U^{235} was 2914 g, and the excess reactivity[3] was about 1%.

The observed reduction in critical mass of the lattice composed of these fuel elements over that of one composed of the BSR elements was expected, since the metal-to-water ratio of a full PSUR fuel element is 0.460, while that of a full BSR element is 0.715.

The critical mass calculated by Breazeale[4] agreed with the experimental value within 100 g. The details of the experiments have been published previously.[5]

[4]W. M. Breazeale, private communication.

[5]E. B. Johnson and K. M. Henry, *Critical Tests for the Pennsylvania State University Reactor*, ORNL CF-55-6-148 (June 30, 1955).

ORSORT TEST WITH THE BSR

During the past year approximately 180 Oak Ridge School of Reactor Technology students from two classes have performed experiments employing the BSR as a part of their laboratory course. The experiments were designed to acquaint the participants with the physical problems of the assembly of a reactor and to consolidate much of their theoretical training with practical experience. One of the experiments was a determination of the exact critical masses of several BSR loadings (Fig. 1.7). Each loading had less than 0.1% excess reactivity. A second experiment consisted in a measurement of the importance of epithermal neutrons in reactor control. In a third experiment the effect on the reactivity of inserting a small sample of either poison or fissionable material in various locations within the reactor was determined, and a fourth experiment was performed to measure the attenuation of the leakage thermal neutrons and gamma rays by the water surrounding the BSR.

These experiments were performed for and by the students, who served in every capacity. The classes were divided into groups, usually about seven students in each. The members were rotated

UNCLASSIFIED
2-01-058-0-8

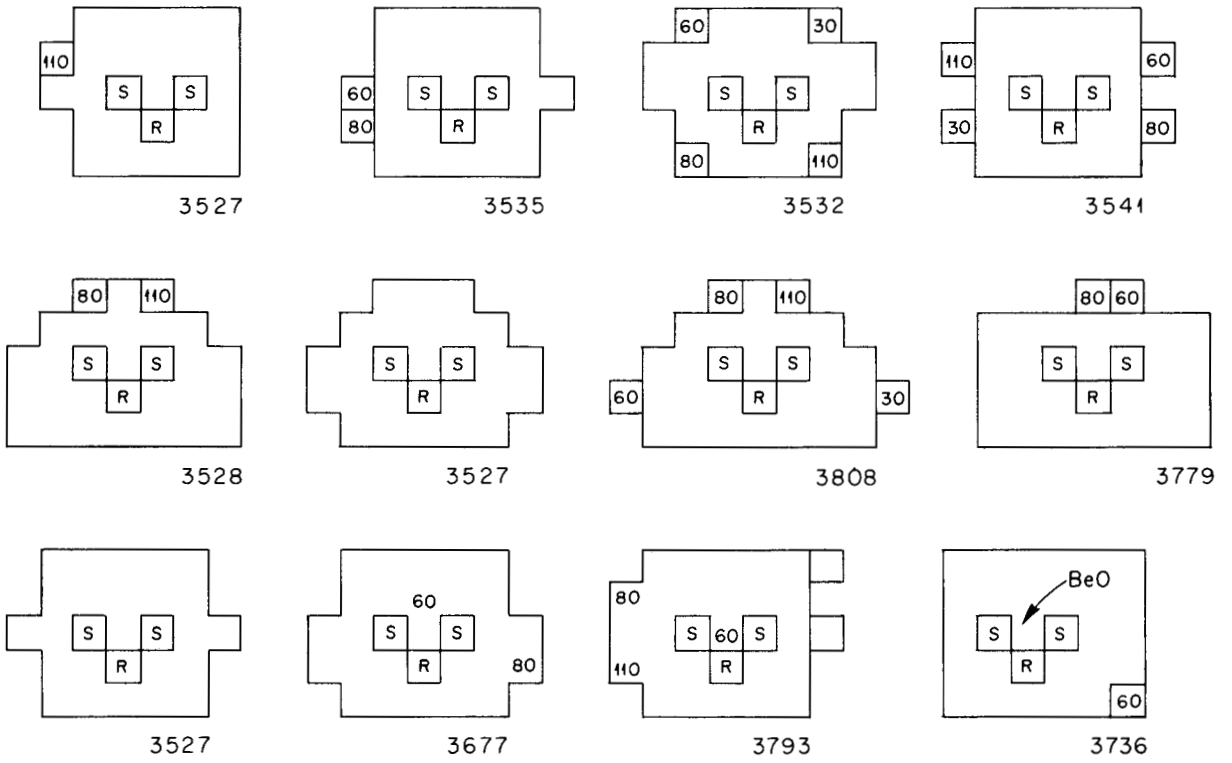

NOTE: ALL NUMERICAL VALUES INDICATE GRAMS OF URANIUM

S SAFETY ROD ELEMENT, 69 g
R REGULATING ROD ELEMENT, 69 g
BeO BERYLLIUM OXIDE ELEMENT

Fig. 1.7. BSR Loadings During ORSORT Experiments.

from assignment to assignment so that all of each group had experience with each portion of the experiment. The staff members of the BSF supervised the experiments, acted as instructors, and also ensured that all operations were conducted in a safe manner.

EFFECT OF A VOID ADJACENT TO THE BSR ON THE REACTIVITY

Several pool-type reactor installations are being designed, most of which incorporate irradiation test facilities extending through the reflector to the reactor core. These proposed beam tubes range in size from a few inches in diameter to facilities covering one or more faces of the reactor. The presence of the large voids will necessitate considerable excess reactivity in addition to that required for operation without voids, and the possible flooding of such chambers represents a potential hazard for a reactor of this type. Since these effects on the reactivity were uncertain, and because it was felt that they could not be adequately treated by existing calculational techniques, a series of experiments was performed with the BSR to determine the magnitude of the reactivities involved.

The particular configuration chosen for installation in the pool of the BSF consisted of a large (26 × 22½ × 36 in.) air-filled tank placed against one of the faces of the reactor lattice.

In addition to the void, two curtains of sufficient size to completely cover the face of the void were provided. One of these was made of 100-mil-thick cadmium and the other of ¼-in.-thick boral. The effect of the void on the reactivity was measured with and without each of these curtains inserted between the reactor and the void. Three iron slabs (½, 1½, and 3 in. thick) were used in conjunction with the neutron-absorbing curtains to simulate experimental equipment placed inside the void. Whenever any of the iron slabs was in place, a neutron-absorbing curtain was adjacent to the reactor. The differences in reactivity in each experiment were determined from the measured positions of the BSR control rods at criticality.

Data showing the change of reactivity produced by flooding the initially air-filled void are presented in Table 1.2. The largest change was observed when there was no curtain between the reactor and the void (+2.62% $\Delta k/k$). When the cadmium curtain was inserted the reactor was shielded sufficiently to reduce the change in reactivity to +0.60% $\Delta k/k$, while the boral curtain reduced the change to +0.42% $\Delta k/k$. Curve A of Fig. 1.8 shows graphically the results of incremental flooding of the void with no curtain between it and the reactor, while curve B shows corresponding data when the boral curtain was between the reactor and the void. It should be pointed out that in the BSF experiment these changes in reactivity occurred very slowly, since it required approximately 50 min to completely fill the void. Such, of course, would not be the case in an accident if the void should suddenly collapse or become physically separated from the reactor.

This experiment is reported in detail elsewhere.[6]

TABLE 1.2. CHANGES IN REACTIVITY RESULTING FROM FLOODING THE INITIALLY AIR-FILLED VOID WITH WATER

Experimental Condition	Change in Reactivity (% $\Delta k/k$)
No curtain	+2.62
Cadmium curtain	+0.60
Cadmium curtain plus ½-in.-thick iron slab	+0.49
Cadmium curtain plus 3-in.-thick iron slab	+0.15
Boral curtain	+0.42
Boral curtain plus ½-in.-thick iron slab	+0.33

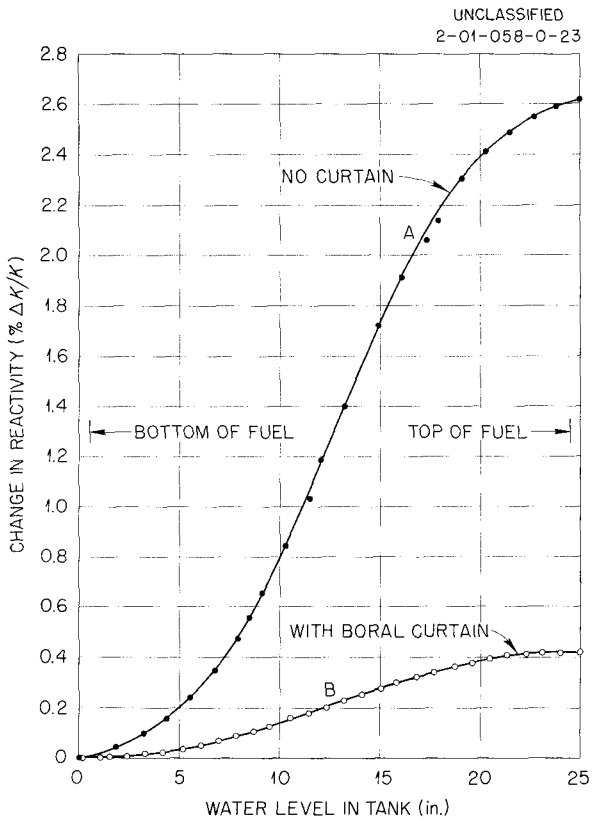

Fig. 1.8. Change in Reactivity Resulting from Flooding the Tank Adjacent to the BSR.

EFFECT OF VOIDS WITHIN THE BSR CORE ON THE REACTIVITY

In order to gain access to the higher fluxes within the cores of some of the pool-type research reactors now being constructed, proposals are being made to incorporate experimental facilities

[6] E. B. Johnson, K. M. Henry, and J. D. Flynn, *The Reactivity Effect of an Air Tank Against One Face of the Bulk Shielding Reactor*, ORNL-2179 (in press).

of various sizes within the core. Such facilities would consist of regions in which fuel has been replaced either by an experiment or by a moderator. Since either type of void will perturb the flux distribution and therefore the reactivity of the reactor, it is necessary to have some knowledge of the magnitude of such perturbations for reactor design.

A series of experiments to determine the effect on the reactivity of introducing voids within the core has been performed. The reactor loading used was a 3 by 7 fuel-element array reflected on one vertical side by 3 in. of beryllium oxide and on the opposite side by 6 in. of beryllium oxide (Fig. 1.9). Two additional safety devices in the

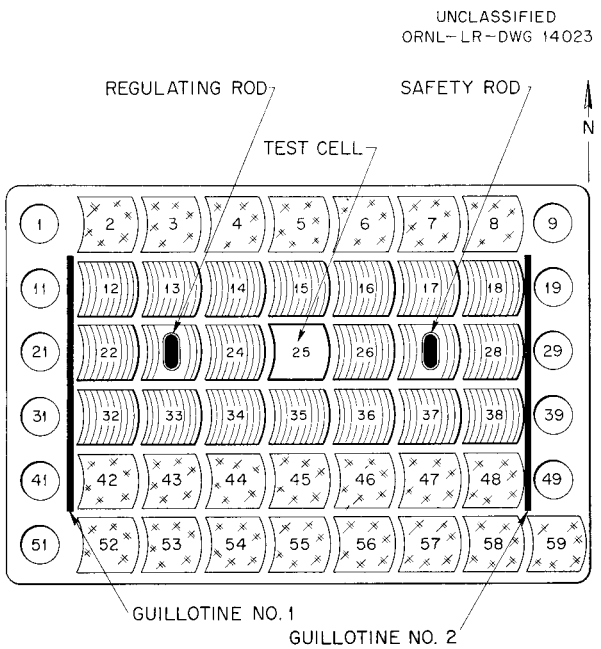

Fig. 1.9. BSR Loading No. 53.

form of cadmium guillotines in two opposite sides of the reactor were employed throughout the experiments. Most of the voids were introduced in position 25 of the loading.

Effect of Removing Fuel Plates from an Element

In one phase of these experiments, 12 of the 18 fuel plates in a special element were removed successively. The two outside plates and the four central plates, which are brazed into the element, were not removed. Several different sequences of fuel-plate removal were used, two of which are shown in Fig. 1.10. In sequence A

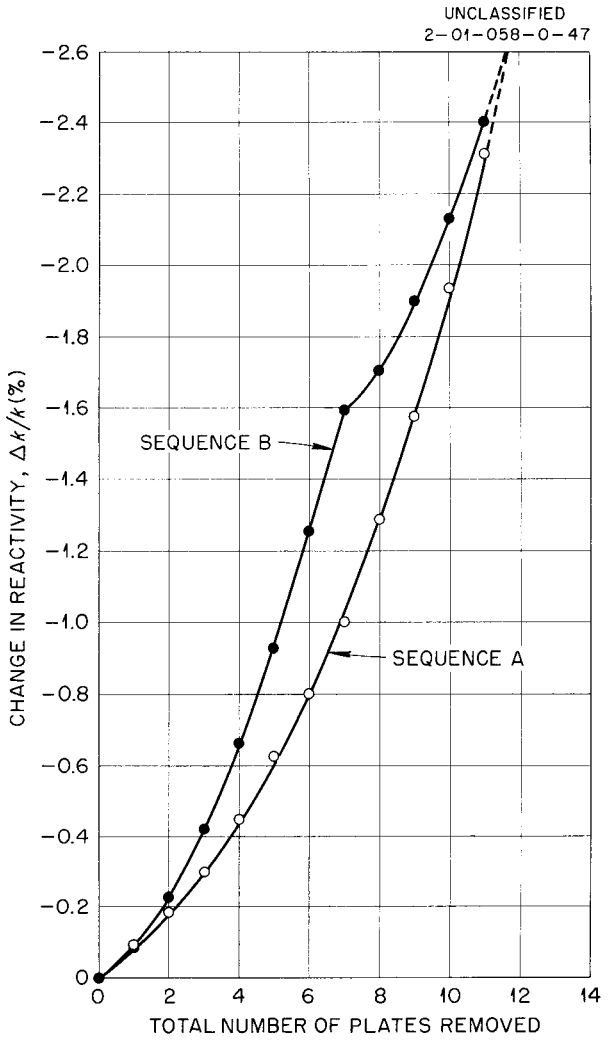

Fig. 1.10. Reactivity Changes Effected by the Removal of Plates from a BSR Element.

each successive plate was removed from the center of the region still containing the greater amount of fuel. In sequence B the plates were removed first from one side of the element, then from the other. The order of plate removal results in differently shaped curves, all of which apparently come to the same end point, as expected. (Since this reactor is limited to an excess reactivity of 2.5%, it was not possible to remove the last or twelfth plate in any sequence and maintain criticality.) At point 7 of sequence A, alternate plates had been removed from the element; in another sequence, alternate plates were removed, first from one side of the element, then from the other. The end point of this

sequence coincided with point 7, although the curve shape was different.

Effect of Introducing Voids Between Fuel Plates

In another phase of the experiment the water channels in a regular BSR element was separately blocked so that the water could be replaced with air in any or all channels. Aluminum tubes were welded in the pieces of metal at the top and bottom of the channels but did not extend into the channels themselves. This arrangement ensured that the aluminum-to-water ratio in the active part of the element remained unchanged. Plastic tubing was attached to the aluminum tubes and extended into a manifold at the side of the pool.

The effect on the reactivity of two sequences of water removal is shown in Fig. 1.11. For sequence A the net change in reactivity was approximately 2.3%, while for sequence B the change was 1.4%. In each case the reactivity change was negative when water was removed from the channels between the fuel plates. This, of course, is the mechanism which has been traditionally postulated for reactor shutdown following runaway.

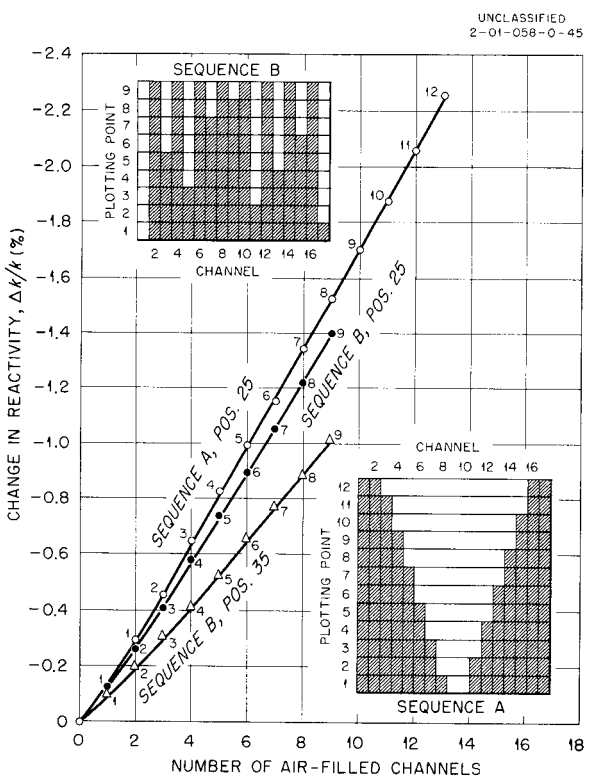

Fig. 1.11. Reactivity Changes Effected by the Removal of Water from a BSR Element.

Effect of Air- or Water-Filled Aluminum Boxes in a Rod Element

Apparently, positive coefficients were observed when voids were located within a regular BSF rod element (also located in position 25). The size of the void was defined by aluminum boxes which could be inserted into the center of a rod element. These boxes, filled alternately with air and water, were located at various positions above and below the center line of the fuel. Figure 1.12 shows the result of such a vertical traverse with the 4-in.-long box. The traverse made with the water-filled box gave a zero or a positive change in reactivity. In the case of the air-filled box, the change in reactivity was negative toward the top of the element, definitely positive as the box was inserted farther, and then was negative again toward the bottom of the element. Similar traverses made with 12- and 20-in.-long boxes showed essentially the same effect.

The question arose as to whether the presence of the aluminum box itself was the reason for the positive reactivity, or whether the partial beryllium oxide reflector was responsible. To investigate the first possibility, two other tests were performed. In the first one a traverse was made with a solid block of aluminum having the same dimensions as the outside of the 4-in.-long box, the results of which are also shown in Fig. 1.12. In the second test the central channel of the rod element was blocked at the top and bottom so that the water could theoretically be removed incrementally without the introduction of extraneous material into the element. This experiment yielded nonreproducible results, possibly because the experimental arrangement was too crude to accurately control or reproduce the water level inside the element.

To investigate the influence of the partial beryllium oxide reflector further, some of the above experiments were repeated in another reactor loading that was completely water-reflected and which had a larger core volume. Positive reactivity changes were again observed with the aluminum boxes, although the effect was not so great as in the smaller beryllium-oxide-reflected loading. Of course, the importance of a given perturbation should be less in a larger core than in a small one.

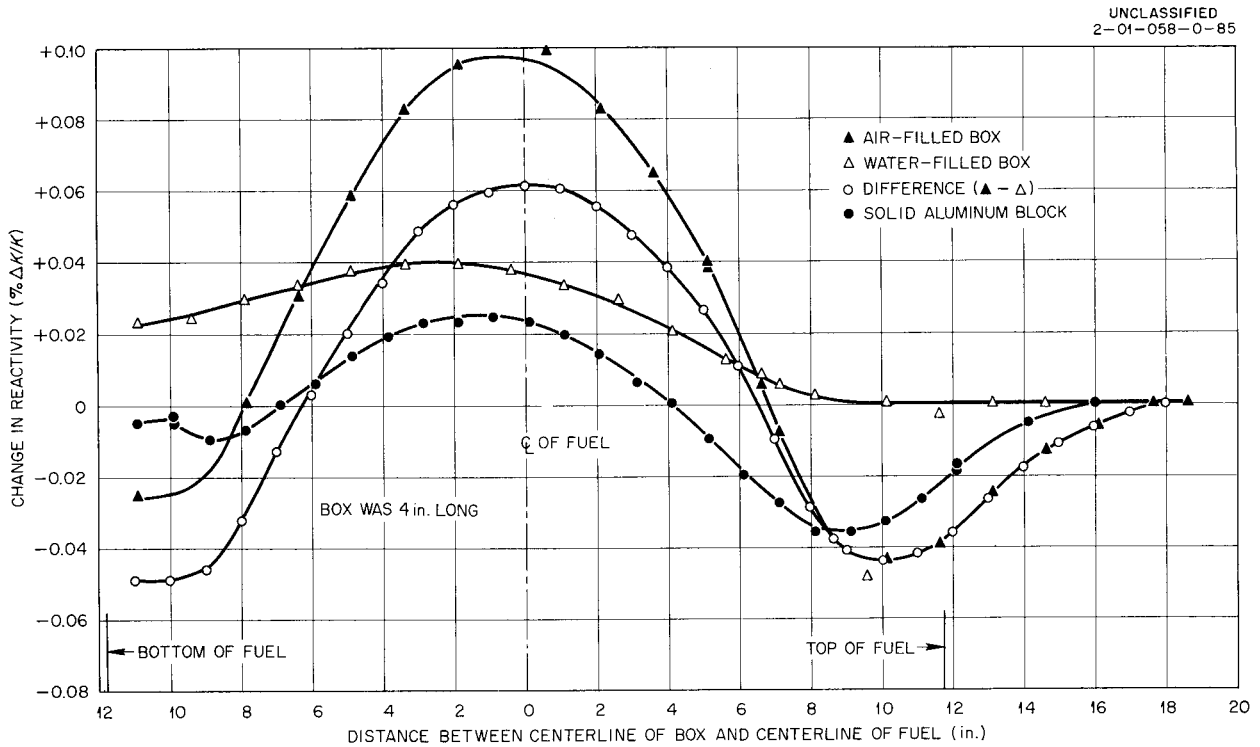

Fig. 1.12. Effect on BSR Reactivity of a Vertical Traverse of Air-, Water-, or Aluminum-filled Boxes in Position 24 of Loading No. 53..

2. EFFECT OF THE REFLECTOR ON THE NEUTRON FLUX IN AN ORR BEAM HOLE MOCKUP

K. M. Henry E. B. Johnson J. D. Kington

The advantage of increasing the flux leakage into beam tubes adjacent to a research reactor without appreciably increasing the total or peak heat generation in the reactor is apparent. For reactors using MTR-type fuel elements in water, a possible simple approach to the problem would consist in changing the reflector (light water) on the face of the reactor against which the beam hole is positioned to one which has less neutron absorption (heavy water). This change would tend to flatten the reactor flux profile and thus help offset the reactivity change introduced by the beam tube. If the reflector were extended an appreciable distance so as to surround the beam tube, it should give rise to higher thermal-neutron fluxes within the tube. The feasibility of this approach for the Oak Ridge Research Reactor (ORR) has been investigated in a series of tests at the BSF.

In the first tests, a tank, in the shape of a right parallelepiped, containing four concentric tubes which were 6, 10, 14, and 18 in. in diameter and 3 to 4 ft long, was placed against the reactor face. The tank was sufficiently large to cover the reactor face. The largest volume in the tank contained either H_2O or D_2O, while the concentric cylinders contained either air, H_2O, or D_2O in various sequences.

The reactor loading (Fig. 2.1) used for these tests was the result of an attempt to mock up a slab geometry and yet retain sufficient reactivity in the control rods to perform the tests without the necessity of changing configurations. The core was moderated by water and reflected by water on five faces. The test tank was adjacent to the north (nine-element) face. The power of the reactor was determined by the standard BSR instrumentation (servo chamber).

For further tests a second tank (Fig. 2.1), which appeared to be a segment of a cylinder and which was a realistic mockup of the proposed ORR installation, was placed against the nine-element reactor face. It contained six independent beam tubes, the central tube being positioned approximately 6 in. above the horizontal center line of the reactor. All measurements were made in the central beam tube, and the contents of the other tubes were changed to simulate different experimental apparatus. Again, the reflector, or largest volume in the tank, was either H_2O or D_2O during these tests.

The central air-filled beam tube was a 6-in.-OD aluminum cylinder which extended from the north reactor face for a distance of 16 ft. Only the first 12-ft length was used in these tests. At the north end of the tube another cylinder was placed perpendicular to the horizontal tube; this cylinder extended above the water level. Small, flexible stainless steel cables positioned a "sled" which carried a spiral U^{235} fission chamber and its preamplifier along the tube axis. The stainless steel cable was connected to a linear potentiometer which was used to indicate the sled and fission-chamber positions on a two-dimensional plotter.

The U^{235} fission chamber ($\frac{1}{2}$ in. in diameter by $\frac{3}{4}$ in. long) was mounted on the end of an 18-in.-long brass tube. During one test to investigate the effect of a heavy absorber, the fission chamber was surrounded by stainless steel. The fission pulses were amplified by a conventional preamplifier combination and were fed to both a log count-rate meter and a scaler. Plots of the counting rate as a function of the detector position were made directly on the two-dimensional plotter. Measurements of the reactor leakage flux at other positions outside the core were made with the reactor fission chamber, located above the core, and two additional fission monitors located at the side and at the rear of the reactor. In addition, a small number of gold foils were exposed within the reactor core for each variation of the reflector condition.

The results of the U^{235} fission chamber measurements in the beam tube of the parallelepiped tank are shown in Fig. 2.2. The responses of the gold foils, the reactor servo chamber, the reactor fission chamber, and two external detectors during the runs are summarized in Table 2.1. Run 1 does not have the supporting values of external monitors and foils and is included in Fig. 2.2 merely to show the effect on the thermal-neutron flux of the displaced moderator around the beam tube.

The results of the measurements in the ORR beam hole mockup are plotted in Figs. 2.3, 2.4, and 2.5. Runs 1 through 8 (Figs. 2.3 and 2.4)

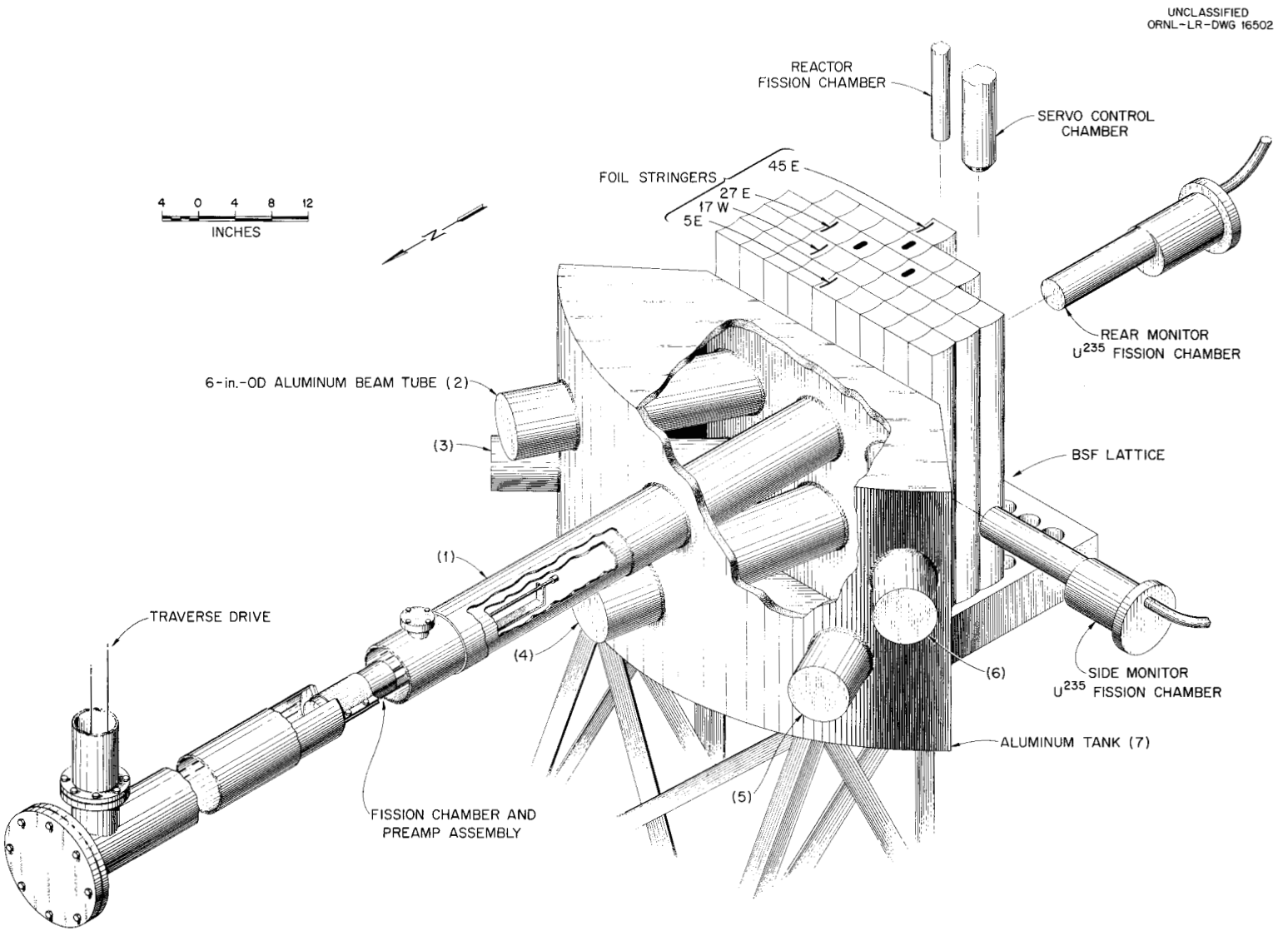

Fig. 2.1. Mockup of an ORR Beam Hole.

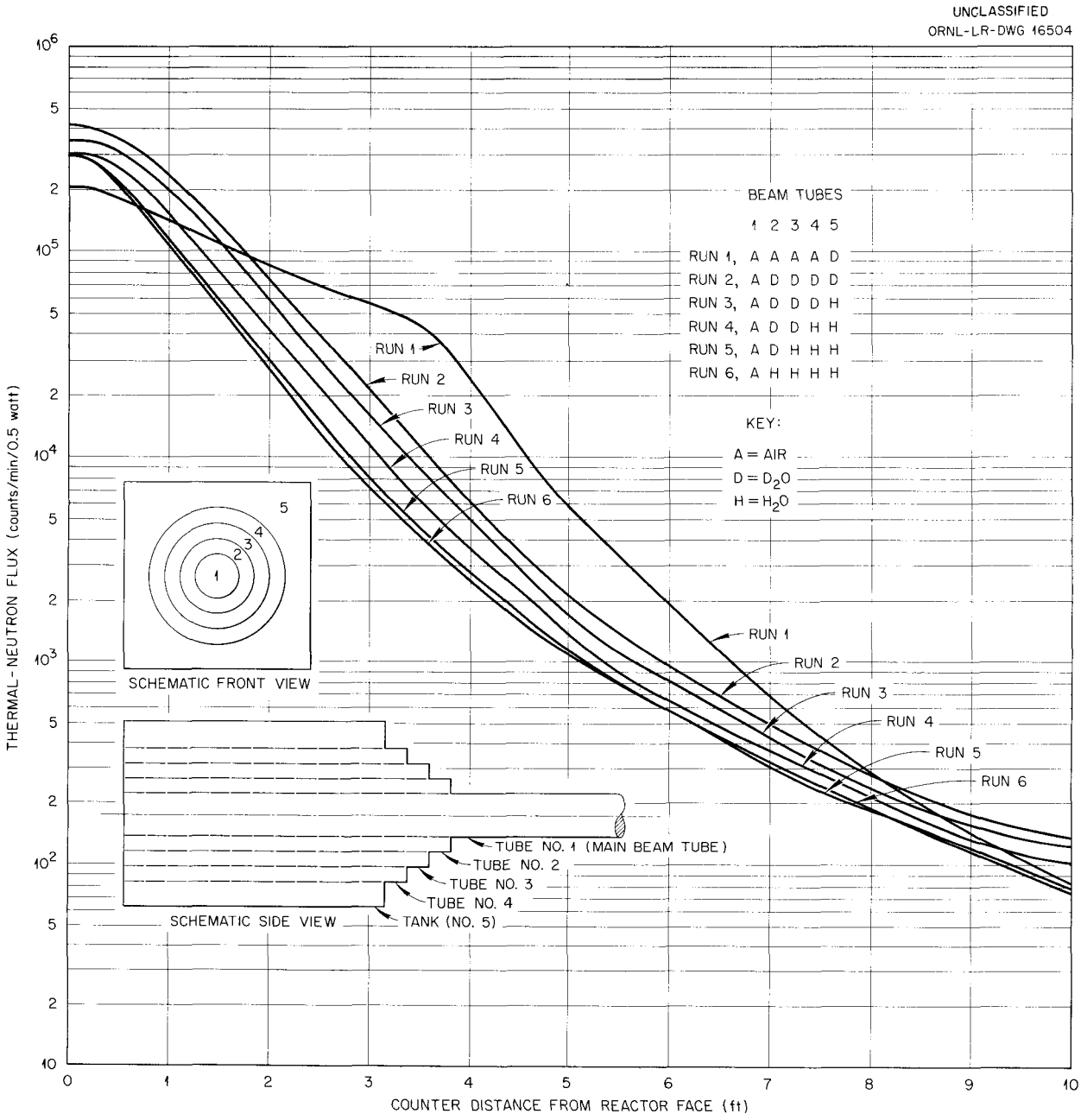

Fig. 2.2. Thermal-Neutron Flux in Air-filled Beam Tube in Parallelepiped Tank for Various Reflector Conditions.

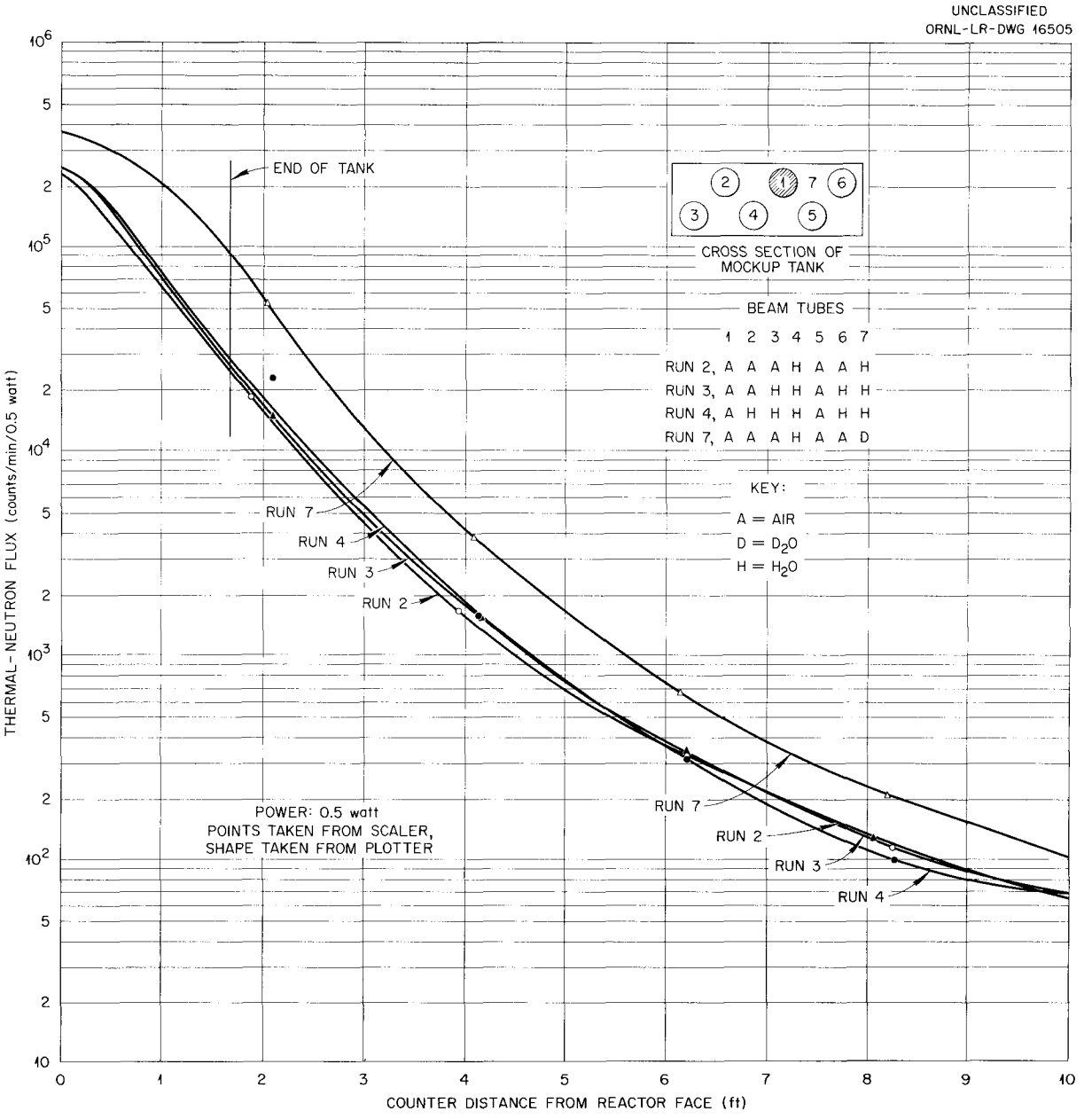

Fig. 2.3. Thermal-Neutron Flux in Air-filled Beam Tube in ORR Beam Tube Mockup Tank for Various Reflector Conditions (Bare U^{235} Fission Chamber) (Runs 2, 3, 4, and 7).

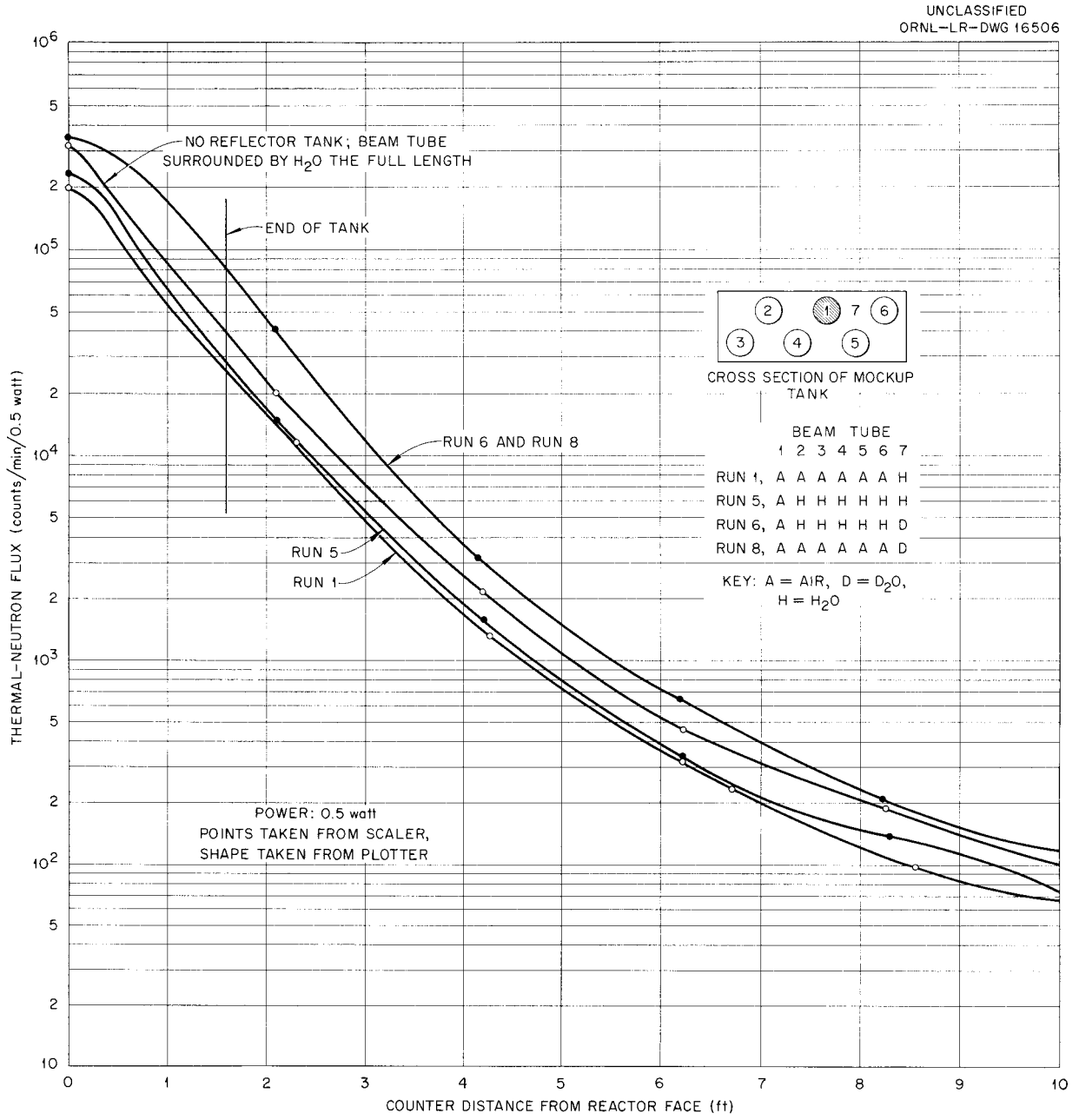

Fig. 2.4. Thermal-Neutron Flux in Air-filled Beam Tube in ORR Beam Tube Mockup Tank for Various Reflector Conditions (Bare U^{235} Fission Chamber) (Runs 1, 5, 6, and 8).

were with a bare U^{235} fission chamber, while runs 9 through 12 (Fig. 2.5) were with a stainless-steel-covered fission chamber (1.6-in. minimal thickness). The corresponding measurements with the other detectors during these runs are summarized in Table 2.2.

The results appear to demonstrate that an appreciable increase in the thermal-neutron flux within the beam tube results from the substitution of the partial heavy-water reflector. However, the degree of certainty of such a conclusion is reduced by the perturbations of the reactor flux distributions caused by the reflector changes. It was not possible in a reasonable length of time to obtain sufficient foil exposure data to determine the extent of the flux distribution changes. It was recognized before the experiment was started that such a limitation would exist, but the experiment was carried out in order to provide engineering data sufficient to choose the reflector for the ORR.

Future similar experiments should profit greatly from the use of the wire scanner now available at the BSF. It is expected that wires may be exposed and scanned in only a fraction of the time that would be required for foil exposure and counting.

TABLE 2.1. THERMAL-NEUTRON FLUX MEASUREMENTS WITHIN AND OUTSIDE THE BSR FOR VARIOUS REFLECTOR CONDITIONS DURING THE PARALLELEPIPED TANK TESTS

Detector	Detector Position	Normalized Thermal-Neutron Flux				
		Run 2, ADDDD[a]	Run 3, ADDDH	Run 4, ADDHH	Run 5, ADHHH	Run 6, AHHHH
Flux Normalized to Response of Foil in Position 5E, on ℄, During Run 6						
Gold foil	5E;[b] on ℄[c]	1.52	1.40	1.25	1.09	1.00
	5E; 6 in. above ℄	1.21	1.10	0.98	0.86	0.85
	5E; 6 in. below ℄	1.49	1.37	1.14	0.94	0.90
	17W; on ℄	1.64	1.54	1.45	1.30	1.27
	17W; 6 in. above ℄	1.18	1.08	1.06	0.97	0.99
	17W; 6 in. below ℄	1.50	1.41	1.21	1.06	1.03
	27E; on ℄	1.27	1.20	1.11	1.00	1.00
	27E; 6 in. above ℄	0.89	0.83	0.81	0.75	0.77
	27E; 6 in. below ℄	1.13	1.03	0.92	0.81	0.80
	45E; on ℄	0.92	0.80	0.91	0.75	0.77
	45E; 6 in. above ℄	0.61	0.58	0.62	0.55	0.57
	45E; 6 in. below ℄	0.87	0.79	0.78	0.62	0.62
Flux Normalized to Response of Detector During Run 6						
Reactor servo chamber		1.00	1.00	1.00	1.00	1.00
Reactor fission chamber		1.04	1.04	0.96	0.97	1.00
External fission chamber	At side of reactor		2.43	1.36	1.03	1.00
	At rear of reactor		1.30	1.17	0.72	1.00
U^{235} fission chamber	In beam tube	1.69	1.45	1.22	1.06	1.00

[a]A = air, D = D_2O, and H = H_2O; the first four symbols designate the contents of beam tubes 1 through 4, respectively; the last symbol designates the contents of the largest volume of the parallelepiped.

[b]Lattice position in reactor.

[c]Horizontal center line.

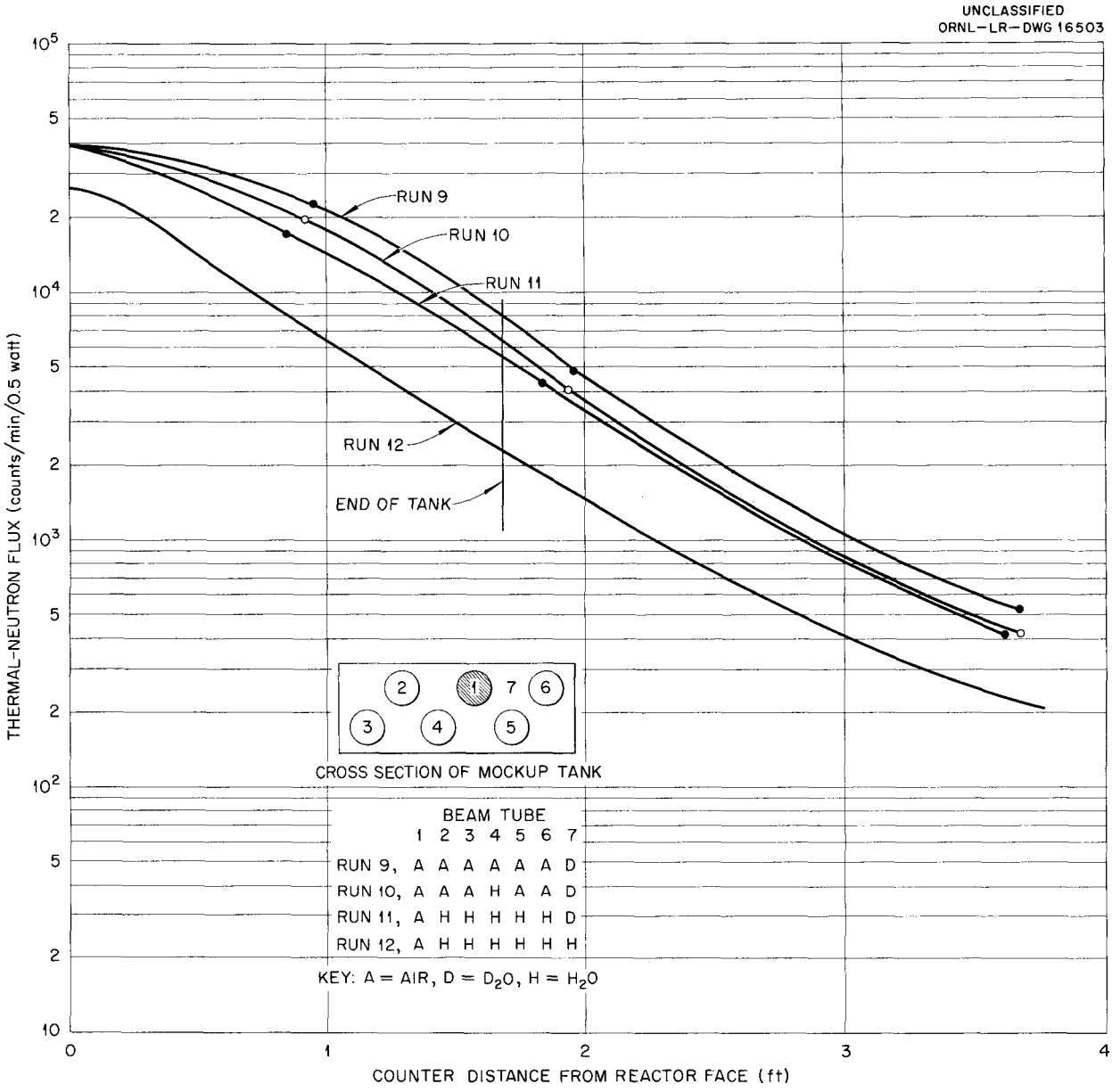

Fig. 2.5. Thermal-Neutron Flux in Air-filled Beam Tube in ORR Beam Tube Mockup Tank for Various Reflector Conditions (Stainless-Steel-Covered U^{235} Fission Chamber).

TABLE 2.2. THERMAL-NEUTRON FLUX MEASUREMENTS WITHIN AND OUTSIDE THE BSR FOR VARIOUS REFLECTOR CONDITIONS DURING THE ORR BEAM TUBE MOCKUP TESTS

Detector	Detector Position	Normalized Thermal-Neutron Flux											
		Run 1, AAAAAAH[a]	Run 2, AAAHAAH	Run 3, AAHHAHH	Run 4, AHHHAHH	Run 5, AHHHHHH	Run 6, AHHHHHD	Run 7, AAAHAAD	Run 8, AAAAAAD	Run 9, AAAAAAD	Run 10, AAAHAAD	Run 11, AHHHHHD	Run 12, AHHHHHH
		Flux Normalized to Response of Foil in Position 5E, on ℄, During Run 1											
Gold foil	5E;[b] on ℄[c]	1.00	1.04	1.16	1.18	1.20	1.46	1.44			1.42		
	5E; 6 in. above ℄	0.74	0.73	0.78	0.81	0.80	1.01	0.99			0.97		
	5E; 6 in. below ℄	0.82	0.91	1.01	1.01	1.06	1.33	1.32			1.31		
	17W; on ℄		1.26	1.36	1.37	1.42	1.55	1.55			1.55		
	17W; 6 in. above ℄		0.93	0.97	1.01	1.00	1.08	1.08			1.08		
	17W; 6 in. below ℄		1.06	1.15	1.18	1.21	1.41	1.39			1.40		
	27E; on ℄	1.01	1.00	1.15	1.13	1.18	1.26	1.22			1.26		
	27E; 6 in. above ℄	0.77	0.76	0.82	0.83	0.84	0.89	0.87			0.89		
	27E; 6 in. below ℄	0.83	0.85	0.94	0.94	0.99	1.11	1.10			1.10		
	45E; on ℄	0.75	0.71	0.87	0.85	0.83	0.81	0.86			0.87		
	45E; 6 in. above ℄	0.55	0.49	0.61	0.60	0.55	0.54	0.57			0.60		
	45E; 6 in. below ℄	0.62	0.67	0.76	0.74	0.72	0.76	0.80			0.81		
		Flux Normalized to Response of Detector During Run 1											
Reactor servo chamber		1.00	1.00	1.00	1.00	1.00	1.00	1.00	1.00	1.00	1.00	1.00	1.00
Reactor fission chamber		1.00	1.01	1.03	1.02	1.05	1.09	1.09	0.97	1.18	1.20	1.33	1.09
External fission chamber	At side of reactor	1.00	1.07	0.91	0.94	0.99	1.18	1.21	1.22	1.22	1.17	1.20	0.98
	At read of reactor	1.00	0.98	1.09	1.03	1.11	1.13	1.16	1.04	1.14	1.09	1.15	1.12
U^{235} fission chamber	In beam tube	1.00	1.04	1.13	1.11	1.11	1.72	1.67	1.71	0.18	0.18	0.18	0.12

[a]A = air, D = D_2O, and H = H_2O; the first six symbols designate the contents of the beam tubes 1 through 6, respectively; the last symbol designates the contents of the largest volume of the mockup tank.

[b]Lattice position in reactor.

[c]Horizontal center line.

3. SENSORY INSTRUMENTATION STUDIES FOR THE BSR

K. M. Henry J. N. Anno[1]

A series of experiments was performed to check the saturation properties and linearity of response of the ionization chambers which supply the basic signals for control and power-level indication of the BSR. Three ORNL-type Q-1045 gamma-compensated chambers, a log N chamber, a servo chamber, and a galvanometer chamber, are used as neutron flux detectors in the BSR instrumentation. The log N chamber is a sealed chamber which actuates the log reactor power indicator, recorder, period meter, and period scram circuit. The servo chamber actuates the servo recorder and is responsible for the automatic operation of the reactor, and the galvanometer chamber sends a signal to a Leeds & Northrup galvanometer, which gives a direct indication of the neutron flux.

SATURATION PROPERTIES OF THE BSR CHAMBERS

The saturation properties (i.e., the current as a function of voltage) of the three gamma-compensated chambers were examined by measuring the output current to each electrode as a function of electrode voltage for various nominal reactor powers. The output current of the boron-coated section was a measure of the ionization due to both alpha particles (from the $B^{10}(n,\alpha)Li^7$ reaction) and gamma rays. The output current of the other section was a measure of the ionization caused by gamma rays alone. Typical results of the tests for the three chambers are plotted in Fig. 3.1.

In order to observe any variation with age in the saturation properties of the log N chamber, the results of this most recent test (performed December 12, 1955, after the chamber had been exposed to 128,000 μa-hr) were compared with those of two earlier tests. The first measurement[2] was made November 27, 1953, during the initial chamber exposure. Several months later, after 11,185 μa-hr of operation, the chamber was again checked. Each of the saturation curves from the three tests was normalized to a net current of 58 μa with 650 v on the positive electrode and 300 v on the negative electrode. A comparison of the results (Fig. 3.2) showed that the characteristics of the chamber have changed no more than about 0.4% (at 600 v) since its initial installation.

LINEARITY OF THE BSR CHAMBERS

In an experiment to determine the actual power of the BSR at various power demand levels (control settings), readings from a BF_3 counter, a U^{235} fission chamber, and a compensated Q-1045 chamber, which were located at relatively large distances through the water shield from the reactor, were compared with those from three reactor chambers. It was assumed that local changes of reactor characteristics, which are seen by the reactor chambers, would not be seen by the chambers located at greater distances. For these chambers the reactor would appear to be a large point source, and the chamber output should be proportional to the total power output. All detectors were operated in their linear or compensated ranges.

Several geometries were used. In the first geometry the external detectors were placed on the horizontal center line of the reactor, and the reactor chambers were positioned so as to give approximately 50 μa of current for 100 kw of reactor power. (Chamber currents larger than 50 μa were not permitted so as to ensure a completely linear response.) The response of each chamber is given in Table 3.1. For a second test the reactor chambers were moved up far enough so as to give only 5 μa for 100 kw. Thus the reactor could have been operated at 1 Mw without exceeding the previous chamber current, but it was actually restricted to 500 kw in deference to the radiation level at the pool surface. In an effort to magnify the relative effect of activated water observed in the second test, the reactor chambers were repositioned so as to give a reading of 0.5 μa at 100 kw. The absence of any observable change seems to indicate that the activated water is not the source of the nonlinearity.

In another geometry the Q-1045 chamber and the U^{235} fission chamber were successively located 4 in. in front of, and 6 in. below, the corner of the reactor core.

---

[1]Battelle Memorial Institute.

[2]Measurements were made by J. G. Gundlach of the Instrumentation and Controls Division.

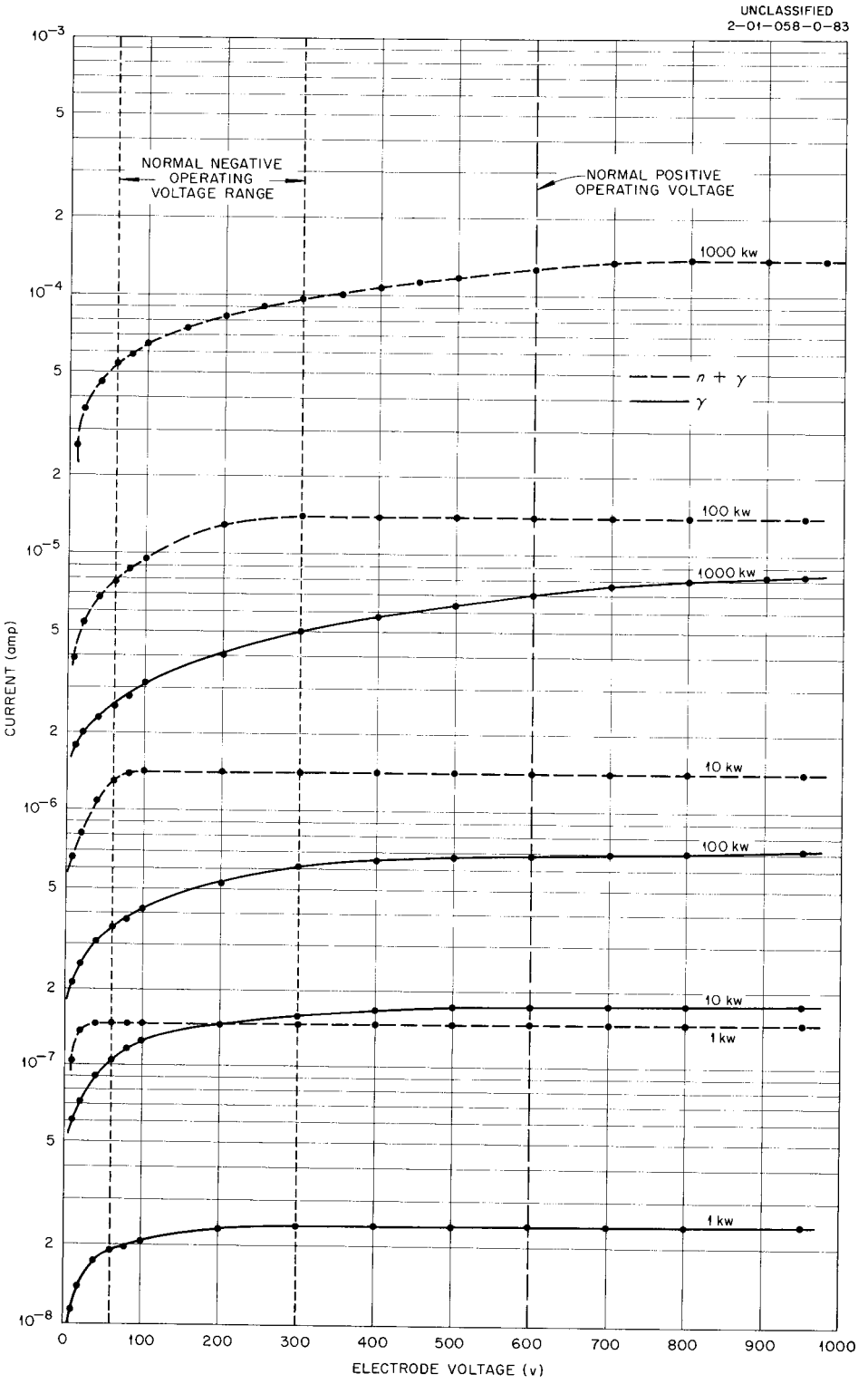

Fig. 3.1. Saturation Properties of Log N Chamber of the BSR for Various Operating Powers.

In a third geometry additional measurements were made along the horizontal center line of the reactor, but water jets were placed around the reactor to reduce any effect due to activated water streaming past the reactor chambers. In one test a jet was placed on both sides of the reactor, and in another a single jet was placed in the rear of the reactor. For reasons given elsewhere (see "Water Purification and Circulation Systems at the BSF," this report), the jets permitted the extension of the power response readings to 1 Mw.

A summary of the results (Table 3.1), which includes the response of the reactor fission chamber, shows that the reactor power sags approximately 2% at 100 kw, 10% at 500 kw, and 16% at 1 Mw. Directing the activated water from the chambers did not reduce the nonlinearity. Readings taken below the reactor did not parallel those taken above the reactor, but agreed with those taken on the horizontal center line (Fig. 3.3). This is not yet understood. It appears that, for swimming-pool-type reactors operated at powers greater than 100 kw with natural convection cooling,

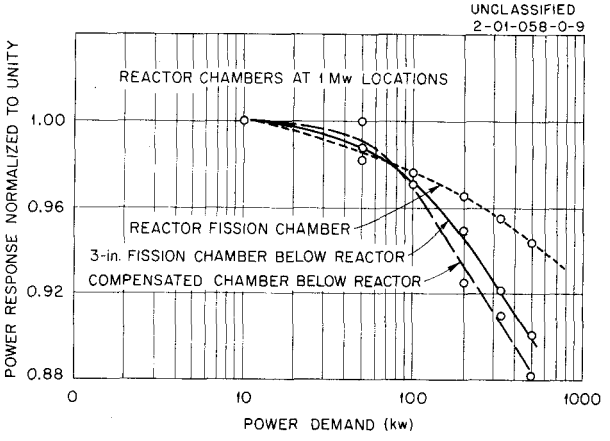

Fig. 3.3. Linearity of the Power of the BSR.

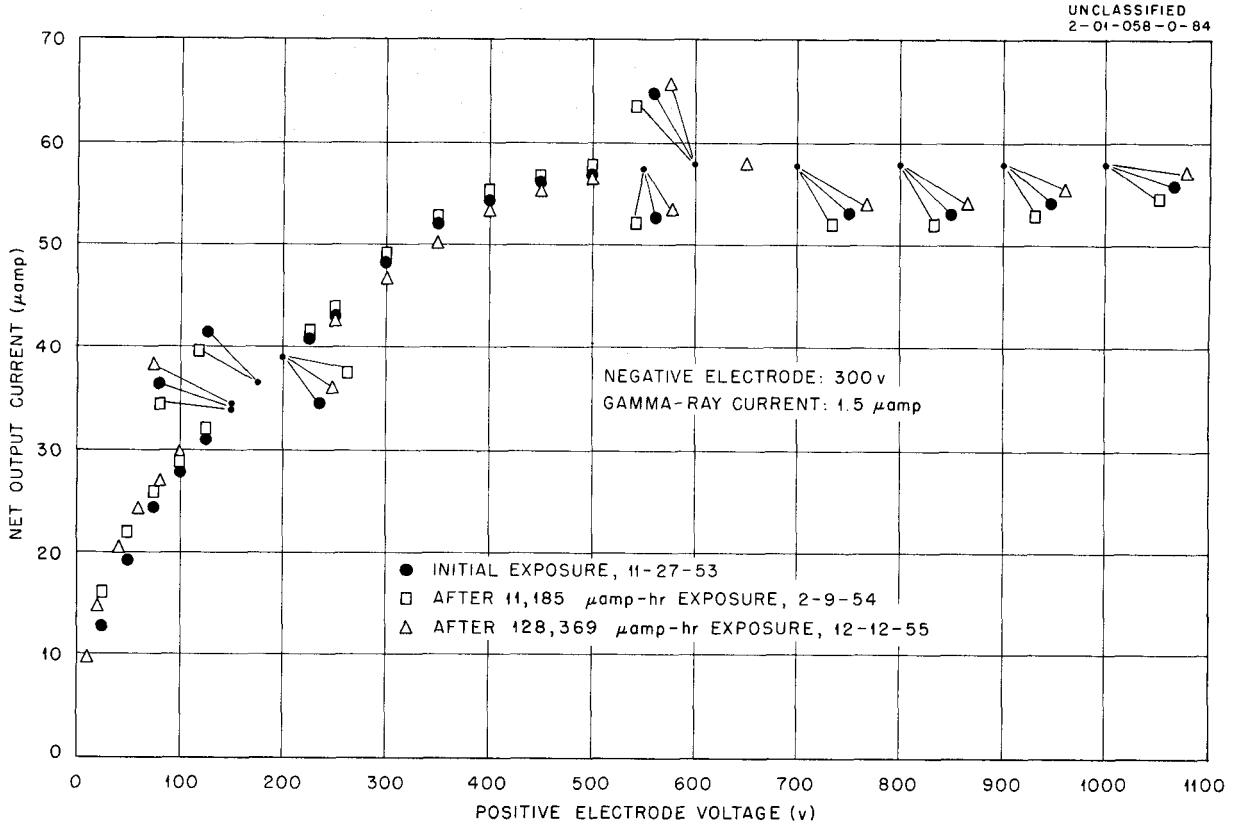

Fig. 3.2. Comparison of Saturation Properties (Normalized) of Log *N* Chamber of BSR with Earlier Tests.

the control chambers should be either on or below the horizontal center line or otherwise corrected to these positions.

It is not believed that the chamber temperature coefficient enters into these errors because of the negative effect of the jets and the speed at which the readings were taken. Accuracies of the order of 2% were attained in the experiment.

TABLE 3.1. COMPARISON OF BSR POWERS INDICATED BY REACTOR CHAMBERS AND BY EXTERNAL DETECTORS

Power Required to Obtain 50-μa Response from Reactor Chambers (kw)	Nominal Power (kw)	Ratio of Power Indicated by Reactor Chamber to Nominal Power		Ratio of Power Indicated by External Detector to Nominal Power		
		Fission Chamber	Galvanometer Chamber	U^{235} Fission	BF_3 Counter	Compensated Chamber
External Detectors on Reactor Center Line; No Jets						
100	1	1.00	1.00	1.00		
	10	0.98	1.00	0.98		
	100	1.01	1.01	0.98		
1,000	10	1.00	1.00	1.00	1.00	
	100	0.98	1.00	0.97	0.95	
	200	0.97	1.01	0.94		
	500	0.96	1.00	0.91	0.89	
External Detectors on Reactor Center Line; Jets at Side						
1,000	10	1.00	1.00	1.00	1.00	
	100	1.01	1.00	0.93		
	500	1.03	1.00	0.88	0.87	
10,000	10	1.00		1.00	1.00	
	100	0.98		0.98	0.95	
	500	0.93		0.90	0.87	
	1000	0.90		0.84	0.84	
External Detectors on Reactor Center Line; Jet at Rear						
1,000	10	1.00		1.00		
	100	0.98		0.97		
	500	0.99		0.92		
	1000	1.00		0.89		
External Detectors Below Reactor; No Jets						
1,000	10	1.00		1.00		1.00
	50	0.98		0.99		1.00
	100	0.97		0.97		0.97
	200	0.96		0.95		0.92
	325	0.95		0.92		0.91
	500	0.94		0.90		0.88

4. TEMPERATURE DISTRIBUTION IN THE BSR UNDER NATURAL CONVECTION COOLING

K. M. Henry J. N. Anno[1]

Heat transfer and nuclear calculations for swimming-pool-type reactors would be greatly facilitated by experimental evidence of the effect of the reactor power on the temperature distribution within the core. Temperature measurements within the BSR have provided this information for a range of operating powers.

The core of the BSR is formed by a lattice of MTR-type elements immersed in a pool of water. Present operation is restricted to power levels not exceeding 1 Mw. Cooling of the reactor depends upon the water in the pool rising through the elements by the natural convection process and dissipating the heat directly into the pool water. Consequently, for operations greater than about 50 kw (at which power level the heat input by the reactor equals the pool heat loss to the air at normal room temperatures) the bulk pool-water temperature gradually rises. One of the purposes of this experiment was to determine the rate of temperature rise, which could not only be used in future calculations but which could also be immediately applied to other reactors of this type under construction.

Various core configurations can be attained in the BSR by arrangement of the fuel elements in the grid lattice. The particular loading used in this experiment was a 5 by 6 fuel-element array with two of the corner elements missing. This loading, designated as loading 33 (Fig. 4.1), has 24 full fuel elements, three control-rod elements, and one partial element in which half the plates contain no fuel. Each full fuel element is roughly a 3- by 3- by 24-in. box containing 18 fuel plates separated by a 0.117-in. gap for water flow. Each plate contains a 20-mil-thick layer of uranium-aluminum alloy, highly enriched in the U^{235} isotope, sandwiched between two 20-mil-thick 2-S aluminum covers. The side plates of the fuel elements and the end boxes are also constructed of aluminum. The total U^{235} content of a full fuel element is approximately 140 g.

Measurements[2] of the thermal-neutron flux in loading 33 with cobalt foils indicated that position 25 (Fig. 4.1) in the core possessed the maximum flux, whereas position 3 had the lowest. Thermocouple measurements of the temperature were made at various locations on the surface and in the core of fuel plates inserted in these two regions while the reactor was operated at nominal (i.e., indicated on control panel but not verified by calibration) powers ranging from approximately 10 kw to 1 Mw. The ratio of the average thermal flux in position 25 to that in position 3 was about 2.0. The ratio of the peak flux (highest flux observed in measurements) to the average flux in the reactor was approximately 1.8.

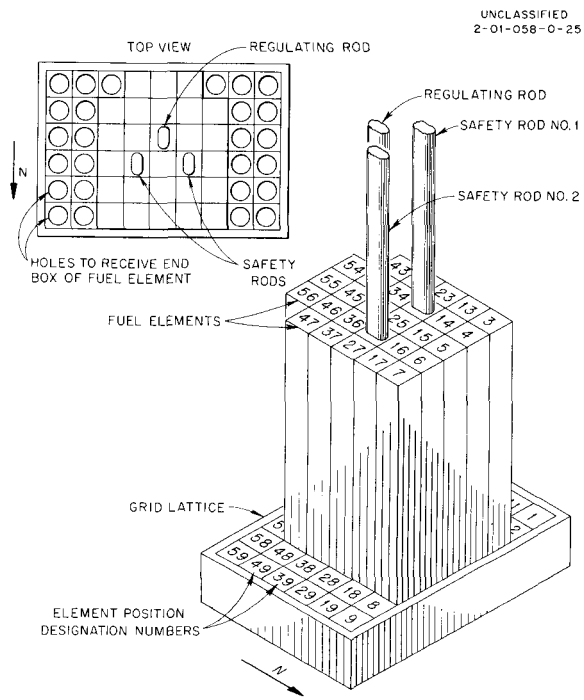

Fig. 4.1. Schematic Diagram of BSR Loading No. 33.

Measurements on the surface of nonfueled plates were also made for various operating power levels in order to differentiate between gamma-ray heating and other possible effects in the elements. Once surface temperature profiles were obtained, a plot of the peak surface temperature vs the power level of the reactor could be extrapolated beyond 1 Mw

[1]Battelle Memorial Institute.

[2]The foil measurements were made by E. B. Johnson.

to estimate the power at which local boiling would first occur. Differences between observed core and surface temperatures were incidentally obtained by a comparison of the results of the experiment; these were verified by additional tests. The effect of the positions of the control rods on the observed temperature was also investigated.

One of the BSR fuel elements, designated element B-112, was constructed so that the third plate from the concave surface of the element could be removed. Plates on which the temperature was to be observed were equipped with No. 30 (10-mil-dia) mechanically bonded Chromel-Alumel thermocouples attached to the surface or embedded in the core of the plates. A maximum of eight thermocouples was used on a single plate. The thermocouple junctions on the plate surface were positioned accurately. However, the positions of the thermocouples in the core were only approximate, so that the comparison between surface and core temperatures is not precise.

Rod Shading Effects on Fuel Temperature

The effect of the control-rod positions on the temperature distribution in the reactor was investigated briefly so that it could be minimized prior to the other measurements in the experiment.

Thermocouples were embedded in the core of a fuel plate at $3\frac{1}{2}$-in. intervals along the vertical center line, and the plate was placed in the special element in reactor position 27. At this position the element was adjacent to safety rod No. 2 but was shielded considerably from the effects of movement of safety rod No. 1 and the regulating rod (Fig. 4.1).

For a constant power level the regulating rod and safety rod No. 1 were completely withdrawn to give maximum insertion of safety rod No. 2. The temperature was allowed to stabilize for about 10 min before data were taken. Then safety rod No. 2 was completely withdrawn, and the other rods were inserted to maintain the constant power level. After the 10-min stabilization period, the temperature distribution along the plate was again observed. This procedure was repeated for four power levels ranging from 100 to 400 kw. The results are shown graphically in Fig. 4.2. To eliminate the effect of the small variation (gradual increase) of inlet water temperature, the temperature difference was plotted.

At a power level of 400 kw the peak temperature on the plate changed by about 1.5°C for a movement of safety rod No. 2 from 15.1 to 21.8 in. The results of this limited experiment emphasized the fact that it was necessary that the control-rod positions be held closely constant as the temperatures of the plates were measured. However, as the reactor power was increased, the rods had to be withdrawn to compensate for the temperature effect of the reactivity. As seen in Fig. 4.1, the two safety rods were symmetric about position 25; for simplicity, a scheme of symmetrical rod movement was devised. The regulating rod was held constant at 18 in. (of withdrawal), and the two safety rods were always moved together to maintain the symmetrical condition. Total safety-rod withdrawal usually amounted to about 2 in., in elevating the nominal power level from 10 kw to 1 Mw.

Nonfueled-Plate Surface Temperature

Measurements were made of the temperature distribution on the surfaces of two nonfueled 2-S aluminum plates having dimensions identical with the standard fueled plates. One of the nonfueled plates had thermocouples positioned along the vertical center line at 6-in. intervals. The other plate had five thermocouples positioned along a horizontal 12 in. from the bottom of the plate.

The distribution of heat along the vertical center line of the plate in the high-flux region (position 25) of the reactor was determined for various power levels (Fig. 4.3). The temperature rise with the plate in the low-flux region (position 3) was 66% of that at the same points with the element in position 25. It can be seen that the temperature rise along the top half of the plate is approximately linear.

After the 1-Mw run for the above measurements, the increased pool temperature and xenon poisoning in the reactor had consumed the remaining excess reactivity. Thus it was necessary to add another fuel element to the reactor in order to attain a 1-Mw power level for temperature measurements across the horizontal on the plate. The additional element was placed in position 28 (Fig. 4.1), and the new loading was designated 33A. The horizontal temperature profiles for a plate in position 25 were approximately symmetrical, but in position 3 the absence of an adjacent element on one side effected an asymmetrical temperature distribution.

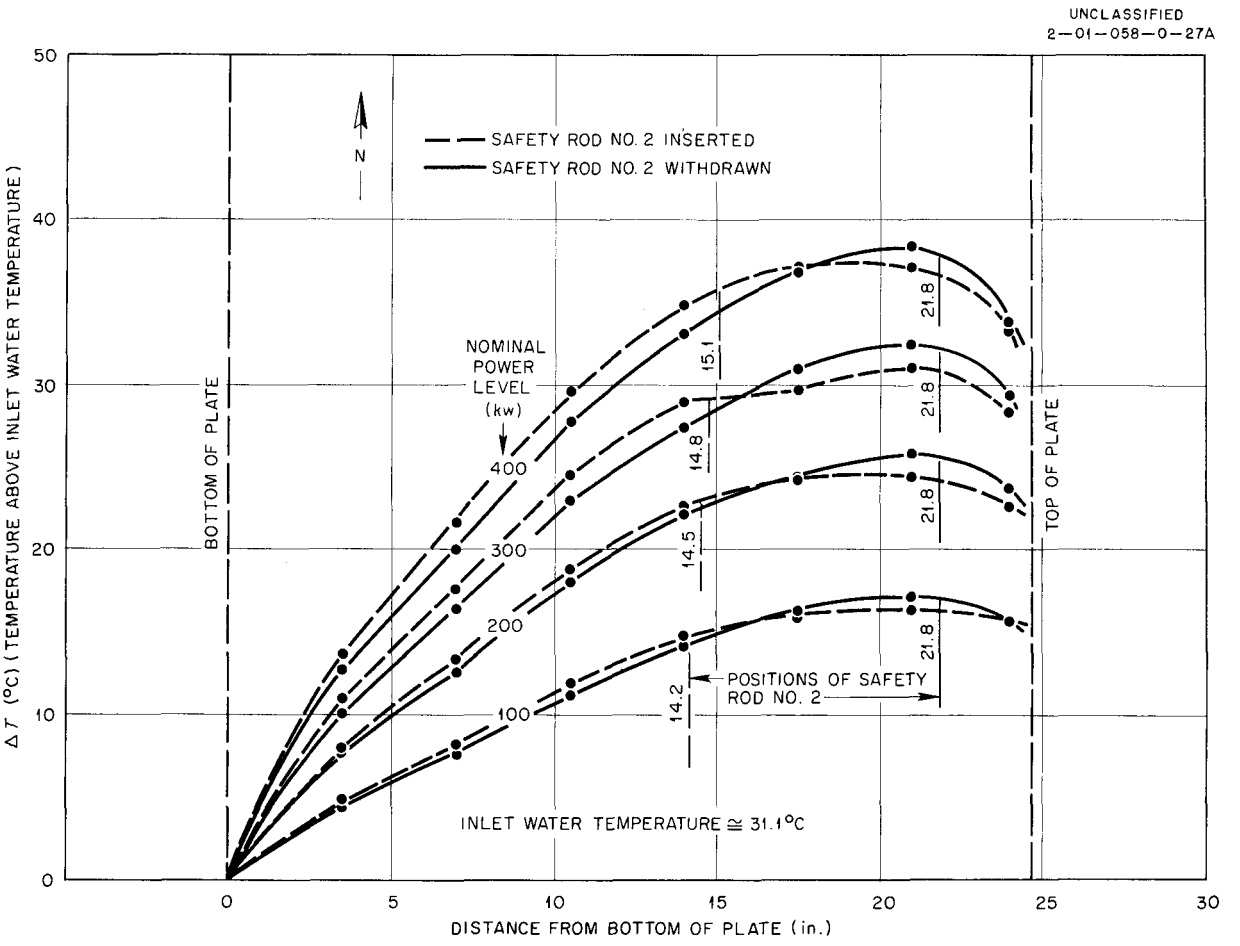

Fig. 4.2. Surface Temperature Distribution Along Vertical Center Line of Nonfueled Plate (Position 27 of BSR Loading 33) as a Function of the Position of Safety Rod No. 2.

It should be pointed out that for these horizontal measurements in position 3 the plate was not completely inserted in the element, and the temperature readings represent the horizontal profile about 14 in. from the bottom of the reactor instead of the intended 12 in.

The addition of the element in position 28 apparently flattened the flux distribution across the reactor. The temperature 12 in. from the bottom of the plate in the vertical profile in loading 33 for the 1-Mw power level was several degrees higher than the temperature at that point in loading 33A.

Fueled-Plate Surface Temperatures

Two standard BSR fuel plates were equipped with surface thermocouples, along the vertical center line at 4-in. intervals on one plate and along a horizontal 12 in. from the bottom of the other plate, for temperature measurements in the element in position 25 of loading 33. The results along the vertical center line are shown in Fig. 4.4.

After each change in power level, at least 10 min was allowed for the temperature to reach equilibrium before any readings were taken. At operating power levels greater than 500 kw the individual readings varied over a small range. These variations can probably be attributed to the uneven heating of the water in the natural convection flow stream. For each power level the average of 20 readings was considered to be the measured temperature.

From these measurements on the surfaces of the fuel plates an estimate of the power level at which

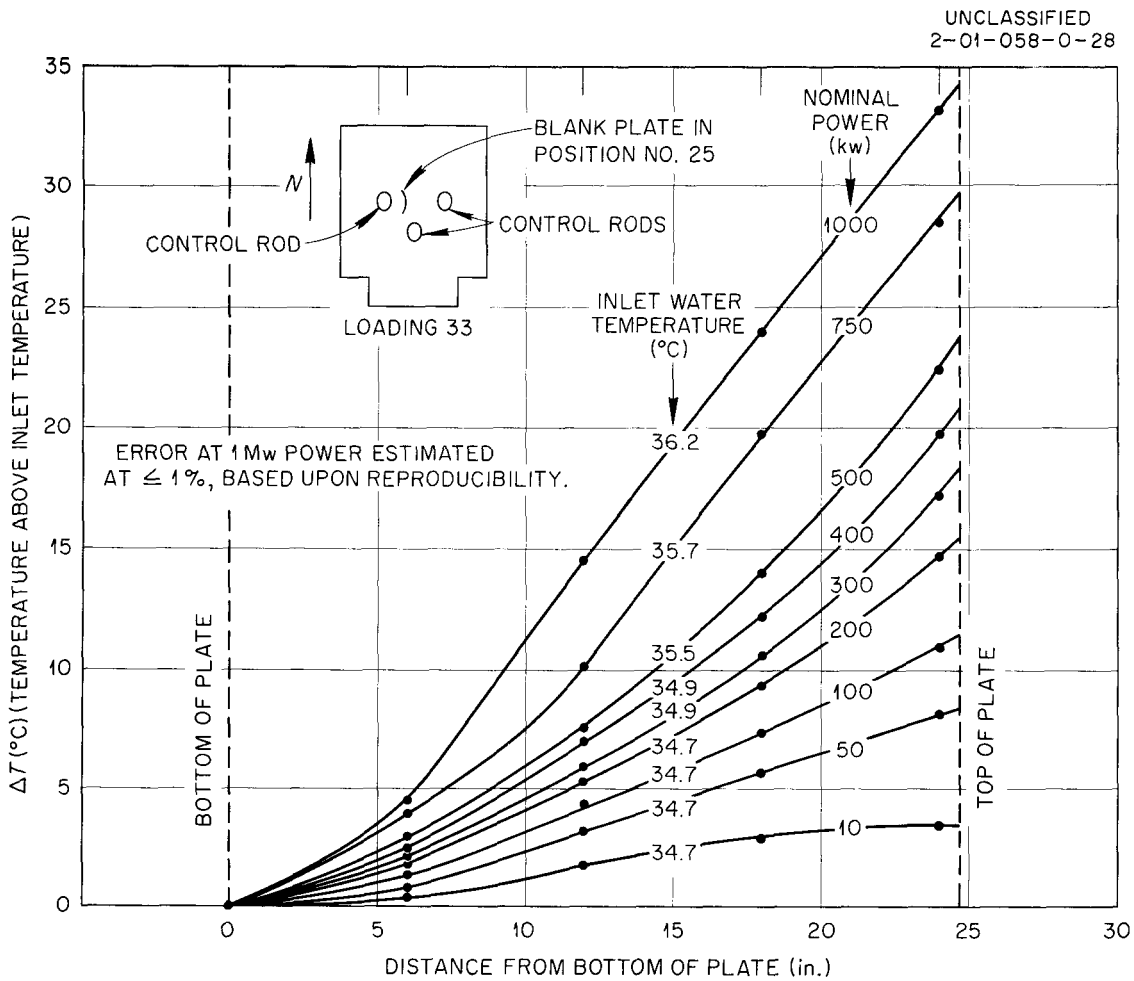

Fig. 4.3. Surface Temperature Distribution Along Vertical Center Line of Nonfueled Plate (Position 25 of BSR Loading 33).

local boiling would first occur can be made from a plot of the maximum temperature observed vs the actual (i.e., from calibration) power (obtained by use of conversion factors resulting from the investigation reported in Chap. 3 and from cobalt foil exposures in the core). The water in the reactor at the position of maximum surface temperature is under a pressure of approximately 22.2 psi (atmospheric pressure plus pressure due to an 18.3-ft head of water). At this pressure the boiling point of water is 111.6°C. The maximum inlet water temperature observed during the surface temperature measurements was about 35°C. Figure 4.5 is a graph of the observed peak surface temperature on a plate in position 25 (loading 33) vs the actual power, with the reactor inlet water temperature assumed to be constant at 35°C. Extrapolation of the curve indicates that local boiling would first occur in the reactor in the neighborhood of 2100 kw.

A comparison of the vertical center line surface temperatures observed for the fueled and nonfueled plates showed that the linearity of temperature increase observed in the nonfueled plate was not present in the surface temperatures of the fueled plate. At the higher power levels the fuel-plate temperatures reached a maximum between 4 and 5 in. above the mid-point and then decreased rapidly.

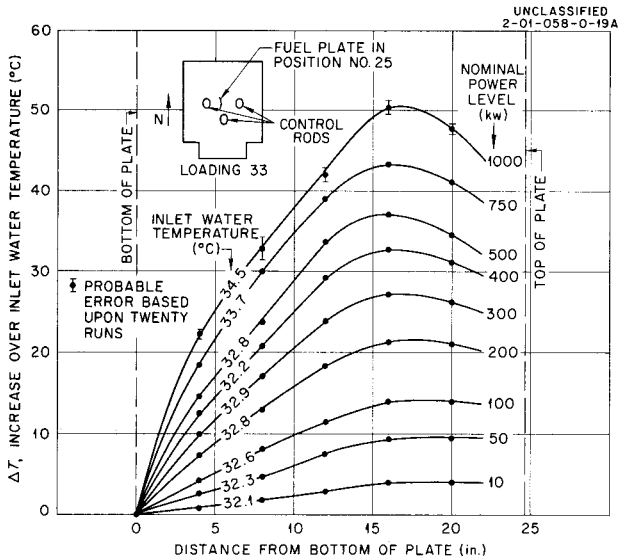

Fig. 4.4. Surface Temperature Distribution Along Vertical Center Line of Fueled Plate (Position 25 of BSR Loading 33).

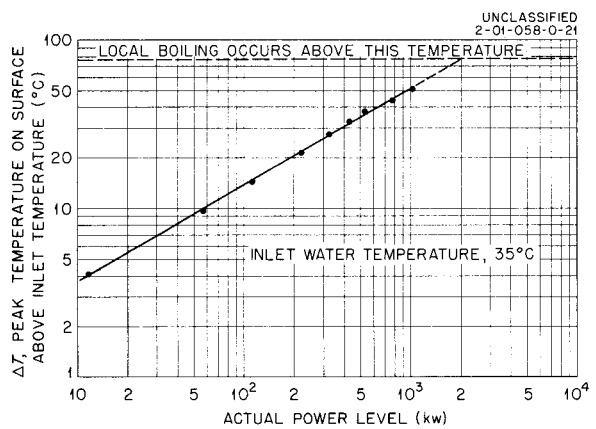

Fig. 4.5. Peak Surface Temperatures on Fueled Plate (Position 25 of BSR Loading 33) as a Function of Power Level.

A comparison of the horizontal surface temperatures across the fueled and nonfueled plates showed several obvious differences. The parabolic distribution observed in the nonfueled plate is not present in the fueled plate. The asymmetry of the profile in the fueled plate is probably caused by a decrease in thermal flux (and hence heat generation within the plate) in the north-south direction, that is, from position 35 to position 15. Also, of course, the magnitude of the temperature difference is much greater in the case of the fueled plate.

Fueled-Plate Core Temperatures

Measurements of the temperature in the core of a fuel plate were taken with thermocouples embedded along the vertical center line of the core at $3\frac{1}{2}$-in. intervals. Before the measurements were made, a brief test of the thermocouples was made to ensure that no extraneous thermoelectric effects were introduced in the technique involved in burying the couples in the core. The fuel plate was placed first in air at 23°C, then in pool water at 38°C, and finally in tap water at 51°C. Thermocouples on the plate surface and in the core responded identically. The temperature distributions in the plate in the element in position 25 (loading 33) are shown in Fig. 4.6. The small deviations which had been observed in the surface temperature measurements were not detectable in these core temperature measurements. To obtain a measure of the accuracy of the readings, three runs were made over a two-day period. The thermocouple readings were reproducible to within 1%.

Core-Surface Temperature Differences

Since the exact position (depth) of the thermocouple junctions within the core were not accurately known, the significance of the core temperature measurements is somewhat clouded. However, the difference (ΔT) between the core temperature and the surface temperature (data available for a comparison for position 25 of loading 33) should show the approximate ΔT value from the plate core to the plate surface.

Since the core temperatures and plate surface temperatures were obtained in separate experiments under conditions of different inlet water temperatures and different fuel plates, a confirmation experiment was performed. A new standard fuel plate was equipped with several sets of thermocouples, each set measuring the temperature 12, 16, and 20 in. from the bottom of the plate along the vertical center line, both in the core and on the surface. Again, accurate positions of the core thermocouples could not be attained, but the other variables were eliminated. The plate was then placed in the element in position 25, and the temperatures were observed for various power

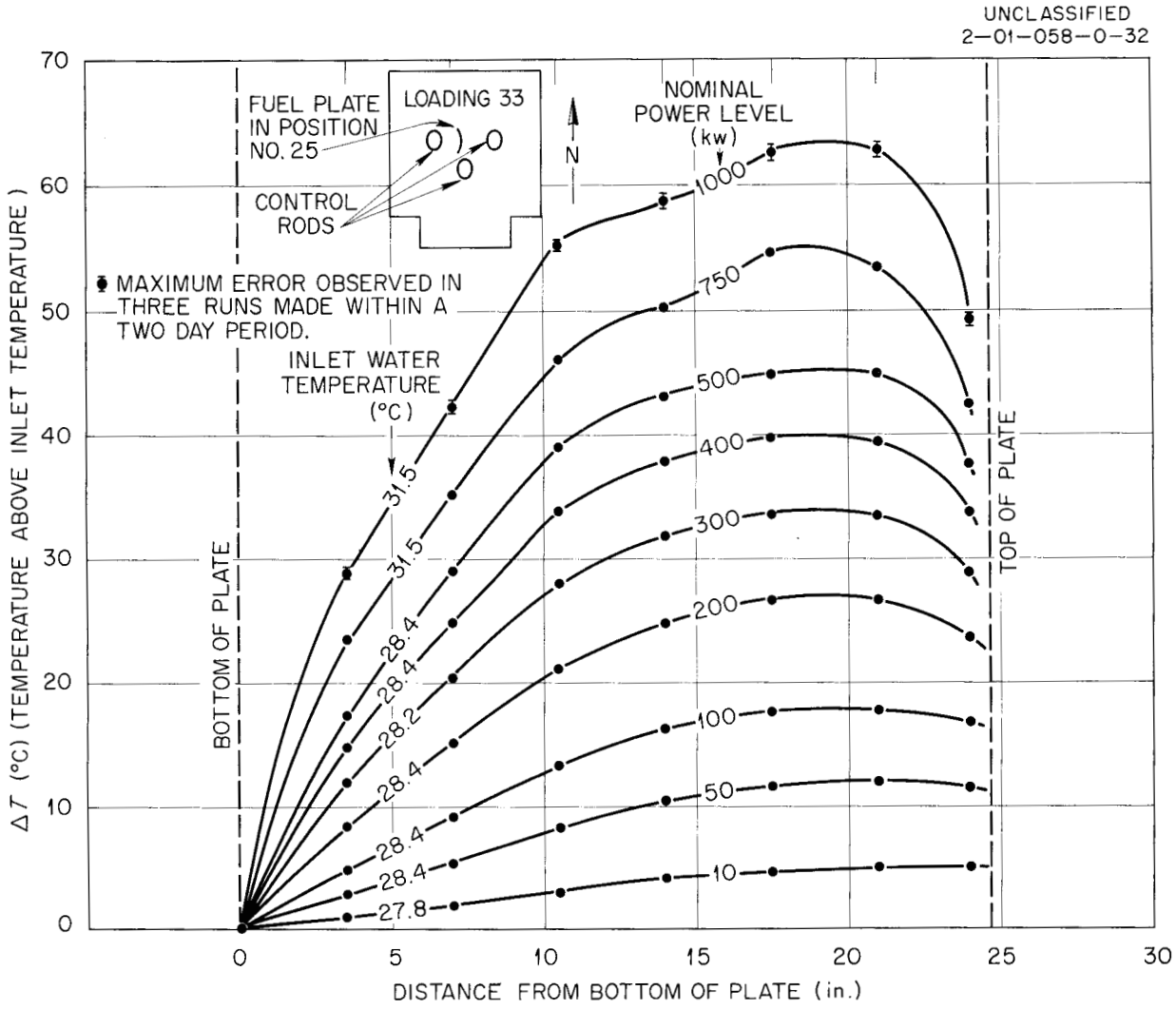

Fig. 4.6. Core Temperature Distributions Along Vertical Center Line of Fueled Plate (Position 25 of BSR Loading 33).

levels. Surface temperature variations were again observed at the higher power levels, at each power level 25 readings being taken. The probable error was calculated from the observed deviations from the mean.

Figure 4.7 shows the differences in the core-surface temperatures along the vertical center line, obtained both from the comparison of the separate core and surface measurements and from the confirmation experiment. The probable errors are rather large, primarily since small differences were taken between large numbers. Also shown on the plot are the thermal-neutron flux values measured 15 in. east of the vertical center line of an element in position 25 (loading 33) by the exposure of cobalt foils. The neutron flux distribution should give a rough estimate of the variation of heat generation in the vertical direction.

The spread of experimental points has been attributed to inaccurate positioning of the thermocouples in the core. The most significant aspect of the ΔT measurements is the magnitude of the differences. Preliminary estimates placed the ΔT in the neighborhood of about 3°C. The maximum observed ΔT was 12.5°C from the confirmation experiment and 15.4°C from the difference between the separately observed surface and core temperatures. Furthermore, these temperature differences are not

necessarily maximum values, since none of the thermocouples may have been located exactly at the core center. The points shown in Fig. 4.7 actually represent values less than (or perhaps equal to) the measured ΔT. The discrepancy between measured and calculated values indicates the difficulty of measuring the temperature distribution without changing it. The thermocouples inevitably disturb the heating and cooling mechanisms in their vicinity.

The largest temperature difference obtained in the confirmation experiment was observed 12 in. from the bottom of the plate. It is possible that the thermocouple in the core was actually closer to the center of the fuel.

This paper will be published in more detail at a later date.

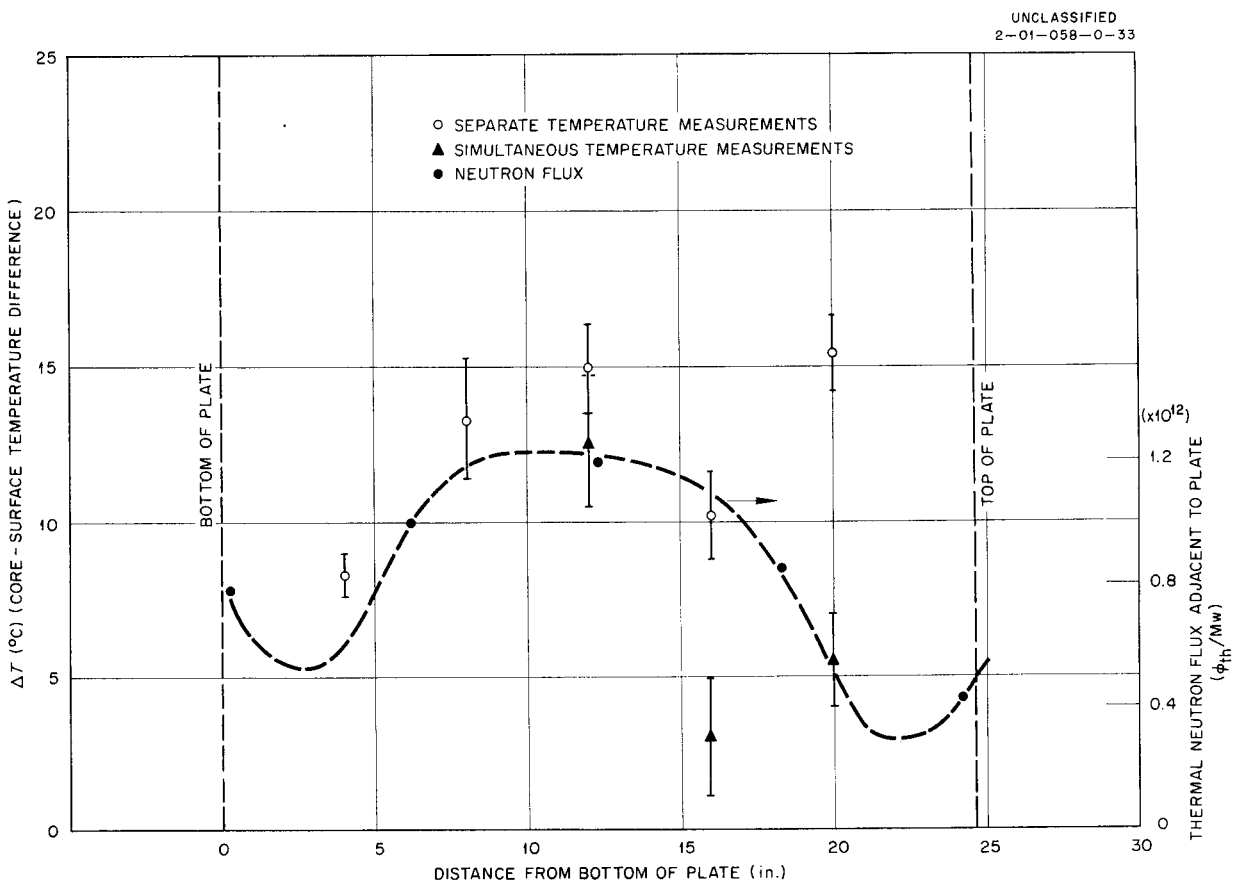

Fig. 4.7. Core-Surface Temperature Differences Along Vertical Center Line of Fueled Plate (Position 25 of BSR Loading 33).

5. WATER PURIFICATION AND CIRCULATION SYSTEMS AT THE BSF

J. D. Flynn

WATER PURIFICATION SYSTEM

Two water-purifying loops for the demineralized water of the reactor pool have been installed at the BSF. One system, built around a Stay-New filter, removes suspended particles from the water, and another system, built around an Elgin Ultra deionizer, maintains a high specific resistance of the water.

Filter System

With the filter system an attempt is made to remove dust and other foreign matter from the surface of the water before they sink below the surface. In order to accomplish this, a pool skimmer has been installed in one corner of the pool. This is merely a tank, placed under and around the suction line of the pump, with the top submerged below the pool level. The distance below the pool level is determined by the diameter of the tank and the capacity of the pump. The tank must be low enough to prevent the vortex from reaching the suction line and producing an air lock in the pump or filter, and yet high enough to cause a fast surface flow into the tank. Once the surface water is in the skimmer tank, the water is pushed through a close-woven, cotton filter several times and then returned to the bottom of the pool. A diagram of the system is shown in Fig. 5.1.

Much of the foreign matter which finds its way to the pool is insoluble. That which sinks to the the bottom before being picked up by the skimmer must be removed by a vacuum cleaner passed over the pool floor. A vacuum cleaning line has been installed on the suction side of the pump for cleaning the bottom and sides of the pool. It has a coarse filter in the line to prevent large objects from damaging the pump. This type of cleaning has been required at intervals ranging from one to four months.

The filtering system is made of 2-in. stainless steel pipe with flange fittings. There is also a 2-in. line coming from the plant demineralizer for adding makeup demineralized water when it is needed in large quantities or for filling the pool. The centrifugal pump for the filter system has a 7-hp Allis-Chalmers motor, rated at 200 gpm against a 75-ft head. A safety device, added to prevent possible overheating of the pump bearings,

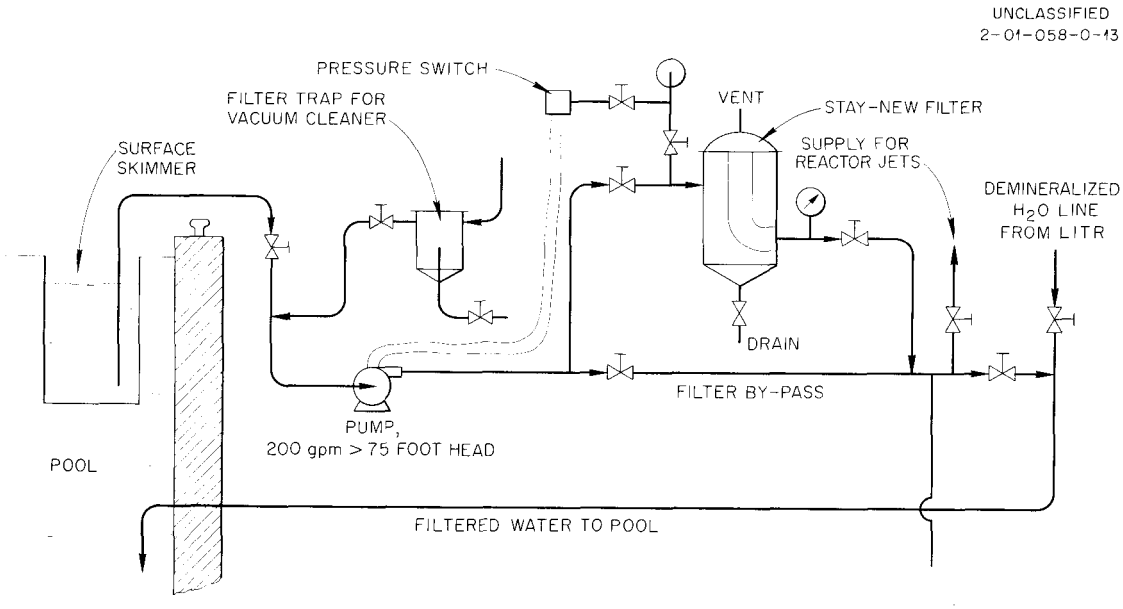

Fig. 5.1. BSF Filter System.

consists of a pressure switch which will stop the pump if an airlock occurs in the line and causes the output pressure to fall below 5 psig. If a leak occurs anywhere in the filter system, the water level in the pool will rapidly be lowered below the pump intake, and this pressure switch will be actuated and will shut off the pump.

The filter itself employs a closely woven fabric over a copper screen. The closest weave available (No. EPHLS-7A-2 from the Dollinger Corporation, Rochester, N.Y.) is used, since looser weaves were almost completely ineffective. The cloth inserts have lasted about two to four months and have measured up to 10 mr/hr when removed from the filter.

There is a flanged fitting on the outlet side of the filter where water may be obtained to supply the reactor jets discussed below. If more pressure is needed at this point, the filter may be bypassed in order to eliminate an approximate 5-psi pressure drop.

Deionizer System

A diagram of the deionizer system is shown in Fig. 5.2. The capacity of the Elgin Ultra deionizer is rated at 20 gpm, but with the pump now being used only 10 to 12 gpm passes through the system. Since this unit is used only for bypass treatment, the input resistance is high, and the output water normally has a resistance of >1.9 megohms/cm for a period of six to nine weeks after resin regeneration. It was necessary to replace the resin after almost one year of operation, since it would not regenerate. The radiation level of the surface of the resin was not measurable.

This deionizing system has been sufficient to maintain the specific resistance of the water in the pool between 250,000 to 350,000 ohms/cm.

WATER CIRCULATION SYSTEM

At operating power levels above 400 kw a set of jets is used to diffuse the water rising upward from the BSR as a result of thermal convection. Demineralized water from the filter system is fed through a fire hose connected to a common T-pipe joined to two headers positioned above the reactor on opposite sides. A typical jet diffuser arrangement is shown in Fig. 5.3. The effect of the jets is primarily to suppress the pool surface N^{16}

UNCLASSIFIED
2-01-058-0-14

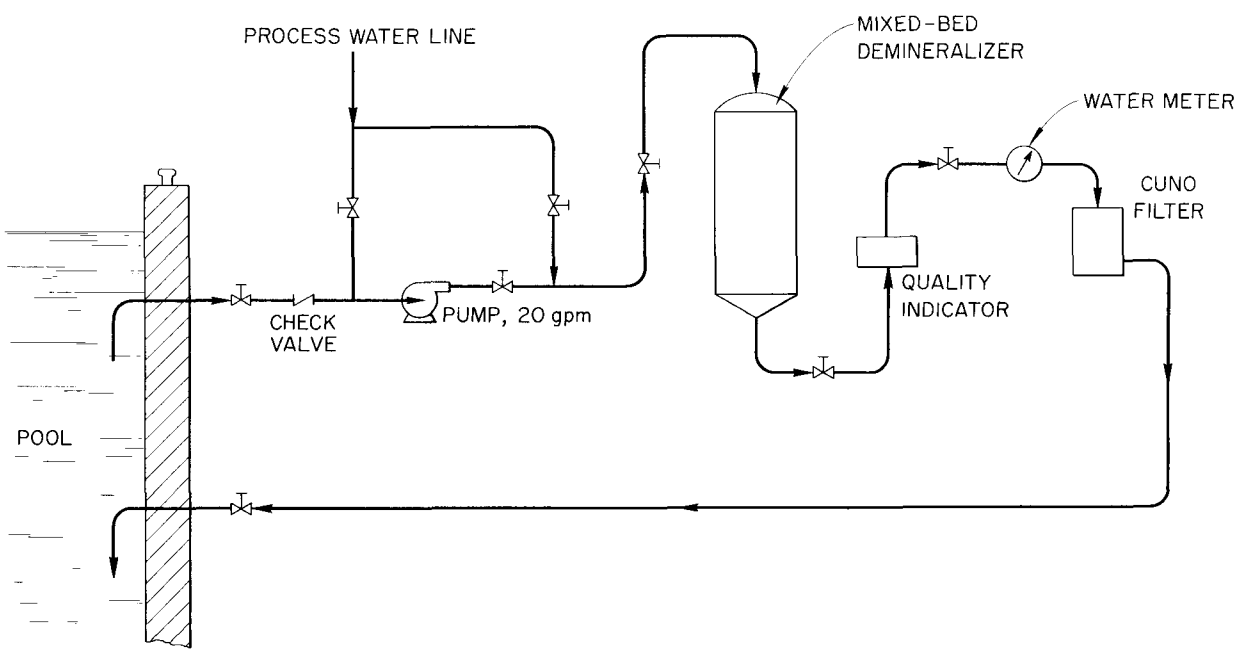

Fig. 5.2. BSF Demineralizer System.

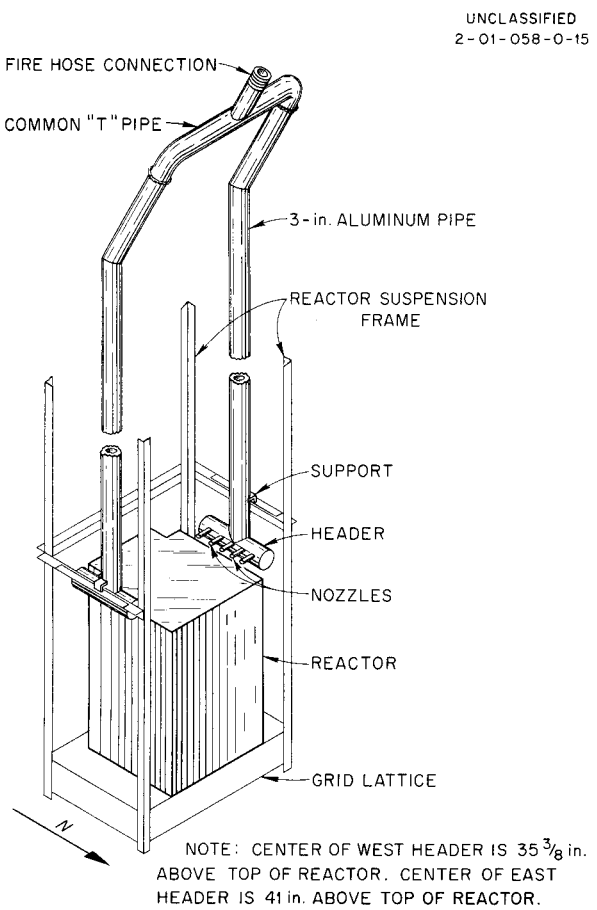

Fig. 5.3. Typical BSF Jet Diffuser Arrangement.

activity (7.3-sec half life). The activity is formed by the $O^{16}(n,p)$ reaction in the pool water as it passes through the reactor. Use of the jets increases the underwater path length, thus increasing the underwater lifetime of the isotope. Without the jets in operation the radiation level 19 ½ in. above the 17 ½ ft of water directly over the reactor operating at a power of 1 Mw is approximately 800 mr/hr, which is excessive for routine operation.

Three types of jet diffusers have been employed (Fig. 5.4). The same piping was used for each type; only the outlet orifices were modified. The type 1 diffusers had five ¾-in.-OD by 1-in. nozzles on each header and were positioned so that the west header was approximately 35⅝ in. higher. The type 1 jets reduced the gamma radiation levels considerably, but the radiation near the reactor bridge was still 62 mr/hr, which was too high for routine operation. The type 2 jets were more effective than the type 1 jets and reduced the radiation level at the reactor to 32 mr/hr. With both type 1 and type 2 jets the radiation level on the east side of the pool was greater than that on the west side. Since the reactor operator is stationed on the east side of the bridge and since, in general, most personnel traffic is along the east side, further modification of the jet diffusers to "push" the radiation to the west side was desirable. The jets were then modified to type 3 and reversed in elevation so that the diffuser on the

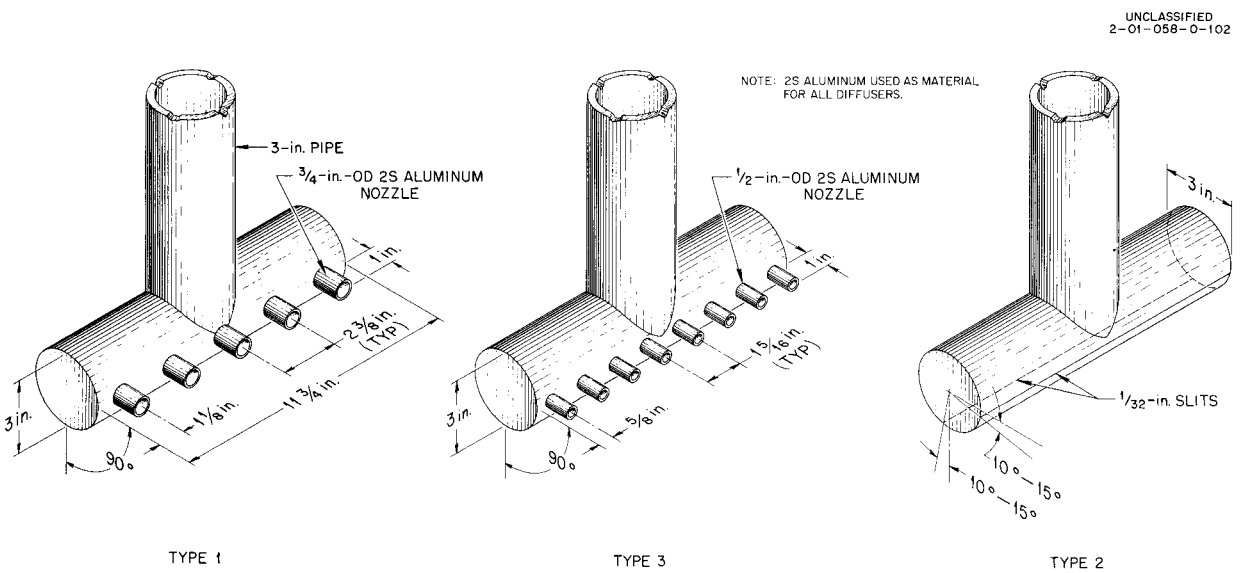

Fig. 5.4. Types of Jet Diffusers Used at the BSF.

east side of the lattice was $35\frac{5}{8}$ in. above the top of the reactor, whereas the west diffuser was $5\frac{3}{8}$ in. higher. The resulting gamma radiation during 1-Mw operation of the BSR is shown in Fig. 5.5. The type 3 jets have proved to be very successful in suppressing the surface radiation and in directing it away from the east side of the pool.

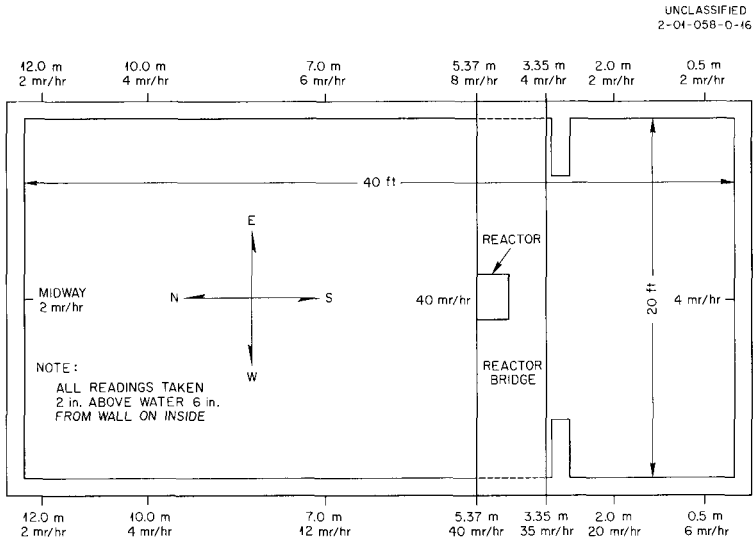

Fig. 5.5. Gamma Radiation Levels at the BSF with Type 3 Jets Used During 1-Mw Operation.

6. AIR ACTIVITY PRODUCED BY THE BSR

W. R. Champion[1]

In the operation of the BSR considerable activity is evolved into the air at powers of a few hundred kilowatts. In order to operate the reactor above about 400 kw it is necessary to employ jets (see Chap. 5) above the reactor to diffuse the activity and increase the length of time required for it to reach the surface of the pool. Without the jets the reactor is scrammed, when the power reaches about 400 kw, by a reactor safety monitor preset at 45 mr/hr and located 3 ft above the pool surface and 10 ft to the side of the vertical center line of the reactor. With the jets this same monitron indicates 25 mr/hr with the reactor operating at a power of 1 Mw, and the level of activity (as measured with a cutie pie) at the edge of the pool surface is 80 mr/hr. At a power of about 400 kw, approximately 1 min is required for a change in power level of the reactor to be reflected in the reading of the reactor safety monitron, thus indicating the time required for the thermal stream to reach the surface of the pool from the reactor.

The level of air-borne activity 40 ft from the reactor is monitored by a recording instrument using a G-M tube as the detector. This detector measures the activity trapped on filter paper. At high reactor powers it indicates a few thousand counts per minute and, when the reactor is scrammed, displays a half life of about 30 min for the gross activity at this location.

Since the activity, as seen by this monitor, was an appreciable fraction of the tolerance level, an attempt was made to determine the origin of the

[1]On loan from Lockheed Aircraft, Marietta, Ga.

activity, with a view toward its possible elimination.

In order to identify the sources of activity, an examination was made of the gamma-ray energy spectra and the time decay characteristics of the gamma-ray activity. Figure 6.1 is a schematic representation of the experiment. The sources of the activity were collected from above the pool water by the air flow through the assembly and deposited on the trap in the shield. The trap was viewed with a single-crystal scintillation spectrometer, and the resultant pulses were analyzed on a 20-channel pulse-height analyzer. In addition, the activity in the pool water pumped from 6 in. above the reactor was measured with the hope that, if the spectrum was the same as that observed from the air, a more intense source would be available for half-life measurements. The data presented here were taken with a 1½- by 1½-in. NaI(Tl) crystal.

Alignment and stability checks on the analyzer and its associated components were made in the usual manner. Energy calibration was accomplished by using known sources in the energy range to be investigated, and over-all linearity checks were made by using these data. Operation of the electronics from the preamplifier through the analyzer was satisfactory with respect to linearity and stability throughout the measurements. Over-all drifts were encountered, however, that appeared to be eliminated by taking care not to expose the counter to intense sources during calibration. A number of crystal-photomultiplier combinations were used. However, the resolution of the system with a 1½- by 1½-in. crystal was consistently about 8%.

Half-life measurements were also made with the 20-channel analyzer, except for those activities that were either shorter than a few minutes or longer than a few hours. These extreme half lives

UNCLASSIFIED
2-01-058-0-91

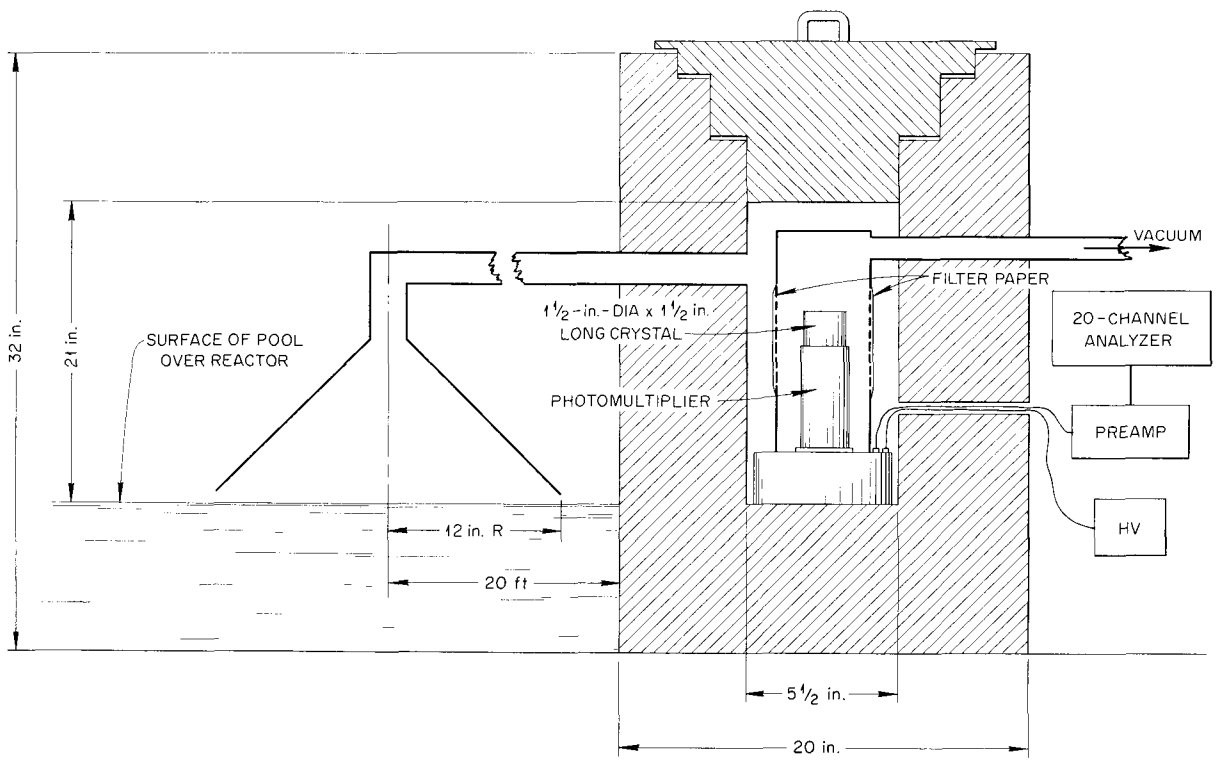

Fig. 6.1. Single-Crystal Spectrometer for Air Activity Measurements.

were measured with a single-channel analyzer, a count-rate meter, and a Brown recorder. When the 20-channel analyzer was used, it was adjusted so that the peak under investigation appeared in channel 10, thus allowing simultaneous observation of the adjacent spectra so that it could be taken into account in computing the half life. Successive observations were corrected for the effect of decay of adjacent spectra and plotted as a function of time to obtain the half life.

Most of the measurements were made at a reactor power of 350 kw. This power was the highest that the reactor could consistently hold without jets, although a few runs were made at 400 kw. From the time the reactor reached operating power and the vacuum pumps were started, the total count rate was recorded on a strip-chart recorder until apparent equilibrium between the rate of accumulation and the rate of decay of the activity was obtained. Data were not recorded until this equilibrium had been reached, the process requiring about 1½ hr.

There was some variation in the gamma-ray spectra from one measurement to another. This may have been due to the previous operating history of the reactor, variation of impurities in the pool water, etc. The spectra of the activity trapped on the filter paper are shown in Figs. 6.2 and 6.3. Measurements have been made of the half lives of the five largest peaks, and they are shown in Table 6.1. (The variations mentioned above were considered in the results.) Other peaks, which were not satisfactory for half-life measurements but which were consistently observed when they should have been resolved, appeared at 636 and 833 kev and at 1.26, 1.60, and 1.77 Mev.

These half-life measurements are suspect for at least two reasons. First, they all fall into the very narrow range of from 18 to 39 min. Although this is in general agreement with the gross half life as seen by the BSF monitor of the air-borne activity, it may only represent the rate of escape of the active material from the trap. The half lives may be suspect also because of the poor statistical accuracy of the measurements, particularly at higher energies. The low count rates available in the limited decay times and the very low peak-to-total ratios account for this.

The spectra of the activity trapped on charcoal are shown in Figs. 6.4 and 6.5. The half lives of the prominent peaks are also listed in Table 6.1,

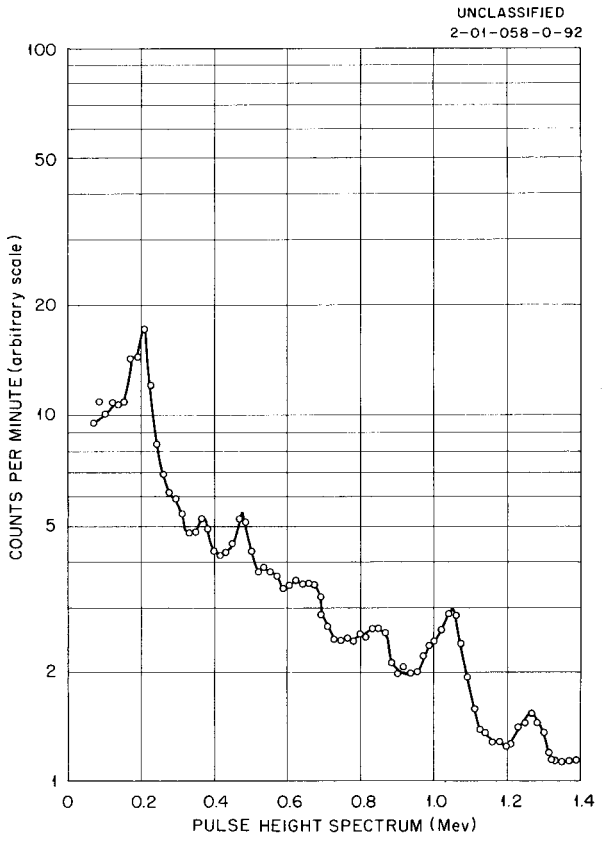

Fig. 6.2. Gamma-Ray Spectra of Activity Trapped on Filter Paper.

TABLE 6.1. HALF LIVES OF PROMINENT PEAKS OBSERVED IN THE GAMMA-RAY SPECTRA OF TRAPPED ACTIVITY

Energy	Half Life
Activity Trapped on Filter Paper	
206 kev	30 min
474 kev	28.5 min
1.03 Mev	18.5 min
1.44 Mev	31.2 min
2.19 Mev	37.8 min
Activity Trapped on Charcoal	
207 kev	11 days
510 kev	13.3 hr
1.04 Mev	22.9 min
5.12 Mev	7.6 sec
5.62 Mev	7.6 sec
6.13 Mev	7.6 sec

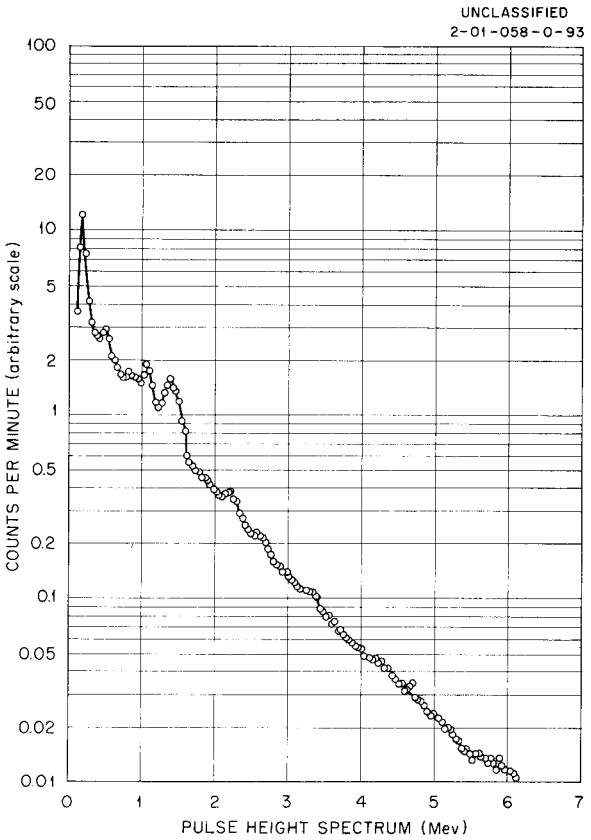

Fig. 6.3. Gamma-Ray Spectra of Activity Trapped on Filter Paper.

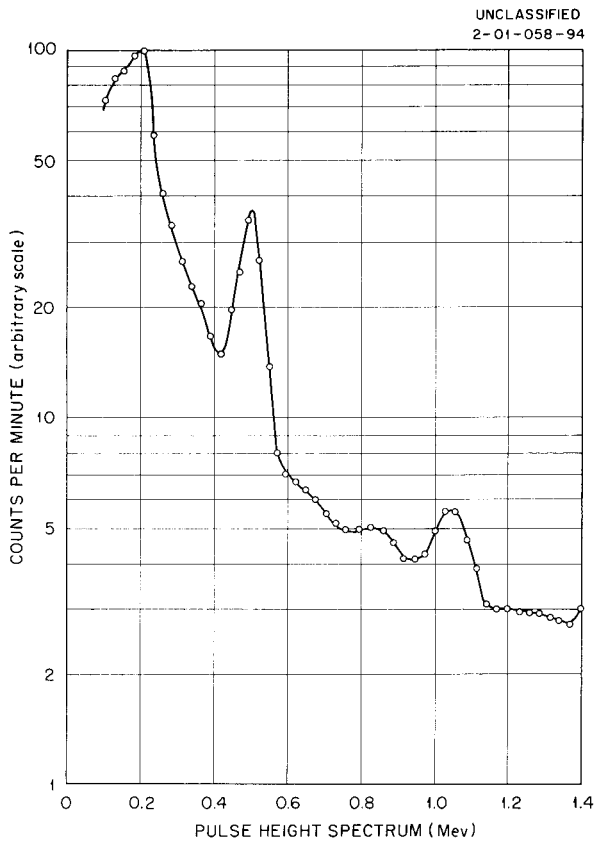

Fig. 6.4. Gamma-Ray Spectra of Activity Trapped on Charcoal.

along with the other consistently observed peaks not suitable for half-life measurements.

The curve in Fig. 6.6 is the spectrum of the activity in the pool water 6 in. above the reactor. This measurement was taken while the water was circulated around the spectrometer crystal after a 23-sec delay in transit. It was useful only in confirming the presence of N^{16} also seen on the charcoal.

An exhaustive comparison with published data[2] has failed to result in any definite assignments other than N^{16}, which was obvious. The only other case which warrants discussion here is Cl^{38}. Consistently, peaks are found at 2.19 and 1.6 Mev on both the filter paper and the charcoal. The half life of the 2.19-Mev peak was measured as 38 min. The peak at 1.6 Mev was too small for a half-life measurement. These data compare with published values of 2.19 and 1.60 Mev and with a half life of 37.29 min for Cl^{38}. This correction suggests that from the chlorine in the pool water the reaction $Cl^{37}(n,\gamma)Cl^{38}$ took place. The chlorine concentration in the water is <0.2 ppm.

Considering the strong bias against sources with short half lives and considering the diminished response of the spectrum at high energy, it is obvious that N^{16} is by far the largest contributor to the activity measured. The results do not indicate that any fission products are escaping from the fuel elements into the water but imply that perhaps all the air activity can be accounted for by the activation of impurities and dissolved gases in the water and by the activation of the water itself.

[2] J. M. Hollander, I. Perlman, and G. T. Seaborg, *Rev. Mod. Phys.* **25**, 469 (1953).

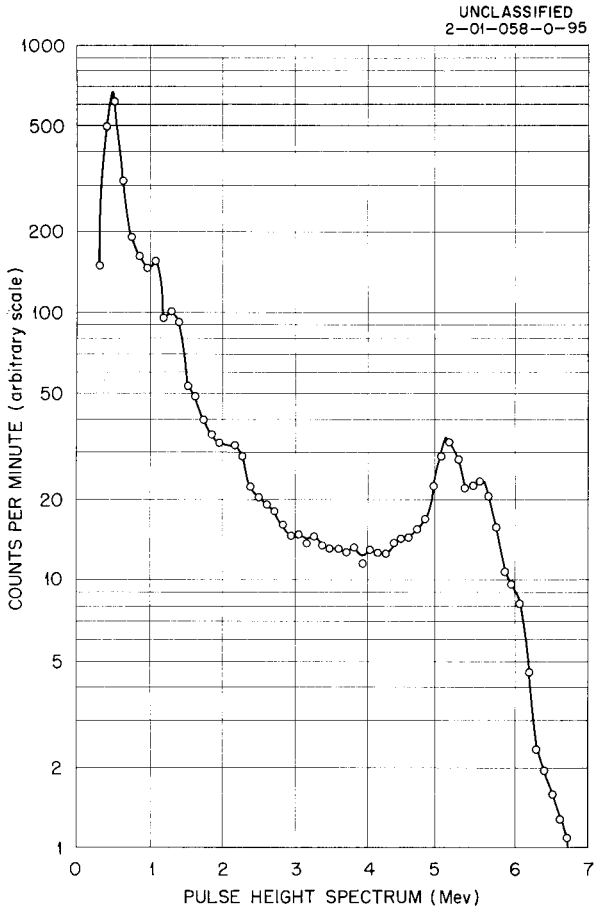

Fig. 6.5. Gamma-Ray Spectra of Activity Trapped on Charcoal.

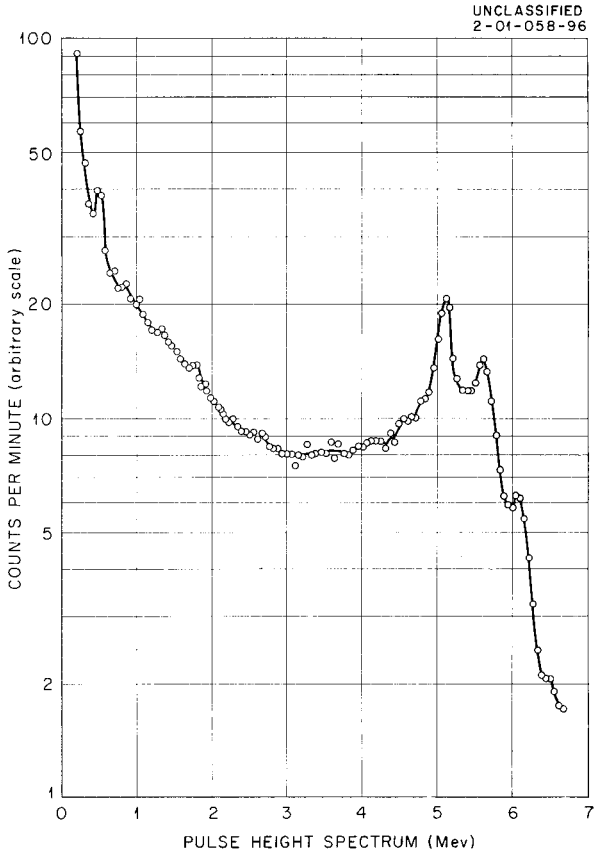

Fig. 6.6. Gamma-Ray Spectra of Activity in Pool Water.

7. MEASUREMENTS OF THE THERMAL-NEUTRON FLUX FROM THE BSF THERMAL COLUMN

E. G. Silver

The thermal column at the BSF can be used for a number of experiments which require thermal neutrons. In order to determine the intensity of the flux available and its uniformity across the column, a number of foil measurements of the flux have been made. The need for a facility such as this one has been emphasized with recent measurements at hole 57 of the ORNL Graphite Reactor which were difficult to interpret because of the uncertainty of the spectra and the lack of geometrical uniformity of the neutron beam.

The thermal column consists of a stack of graphite which is positioned in the pool so that the reactor may be brought into close proximity to one face of the column (Fig. 7.1). A 10-in.-thick lead shield between the graphite and the reactor face serves to attenuate the gamma-ray flux from the reactor, thus diminishing the gamma-ray heating of the graphite with its attendant dimensional instability problems. The entire graphite block is encased in a water-proof steel tank which is lined with Tybor[1] to absorb neutrons and prevent activation of the steel. The radiation port consists of a 9- by 9-in. square hole which extends from the top of the graphite down to 2 in. below the horizontal center line of the reactor; it is covered at the top by a $^5/_{16}$-in.-thick aluminum

[1] Tybor is a plastic heavily loaded with B_4C.

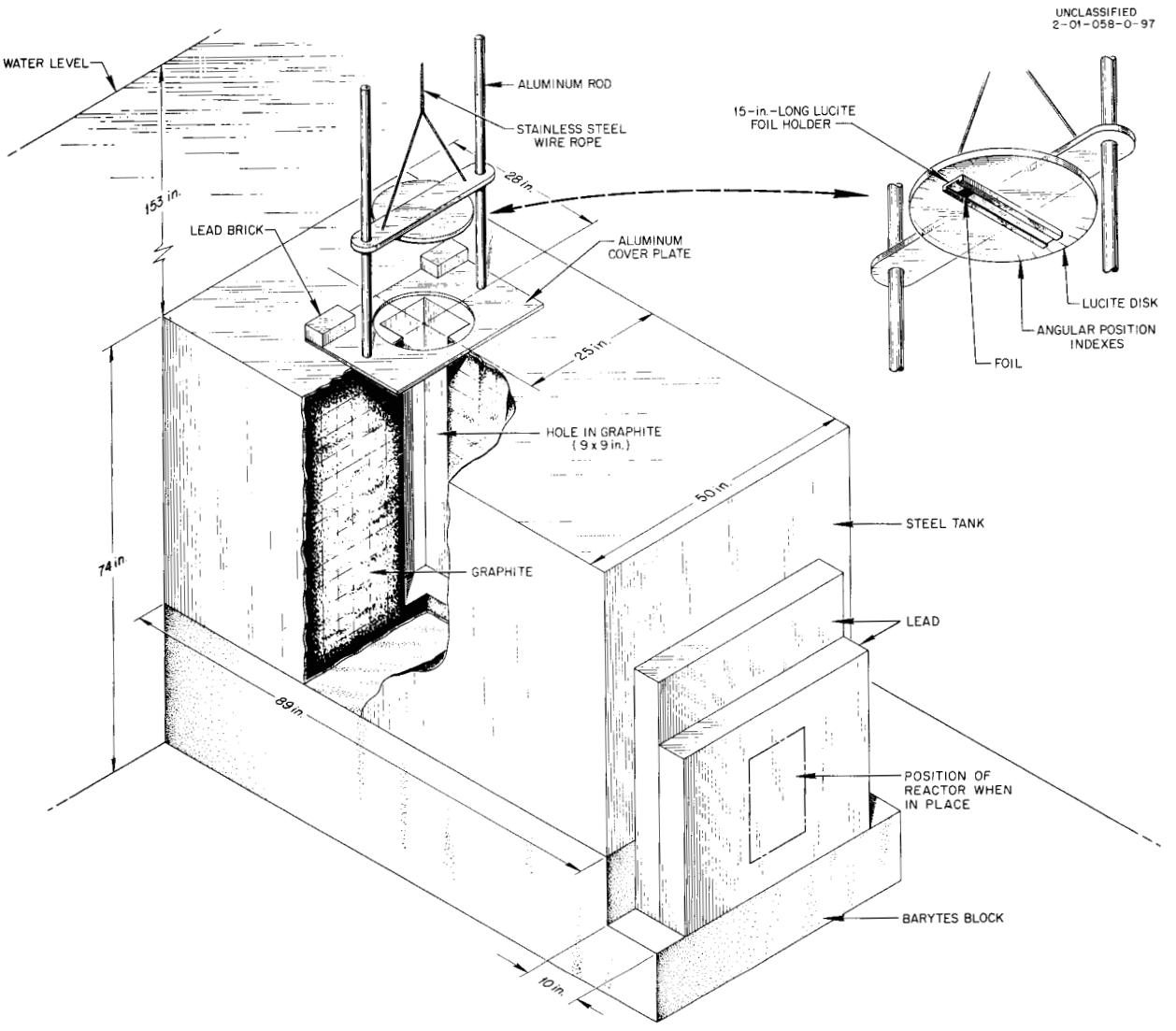

Fig. 7.1. Schematic Diagram of BSF Thermal Column.

disk. The water level of the reactor pool is $12\frac{3}{4}$ ft above the top of the tank.

The measurements were made with gold foils, 1 cm square and 5 mils thick, which were counted on continuous-flow beta proportional counters. (The counters were calibrated by means of an identical foil exposed in the ORNL Standard Pile.) The foils were positioned to within 0.02 in. of the radiation port cover. They could be positioned both in angle and radius, all foils in any one exposure being along one diameter of the aluminum disk. The spacing between foils was always maintained sufficiently large to prevent perturbations due to adjacent foils. In order to make the results of the several runs comparable, one foil, called the monitor, was always included at the center of the foil holder, and all foils were normalized to this center foil.

The comparative results, that is to say, the results normalized to unity at the monitor position, were self-consistent within statistical deviations. For example, the standard deviation of six measurements 1 in. from the center was 0.72%. The value for the absolute flux magnitude was not as certain, yielding a standard deviation of 3.6% from eight measurements. This may be ascribed, in part, to the fact that the temperature in the pool varied as much as 30°C during the measurements.

The location and magnitude of the measured fluxes with relation to the hole in the column are shown in Fig. 7.2. Figure 7.3 shows the normalized flux along one diameter. Figure 7.4 gives

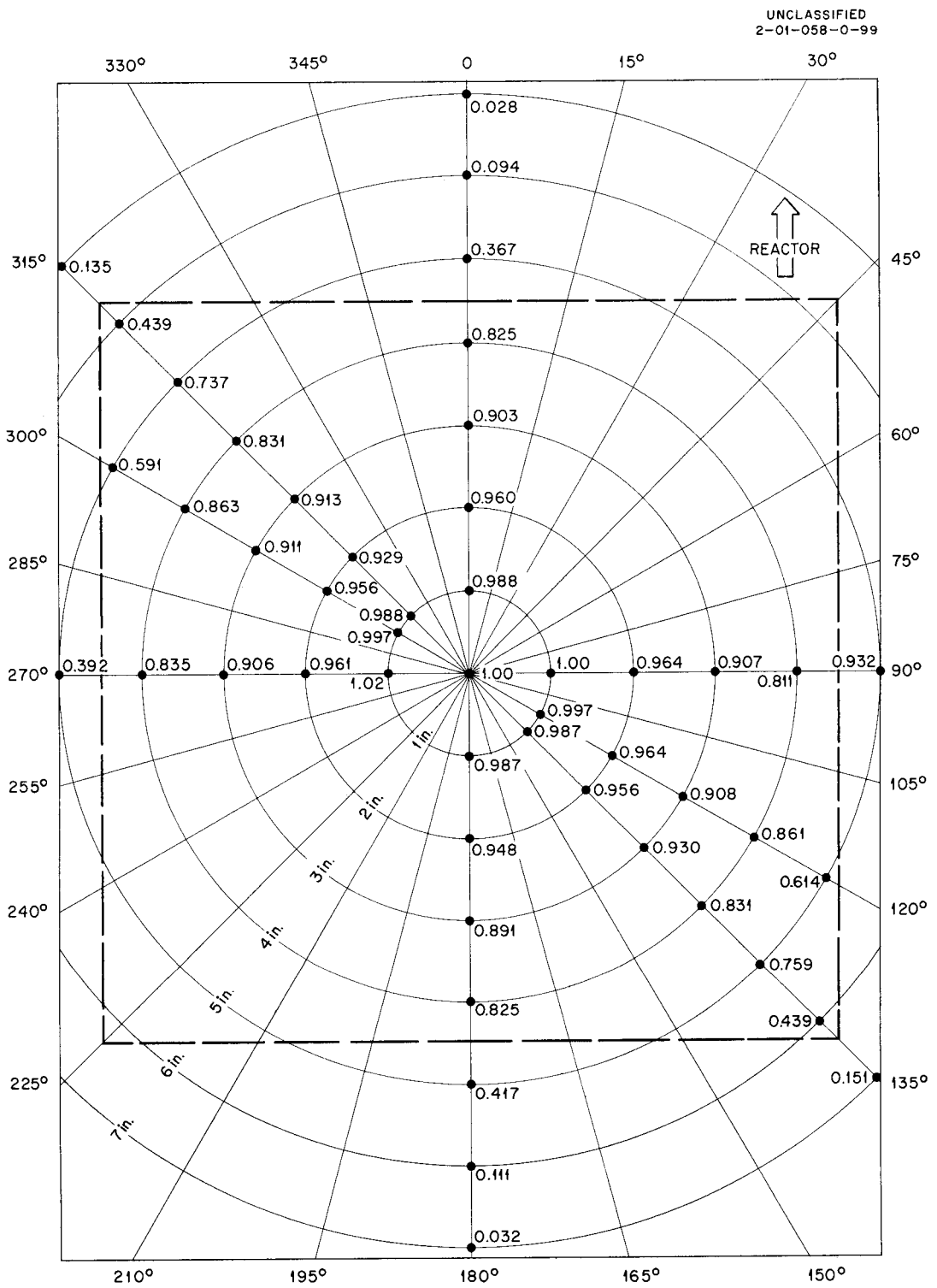

Fig. 7.2. Relative Thermal-Neutron Flux at Various Positions on Radiation Port.

the results of a survey of fluxes at various levels above the cover plate in the water. The value of the flux at the center point was $(7.13 \pm 0.26) \times 10^6$ neutrons·cm^{-2}·sec^{-1} at a reactor power of 100 kw. The corresponding epicadmium flux was measured to be $(4.84 \pm 1.22) \times 10^3$ neutrons·cm^{-2}·sec^{-1}. (The poor statistics for the epicadmium flux are due to the fact that the counting rate was only about half the background rate.) The cadmium ratio was therefore approximately $\geqq 1500$ for the gold foils used.

It may be concluded that an area of 4π in.^{2} is available above the thermal column in which the flux is uniform to within ±3%. The exact relation of the absolute value of the flux level at a given reactor power to water temperature remains to be investigated.

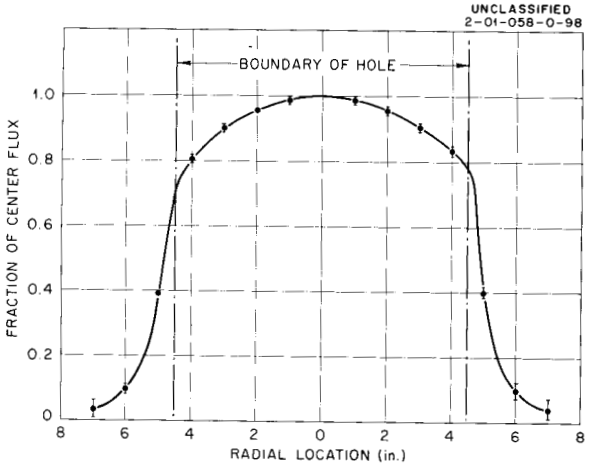

Fig. 7.3. Radial Variation of Thermal-Neutron Flux at Radiation Port.

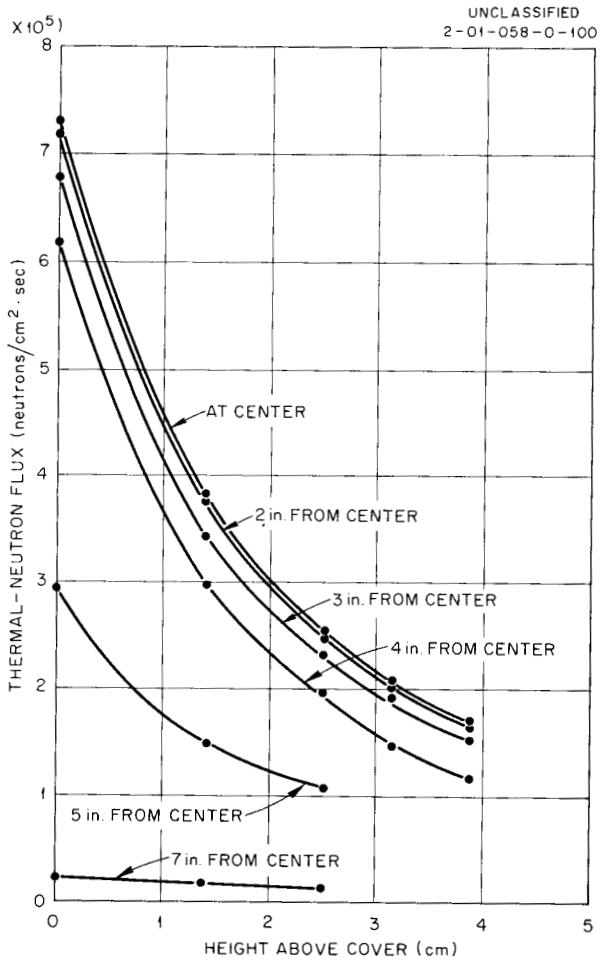

Fig. 7.4. Thermal-Neutron Fluxes at Various Points Above the BSF Thermal Column.

8. CALCULATION OF THE EFFECT ON REACTIVITY WHEN HEAVY WATER IS ADDED TO A LIGHT-WATER-MODERATED REACTOR

E. G. Silver

A calculation of the effect on reactivity when D_2O in various proportions is added to the moderator of H_2O-moderated reactors has been made. In the calculation it was assumed that the reflector properties are unchanged by enriching the moderator. ("Enrichment" in this report refers to the fraction of D_2O in the moderator. The fuel enrichment is not involved.) This assumption is deemed applicable for safety considerations, even in the case of swimming-pool-type reactors, since only short-time effects (that is, the effects before any D_2O introduced into the core could diffuse throughout the bulk of the surrounding water) are of interest. In any case, the amount of D_2O which could be diffused uniformly throughout the entire pool would be too low to be of interest. It was also assumed that the D_2O is uniformly distributed in the core, which is considered to be homogeneous throughout.

The parameters used in the calculations were determined from the following expressions:

$$D_{core} = \frac{D_{H_2O} D_{D_2O} D_{Al}}{V_{H_2O} D_{D_2O} D_{Al} + V_{D_2O} D_{H_2O} D_{Al} + V_{Al} D_{H_2O} D_{D_2O}} ,$$

where V_i is the volume fraction of constituent i, and D_i is the diffusion coefficient of constituent i in the core;[1]

$$L^2 = \frac{D_{core}}{\Sigma_a^{core}}$$

where L is the diffusion length (cm) in the core and Σ_a^{core} is the macroscopic total absorption cross section of the core;

$$\tau = \frac{\tau_{Al} \tau_{mix}}{\left(V_{Al} \sqrt{\tau_{mix}} + V_{mix} \sqrt{\tau_{Al}} \right)^2}$$

where τ is the Fermi age in the core (cm^2), τ_{Al} is the Fermi age in pure aluminum, τ_{mix} is the Fermi age in the $H_2O + D_2O$ mixture, and V_{mix} is the volume fraction of the $H_2O + D_2O$ mixture in the core. This equation, which was also used to calculate τ_{mix} from τ_{H_2O} and τ_{D_2O}, is based on the fact that $\sqrt{\tau}$ varies as the mean free path. Experimental evidence on the age in aluminum-water mixtures[2] agrees well with this equation and therefore lends support to its use.

The equation[3] for k, the multiplication constant, is

$$k = \frac{\nu \Sigma_f \epsilon p}{\Sigma_a^{core} \left[1 + (L^2 + \tau) B^2 \right]} = \frac{\nu \Sigma_f \epsilon p}{\left[\Sigma_a^{fuel} + \Sigma_a^{Al} + \Sigma_a^{mix} \right] \left[1 + (L^2 + \tau) B^2 \right]} ,$$

where ν is the number of neutrons released per fission, Σ_f is the fission cross section, ϵ is the fast-fission coefficient, and p is the resonance escape probability. Thus, for the case in which the reflector remains unchanged but the moderator

[1] D is the volume fraction weighted average of the diffusion coefficients of the components.

[2] L. D. Roberts, J. E. Hill, and T. E. Fitch, *J. Appl. Phys.* 26, 1018 (1955).

[3] S. Glasstone and M. C. Edlund, *Elements of Nuclear Reactor Theory*, Van Nostrand, New York, 1952.

is enriched, the ratio of $k_{H_2O+D_2O}$ to k_{H_2O} is

$$\frac{k_{H_2O+D_2O}}{k_{H_2O}} = \frac{\Sigma_a^{fuel} + \Sigma_a^{Al} + \Sigma_a^{H_2O}}{\Sigma_a^{fuel} + \Sigma_a^{Al} + \Sigma_a^{mix}} \; \frac{\left[1 + (L^2 + \tau) B^2\right]_{H_2O}}{\left[1 + (L^2 + \tau) B^2\right]_{H_2O+D_2O}} ,$$

where B^2 is the buckling and the subscripts ($H_2O + D_2O$) and H_2O describe the composition of the moderator.

The values of the absorption cross sections and diffusion coefficients used in this calculation were as follows:

$$\Sigma_a^{H_2O} = 0.01915 \text{ cm}^{-1} \qquad D_{H_2O} = 0.160 \text{ cm}$$

$$\Sigma_a^{D_2O} = 0.000074 \text{ cm}^{-1} \qquad D_{D_2O} = 0.80 \text{ cm}$$

$$\Sigma_a^{Al} = 0.0120 \text{ cm}^{-1} \qquad D_{Al} = 3.97 \text{ cm}$$

These absorption cross sections are averages over a Maxwellian distribution at 30°C.

The results of the calculations, in terms of $k_{(H_2O+D_2O)}/k_{H_2O}$ as a function of the volume fraction of D_2O in the moderator, are presented in Figs. 8.1 through 8.9 for all nine combinations of the following parameters:

$$\Sigma_a^{fuel} = 0.03, 0.052, \text{ and } 0.07 \text{ cm}^{-1} ,$$

$$\frac{M}{W} = 0.5, 0.733, \text{ and } 1.0 ,$$

where M/W refers to the fraction of metal (aluminum and uranium) in the total core volume divided by the fraction of moderator. For each of the nine parameter pairs, four values of B^2 (0.01, 0.007, 0.004, and 0.001) were considered, and a curve for each is plotted in the figures.

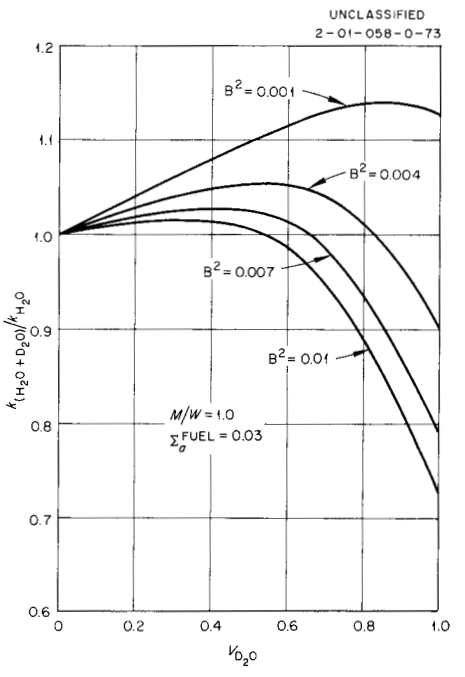

Fig. 8.1. Ratio of the Reactivity of an H_2O-D_2O-Moderated Reactor to the Reactivity of an H_2O-Moderated Reactor as a Function of the Volume Fraction of D_2O in the Moderator.

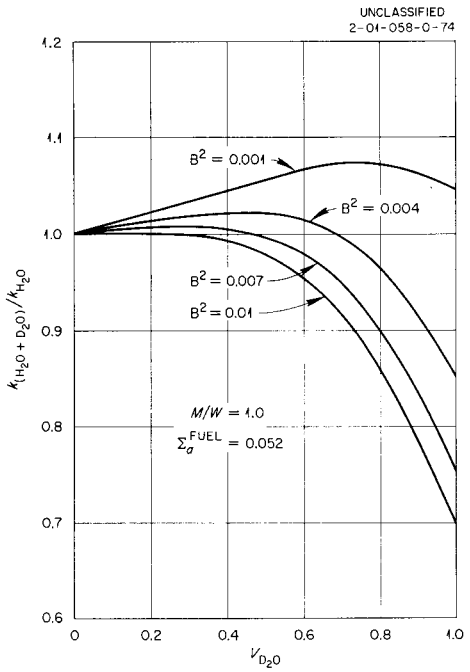

Fig. 8.2. Ratio of the Reactivity of an H_2O-D_2O-Moderated Reactor to the Reactivity of an H_2O-Moderated Reactor as a Function of the Volume Fraction of D_2O in the Moderator.

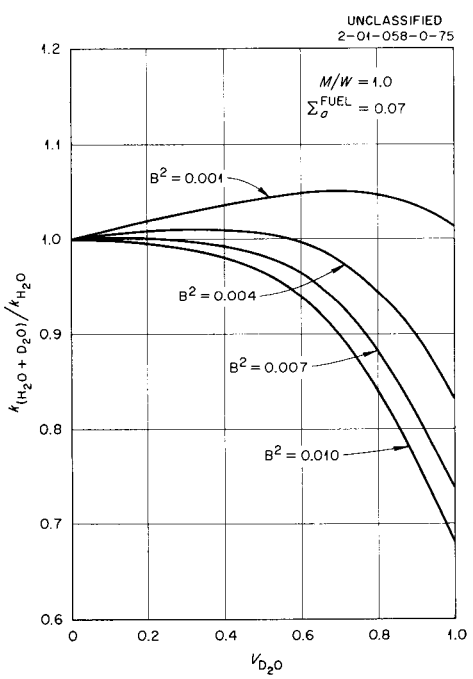

Fig. 8.3. Ratio of the Reactivity of an H_2O-D_2O-Moderated Reactor to the Reactivity of an H_2O-Moderated Reactor as a Function of the Volume Fraction of D_2O in the Moderator.

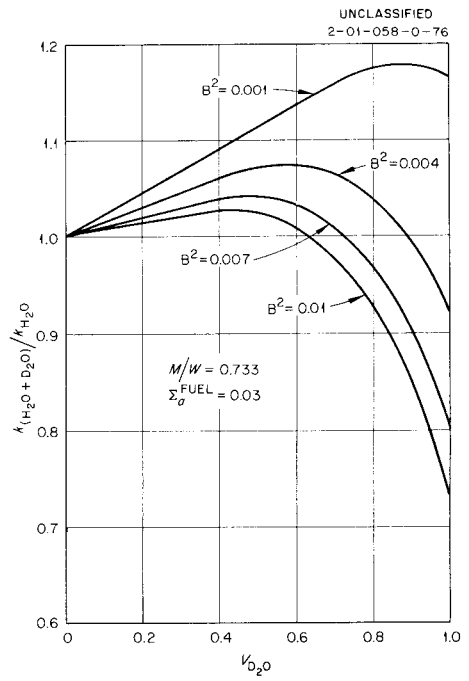

Fig. 8.4. Ratio of the Reactivity of an H_2O-D_2O-Moderated Reactor to the Reactivity of an H_2O-Moderated Reactor as a Function of the Volume Fraction of D_2O in the Moderator.

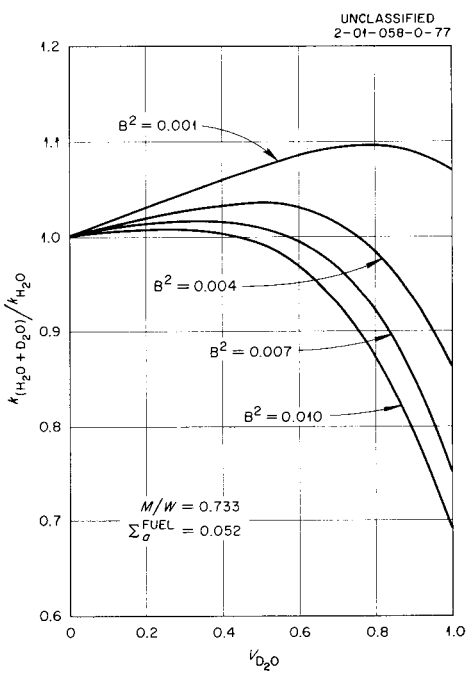

Fig. 8.5. Ratio of the Reactivity of an H_2O-D_2O-Moderated Reactor to the Reactivity of an H_2O-Moderated Reactor as a Function of the Volume Fraction of D_2O in the Moderator.

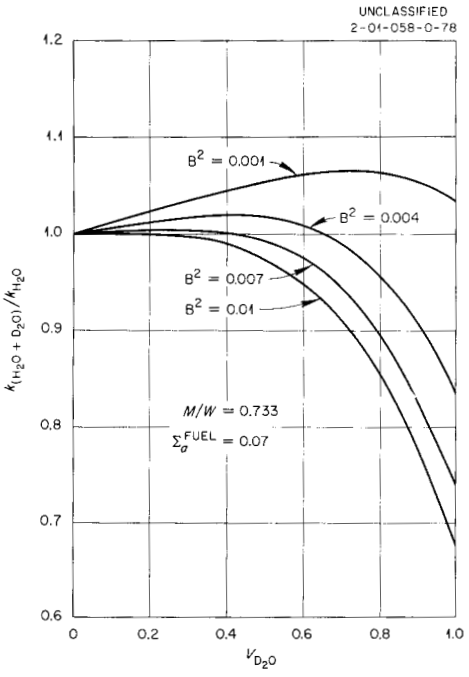

Fig. 8.6. Ratio of the Reactivity of an H_2O-D_2O-Moderated Reactor to the Reactivity of an H_2O-Moderated Reactor as a Function of the Volume Fraction of D_2O in the Moderator.

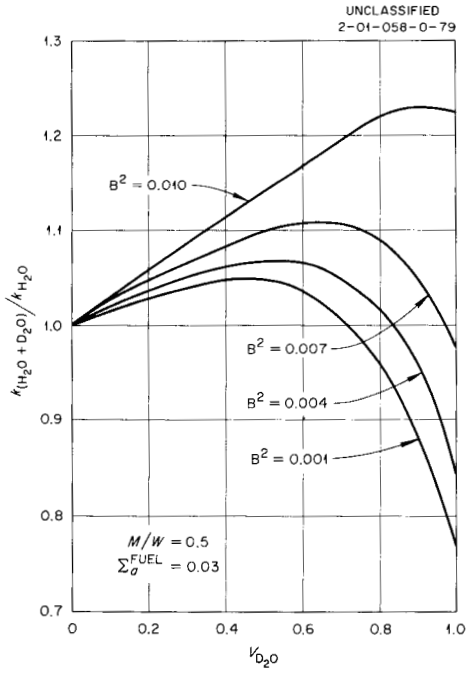

Fig. 8.7. Ratio of the Reactivity of an H_2O-D_2O-Moderated Reactor to the Reactivity of an H_2O-Moderated Reactor as a Function of the Volume Fraction of D_2O in the Moderator.

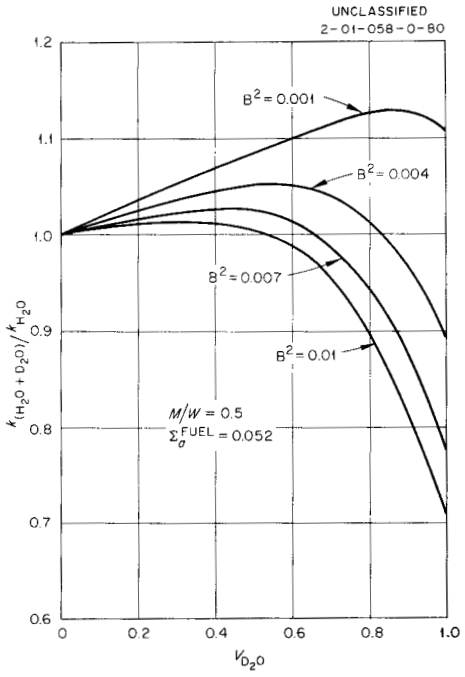

Fig. 8.8. Ratio of the Reactivity of an H_2O-D_2O-Moderated Reactor to the Reactivity of an H_2O-Moderated Reactor as a Function of the Volume Fraction of D_2O in the Moderator.

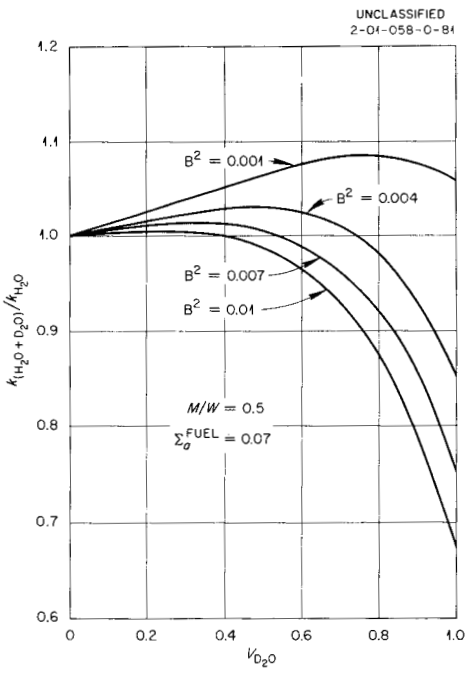

Fig. 8.9. Ratio of the Reactivity of an H_2O-D_2O-Moderated Reactor to the Reactivity of an H_2O-Moderated Reactor as a Function of the Volume Fraction of D_2O in the Moderator.

9. COMPARISON OF CALCULATED CRITICAL MASS OF THE BSR WITH EXPERIMENT

E. G. Silver

The critical masses of three swimming-pool-type reactors have been computed and compared with corresponding experimental critical masses for the specified loadings in the BSR. Two reactor codes were employed in the calculations: the UNIVAC Eyewash 30-group code using three concentric spherical regions (control rod, fuel, and reflector); and the Oracle three-group, three-region (3G3R) code. The latter was used both as a two-region and as a three-region problem for a cylindrical or spherical reactor. A discussion of the experiments, the calculations, and the correlated results are given below.

Critical Experiments[1]

Critical experiments were performed with three water-reflected reactor loadings in as clean a geometry as possible. In each case only one control rod, located at or near the center of the loading, was used. The required safety characteristics were supplied by two cadmium curtains which were suspended, guillotine fashion, on opposite sides of the reactor above the core-reflector interface by means of a control-rod-type electromagnet. These curtains were connected to the safety system of the reactor so that any of the usual scram signals would drop them between the core and the reflector.

The three configurations used in the experiment included (1) a 3 by 9 element array, (2) a 5 by 5 element array that contained four partial elements (Fig. 9.1), and (3) a 6 by 4 element array (Fig. 9.1)

[1]These experiments were performed by K. M. Henry, E. B. Johnson, and J. Kington.

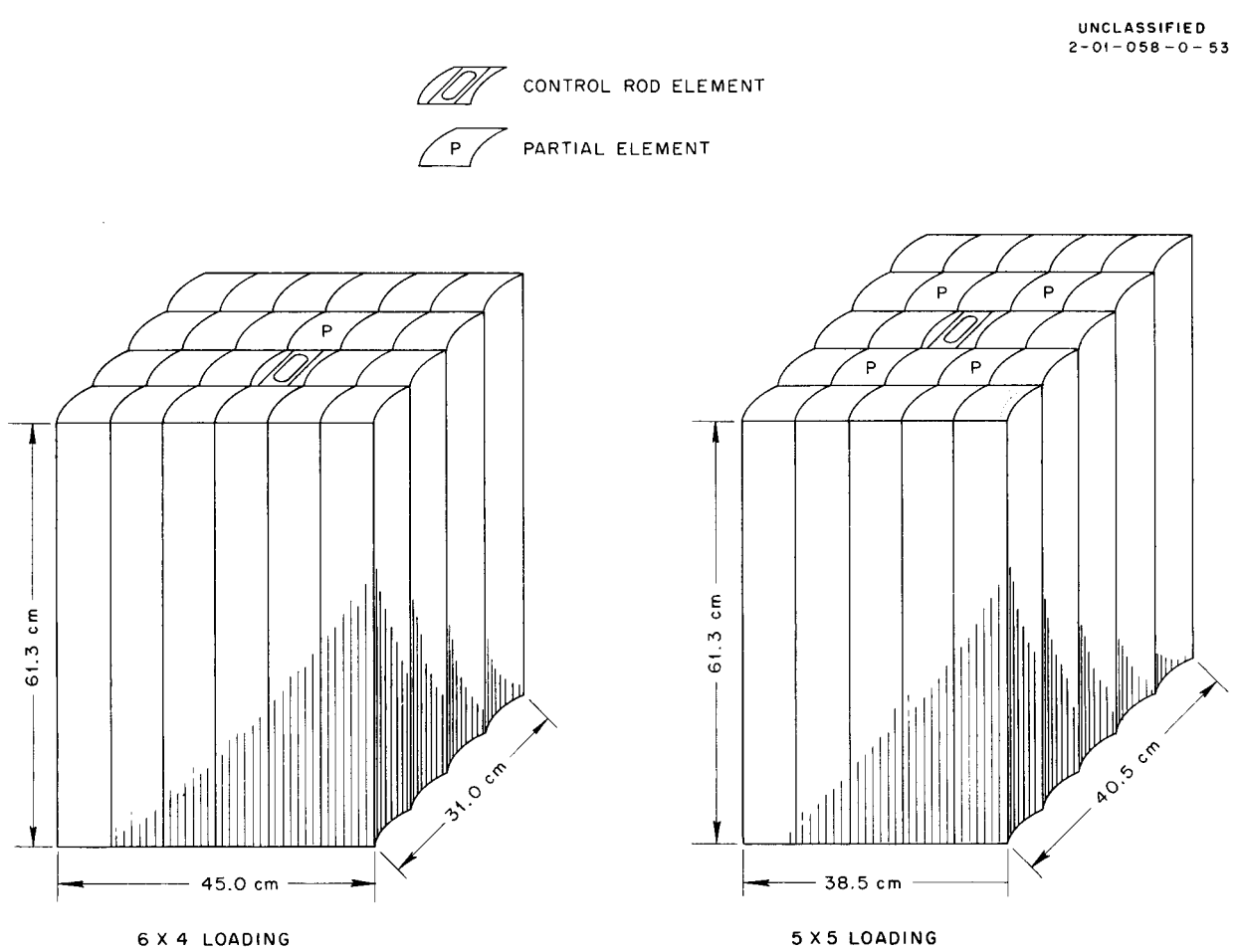

Fig. 9.1. Experimental Critical Reactor Loadings Used for Calculations.

that contained one partial element. The grid was loaded so that criticality was achieved with the control rod fully withdrawn, in order to eliminate any vertical variation in the poison concentration. Each partial element used in the 5 by 5 and the 6 by 4 element loadings had the full complement of plates, so that its metal-to-water ratio was equal to that of the other elements. The control-rod element has $^{13}/_{32}$-in. control-rod guide plates so that, with the rod fully withdrawn, the metal-to-water ratio in this element is equal to this ratio in the other elements. With this arrangement the critical assembly had a uniform metal-to-water ratio. All elements used in the experiments were cold elements; that is, they had not been previously operated at powers high enough for them to be contaminated with fission products.

The 3 by 9 loading did not go critical, even with a complete set of full fuel elements. However, the extrapolation of the reciprocal count rate as a function of mass (Fig. 9.2) gave a predicted critical mass.

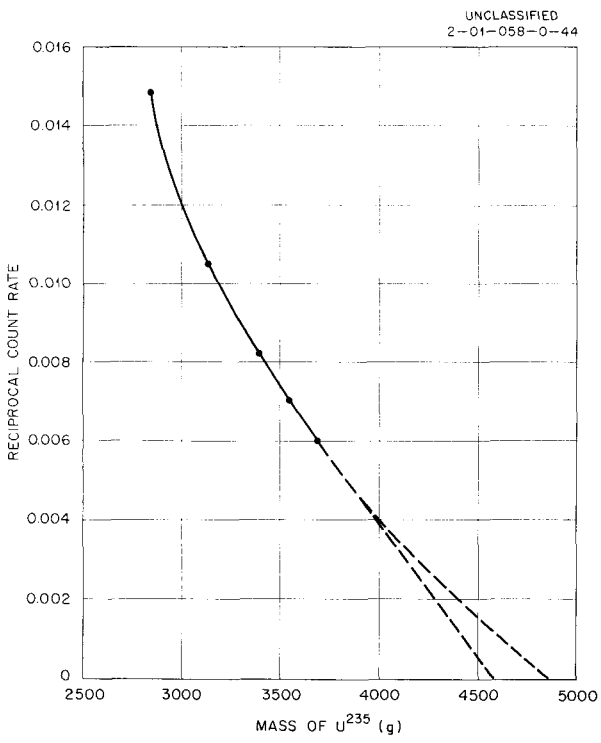

Fig. 9.2. Experimental Subcritical Multiplication Curve for the 3 by 9 Element BSR Loading.

The full fuel elements and the control-rod element used in these configurations were elements constructed for the University of Michigan Reactor. During the tests the worth (in % $\Delta k/k$) of each element compared with the worth of a full BSR element (No. 90) was determined. The results are listed in Table 9.1.

TABLE 9.1. MEASURED REACTIVITY WORTH OF THE UNIVERSITY OF MICHIGAN REACTOR FUEL ELEMENTS

Element No.	Reactivity Worth $\left[\frac{\% \Delta k/k \text{ (Michigan)}}{\% \Delta k/k \text{ (BSR No. 90)*}}\right]$	Difference in Worth from Average of Entire Set (% $\Delta k/k$)
1	−0.143	+0.0021
2	−0.142	+0.0011
3	−0.153	+0.0121
4	−0.145	+0.0041
5	−0.153	+0.0121
6	−0.150	+0.0091
7	−0.137	−0.0039
8	−0.129	−0.0119
9	−0.137	−0.0039
10	−0.154	+0.0131
11	−0.135	−0.0059
12	−0.124	−0.0169
13	−0.137	−0.0039
14	−0.131	−0.0099
15	−0.147	+0.0061
16	−0.137	−0.0039
17	−0.137	−0.0039
18	−0.145	+0.0041
19	−0.142	+0.0011

*BSR element No. 90 is a "hot" element; it had the lowest worth of the BSR elements tested and had a nominal fuel content of 139.149 g of U^{235}, adjusted for burnup.

Critical-Mass Calculations

Since the codes available for reactor calculations are largely one-dimensional and are most suitably applied to a sphere or cylinder, it was necessary to convert the parallelepiped geometry of the actual loadings to equivalent spheres or cylinders. In order to do this the bucklings B with reflector

savings δ were assumed to be equal[2] in the two geometries. That is to say, the reflector savings were added to the dimensions of the parallelepiped, and the geometric buckling of this figure was set equal to that of the sphere or cylinder with the same reflector savings. For example, the radius R of a sphere equivalent to a parallelepiped with dimensions a, b, and c is determined as follows:

$$R = \frac{\pi}{B} - \delta ,$$

where

$$B = \sqrt{\left(\frac{\pi}{a + 2\delta}\right)^2 + \left(\frac{\pi}{b + 2\delta}\right)^2 + \left(\frac{\pi}{c + 2\delta}\right)^2} ,$$

$$\delta = \frac{D_c}{D_r} L_r ,$$

D_c = thermal diffusion coefficient in the core,

D_r = thermal diffusion coefficient in the reflector,

L_r = thermal diffusion length in the reflector.

In the same fashion an equivalent cylinder may be found. These configurations are equivalent to the actual reactor, in that the fuel concentration and cross sections are the same for the same multiplication constant, k.

A further geometrical consideration involved the control-rod well, which was treated in three ways. For some calculations, it was ignored; that is, only two regions (fuel and reflector) were included in the calculation. In this case the fuel was homogenized over the entire core region. In a second method the control-rod well was treated as a separate region, the size of which was obtained in a simple approximation by assuming it to have the same volume fraction in the sphere or cylinder as it has in the parallelepiped. This assumption is referred to as the "direct control-rod volume ratio" assumption. A third method[3] was used in which the volume fraction was adjusted to account for the fact that the peak-to-average flux ratio in a sphere or cylinder is different from that in a parallelepiped. The adjustment was therefore made by multiplying the volume fraction of the control rod in the parallelepiped by the ratio of the peak-to-average flux in the core or cylinder to that in the parallelepiped when the two configurations are homogeneous. For the parallelepiped-to-sphere transformation,

$$\frac{V_{CR(S)}}{V_S} = \frac{1.2159 V_{CR(P)}}{V_P} ,$$

while for the parallelepiped-to-cylinder transformation,

$$\frac{V_{CR(C)}}{V_C} = \frac{1.0778 V_{CR(P)}}{V_P} ,$$

where V is the volume, and the subscripts S, C, P, and CR refer, respectively, to the sphere, cylinder, parallelepiped, and control-rod well in the indicated geometry. When this assumption is used it is referred to as the "adjusted control-rod volume ratio" assumption.

One of the reactor codes used was the UNIVAC 30-group Eyewash code, using three concentric spherical regions. The direct control-rod volume ratio assumption was used for all the calculations with this code. The nuclear cross sections and other parameters are incorporated in the code, and did not, therefore, have to be submitted separately. The code utilizes Selengut-Goertzel slowing-down in the hydrogenous moderator and reflector.[4] This method is an improvement over the age-diffusion slowing-down in these materials, where age-diffusion is inapplicable owing to the large fractional energy loss which a neutron may suffer in a single collision with a proton. This large energy loss is inconsistent with continuous slowing-down, which is assumed in age-diffusion theory. The Selengut-Goertzel method employs the correct energy-loss probabilities in neutron-proton collision, though not the correct angular distribution for these collisions.

The second reactor code used in the calculations was the Oracle 3G3R code. This is a one-dimensional code which can be used to calculate the critical

[2]The procedure used was that developed by F. C. Prohammer, *A Comparison of One-Dimensional Critical Mass Computations with Experiments for Completely Reflected Reactors*, ORNL-2007 (Mar. 16, 1956); see also Chap. 15 in this report.

[3]Suggested by A. Simon.

[4]G. Goertzel, *Criticality of Hydrogen Moderated Reactors*, TAB-53 (July 25, 1950); D. Selengut, private communication to G. Goertzel.

masses of reactors in spherical, cylindrical, or slab geometry with up to three energy groups and regions.

It was with this 3G3R code, used as a two-group code, that investigations of the effects of various assumptions were made. (The code has the advantages of flexibility as to geometry and requires only about 2 min computing time per case.) The effect of calculating the parallelepiped as a two- or three-region cylinder or sphere was determined. For the three-region calculations both the direct and the adjusted control-rod volume ratio assumptions were used. In the cylindrical geometry, one-dimensional *radial* calculations were made in which the noninfinite axial length of the core is taken into account in the form of a buckling in the axial direction for both fast and slow groups. This buckling must take into consideration the height of the core and the effect of the reflector capping the ends of the cylinder. Two methods for this were tested. In the first method the axial buckling for the fast and slow groups was assumed to be equal and was calculated as follows:

$$B = \frac{\pi}{h + 2\delta} ,$$

where

h = height of reactor,

$\delta = (D_{f_c}/D_{f_r})M_r$,

D_{f_c} = fast-group diffusion coefficient in the core,

D_{f_r} = fast-group diffusion coefficient in the reflector,

M_r = migration length in the reflector.

In the second method the axial bucklings for the fast and slow groups were calculated separately as follows:

$$B_{fast} = \frac{\pi}{h + 2\delta_f} ,$$

where

$\delta_f = (D_{f_c}/D_{f_r})L_{f_r}$,

L_{f_r} = diffusion length for the fast group in the reflector

$= \sqrt{D_{f_r}/\Sigma_{x_f}}$,

Σ_{x_f} = fast-transfer cross section in the reflector;

$$B_{slow} = \frac{\pi}{h + 2\delta_s} ,$$

where

$\delta_s = (D_{s_c}/D_{s_r})L_{s_r}$,

D_{s_c}, D_{s_r} = slow-group diffusion coefficients in the core and reflector,

L_{s_r} = slow-diffusion length in the reflector.

The dimensions of the various reactors used in the calculation are listed in Table 9.2. They were

TABLE 9.2. REACTOR DIMENSIONS USED IN CRITICAL-MASS CALCULATIONS

Core Configuration	Control-Rod Well Equivalent Radius (cm)		Core Radius (cm)	H_2O Reflector Thickness (cm)	Cylinder Height (cm)
	Direct Volume Fraction	Adjusted Volume Fraction			
		Cylindrical Reactor			
5 × 5	3.35	3.48	21.75	20	61.28
6 × 4	3.28	3.41	20.87	20	61.28
		Spherical Reactor			
3 × 9	6.48		23.14	20	
5 × 5	7.58	8.09	26.36	20	
6 × 4	7.52	8.02	25.79	20	

obtained by applying the Prohammer method[2] to the experimental core dimensions shown in Fig. 9.1.

The nuclear parameters used in calculations with the 3G3R code were as follows:

$\Sigma_{a_f}, \Sigma_{a_s}$ = macroscopic absorption cross sections, fast and slow, in each region,

D_f, D_s = diffusion coefficients, fast and slow, in each region,

τ = Fermi age to thermal,

$\Sigma_{x_f}, \Sigma_{x_s}$ = macroscopic transfer cross sections, fast and slow, in each region,

$\nu\Sigma_{f_f}, \nu\Sigma_{f_s}$ = neutrons per fission times the macroscopic fission cross section, both fast and slow, in each region.

The slow-group absorption cross sections were obtained from data in BNL-325,[5] adjusted to average over a Maxwellian distribution at a temperature corresponding to 2200 m/sec and multiplied by 1/1.017 to convert them to a temperature of 30° C, which was assumed to be the pool temperature when the critical experiments were performed. The U^{235} cross sections were further adjusted for non-$1/v$ behavior, according to the curve in BNL-325. The values of these cross sections were calculated under the assumption that the volume fractions of aluminum and water in both the core and the control-rod well were: aluminum, 0.4229; H_2O, 0.5771. The reflector was assumed to be pure water.

The fast-group absorption cross sections were set equal to zero; that is, it was assumed that all the fast-group neutrons were removed either by leakage or by throwing the neutron into the slow group. This assumption essentially neglects resonance absorption, and thus would tend to give too large a multiplication constant. However, the fast-group fission cross sections are also set equal to zero, so that this combination of assumptions corresponds to the assumption that $\epsilon p = 1.0$, where ϵ is the fast-fission factor and p is the resonance escape probability. The assumption that $\epsilon p = 1$ is found to be very nearly true for highly thermal reactors such as these.

The diffusion coefficients were calculated on the assumption that the fuel does not affect them. The slow, or thermal, diffusion coefficient in the core was obtained from IDO-16127,[6] where it is calculated by the following equation:

$$D = \frac{1}{3\Sigma_i \Sigma_{i_{tr}}},$$

where $\Sigma_{i_{tr}}$ is the transport cross section of the ith component of the core, and the contributions from the i components are summed (Σ_i). The slow-diffusion coefficient for the reflector which was pure water, was taken to be

$$D_{s_r} = 0.16025 \text{ cm} = \frac{1}{3 \times 2.08}.$$

The quantity $\Sigma_{H_2O_{tr}} = 2.08 \text{ cm}^{-1}$ for H_2O was calculated from experiments and was quoted in IDO-16127.

The fast-diffusion coefficients, calculated from $D(E)$ values weighted by the spectrum given in WAPD-45,[7] are taken from IDO-16133.[8] The Fermi ages to thermal are quoted in IDO-16083[9] and are taken from curves presented in MonP-219,[10] which give the effect of the aluminum-to-water ratio on the age. The fast-group transfer cross sections are given by $\Sigma_x = D_f/\tau$. The slow-group transfer cross sections are zero.

A summary of the nuclear parameters used in the calculations is presented in Table 9.3.

---

[5] D. J. Hughes and J. A. Harvey, *Neutron Cross Sections*, BNL-325 (July 1, 1955).

[6] H. L. McMurry, *Nuclear Constants for the MTR as a Function of Fuel Content, Poison Content, and Al/H_2O Ratio*, IDO-16127 (Oct. 23, 1953).

[7] F. C. Brooks and H. L. Glick, WAPD-45 (Nov. 1951) (Secret).

[8] J. W. Webster, *Reactivity Effect of Reducing the Al/H_2O Ratio in the MTR Core*, IDO-16133 (Oct. 26, 1952).

[9] H. L. McMurry, *Calculated Reactivity Changes Due to Reductions of Aluminum in the MTR Core*, IDO-16083 (Mar. 16, 1953).

[10] N. M. Dismuke and M. R. Arnette, *Age to Thermal Energy (.025 e.v.) of Fission Neutrons in H_2O-Al Mixture*, MonP-219 (Dec. 5, 1946).

TABLE 9.3. NUCLEAR PARAMETERS USED IN CRITICAL-MASS CALCULATIONS WITH 3G3R CODE

Region	Absorption Cross Section (cm^{-1})		Diffusion Coefficient (cm)		Fermi Age, $\tau(cm^2)$	Transfer Cross Section (cm^{-1})	
	Fast, Σ_{a_f}	Thermal, Σ_{a_s}	Fast, D_f	Thermal, D_s		Fast, Σ_{x_f}	Thermal, Σ_{x_s}
Control-rod well	0.0	0.01619	1.31	0.269	64.0	0.02062	0.0
Core	0.0	$0.01619 + \Sigma_{a_s}^{25}$	1.31	0.269	64.0	0.02062	0.0
Reflector	0.0	0.01916	1.19	0.160	32.8	0.0363	0.0

Results and Discussion

The calculated critical masses are listed in Table 9.4, together with the resulting prediction of the amount of fuel necessary for criticality for each model. The experimental critical masses are also listed for comparison. In comparing the calculations with the experiments, the differences between the assumptions and the experimental case must be considered. For instance, the temperature of the water in the pool when the experiments were carried out was 20°C, not 30°C as was assumed in the calculations. Accordingly, the critical mass was corrected to what it would have been had the temperature been 10°C higher. The measured temperature coefficient of the BSR in this temperature range is $5 \times 10^{-6}/°C$, and this figure, together with the plots of the mass as a function of k (the multiplication constant), yields a correction of −8 g. This is small enough so that a high degree of accuracy in the temperature coefficient, or Δk/mass value, is not necessary.

Another correction is necessitated by the presence of partial fuel elements in the core. In the case of the 5 by 5 loading there was a total of about 160 g less fuel in the core than there would have been if the core had consisted of full elements throughout. In the case of the 6 by 4 loading, the effective difference was only 26 g. The latter number was determined by tests in which a full element was located in the reactor lattice position previously occupied by the partial element. The loading was supercritical with a slow positive period that indicated an excess reactivity of about 0.25%. With a 109-g element (31 g less than the full element) substituted in the same position, the reactor was not quite critical, with a deficiency judged, from its period, to be 0.05%. Therefore, the critical mass was determined to be 114 g in this location, making a 26-g defect in this element at criticality.

In order to assess the effect of these fuel inhomogeneities it is necessary to find the relative effectiveness of the "missing" fuel as compared with the average fuel effectiveness. In a bare reactor small perturbations in the fuel density would be weighted by the square of the flux, and, while this is not strictly true in a reflected reactor, the square of the flux was used as the weighting function, since the adjoint fluxes are not available. Thus, the best calculated values for the thermal-flux shape were used to obtain the flux-squared weighted effectiveness, which was computed to be 1.4 times the average at the location of the partial elements. The resulting corrections were −64 ± 15 g for the 5 by 5 element configuration and −10 ± 3 g for the 6 by 4 element configuration.

Inspection of the calculated and experimental critical masses in Table 9.4 shows that, in general, the agreement is quite good. The calculations for cylindrical reactors would be expected to be better than those for spherical reactors from the point of view that a less extreme geometrical transformation was involved; however, for cylindrical reactors there is the uncertainty as to the best method of calculating the buckling. It appears that the diffusion-length method is actually the best method. The best model would also include three regions rather than two. In addition, the adjusted rather than the direct control-rod well volume ratio should be best. As can be seen in Table 9.4, the calculations using this cylindrical model yield masses that are correct to within 0.5% for one configuration and 1.2% for the other.

It is evident that the spherical model tends to give results that are too high by about 5 to 7% and that the two-region assumption gives results

that are too low by about 4 to 6%. The calculations for the two-region sphere thus show fair agreement with experiment (better than 2%) due to the partial cancellation of these two errors. The results of the calculations for the three-region sphere, having only the "geometry" error, are too high.

The two-region cylinder calculations show too low a result with the diffusion-length assumption, but too high a result with the migration-length assumption. In accordance with the ideas developed above, the conclusion is that the diffusion-length assumption is the preferred one, since a two-region calculation should give too low a result, as was observed in the case of the sphere. The high result for the two-region cylinders with the migration-length assumption is then due to the poorer agreement of this assumption with the physical reality. That is to say, it is concluded that equating the buckling for the fast and slow groups leads to an error of the order of about +4 to 5%. The effect of the adjustment of the control-rod well volume is seen to be small, of the order of 0.3 to 0.4%, and the other uncertainties in the comparison preclude a definite decision as to which is better. The conclusion, however, is clear: the calculation with the best assumptions was capable of results that were within about 1% of the correct critical mass and within about 0.4% of the reactivity, which is surprisingly good.

The calculations utilizing the UNIVAC Eyewash code are all for spherical, three-region reactors, with the control-rod well volume having the same volume fraction as the actual reactors. These calculations are therefore exactly the same, as far as the geometry is concerned, as the similar 3G3R work.

The Eyewash results for the 3 by 9 element configuration fall well within the predicted mass from the critical experiment extrapolation and therefore are correct to within the accuracy that this experiment permits. The Eyewash results for the 5 by 5 and the 4 by 6 element loadings are somewhat closer to the experimental results than are the 3G3R results for the identical geometry. This is to be expected from the improved nuclear sophistication inherent in a 30-group calculation. What is surprising, and not readily explained, is that this calculation did not correctly predict the sign of the difference between the 5 by 5 and the 6 by 4 configurations. All the 3G3R results correctly indicate that the 6 by 4 reactor requires somewhat more fuel than the 5 by 5. However, the difference is small, and it may be concluded that with Eyewash a rather good calculation of critical mass may be made, even in spherical geometry.

It is of interest that the Eyewash output can include detailed information about all the 30 energy-group fluxes, at 60 space points each. From this information, informative plots of the flux as a function of energy at any location, or the fluxes at several energies, can be constructed. These may be useful in predicting the leakages and energy distributions into a reactor shield. Examples of this type of information are given in Figs. 9.3 and 9.4.

The radial flux distribution in the cylindrical representation of the 5 by 5 configuration, as calculated by the 3G3R two- and three-region methods, is shown in Fig. 9.5 for the slow group. The corresponding information for the fast group is shown in Fig. 9.6. It is interesting to observe that the differences in the flux shapes are quite large, and it is perhaps surprising that the difference in reactivity calculated in the two cases is no larger than it is. The small difference is probably due to the fact that the largest perturbation occurs in a comparatively small region of the core.

TABLE 9.4. CALCULATED AND EXPERIMENTAL CRITICAL MASSES OF THE BSR

Reactor Configuration	Calculations					Experimental Critical Mass (kg)	Per Cent Difference Between Calculated and Experimental Critical Masses
	Reactor Code	Reactor Model	Assumed Mass (kg)	Reactivity	Critical Mass (kg)		
3 × 9	Eyewash	Three-region sphere; direct control-rod volume ratio			4.68[a]	(4.6–4.9)[b]	
5 × 5	Eyewash	Three-region sphere; direct control-rod volume ratio			3.27	3.246 (3.226)[c]	
	3G3R	Three-region sphere					
		Direct control-rod volume ratio	3.40	1.001	3.38		+6.1
			3.10	0.976			
			2.70	0.936			
		Adjusted control-rod volume ratio	3.38	0.995	3.44		+7.9
			3.08	0.970			
			2.69	0.930			
		Two-region sphere	3.30	1.012	3.16		−0.8
			3.00	0.985			
			2.60	0.943			
		Three-region cylinder					
		Direct control-rod volume ratio					
		Equal fast- and slow-group bucklings; migration-length assumption	3.40	1.012	3.25		+1.9
			3.10	0.987			
			2.70	0.947			
		Different fast- and slow-group bucklings; diffusion-length assumption			3.16[d]		−0.8
		Adjusted control-rod volume ratio					
		Equal fast- and slow-group bucklings; migration-length assumption	3.39	1.011			
			3.09	0.985	3.26		+2.2
			2.69	0.945			
		Different fast- and slow-group bucklings; diffusion-length assumption			3.17[d]		−0.5
		Two-region cylinder					
		Equal fast- and slow group bucklings; migration-length assumption	3.30	1.013	3.16		−0.9
			3.00	0.985			
			2.60	0.944			
		Different fast- and slow-group bucklings; diffusion-length assumption	3.30	1.019	3.08		−3.5
			3.00	0.993			
			2.60	0.950			

4 × 6	Eyewash	Three-region sphere; direct control-rod volume ratio			3.26	3.242 (3.236)[c]	+0.6
	3G3R	Three-region sphere					
		Direct control-rod volume ratio	3.40 3.10 2.70	1.012 0.987 0.947	3.42		+5.5
		Adjusted control-rod volume ratio	3.39 3.09 2.69	0.993 0.968 0.929	3.48		+7.4
		Two-region sphere	3.30 3.00 2.60	1.010 0.943	3.18		−1.7
		Three-region cylinder					
		Direct control-rod volume ratio					
		Equal fast- and slow-group bucklings; migration-length assumption	3.40 3.10 2.70	1.004 0.980 0.941	3.35		+3.2
		Different fast- and slow-group bucklings; diffusion-length assumption			3.26[d]		+0.8
		Adjusted control-rod volume ratio					
		Equal fast- and slow-group bucklings; migration-length assumption	3.39 3.09 2.69	1.003 0.978 0.939	3.36		+3.6
		Different fast- and slow-group bucklings; diffusion-length assumption			3.28[d]		+1.2
		Two-region cylinder					
		Equal fast- and slow-group bucklings; migration-length assumption	3.30 3.00 2.60	1.006 0.980 0.939	3.23		−0.4
		Different fast- and slow-group bucklings; diffusion-length assumption	3.30 3.00 2.60	1.012 0.986 0.945	3.15		−2.7

[a]Calculated result falls within range predicted by experiment.

[b]Did not go critical; subcritical multiplication extrapolation gave 4.6 to 4.9 kg.

[c]Value when adjusted for homogeneous fuel density.

[d]These values are obtained by assuming that the control-rod well volume effect and axial buckling effects are independent of each other and that the ratio of masses calculated with the two buckling assumptions in the two-region cylinder is the same as in the three-region cylinder. This is especially true, since the ratios are very close to unity. Setting differences rather than ratios equal gave virtually identical results again because the differences are small.

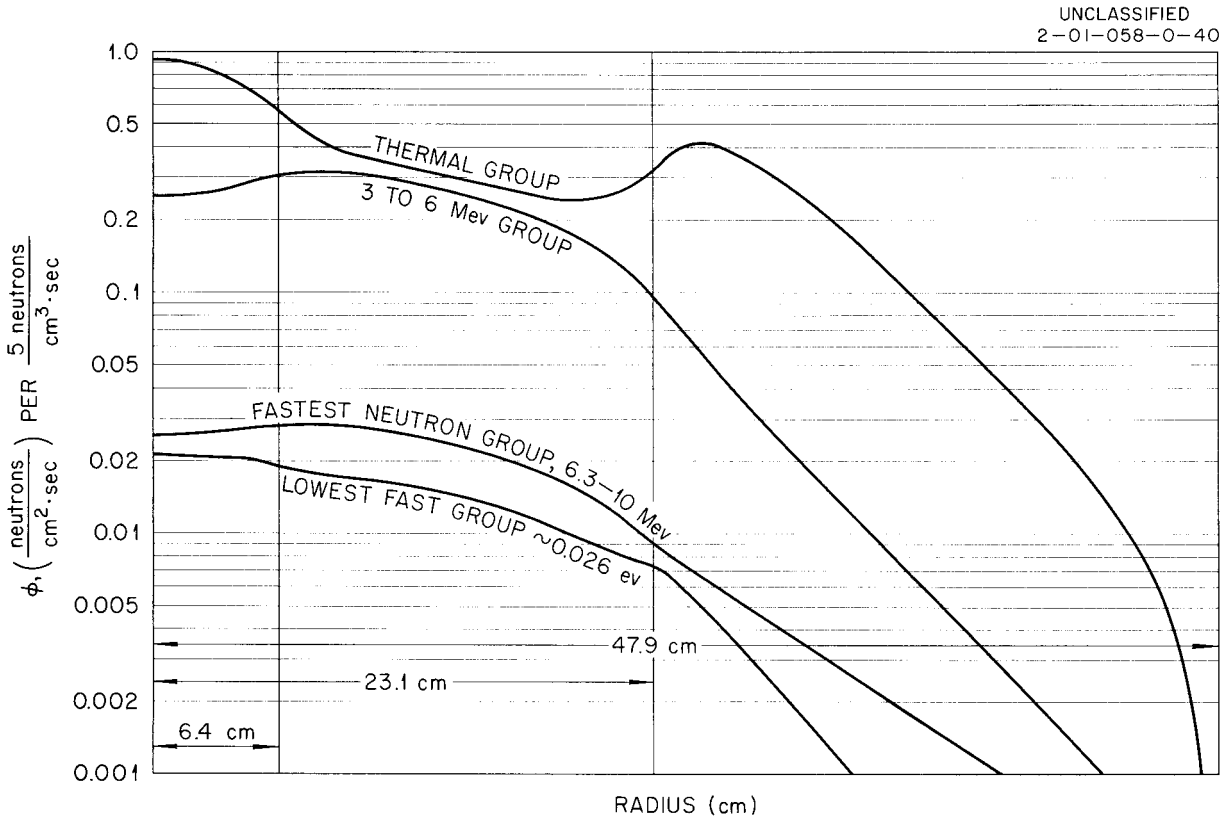

Fig. 9.3. Logarithmic Plot of Flux vs Radius for Eyewash Calculation of 3 by 9 Element Configuration.

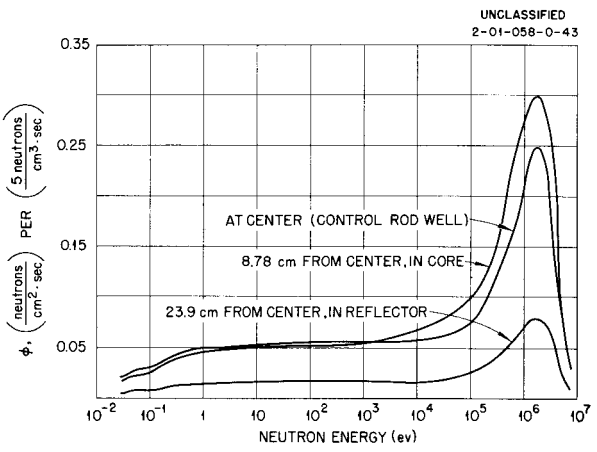

Fig. 9.4. Flux vs Energy in Spherical Representation of 3 by 9 Element Configuration.

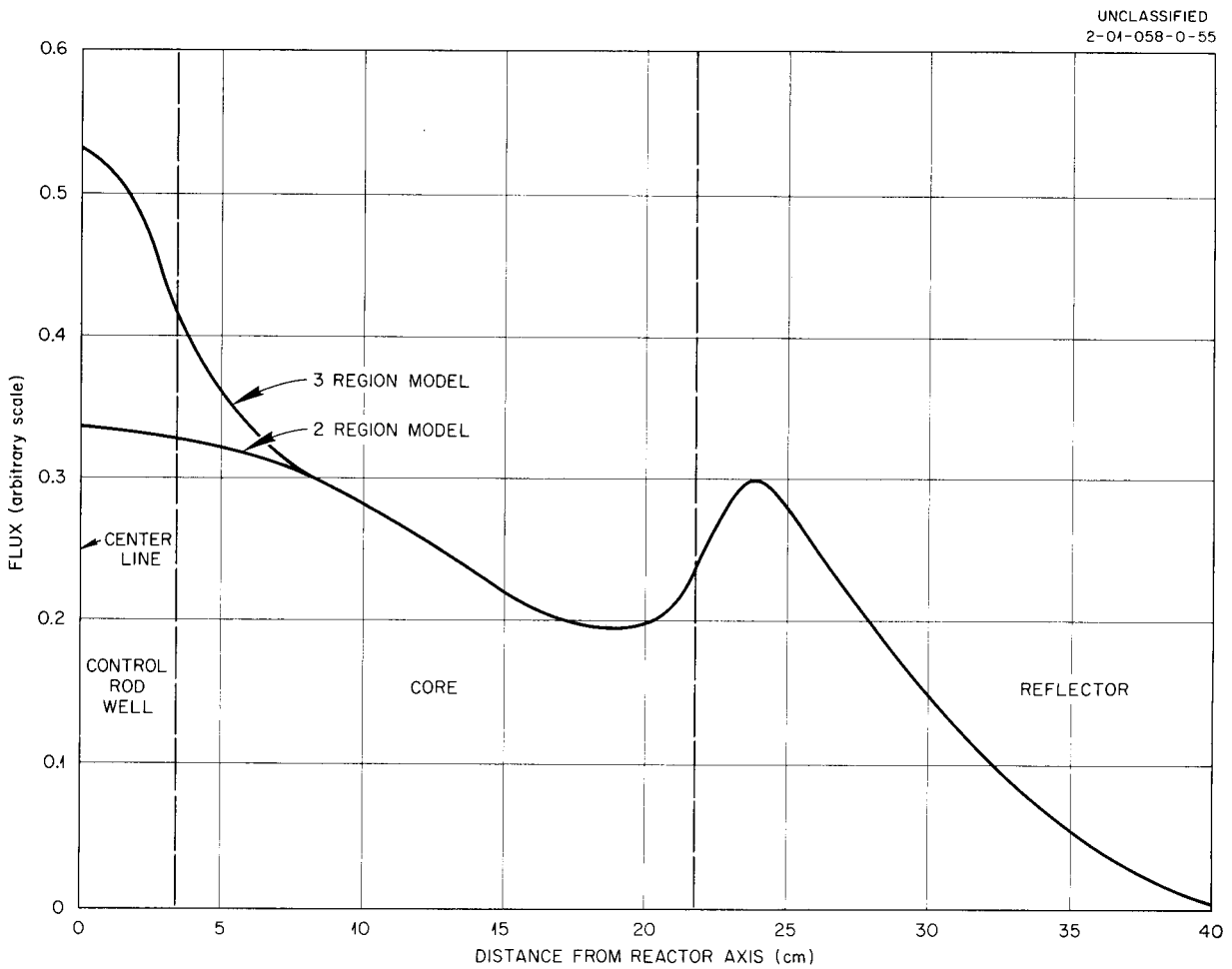

Fig. 9.5. Calculated Thermal-Neutron Flux Distribution in a 5 by 5 Element Loading: 3G3R Code Using a Cylindrical Model

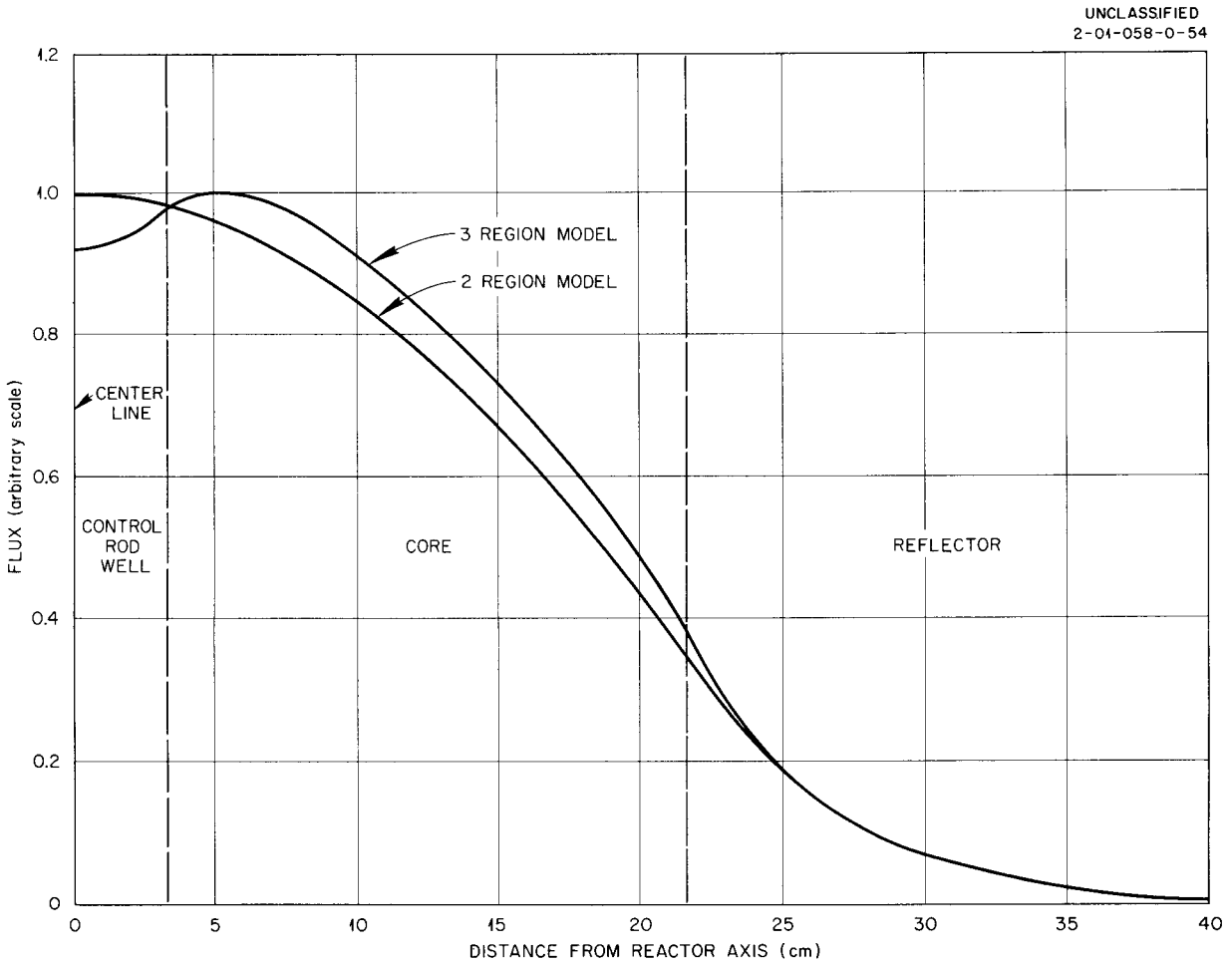

Fig. 9.6. Calculated Fast-Neutron Flux Distribution in a 5 by 5 Element Loading: 3G3R Code Using a Cylindrical Model.

Part II

CRITICAL EXPERIMENTS

10. CRITICAL EXPERIMENTS WITH AQUEOUS SOLUTIONS OF U^{235}

J. K. Fox L. W. Gilley

A number of experiments have been performed to determine the critical conditions for vessels containing highly enriched (~90%) uranium in water solutions of UO_2F_2. They include experiments with single cylindrical containers of stainless steel and aluminum and experiments with interacting arrays of aluminum cylinders. In addition, the effect of some neutron reflector materials on the critical parameters of cylindrical reactors has been studied.

CRITICAL PARAMETERS OF ENRICHED U^{235} SOLUTIONS IN VESSELS OF SIMPLE GEOMETRY

A study of the conditions under which enriched U^{235} solutions contained in aluminum and stainless steel cylinders become critical was initiated several years ago.[1] This work has been extended so that data are now available for aluminum cylinders with diameters up to 30 in. Experiments have been performed with unreflected cylinders and with cylinders that were either partially or totally water-reflected. The total water reflector was effectively infinite. The critical parameters for solutions in a few stainless steel cylinders and in aluminum containers that were rectangular in cross section have also been determined. The results of all the experiments, as well as the critical parameters of a 9-in.-dia sphere, are presented in Table 10.1.

A plot of the critical height as a function of the reactor diameter for water-reflected aluminum cylinders containing solutions with an $H:U^{235}$ ratio of 27.1 is shown in Fig. 10.1. The corresponding curve for unreflected cylinders containing solutions with an $H:U^{235}$ atomic ratio of 44.3 is also shown.

The variation of the critical mass with the diameter of unreflected cylinders containing solutions with $H:U^{235}$ atomic ratios of 27.1, 44.3, and 73.5 is shown in Fig. 10.2. Actually, the $H:U^{235}$ ratio of 73.5 is an average of 72.3, 73.4, and 74.6, whereas the data were plotted directly from the table without averaging. It was found that an unreflected aluminum cylinder 8.76 in. in diameter had a critical solution height of 218.5 cm, which is a height:diameter ratio of 9.8, at near optimum concentration. This indicates that for these conditions 8.76 in. is very near the diameter of an infinitely high critical cylinder. Also (see Table 10.1), for the 8.5-in.-dia stainless steel cylinder, extrapolation of the M^{-1} curve indicates that the cylinder would not be critical at infinite height, when unreflected, while the 9.0-in.-dia stainless steel cylinder was critical at a height of 59.0 cm and at a less optimum solution concentration. Hence, the diameter of the just-critical, unreflected, infinitely high stainless steel cylinders is between 8.5 and 9.0 in. It is probably less than 8.76 in., since this is very near the diameter for the just-critical, unreflected, infinitely high aluminum cylinders.

These investigations will be reported in more detail in a forthcoming report.[2]

[1] C. K. Beck *et al.*, K-343 (April 19, 1949) (Classified).

[2] J. K. Fox and L. W. Gilley, *Preliminary Data from Critical Experiments with Aqueous Solutions. Part I*, ORNL CF-55-12-6 (to be published).

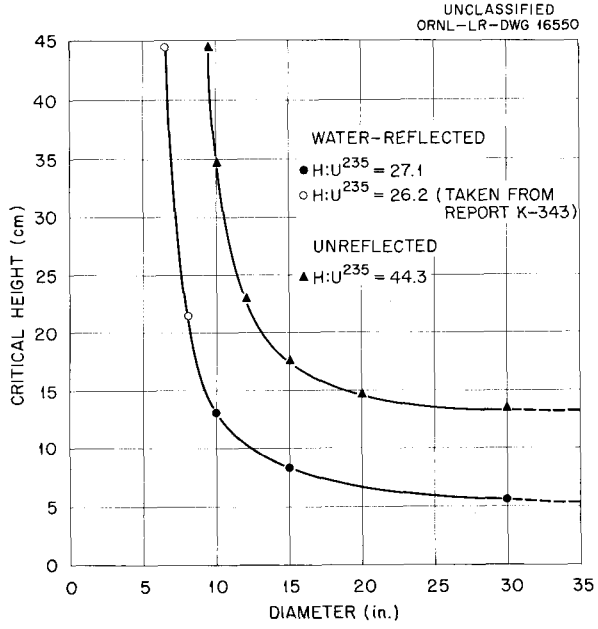

Fig. 10.1. Critical Height as a Function of Diameter for Unreflected and Water-reflected Aluminum Cylinders Containing Enriched U^{235} Solutions.

TABLE 10.1. CRITICAL PARAMETERS OF AQUEOUS SOLUTIONS OF ENRICHED URANIUM

Fissionable material: highly enriched aqueous solutions of UO_2F_2
Reactor container material: (1) $\frac{1}{16}$-in.-thick 2S aluminum coated with Heresite
(2) $\frac{1}{16}$-in.-thick stainless steel

Solution Container and Size	Solution Concentration		Critical Values		
	$H:U^{235}$ Atomic Ratio	g of U^{235} per cc	Height (cm)	Volume (liters)	Mass (kg of U^{235})
Totally Water-Reflected					
Aluminum					
6-in.-dia cylinder	27.1	0.8288	90.0	16.38	13.58
6.5-in.-dia cylinder	44.3	0.5376	39.4	8.43	4.53
10-in.-dia cylinder	27.1	0.8288	13.13	6.67	5.53
15-in.-dia cylinder	27.1	0.8288	8.41	9.60	7.96
30-in.-dia cylinder	27.1	0.8288	5.72	26.08	21.6
	44.3	0.5376	5.46	24.9	13.39
	72.4	0.3423	6.20	28.27	9.68
20 × 20 in. square in cross section	27.1	0.8288	6.99	18.03	14.94
	44.3	0.5376	4.95	12.77	6.87
	72.4	0.3423	6.88	17.75	6.08
9-in.-dia sphere	47.3	0.5061		6.32[a]	3.20
Stainless steel					
6-in.-dia cylinder	44.3	0.5376	118.4	21.55	11.59
	74.6	0.3314	∞[b]		
Partially Water-Reflected[c]					
Aluminum					
6-in.-dia cylinder	44.3	0.5376	76.2	13.87	7.46
7.5-in.-dia cylinder	44.3	0.5376	26.4	7.54	4.05
8-in.-dia cylinder	44.3	0.5376	24.3	7.89	4.24
	72.4	0.3423	24.0	7.79	2.66
10-in.-dia cylinder	72.4	0.3423	17.4	8.81	3.02
	73.4	0.3370	17.5	8.90	3.00
15-in.-dia cylinder	74.6	0.3314	12.7	14.44	4.79
20-in.-dia cylinder	72.4	0.3423	11.3	22.86	7.83
30-in.-dia cylinder	72.4	0.3423	9.9	44.96	15.39
30 × 60 in. in cross section[d]	57.0	0.4240	8.9	103.2	43.7
No Reflector					
Aluminum					
8.76-in.-dia cylinder	44.3	0.5376	218.5	84.8	45.6
9.5-in.-dia cylinder	44.3	0.5376	44.2	20.26	10.89
10-in.-dia cylinder	27.1	0.8288	38.5	19.56	16.21
	44.3	0.5376	34.7	17.63	9.49
	73.4	0.3370	33.3	16.89	5.70

TABLE 10.1. (continued)

Solution Container and Size	Solution Concentration		Critical Values		
	$H:U^{235}$ Atomic Ratio	g of U^{235} per cc	Height (cm)	Volume (liters)	Mass (kg of U^{235})
	No Reflector				
Aluminum					
12-in.-dia cylinder	44.3	0.5376	22.8	16.60	8.92
15-in.-dia cylinder	27.1	0.8288	18.1	20.70	17.16
	44.3	0.5376	17.5	20.00	10.80
	74.6	0.3314	16.4	18.75	6.21
20-in.-dia cylinder	27.1	0.8288	15.4	31.26	25.9
	44.3	0.5376	14.6	29.59	15.9
	73.4	0.3370	14.8	29.92	10.1
30-in.-dia cylinder	44.3	0.5376	13.3	60.47	32.5
	72.4	0.3423	13.5[e]	61.6	21.1
20 × 20 in. square in cross section	27.1	0.8288	16.3[e]	42.0	34.8
	72.4	0.3423	13.9	35.84	12.3
Stainless steel					
8.5-in.-dia cylinder	44.3	0.5376	[f]		
9-in.-dia cylinder	74.6	0.3314	59.0	24.30	8.05

[a]Sphere lacked 80 cc being full; the data extrapolate to a critical mass in concentration of 3.09 kg of U^{235} (0.483 g/cc, $H:U^{235}$ = 49.9) in a full sphere with a capacity of 6.40 liters.

[b]Extrapolated from a solution height of 143.7 cm.

[c]No top reflector.

[d]This vessel was coated with Unichrome rather than Heresite.

[e]Extrapolated values.

[f]Solution height raised to 90 in.

CRITICAL PARAMETERS OF ENRICHED U^{235} SOLUTIONS IN INTERACTING ARRAYS OF CYLINDERS

The lack of experimental data on the nuclear safety of interacting systems of several right cylinders containing highly enriched uranium solutions has necessitated the use of large safety factors in the storage of these solutions. The interaction of a two-cylinder system was studied previously.[3] In this series of experiments the number of interacting cylinders has been extended to seven. The parameters studied were: the effect of the separation distance, the effect of the number of cylinders, the effect of the geometry of the array, the effect of wrapping the cylinders with cadmium, and the effect of water as reflector and moderator on the interacting system. Several combinations of these parameters were also studied.

The solution used in these experiments had an $H:U^{235}$ atomic ratio of approximately 45, a moderation that gives minimum critical volumes for reflected systems. The solution was contained in 6- and 8-in.-dia aluminum cylinders (0.060-in.-thick walls) which in turn were placed in various arrangements inside a large 9.5-ft-dia by 10-ft-high steel reflector tank. The solution was fed into a central cylinder of the array through a 3-in.-dia pipe which was connected to the permanent solution-storage system. The pipe extended 12 in. from the floor of the tank to allow room for attaching movable cylinders, as shown in Fig. 10.3. The solution was carried to the movable cylinders through six 1-in.-dia Tygon tubes that were attached to the 3-in. feed pipe. Each of the cylinders

[3]A. D. Callihan *et al.*, K-406 (1949) (Classified).

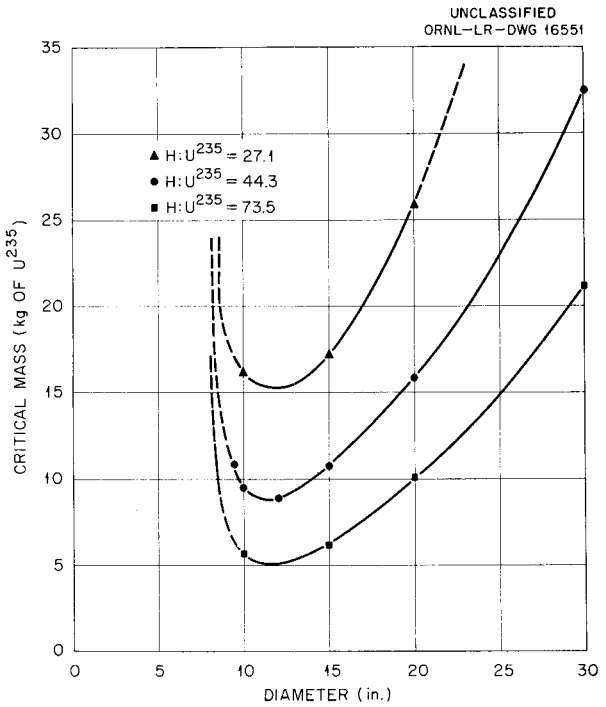

Fig. 10.2. Critical Mass as a Function of Diameter for Unreflected Aluminum Cylinders Containing Enriched U^{235} Solutions.

was coated on the inside with Heresite for protection against corrosion.

The solution height in the central reactor was measured by a rack-driven probe rod connected to selsyns. A small d-c potential in series with an indicator light was used to determine probe contact with the solution.

The safety circuits of the system activated two different safety devices. One was a 3-in. solution dump valve under the central cylinder. The other was a safety rod suspended above the solution in the central cylinder (not shown in the photograph). It was not felt necessary to have safety rods in the movable cylinders, even for experiments in which there was little or no interaction. This is due to the fact that during the addition of solution to the system the solution height was always higher in the central cylinder and to the fact that there was a 3-in. section of pipe under the central cylinder. This pipe was equivalent to about 2 to 3 cm of additional length on a 6-in.-dia cylinder. Hence, the central cylinder was always the most reactive. The source (not shown) was mounted so that when it was in the "in" position it was against the outside of the central cylinder near the bottom. Only one fairly strong source was used.

After each addition of solution to the central cylinder, sufficient time was allowed for the solution to flow into the outer cylinders and come to equilibrium. At criticality the reflector water height was adjusted so that the critical parameters reported here are for arrays in which the water height is the same as that of the solution. Since each movable cylinder was securely bolted in place for a given experiment, it was necessary to drain the system of the solution and water before the cylinders were repositioned.

Figure 10.4 is a graph of the critical solution height of water-reflected (except at top) 6-in.-dia cylinders as a function of edge-to-edge spacing of the cylinders in the arrays. The values of the critical heights for the three- and seven-cylinder arrays approach the value of the critical height for a single cylinder at an edge-to-edge spacing of about 15 in. The effect of wrapping the cylinders with 28-mil-thick cadmium sheets is also shown for a water-reflected seven-cylinder array. The extrapolated curve for this array indicates that the infinite critical height is for an edge-to-edge spacing of 2 in.

The critical solution height as a function of edge-to-edge spacing for arrays of water-reflected 8-in.-dia cylinders is shown in Fig. 10.5. The critical height value approaches that of a single cylinder at an edge-to-edge spacing of about 9 in. This is less than for the corresponding 6-in.-dia cylinders and may be due to the much greater end leakage, with the over-all geometry of the array approaching that of a slab. A single cadmium-wrapped water-reflected 8-in.-dia cylinder becomes critical, and the values of the critical heights of arrays of cadmium-wrapped water-reflected 8-in.-dia cylinders approach the value for the single cylinder at large edge-to-edge spacings.

Figure 10.6 shows the critical height of seven 6-in.-dia cylinders as a function of edge-to-edge spacing for three reflector conditions: (1) unreflected, (2) cadmium-wrapped (no water), and (3) cadmium-wrapped and water-reflected. It will be noted that, except for the near-contact case, the critical heights for the cadmium-wrapped arrays are higher when surrounded by water. This makes it imperative to drain the fuel before draining the water.

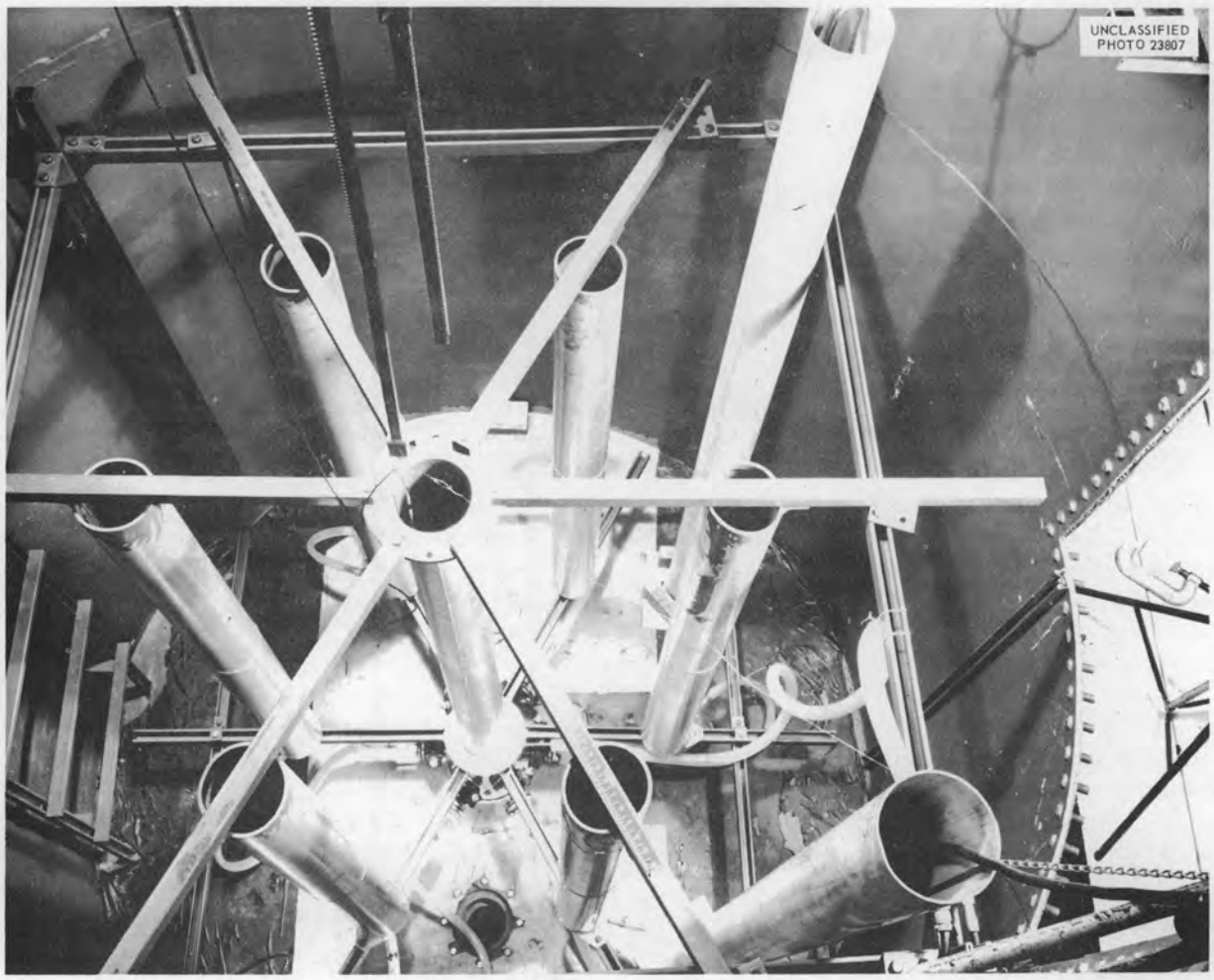

Fig. 10.3. Typical Arrangement for Critical Experiments with Interacting Arrays of Cylinders Containing Enriched U^{235} Solutions.

The critical heights of arrays of 8-in.-dia cylinders as a function of edge-to-edge spacing with no water present are shown in Fig. 10.7. The data are plotted for both three and seven cylinders and show the displacement of the curve due to the addition of four cylinders. While three cylinders would become infinite in height at about a 9-in. edge-to-edge spacing, seven cylinders require about an 18-in. spacing. Wrapping the cylinders with cadmium increased the critical heights slightly for a given spacing.

The critical conditions of 6- and 8-in.-dia cylinders in straight-line arrays have also been investigated but are not reported here. The effect of the angular position of a third cylinder with respect to two other cylinders in fixed positions has also been determined. The data for these experiments will be included in a topical report.[2]

NEUTRON REFLECTOR PROPERTIES OF SOME MATERIALS

A few critical experiments have been performed to determine the relative effect of some neutron reflector materials on the critical parameters of cylinders containing highly enriched uranium solutions. In particular, the neutron reflector properties of furfural, concrete, graphite, and firebrick have been compared with those of water.

The comparison of the relative effectiveness of furfural and water as reflectors was made by using a 10-in.-dia aluminum cylindér and a UO_2F_2 solution which had a U^{235} concentration of

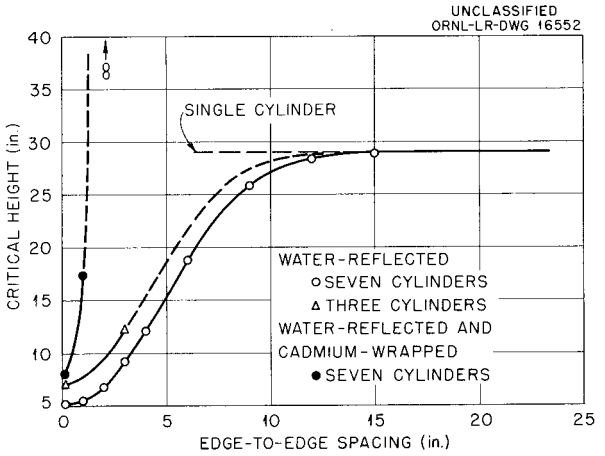

Fig. 10.4. Critical Height as a Function of Edge-to-Edge Spacing and Reflector Condition of 6-in.-dia Cylinders Containing Enriched U^{235} Solution with an $H:U^{235}$ Ratio of 44.3.

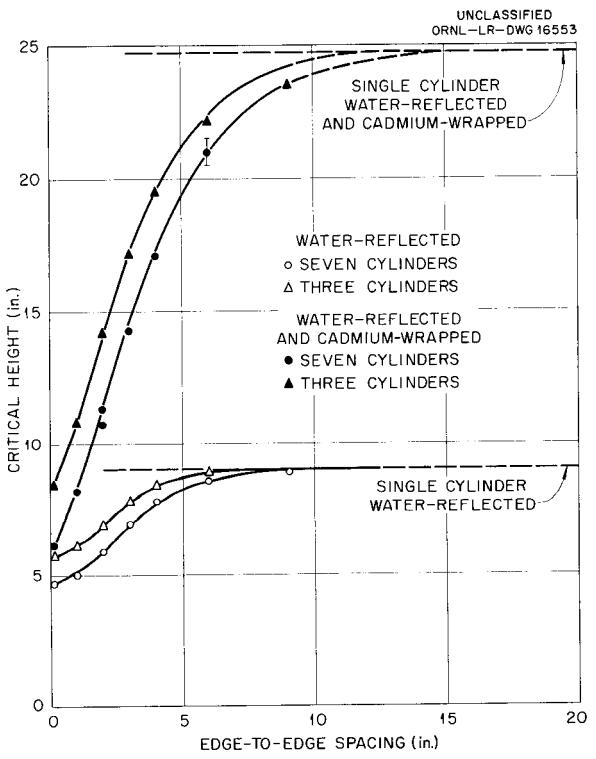

Fig. 10.5. Critical Height as a Function of Edge-to-Edge Spacing and Reflector Condition of 8-in.-dia Cylinders Containing Enriched U^{235} Solution with an $H:U^{235}$ Ratio of 44.3.

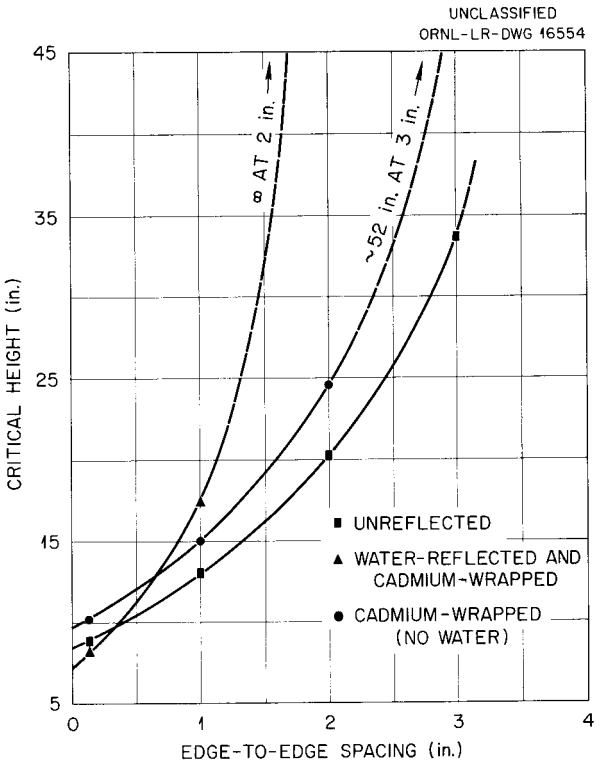

Fig. 10.6. Critical Height as a Function of Edge-to-Edge Spacing and Reflector Condition of Seven 6-in.-dia Cylinders Containing Enriched U^{235} Solutions with an $H:U^{235}$ Ratio of 44.3.

0.3370 g/cc, corresponding to an $H:U^{235}$ atomic ratio of 73.4. The critical height of the solution was measured as the thickness of the furfural or the water on the sides of the cylinder was varied in approximately 1-in. steps by using up to four concentric 1-in.-thick aluminum annular "cans" as containers for the reflector along the lateral surface of the solution container. It should be noted that the annular containers were 1 in. thick, including wall thickness, and, since each wall was $\frac{1}{16}$ in., the reflector thickness in each container was 0.88 in. A plot of the critical height as a function of the reflector thickness (Fig. 10.8) shows that water, which has a hydrogen density 2.4 times that of furfural (C_4H_3OCHO), is more effective as a reflector than furfural up to a thickness of approximately 3.5 in., after which the two materials have essentially the same effectiveness as a reflector.

The effectiveness of concrete as a neutron reflector was measured by determining the critical

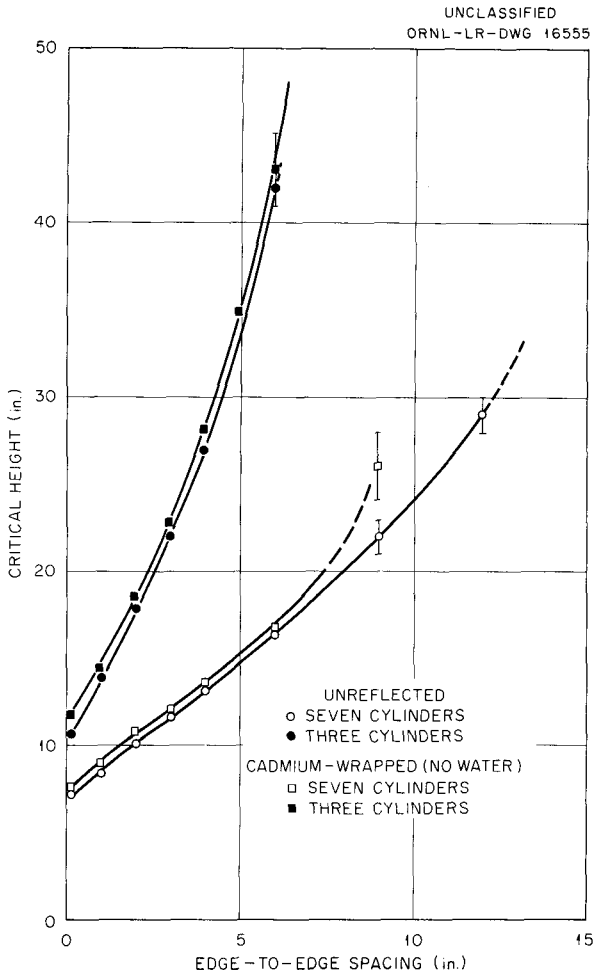

Fig. 10.7. Critical Height as a Function of Edge-to-Edge Spacing and Reflector Condition of 8-in.-dia Cylinders Containing Enriched U^{235} Solution with an $H:U^{235}$ Ratio of 44.3.

mass of an enriched uranium solution contained in a 9-in.-dia stainless steel cylinder as a function of the distance from the cylinder to a 4 × 4 × ½ ft thick concrete wall. The solution had a U^{235} concentration of 0.3314 g/cc, corresponding to an $H:U^{235}$ atomic ratio of 74.6. The concrete wall consisted of blocks of shielding concrete having a density of 2.14 g/cc. A plot of the results (Fig. 10.9) shows that little interaction occurs after the edge-to-edge separation is increased to about 24 in. Doubling the concrete wall thickness

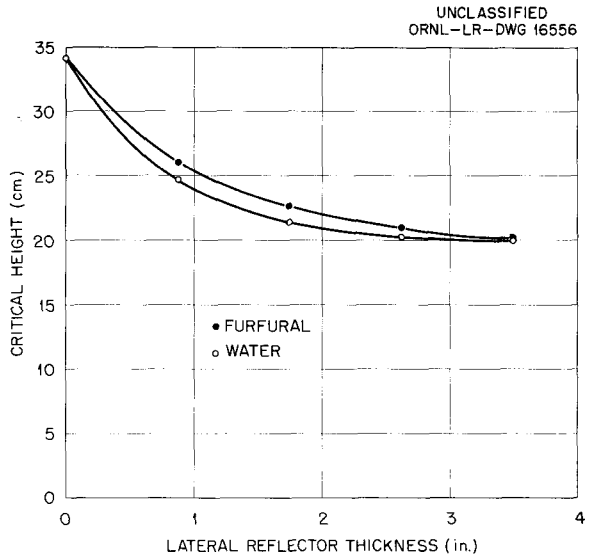

Fig. 10.8. Critical Height as a Function of Thickness of Water or Furfural Reflector on Lateral Surface of 10-in.-dia Cylinder Containing Enriched U^{235} Solution with an $H:U^{235}$ Ratio of 73.4.

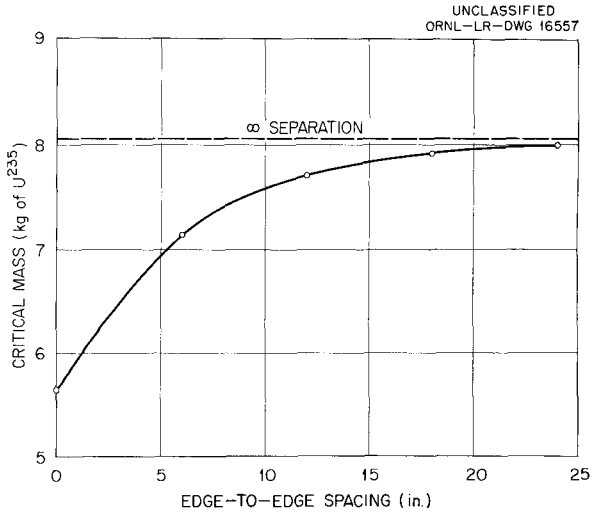

Fig. 10.9. Critical Mass of an Enriched U^{235} Solution ($H:U^{235}$ = 74.6) Contained in a 9-in.-dia Cylinder as a Function of the Distance Between the Cylinder and a Concrete Wall (6 in. Thick by 48 in. by 48 in.).

(i.e., from 6 to 12 in.) increased the critical mass by about 2.5% when the wall was adjacent to the reactor.

A determination was made of the variation of the critical mass with the type and thickness of a reflector material placed against the bottom of a 20-in.-dia aluminum cylinder containing an aqueous solution of UO_2F_2 at a U^{235} concentration of 0.8288 g/cc, corresponding to an $H:U^{235}$ atomic ratio of 27.1. The reflectors consisted of carbon, firebrick, and water in various laminated arrangements. Figure 10.10 shows the variation of the critical mass with firebrick thickness for three different thicknesses of carbon between the cylinder and the firebrick. Figure 10.11 shows the variation of critical mass with the thickness of carbon (no firebrick) adjacent to the bottom of the cylinder. Figure 10.12 is a plot[4] showing the variation of critical mass with the thickness of a water reflector between the reactor and a constant thickness (5.5 in.) of carbon which is moved back stepwise. It can be seen that, up to about 0.5 in., replacing carbon with water decreases the critical mass, since water is a better moderator. After about 0.5 in., however, the greater absorption of water more than compensates for the increased moderation, and the critical mass rises again.

[4]The dashed portion of the curve is a somewhat arbitrary extrapolation of the data.

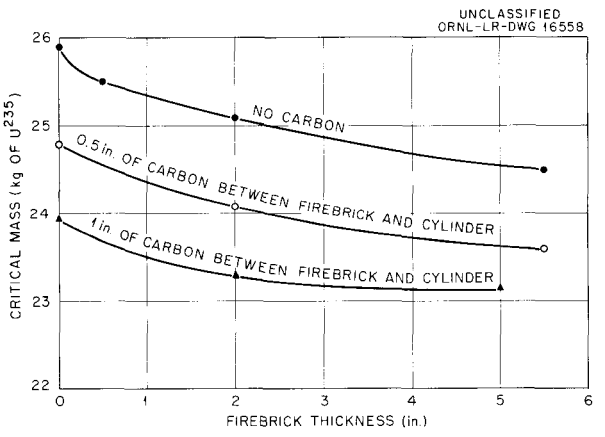

Fig. 10.10. Critical Mass of an Enriched U^{235} Solution ($H:U^{235}$ = 27.1) Contained in a 20-in.-dia Cylinder as a Function of the Thickness of Carbon and Firebrick on the Bottom of the Cylinder.

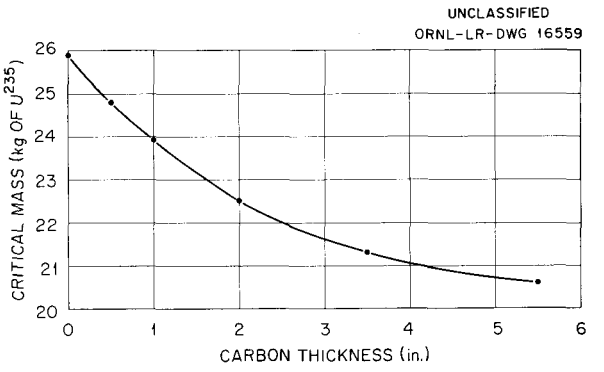

Fig. 10.11. Critical Mass of an Enriched U^{235} Solution ($H:U^{235}$ = 27.1) Contained in a 20-in.-dia Cylinder as a Function of the Thickness of Carbon on the Bottom of the Cylinder.

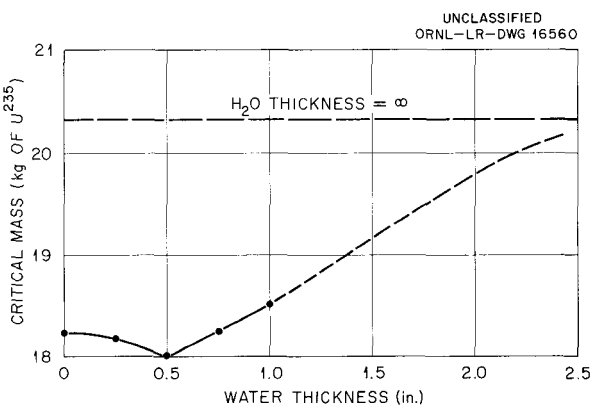

Fig. 10.12. Critical Mass of an Enriched U^{235} Solution ($H:U^{235}$ = 27.1) Contained in a 20-in.-dia Cylinder as a Function of the Thickness of Water Between the Bottom of the Cylinder and a 5.5-in.-thick Carbon Reflector.

11. TWO BERYLLIUM-MODERATED CRITICAL ASSEMBLIES

E. L. Zimmerman

Two bare beryllium-moderated critical assemblies have been built in a simple geometry in order to check the critical parameters predicted for them by multigroup reactor calculational methods. The first assembly, designated as CA-1, was built in the NEPA-ORNL Critical Experiments Facility in 1951. It had a regular lattice of 10-mil-thick enriched uranium metal fuel disks separated by 1-in. blocks of beryllium metal. The CA-1 remained the only simple beryllium-moderated critical assembly until the second assembly, designated as CA-18 was built. This assembly was similar to the first except that the fuel spacing was changed from 1 to 4 in.

The comparison of theory with these experiments has been published,[1] and a further discussion of the calculations as well as the details of the experiments will be presented in a topical ORNL report.[2] A brief description of the experiments is presented here.

Description of Assemblies

The matrix into which the reactor materials were placed was a 6-ft cube made of 3-in.-OD square 2S aluminum tubes, each having a wall thickness of 0.047 in. The matrix was divided vertically into halves which could be separated by remote control. Fuel elements were placed in both halves of the matrix, and the assembly was completed by bringing them together. Control and safety rods were similar to other core elements except that they were moved within the assembly. (Poison rods were not used.) The safety rods were inserted by compressed air and were spring-loaded and magnet-held. All safety rods tripped automatically in the event of an excessive radiation level. They could also be tripped manually, either singly or collectively. The control rods were inserted or withdrawn by means of a screw-drive mechanism. A photograph of one of the assembly halves (Fig. 11.1) shows one core element displaced from its normal position.

Core elements consisted of highly enriched, 2.860-in.-dia, 0.01-in.-thick uranium disks (average mass of U^{235} = 16.774 g) separated by one (CA-1) or four (CA-18) 1-in.-thick by $2\frac{7}{8}$-in. by $2\frac{7}{8}$-in. beryllium metal blocks of average density 1.86 g/cc. These were held together by $\frac{3}{16}$-in.-dia stainless steel skewers through 0.196-in. center holes in the fuel disks and the beryllium blocks. The elements were designed to maintain a constant fuel spacing throughout the assembly.

The arrangements of the core elements in the aluminum grid for CA-1 and CA-18 are indicated in Figs. 11.2 and 11.3, respectively. Row 8 of CA-18 contained quarter-sized core elements. They were $1\frac{7}{16}$ in. square but otherwise had the same composition as the other elements.

A comparison of the physical compositions of the two assemblies is given in Table 11.1. Each stainless steel volume fraction includes the stainless steel skewers plus an artificial quantity having the same absorption cross section as the impurities in other parts of the system. The values of k_{eff} correspond to the regular assembly having the indicated fuel loadings extrapolated to the condition of all control rods fully inserted. Criticality in either assembly was reached with a control rod slightly withdrawn. Table 11.1 and Figs. 11.2 and 11.3 describe the nearest approaches to simple, bare cube critical assemblies for each of the two fuel spacings. In subsequent experiments the necessary excess multiplication was provided by placing additional core elements just outside the clean assembly.

Experimental Measurements

CA-1. – In the approach to criticality with CA-1, uranium fuel disks were added to the core elements nearest the center of a 24 × 24 × 25 in. array of beryllium until the assembly became critical. This first critical array consisted of a 4 × 4 cell core, with one 3-in.-square corner element missing. It contained 6.05 kg of U^{235} and had a 6-in. reflector on four sides. One control rod (D) in the reflector was withdrawn 3.7 in. The clean, bare critical assembly was reached by alternately removing outside beryllium and adding fuel. The final bare parallelepiped had

[1] H. Hurwitz, Jr., and R. Ehrlich, *Proceedings of the International Conference on the Peaceful Uses of Atomic Energy*, vol 5, p 423, United Nations, New York, 1956.

[2] E. L. Zimmerman, *Two Beryllium-Moderated Critical Assemblies*, ORNL-2201 (to be published).

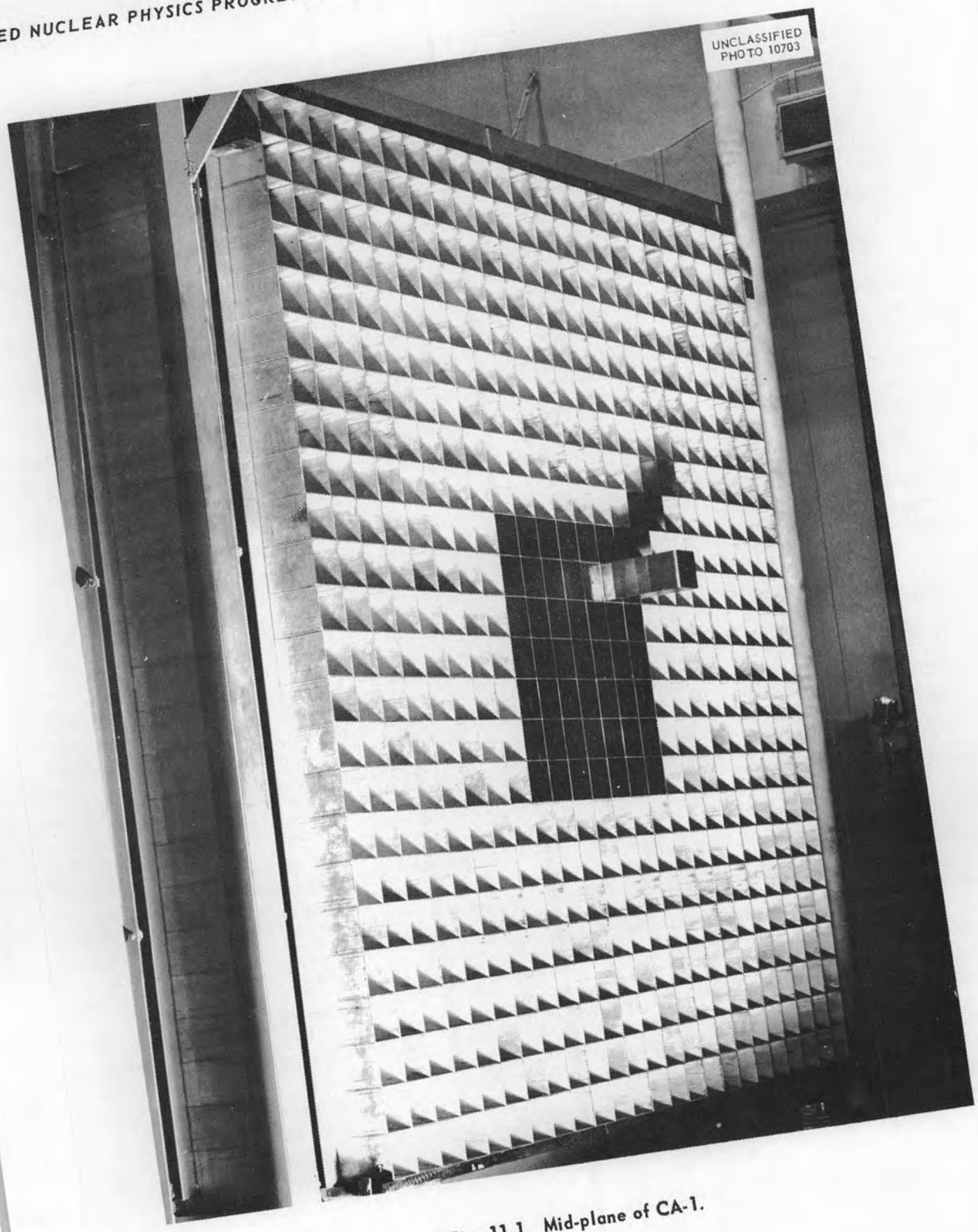

Fig. 11.1. Mid-plane of CA-1.

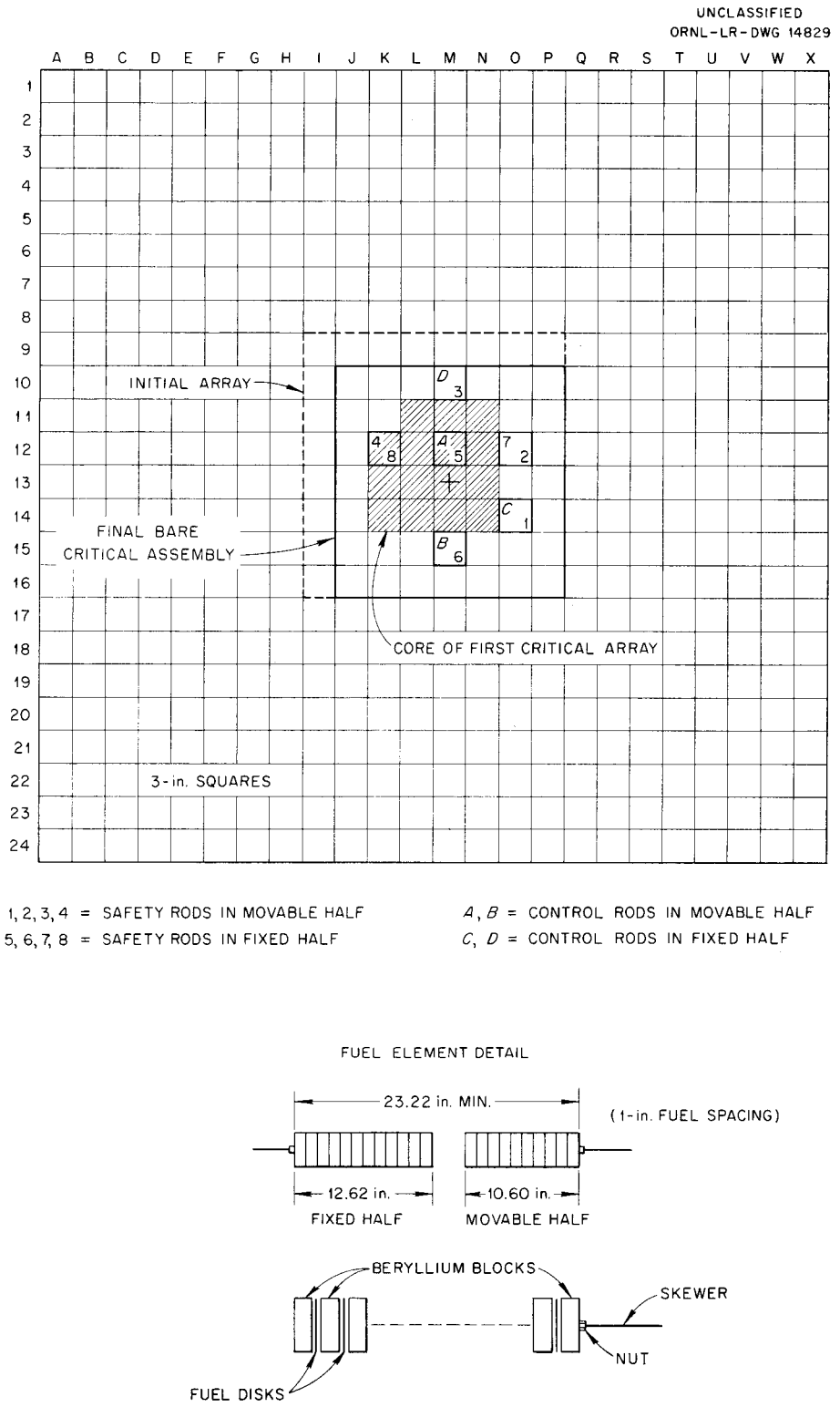

Fig. 11.2. Arrangement of Core Elements in CA-1 (Fixed-Half Interface).

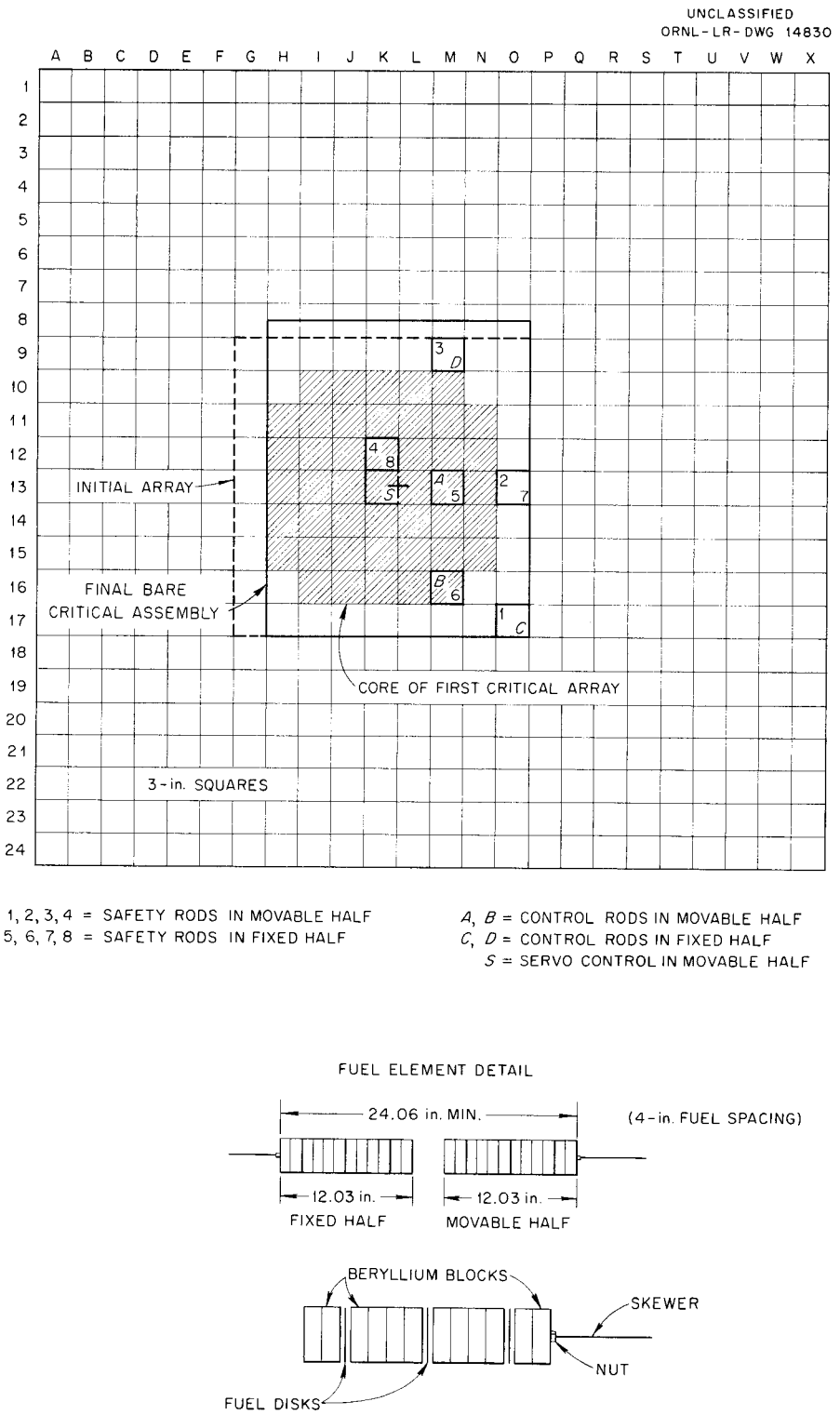

Fig. 11.3. Arrangement of Core Elements in CA-18 (Fixed-Half Interface).

TABLE 11.1. COMPARATIVE DESCRIPTIONS OF CA-1 AND CA-18

	CA-1	CA-18
Outside dimensions, in.	21.0 × 21.0 × 23.2	24.0 × 28.4 × 24.1
Spacing of 10-mil-thick fuel disks, in.	1	4
U^{235} loading, kg	18.08	7.65
k_{eff}	1.0054	1.0020
Be:U^{235} atomic ratio	390	1560
Volume fractions		
Aluminum (grid)	0.0610	0.0611
Beryllium (moderator)	0.9060	0.9128
Uranium (fuel)	0.0064	0.0016
Stainless steel (skewers)	0.0004	0.0003
Void	0.0262	0.0242

the dimensions 21 × 21 × 23.22 in. and contained 18.08 kg of U^{235}. Each of the 49 cells contained 23 in. of beryllium and 22 fuel disks of average thickness 0.01 in. The assembly was critical with control rod C withdrawn 2.59 in., corresponding to 0.0054 in reactivity.

The power distribution within the assembly was observed by measuring the gamma-ray activity of the fuel disks. The results were in substantial agreement with the expected cosine distribution as indicated in Figs. 11.4 and 11.5. The terms lateral and longitudinal are used to define directions parallel or normal, respectively, to the interface of the two assembly halves.

A danger-coefficient measurement on the fuel was made by removing the fuel disk nearest the center of the assembly and replacing it with a smaller fuel disk. The observed loss in specific reactivity was 0.29¢ per gram of U^{235}. Assuming the fuel importance to be proportional to the flux squared and taking the value 100¢ = 0.0073, it is found that $\delta k = 4.75\ \delta M/M$, where M is the mass of U^{235} in the critical assembly. The reactivity measurements in a number of experiments were inconsistent, although all movable parts of the system were found to be mechanically reproducible. The difficulty was attributed to photoneutrons from the beryllium, but no quantitative conclusions could be drawn.

CA-18. – The first critical array using the 4 in. fuel spacing had an over-all size of 27 × 27 × 24 in. and contained 4.97 kg of U^{235} (Fig. 11.3). Except for the four 3-in.-square corner cells, the core was 21 × 21 × 24 in. and had a 3-in. beryllium reflector on four sides. The assembly was critical with one reflector rod (D) displaced 2.25 in. The final, bare critical assembly had dimensions 24.00 × 28.4 × 24.06 in. and contained 7.65 kg of U^{235}. The assembly was critical with control rod A displaced 2.60 in., corresponding to 0.0020 in reactivity.

Fission rate measurements within CA-18 were made by a catcher foil technique, that is, by observing the activity of fission fragments on thin aluminum foils which were in direct contact with the uranium during a run. All cadmium covers had a thickness of 20 mils. Catcher foil power distribution measurements are shown in Figs. 11.6 and 11.7. In some cases measurements on opposite sides of the same fuel disks are indicated. The cadmium fraction for fuel is seen to vary between 0.852 and 0.880.

Other Measurements. – Other tests which have been performed with the two assemblies and which will be reported in the topical report[2] have included control-rod calibrations and measurements of the effect on the reactivity of introducing various materials near the assemblies.

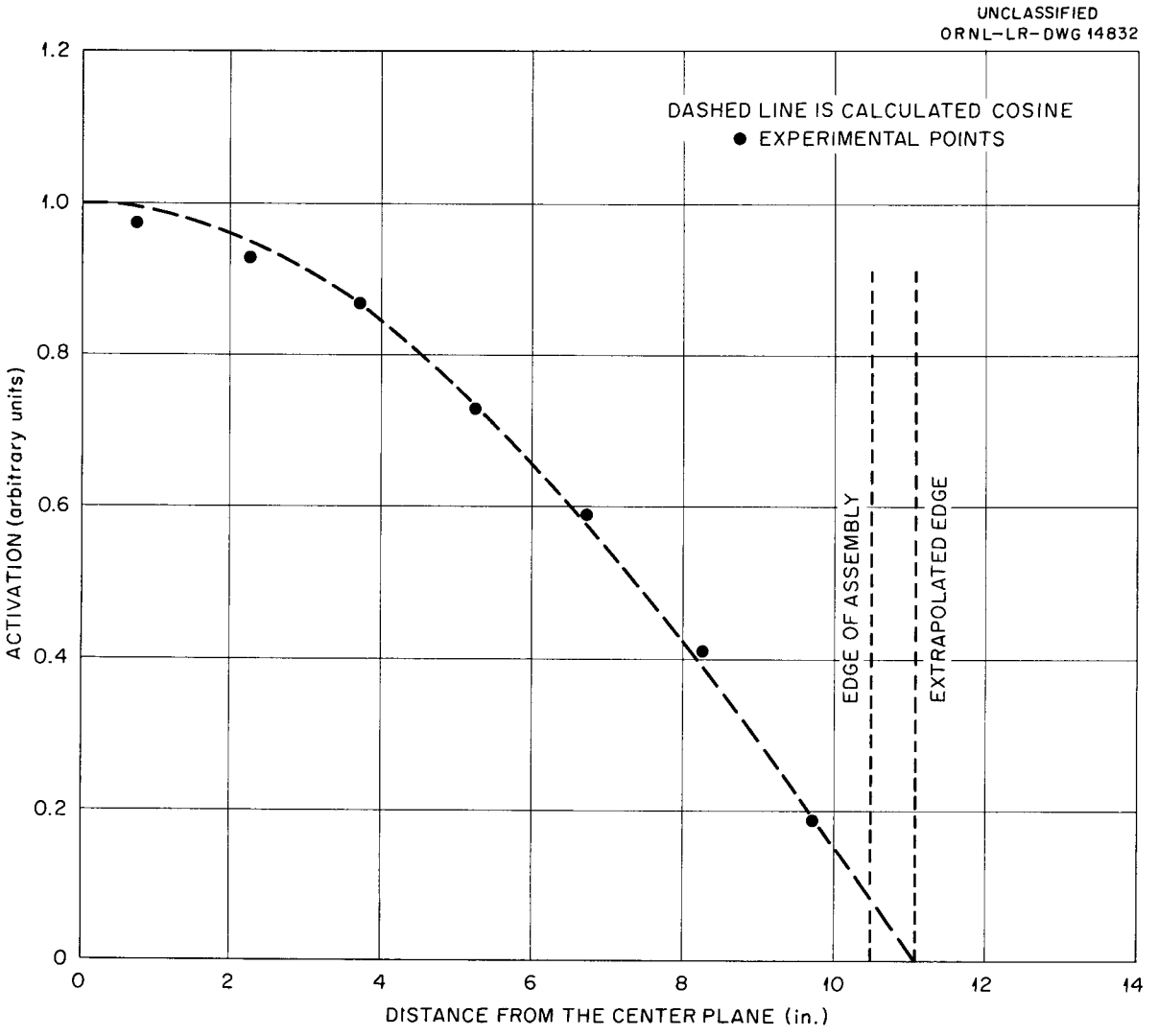

Fig. 11.4. Power Distribution Along a Lateral Axis in CA-1 (Gamma-Ray Activity of Uranium Disks).

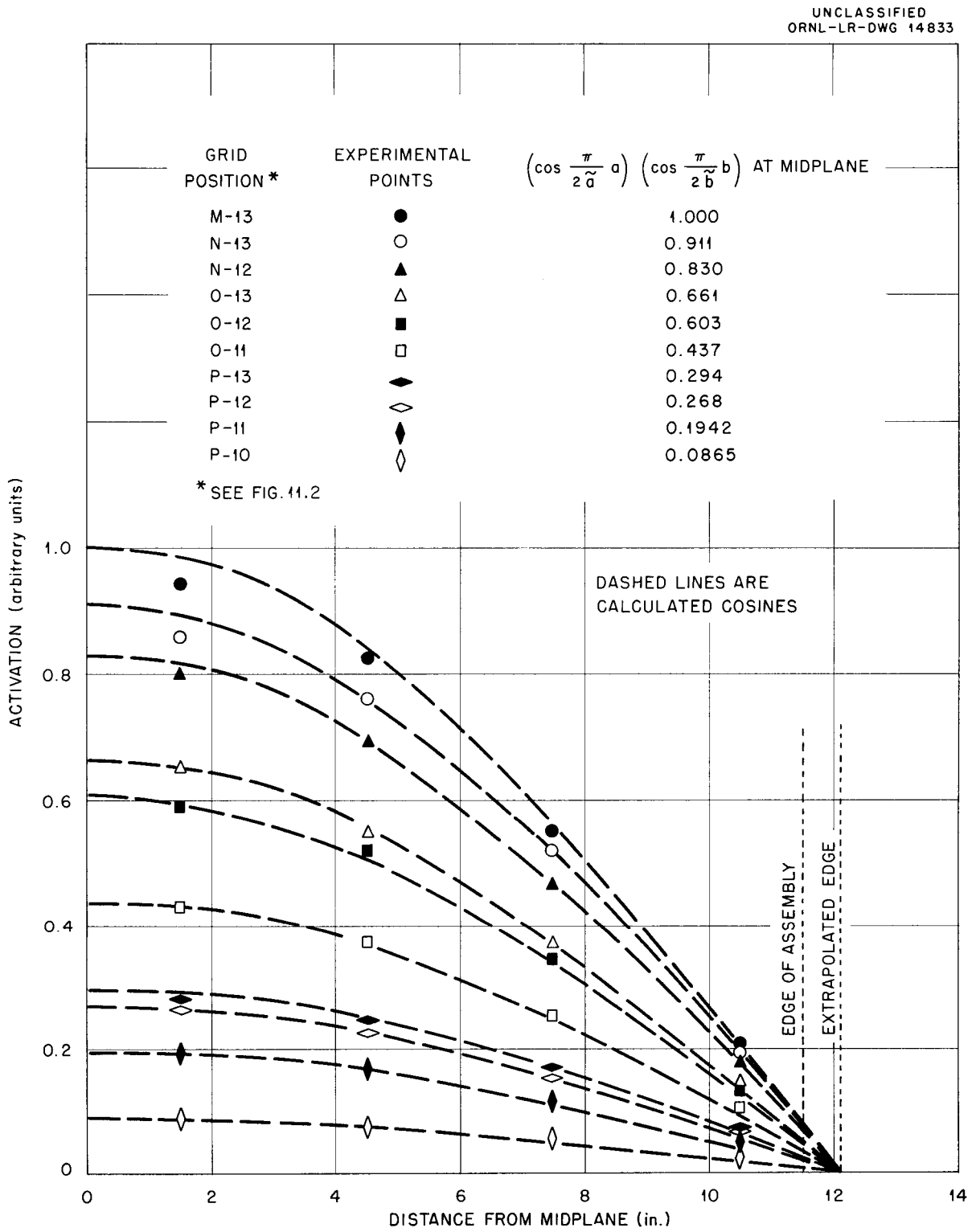

Fig. 11.5. Power Distribution Along Several Longitudinal Traverses in CA-1 (Gamma-Ray Activity of Uranium Disks).

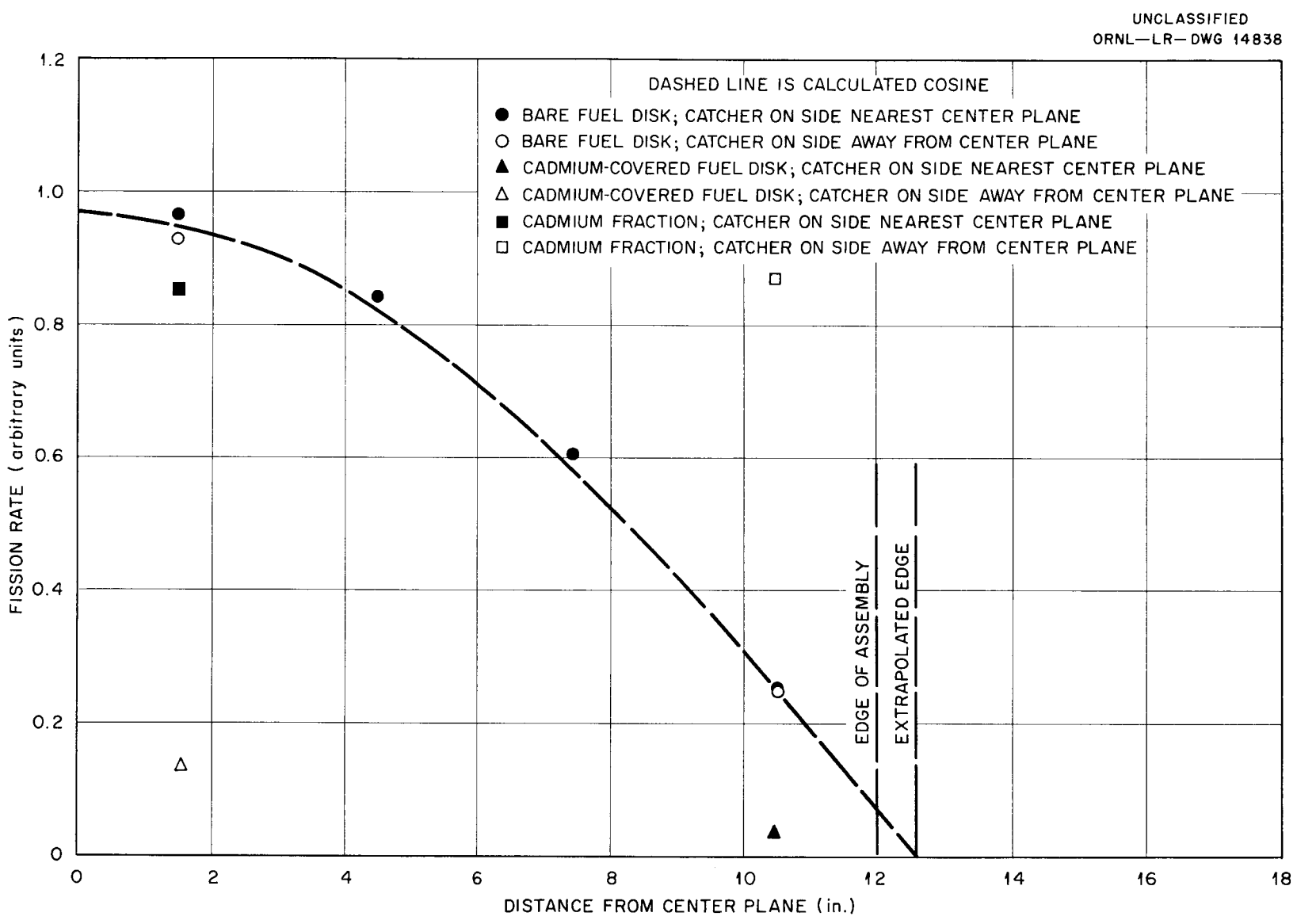

Fig. 11.6. Power Distribution Along a Lateral Axis of CA-18 (Fission Rate of Fuel Disks).

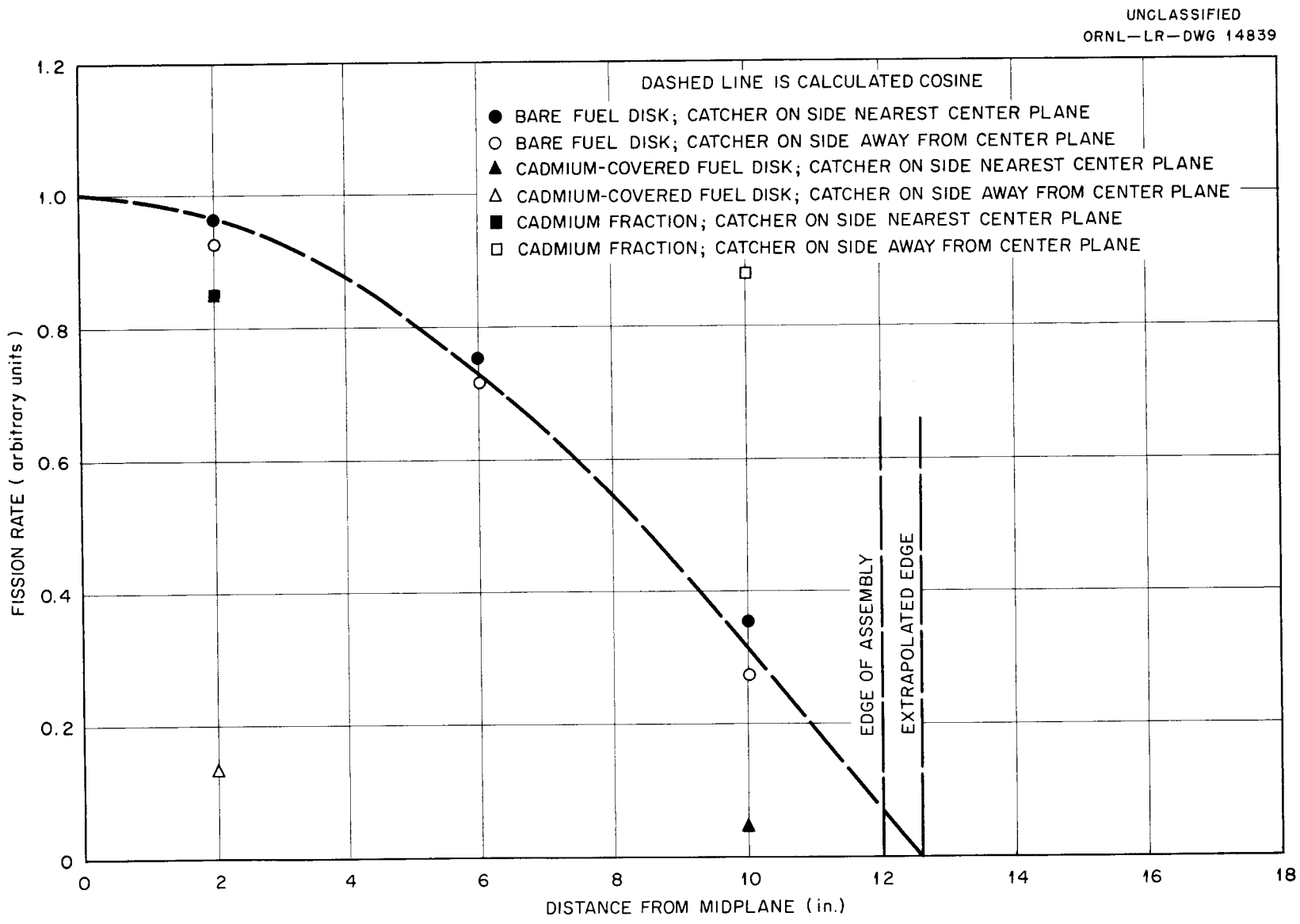

Fig. 11.7. Power Distribution Along the Longitudinal Axis of CA-18 (Fission Rate of Fuel Disks).

12. LIMITING CRITICAL CONCENTRATIONS OF AQUEOUS SOLUTIONS OF FISSILE ISOTOPES

J. T. Thomas

The limiting critical concentrations of aqueous solutions of the fissile isotopes are of particular interest to the chemical processing groups in the matter of nuclear safety. The purpose of this paper is to define the concentration regions wherein criticality is not possible. The method utilized defines safe concentrations with a rather wide but comforting margin.

It is conservative to assume that, in ordinary processing systems, the absorption of neutrons by materials other than hydrogen and the fissile isotopes is negligible. Further, the system is assumed to be aqueous, homogeneous, and large. The resonance escape probability and the fast-fission factor may be taken as unity (at least for the higher enrichments of fissionable isotopes) in the following equation[1] of the critical concentration:

$$k_{\text{eff}} = \frac{\eta f p \epsilon e^{-B^2\tau}}{(1 + L^2B^2)} . \tag{1}$$

Since the system is to be critical with very dilute solutions, the analysis is more conservative by neglecting the fast and thermal leakage factors. The critical concentration is thus defined by the relation

$$k_{\text{eff}} = 1 = \eta f , \tag{2}$$

where

$$\eta = \frac{\nu_i \Sigma_f(i)}{\Sigma_f(i) + \Sigma_c(i)} = \frac{\Sigma_f(i)\nu_i}{\Sigma_a(i)} ,$$

$$f = \frac{\Sigma_a(i)}{\Sigma_a(i) + \Sigma_a(H)} . \tag{2a}$$

The subscript i refers to the particular fissile isotope U^{233}, U^{235}, or Pu^{239}, and H refers to hydrogen. Substituting Eq. 2a into Eq. 2 gives the limiting ratio of hydrogen to fissionable atoms as

$$\left(\frac{N_H}{N_i}\right)_0 = \frac{\sigma_a(i)}{\sigma_a(H)} (\eta_i - 1) . \tag{3}$$

Since the solution is so dilute, the concentration of fissionable isotope may be taken to be the concentration in grams per cubic centimeter. Table 12.1 lists the nuclear data for the isotopes,[2] and Table 12.2 summarizes the calculated values for the limiting concentrations.

TABLE 12.1. NUCLEAR DATA FOR FISSILE ISOTOPES

i	σ_f (barns)	σ_a (barns)	ν	σ_c/σ_f	η	f*
U^{233}	533	585	2.54	0.098	2.31	1
U^{235}	569	674	2.46	0.184	2.08	0.981
Pu^{239}	806	1145	2.88	0.420	2.03	1.075

*f is the non-Maxwellian distribution correction factor.

TABLE 12.2. LIMITING CONCENTRATIONS OF AQUEOUS SOLUTIONS OF FISSILE ISOTOPES

i	N_H/N_i	Grams of i per Gram of Solution	Grams of i per Liter of Solution
U^{233}	2335	0.01092	10.92
U^{235}	2219	0.01159	11.59
Pu^{239}	3596	0.00727	7.27

The processing of used fuels raises the problem of limiting concentrations when more than one fissile isotope is present in appreciable quantities. Specifically, the used fuel from breeder- or conversion-type reactors may contain both U^{235} and Pu^{239} isotopes. This further necessitates the consideration of the effect of initial enrichment of U^{235} on the limiting concentration. If it

[1] The notation used throughout this paper is that of S. Glasstone and M. C. Edlund, *The Elements of Nuclear Reactor Theory*, Van Nostrand, New York, 1952.

[2] D. J. Hughes and J. A. Harvey, *Neutron Cross Sections*, BNL-325 (July 1, 1955).

is assumed that a Pu^{239} atom has been produced for each U^{235} atom destroyed, and if β' is defined as the fractional burnup of U^{235}, and the initial fractional enrichment of the fuel is denoted by α, the expected fuel composition after an exposure will be

$$N_{25} = (1 - \beta')\alpha N ,$$
$$N_{49} = \beta'\alpha N ,$$
$$N_{28} = (1 - \alpha) N - \beta'\alpha N ,$$

where $N = N_{25} + N_{28}$ initially. From these relations,

$$f = \frac{(1 - \beta')\sigma_a(25) + \beta'\sigma_a(49)}{(1 - \beta')\sigma_a(25) + \beta'\sigma_a(49) + [1/\alpha - (1 + \beta')]\sigma_a(28) + N_H/(N_{25} + N_{49})\sigma_a(H)} ,$$

$$\eta = \frac{\nu_{25}(1 - \beta')\sigma_f(25) + \nu_{49}\beta'\sigma_f(49)}{(1 - \beta')\sigma_a(25) + \beta'\sigma_a(49)} .$$

Applying these results to Eq. 2 gives the limiting ratio of hydrogen to fissile atoms as

$$(4) \quad \frac{N_H}{N_{25} + N_{49}} = (1 - \beta')\left(\frac{N_H}{N_{25}}\right)_0 + \beta'\left(\frac{N_H}{N_{49}}\right)_0 - \frac{\sigma_a(38)}{\sigma_a(H)}\left[\frac{1}{\alpha} - (1 + \beta')\right] ,$$

where the subscript zero refers to the limiting concentration defined by Eq. 3. The initial fuel enrichment, α, appears only in the last term of Eq. 4. It may be seen that if $\beta' = 0$ and if the U^{238} absorption is neglected (an exculpable act for α greater than 90%) Eq. 4 reduces to Eq. 3. The limiting atomic ratio of $N_H/(N_{25} + N_{49})$, defined by neglecting the U^{238} absorption term in Eq. 4, is conservative and certainly useful for all enrichments.

Figure 12.1 presents the atomic ratio defined in Eq. 4 as a function of both the fractional burnup of U^{235} and of the atomic ratio of plutonium to uranium, neglecting the presence of U^{238}. The plutonium-to-uranium ratio, β, is related to the fractional burnup by the expression

$$\beta = \frac{\beta'}{1 - \beta'} .$$

If the fractional enrichment, α, is retained as a parameter; that is, if the last term in Eq. 4 is kept, the results presented in Fig. 12.2 are obtained. It may be seen that the variation of limiting atomic ratio with fractional enrichment for any constant burnup does not become large until low enrichment values are considered. This is exemplified in Fig. 12.3, where the limiting atomic ratio is shown as a function of fractional enrichment for $\beta' = 0.1$.

It may be concluded that the effect of initial enrichment is to increase the margin of safety for

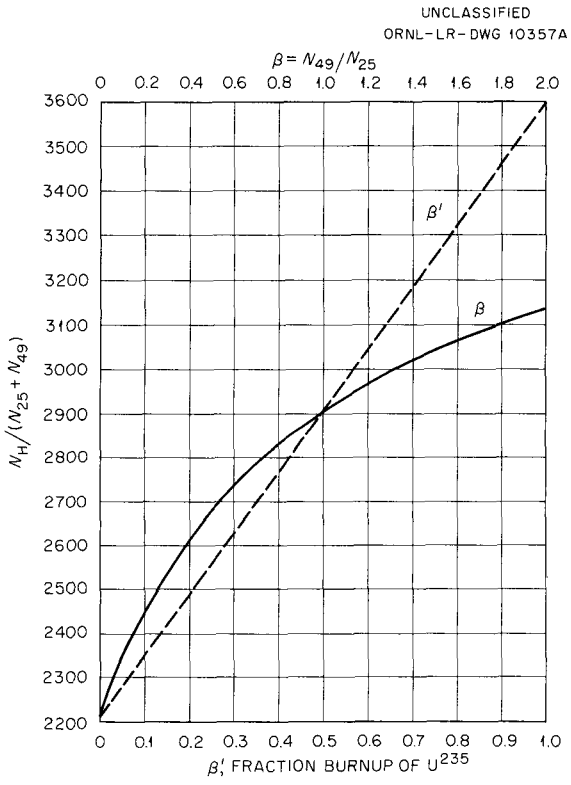

Fig. 12.1. Ratio of Hydrogen to Fissile Atoms as a Function of Per Cent Burnup in U^{233} and of Atoms Ratio Pu^{239}/U^{235}.

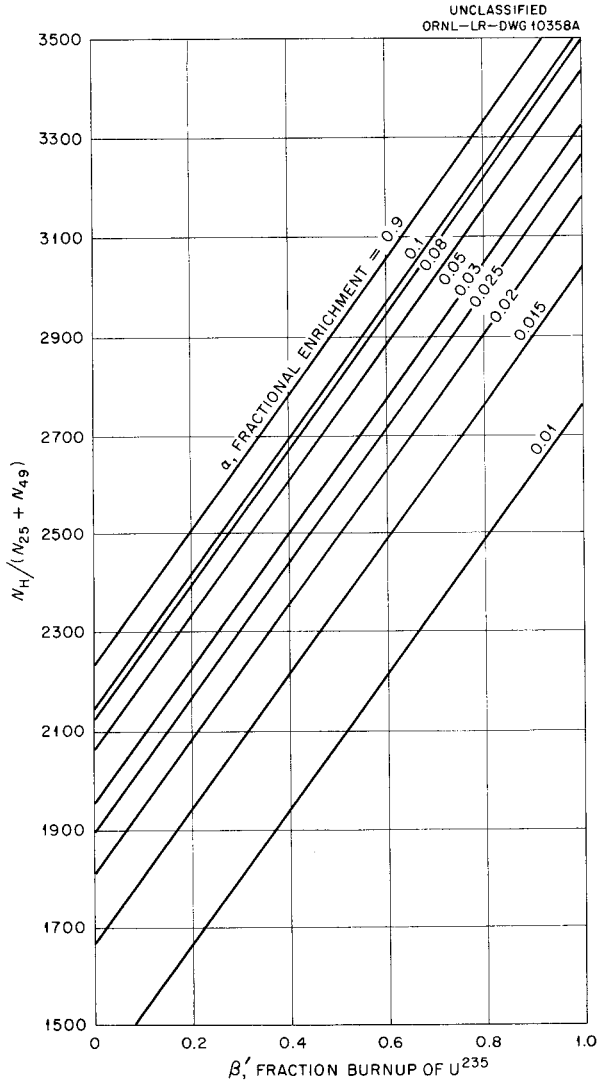

Fig. 12.2. Limiting Atomic Ratio $N_H/(N_{25} + N_{49})$ as a Function of Initial Enrichment and Fractional Burnup of U^{235}.

enrichments below about 2.5% and that the conservatism implied by Fig. 12.1 is adequate for any enrichment.

This paper has been published previously.[3]

[3] J. T. Thomas, *Limiting Concentrations for Fissile Isotopes*, ORNL CF-55-11-104 (Nov. 17, 1955).

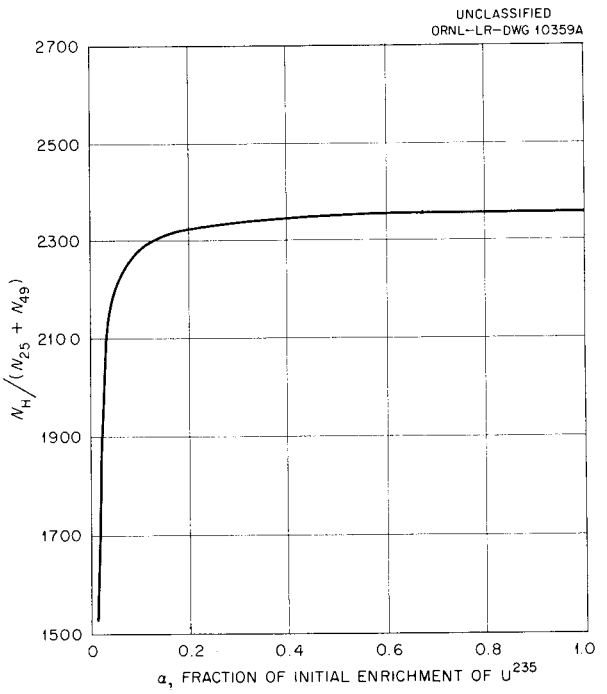

Fig. 12.3. Variation of Limiting Atomic Rate $N_H/(N_{25} + N_{49})$ with Fraction of Enrichment of U^{235} for the Case of 10% Burnup.

13. PARAMETERS FOR TWO-GROUP ANALYSIS OF CRITICAL EXPERIMENTS WITH WATER-REFLECTED SPHERES OF UO_2F_2 AQUEOUS SOLUTIONS

J. T. Thomas

A great many critical experiments have been performed with water-reflected UO_2F_2 aqueous solutions over an extensive range of concentrations. Those in spherical geometry are particularly attractive for calculations because of their simplicity. Using the data from spheres it is possible to obtain a system of parameters that will permit simple two-group, two-region calculations to be made with reasonable accuracy. The range of concentrations used in the experiments is such that determinations of the minimum critical volume and mass are possible.

The experiments were performed with three spheres, spun of 2S aluminum, having nominal radii of 11.52, 13.21, and 15.96 cm. Their critical conditions are listed in Table 13.1.

The parameters to be characterized are the fast- and slow-diffusion coefficients, D, the thermal diffusion areas, L^2, the ages to fission, τ, for both the core and reflector, and the infinite multiplication factors, k_∞. (Throughout this chapter the subscript notations c and R will refer to the core and reflector, respectively; and 1 and 2 will refer to the fast- and slow-neutron groups.) The reflector water constants were assumed to be independent of core concentration and equal to the following values:

$$D_{1R} = 1.135 \text{ cm} ,$$
$$D_{2R} = 0.160 \text{ cm} ,$$
$$L^2_{2R} = 8.123 \text{ cm}^2 ,$$
$$\tau_R = 27.00 \text{ cm}^2 .$$

The variation of L^2_{2c} with concentration is obtained from the expression

$$L^2_{2c} = \frac{D_{2c}}{\Sigma_a(c)} , \tag{1}$$

where

$$D_{2c} = \Sigma_a(H)\, L_0^2 \left(\frac{\rho_0}{\rho}\right)^2 , \tag{2}$$

in which Σ_a is the macroscopic hydrogen absorption cross section, the subscript zero refers to water, and the density ratio (ρ_0/ρ) is that of water to hydrogen in the core. The age, however, is not taken as the age to thermal energy but rather as the age to some mean energy of fission production, E_m. Since the mean energy at which fissions occur increases as the concentration increases, the age is expected to decrease with increasing concentration. The simple expression which corrects the age for density variation,

$$\tau_c \propto \rho^{-2} , \tag{3}$$

is not satisfactory because, at high concentrations, τ_c will not satisfy the usual determinant. It can be shown that for a sphere of radius r the material

TABLE 13.1. CRITICAL CONDITIONS OF WATER-REFLECTED SPHERES CONTAINING UO_2F_2 AQUEOUS SOLUTIONS

Radius (cm)	Concentration		Volume (liters)	Mass (kg of U^{235})
	U^{235} (g/liter)	Atomic Ratio: H/U^{235}		
11.52	649.05	35.8	6.400	4.154
11.52	483.13*	49.9	6.400	3.092
13.21	95.11	269.8	9.660	0.918
15.96	49.41	524.0	17.020	0.841

*This critical concentration was obtained from the extrapolation of a series of measurements made with the sphere about 99% filled.

buckling, μ^2, and ν^2 (functions of τ_c, L_{2c}^2, and k_∞ defined in Eq. 7 below) must satisfy the relation

$$\cot \mu r < \frac{\nu}{\mu} \tag{4}$$

in order that the determinant vanish when positive real constants are used. The relation given in Eq. 3 is inadequate because the resulting τ_c fails to satisfy this inequality. In order to approximate τ_c as a function of concentration, E_m is assumed to be proportional to the fuel cadmium fraction[1] (C.F.) measured near the center of reactivity; hence

$$\frac{1}{\tau_c} \propto E_m \propto \text{C.F.} \tag{5}$$

The fuel cadmium fraction measured in partially filled water-reflected spheres[2] at a few values of H/U^{235} are shown in Fig. 13.1. Also shown is the variation of τ_c with concentration obtained from Eq. 5. The infinite multiplication factor is taken as

$$k_\infty = \eta f p \epsilon \ , \tag{6}$$

where the fast-fission factor, ϵ, has been assumed to be equal to unity, and the resonance escape probability, p, is taken from Fig. 13.2.

[1]Preliminary unpublished measurements and analysis by R. Gwin at the ORNL Critical Experiments Facility give ages in fair agreement with those used here.

[2]A portion of this data appears in *Phys. Semiann. Prog. Rep. March 10, 1955*, ORNL-1926 (Classified).

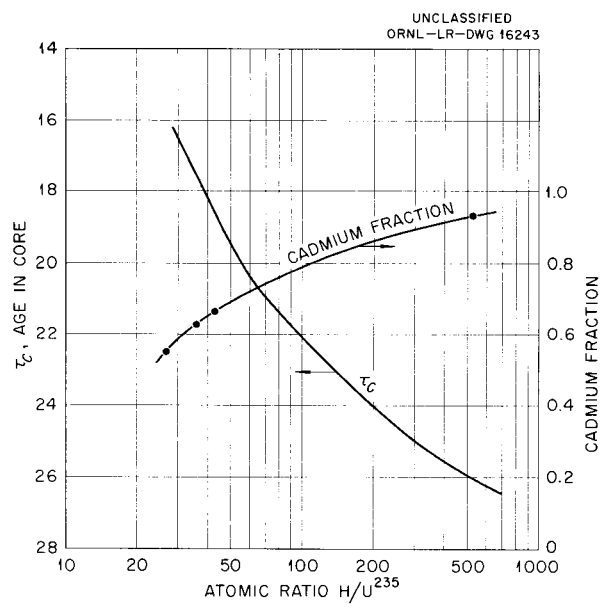

Fig. 13.1. Fuel Cadmium Fraction and Age to Fission as a Function of the H/U^{235} Atomic Ratio of Partially Filled Water-reflected Spheres of UO_2F_2 Aqueous Solutions.

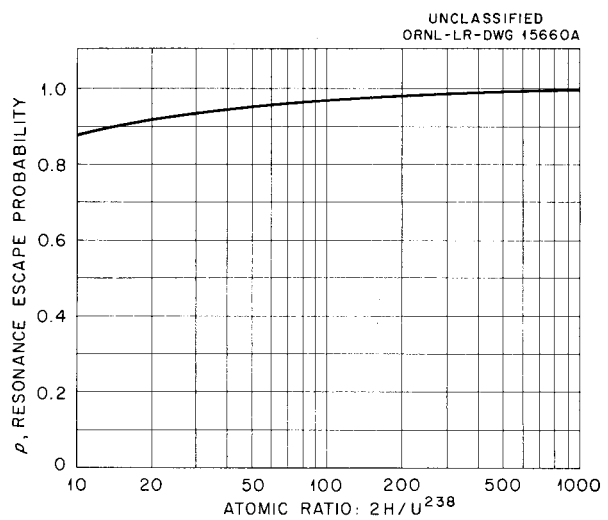

Fig. 13.2. Resonance Escape Probability as a Function of the $2H/U^{238}$ Atomic Ratio.

The normalized values of the parameters used in Eqs. 1, 3, and 5 are those for the most dilute solutions, $H/U^{235} = 524$. Figure 13.3 shows the variation of L_{2c}^2 and D_{2c} with the atomic ratio, H/U^{235}, obtained from Eqs. 1 and 2. Figure 13.4 shows the parameter μ as a function of H/U^{235} obtained from the expression

$$\begin{matrix}\mu^2 \\ -\nu^2\end{matrix} = \frac{1}{2}\left[-\left(\frac{1}{L_{2c}^2} + \frac{1}{\tau_c}\right) \pm \sqrt{\left(\frac{1}{L_{2c}^2} + \frac{1}{\tau_c}\right)^2 + \frac{4(k_\infty - 1)}{\tau_c L_{2c}^2}}\right], \tag{7}$$

using the values of τ_c and L_{2c}^2 from Figs. 13.1 and 13.3, and k_∞ from Eq. 6. Cross-section values at 2200 m/sec are used in all the calculations.

The fast-diffusion coefficient in the core (see Fig. 13.4), as a function of concentration, was obtained by solving the critical determinant for

D_{1c}, using the experimental data of Table 13.1 and the reflector water constants listed above.

Figure 13.5 presents the calculated critical radii, using the above constants. The circled points are the experimental data of Table 13.1. The determination of minimum critical volume and mass resulted in the values in Table 13.2.

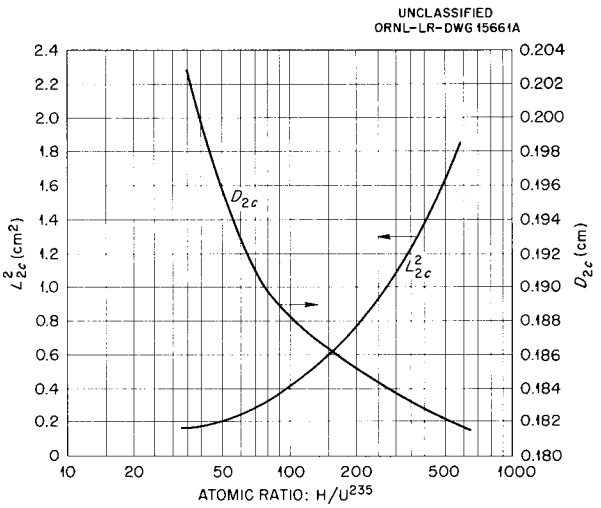

Fig. 13.3. Square of the Thermal Diffusion Length and the Thermal Diffusion Coefficient as a Function of the H/U^{235} Atomic Ratio of Water-reflected Spheres of UO_2F_2 Aqueous Solutions.

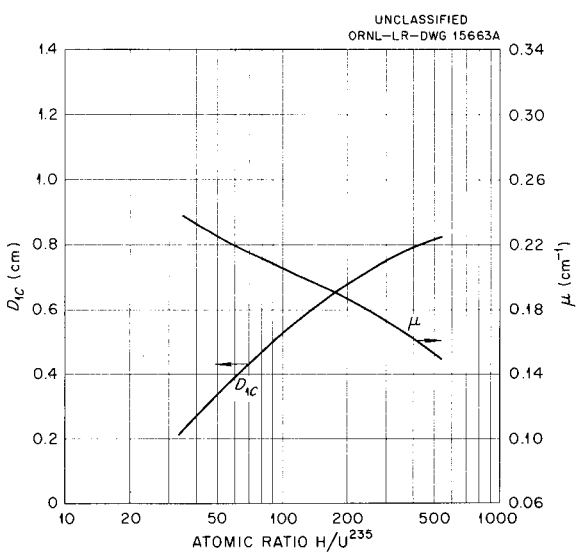

Fig. 13.4. Square Root of the Core-Material Buckling and the Fast-Diffusion Coefficient as a Function of the H/U^{235} Atomic Ratio of Water-reflected Spheres of UO_2F_2 Aqueous Solutions.

It is significant that these constants fail to give satisfactory results when used for the geometries of the infinite slab and infinite cylinder. This is probably due to the dependence of the measured fuel cadmium fraction on geometry; that is, given a fixed concentration the measured cadmium fraction will be different in the sphere, cylinder, and slab. Thus it is improper to assume the age to fission given in Fig. 13.1 to be universal; rather, a proper variation of the age to fission with concentration exists for each of the geometries. In this sense it is improper for the age to fission measured in partially filled spheres to be used for full spheres. However, the difference between the measured cadmium fraction shown in Fig. 13.1 and that expected for full spheres will not be as great as the difference caused by geometry change.

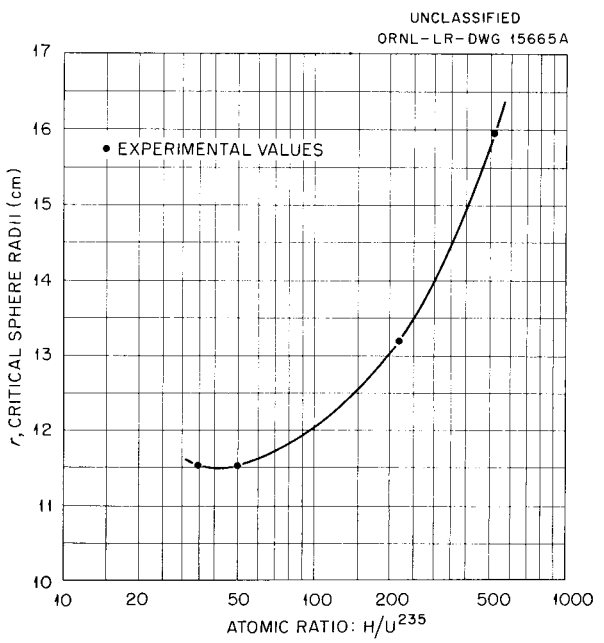

Fig. 13.5. Critical Spherical Radii as a Function of the H/U^{235} Atomic Ratio of Water-reflected Spheres of UO_2F_2 Aqueous Solutions.

TABLE 13.2. CRITICAL CONDITIONS FOR MINIMUM VOLUME OR MINIMUM MASS

	Concentration		Critical Volume (liters)	Critical Mass (kg of U^{235})
	U^{235} (g/liter)	Atomic Ratio: H/U^{235}		
Minimum volume	537.86	44	6.291	3.383
Minimum mass	58.81	440	13.434	0.790

14. DETERMINATION OF REACTOR PARAMETERS FROM PERIOD MEASUREMENTS

R. Gwin

An experimental program designed to evaluate ages of prompt and delayed neutrons and extrapolation distances is in progress. Data have been obtained from critical volumes of aqueous enriched uranium solutions contained in unreflected right cylinders and in unreflected parallelepipeds. The extrapolation distances measured are associated with the plane boundaries of the reactors. In the theoretical model, which is based on age theory, it is assumed that all delayed neutrons have the same age. The basic relations are[1]

$$(1)\quad k_{\text{eff}} = \frac{(1-\beta)\,k\exp(-\tau_p B^2)}{1+L^2B^2} + \frac{\beta k\exp(-\tau_d B^2)}{1+L^2B^2},$$

$$(2)\quad \rho = \frac{k_{\text{eff}}-1}{k_{\text{eff}}},$$

$$(3)\quad B^2 = f(r) + \frac{\pi^2}{(h+2d)^2},$$

$$(4)\quad \rho = \gamma\sum_i\left(\frac{\beta_i}{1+\lambda_i T}\right) = \gamma\rho_0,$$

$$(5)\quad \gamma = \frac{1}{(1-\beta)\exp\left[-(\tau_p^2-\tau_d^2)B^2\right]+\beta},$$

in which d is the extrapolation length for a plane boundary, h is the actual cylinder height, $f(r)$ is the radial buckling, and τ_d and τ_p are the ages of the delayed and prompt neutrons, respectively. The effective delayed neutron fraction is, therefore, $\gamma\beta$. From Eqs. 1, 2, and 3 the critical height of the reactor is

$$(6)\quad h_0 = \left(\frac{c}{\gamma}\right)^{1/3}\left(\frac{\Delta\rho_0}{\Delta h}\right)^{-1/3} - 2d,$$

$$(7)\quad c = \frac{2\pi^2}{1+L^2B^2}\left[L^2+(1-\beta)\,k\tau_p\exp(-\tau_p B^2) + \beta k\tau_d\exp(-\tau_d B^2)\right].$$

Insertion of experimental values of h_0 and $(\Delta\rho_0/\Delta h)^{-1/3}$ yields the constants $(c/\gamma)^{1/3}$ and d. Since the extrapolation length establishes the buckling, the ages of prompt and delayed neutrons can be calculated from Eq. 1 and the derived value of (c/γ), using the thermal constants, L^2 and k.

A least-squares analysis of the data obtained from critical experiments using an aqueous solution of UO_2F_2, the uranium being enriched to about 90% in U^{235}, yields the results given in Table 14.1.

The data obtained from several reactors are presented in Fig. 14.1 in the form represented by Eq. 6. A complete evaluation of the sources of error has not been made.

[1]The notation used is that of S. Glasstone and M. C. Edlund, *The Elements of Nuclear Reactor Theory*, Van Nostrand, New York, 1952.

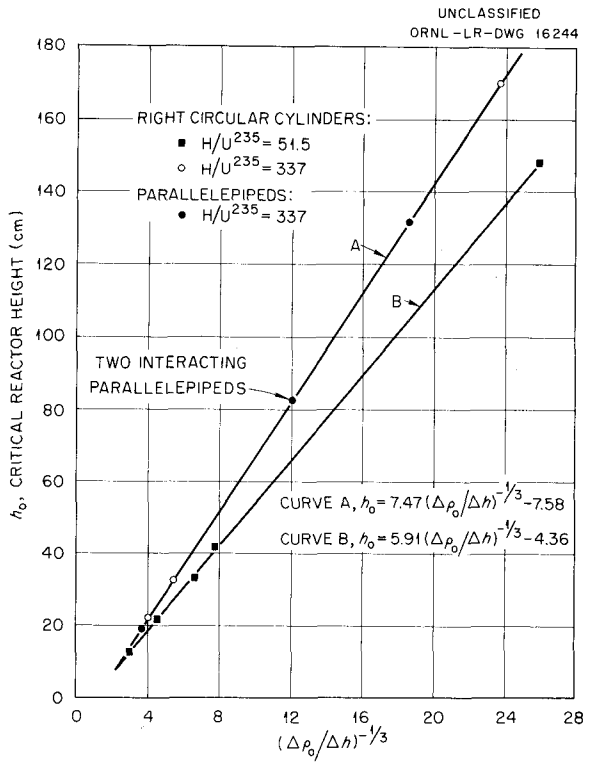

Fig. 14.1. Critical Heights as a Function of $(\Delta\rho_0/\Delta h)^{-1/3}$ for Unreflected Reactors in Aluminum Containers.

TABLE 14.1. REACTOR PARAMETERS DETERMINED FROM PERIOD MEASUREMENTS

Concentration	d (cm)	τ_p (cm^2)	τ_d (cm^2)	$\gamma\beta$
U^{235}, 0.0763 g/cc; $H/U^{235} = 337$	3.8	25.4	14.1	0.0096
U^{235}, 0.5436 g/cc; $H/U^{235} = 51.5$	2.2	*	*	

*Evaluations of L^2 and k at this high concentration are uncertain because an appreciable fraction of the fissions are produced by neutrons having epithermal energies.

15. COMPARISON OF ONE-DIMENSIONAL CRITICAL MASS COMPUTATIONS WITH EXPERIMENTS FOR COMPLETELY REFLECTED REACTORS

F. G. Prohammer

The completely reflected cylindrical reactor, which occurs frequently in reactor designs, poses a difficult problem in critical-mass calculations because the differential equation for the neutron density in such a system is not spatially separable. The problem is further complicated by the fact that most of the machine reactor computational programs presently available are one-dimensional. As a result, a short cylinder is usually converted into a sphere, and the critical mass of this equivalent sphere is then computed by machine calculations. The analysis of several experiments has been performed to find a suitable means for obtaining an equivalent sphere for machine computation of short, water-moderated, water-reflected cylinders.

The multigroup machine calculational program available was a 30-group Goertzel-Selengut program known as Eyewash and coded for the UNIVAC. This code, which has been discussed in detail by Alexander and Given,[1] is suitable only for spherically symmetric reactors.

Conversion of Experimental Cylindrical Reactors to Equivalent Spheres

The critical experiments of Beck *et al.*[2] provide ample information for the determination of a suitable criterion for obtaining an equivalent sphere for a short cylindrical reactor. All these experiments were performed with just critical cylindrical cores of water solutions of uranyl fluoride (UO_2F_2) contained in thin aluminum or stainless steel cans, which in turn were immersed in much larger cylinders of water. In this analysis the material of the cans could not be taken into account; thus it was ignored except for a grouping of results into aluminum-contained and stainless-steel-contained reactors.

Among the experimental reactors there were 24 different critical concentrations. The critical sizes of corresponding spherical reactors with most of the 24 concentrations were computed, and the results in terms of the sphere radius R vs concentration are plotted in Fig. 15.1, together with an experimental curve for spherical reactors.[3] From Fig. 15.1 a spherical reactor could be associated with each of the experimental cylindrical reactors through the common concentrations. The relationship between the geometric properties of cylinders and associated spheres is depicted by the curves marked "aluminum container" and "stainless steel container" in Fig. 15.2, in which D/d is plotted as a function of h/d (D = sphere diameter, d = cylinder diameter, h = cylinder height). The next step is to find a suitable criterion for duplicating as nearly as possible the two curves.

[1] J. H. Alexander and N. D. Given, *A Machine Multigroup Calculation. The Eyewash Program for UNIVAC*, ORNL-1925 (Sept. 15, 1955).

[2] C. K. Beck *et al.*, K-343 (April 19, 1949) (Confidential).

[3] A. D. Callihan, J. W. Morfitt, and J. T. Thomas, *Proceedings of the International Conference on the Peaceful Uses of Atomic Energy*, vol 5, p 145, United Nations, New York, 1956.

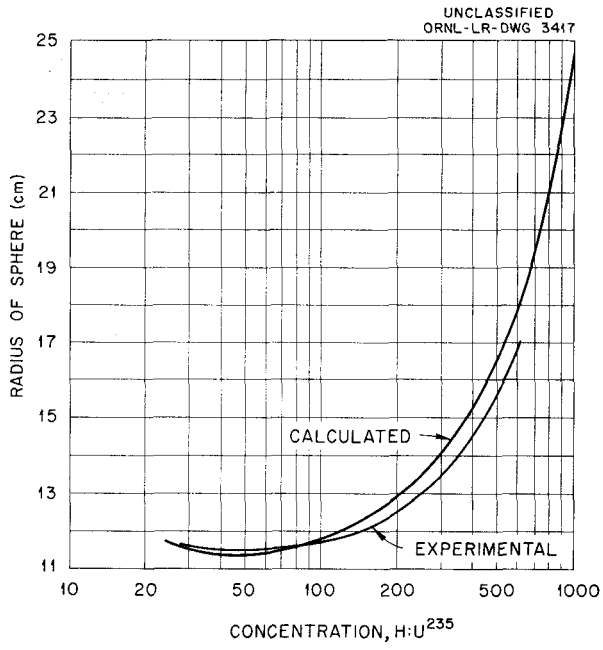

Fig. 15.1. Effect of Concentration on Critical Radius of Water-reflected Spheres.

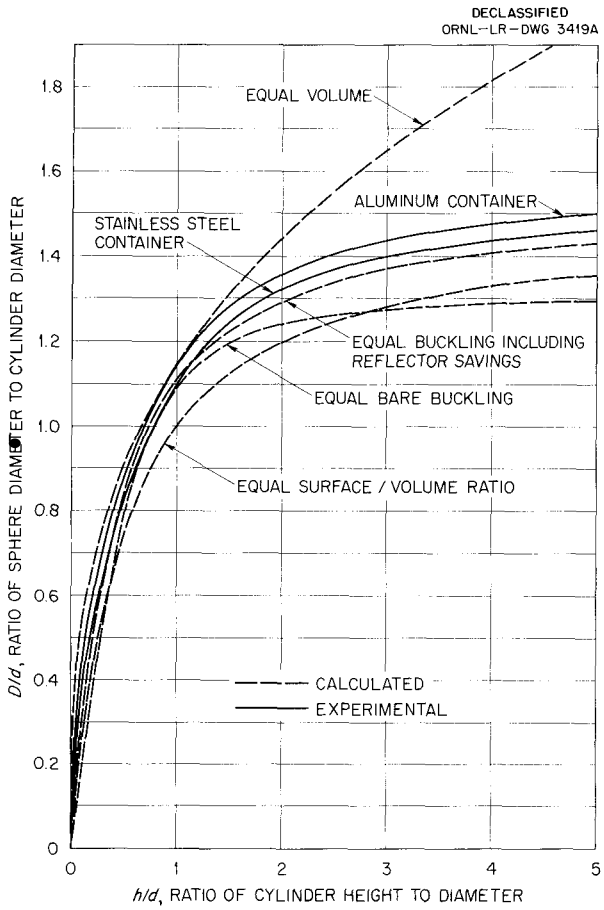

Fig. 15.2. Geometrical Comparison of Cylindrical and Spherical Reactors.

Geometrical Comparison of Cylindrical and Spherical Reactors

In seeking the criterion, four methods for obtaining equivalent spheres for the cylindrical reactors were considered. In the first method a sphere with its volume equal to that of the original cylinder was chosen. This relationship (labeled "equal volume" in Fig. 15.2) is a reasonably good fit up to an h/d of unity.

In the second method a sphere with its surface-to-volume ratio equal to that of the original cylinder was selected. This relationship (labeled "equal surface-volume ratio" in Fig. 15.2) gives the poorest fit of the four methods. Better results might have been expected, since the leakage of neutrons is proportional to the surface area, while the production of neutrons is proportional to the volume.

A sphere with its buckling equal to that of the original cylinder was chosen in the third method:

$$\frac{\pi}{R} = \left[\left(\frac{2.4048}{r}\right)^2 \left(\frac{\pi}{h}\right)^2\right]^{1/2} .$$

This relationship (labeled "equal bare buckling" in Fig. 15.2) gives fair values up to an h/d of unity.

Finally, a fourth method was chosen in which the buckling of a sphere was again equal to that of the original cylinder, but the reflector savings δ were also included:

$$\frac{\pi}{R + \delta} = \left[\left(\frac{2.4048}{r + \delta}\right)^2 + \left(\frac{\pi}{h + 2\delta}\right)^2\right]^{1/2} .$$

The reflector savings were chosen equal to the thermal-diffusion length in water, $L = 2.85$ cm. This relationship is labeled "equal buckling including reflector savings" in Fig. 15.2.

This fourth curve is by far the closest fit to the aluminum and stainless steel curves and consequently represents the criterion sought. In fact, if the reflector savings were increased, the last curve could be made to duplicate very nearly either the aluminum or the stainless steel curve, yielding a different reflector savings for each.

This paper has been published in more detail in a separate report.[4]

[4] F. G. Prohammer, *A Comparison of One-Dimensional Critical Mass Computations with Experiments for Completely Reflected Reactors*, ORNL-2007 (March 16, 1956).

Part III

FISSION PHYSICS

16. MEASUREMENT OF THE SPECTRUM OF SHORT-LIVED FISSION-PRODUCT DECAY GAMMA RAYS EMITTED FROM A ROTATING FUEL BELT

R. W. Peelle W. Zobel T. A. Love

The fission-product decay gamma rays are defined to be those gamma rays emanating from the primary fission products or their daughters at times measurably later than the fission itself. Such gamma rays invariably comprise one source of radiation in any operating fission reactor system, yet heretofore no reasonably adequate measurement had been made of their gross spectrum or intensity. Radiochemical studies on gamma-active fission-product nuclides have, however, yielded information from which the spectrum of after-shutdown radiation may be inferred for times of the order of hours after shutdown.

Although capture gamma-ray sources usually predominate in shielding considerations, in some cases the fission-product decay photons are of considerable consequence. On the basis of the known fission-product gamma-ray emitters, it has often been concluded that the fission-product gamma rays are of little importance during the operation of a reactor, and become important only after shutdown. Since the total gamma-ray energy released by the known fission products is only about 1.1 Mev (ref 1) or 1.42 Mev (ref 2) per fission, compared with the generally accepted estimate[3] of 6 Mev per fission for all the fission-product gamma-ray emitters, it appears that very little can be said about the spectrum of the complete fission-product mixture on the basis of known gamma-ray emitters. The fission-product photon spectrum during operation of a reactor depends largely upon radionuclides with half lives too short to allow measurement by the chemical techniques which have always been applied.

Some efforts have been made to calculate the gross fission-product spectrum at various times after shutdown of a reactor.[1,4,5] Unfortunately, these calculations had to be based on the experimentally known fission-product gamma-ray emitters. Therefore, the results can be applied only for the spectrum which would be observed at times >10 min after fission. It was with the hope that this span could be reduced appreciably (to times as short as about 1 sec after fission) that the present series of experiments was initiated. Two methods of approach to the solution of the problem became apparent:

1. An arrangement could be made with a continuously moving belt containing fissionable material on its entire circumference. Thermal neutrons would cause fissions at one end of its orbit, while the gamma-ray spectrometer would view the other end. If the belt were rotated with extreme rapidity and if the region within the circumference of the belt contained enough shielding material to prevent the gamma-ray spectrometer from detecting the prompt fission photons originating at the points of fission, then after long-time operation the gamma-ray spectrometer would measure the total gross fission-product photon spectrum. The bias against short half lives in this case depends upon the length of time required for rotation of the belt.

2. A sample of uranium could be exposed to a neutron flux for a very short time and then removed quickly to a gamma-ray spectrometer. If the spectra so obtained as a function of time after the short irradiation were integrated over this time, the desired total spectrum would be obtained. In this case, however, the spectra would not account for gamma-ray emitters with a half life comparable with the time required to irradiate the sample and remove it to a position at the spectrometer.

Both the above methods have been used. The results of an experiment utilizing method 1 are given in this paper, while the results of an experiment utilizing method 2 are presented in Chap. 17. Instrumentation development carried out in support of method 2 is separately reported in Chap. 50.

Experimental Apparatus

A moving fuel belt was set up in the Lid Tank Shielding Facility (LTSF) (Fig. 16.1) to replace

[1] F. H. Clark, *Decay of Fission Product Gammas*, NDA-27-39 (Dec. 30, 1954).

[2] J. O. Blomeke, *Nuclear Properties of U^{235} Fission Products*, ORNL-1783 (Nov. 2, 1955).

[3] This has frequently been inferred from results published by K. Way and E. P. Wigner, *Phys. Rev.* **73**, 1318 (1948).

[4] J. Moteff, *Fission Product Decay Gamma Energy Spectrum*, APEX-134 (Aug. 5, 1953).

[5] L. H. Boyer, *Decay Gamma Energy Spectrum from Uranium Fission Products*, IDO-16218 (April 13, 1955).

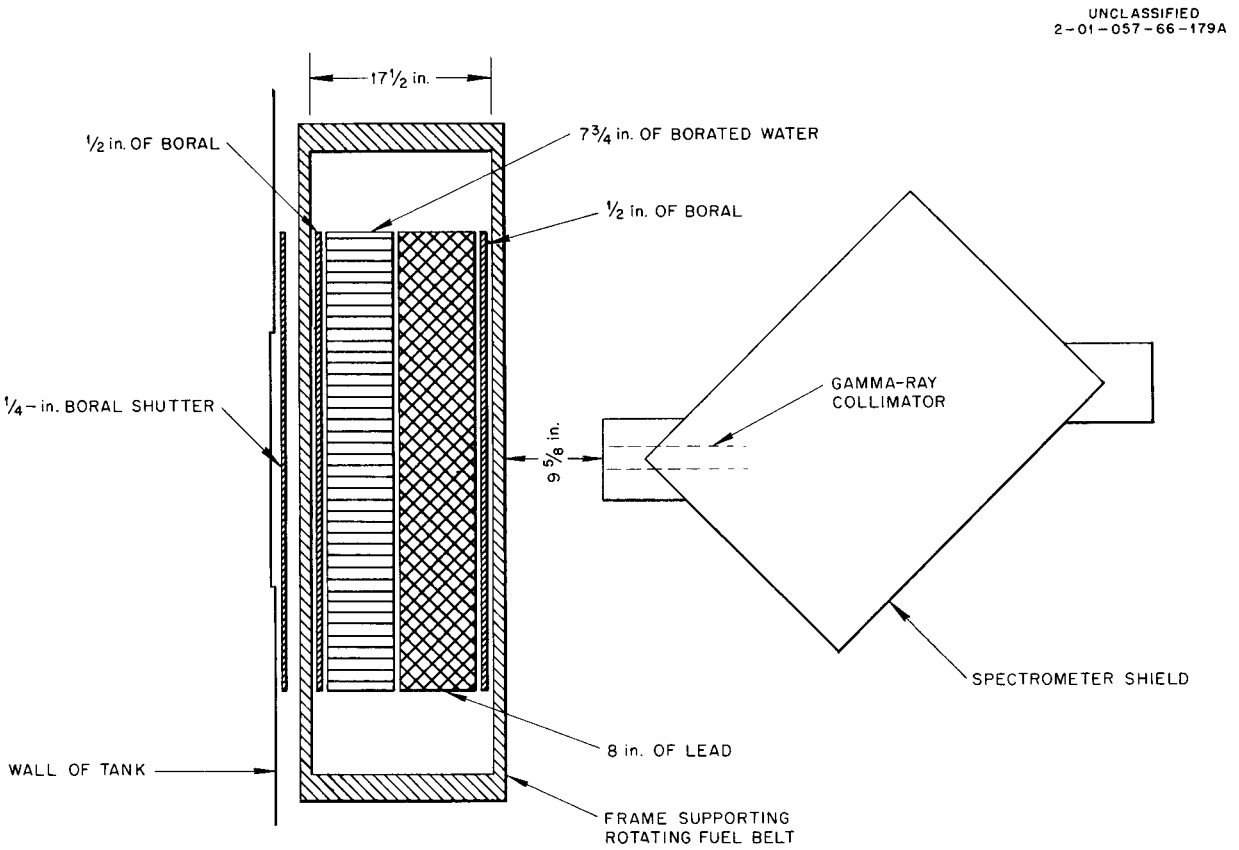

Fig. 16.1. Experimental Arrangement for the Measurement of the Spectrum of Fission-Product Gamma Rays from a Rotating Fuel Belt.

the usual uranium converter source plate, and the spectrum of fission-product gamma rays emitted from the belt was measured by a gamma-ray scintillation spectrometer. The belt consisted of fuel-plate sections containing only enriched uranium and aluminum, and it was irradiated by thermal neutrons leaking from the reflector of the ORNL Graphite Reactor. The active region of the belt was confined to a 4-in.-wide strip around its circumference. In order to shield the spectrometer from prompt gamma rays and other unwanted background as much as possible, the region within the circumference of the belt was filled with a massive shield consisting of borated water and lead. The spectrometer itself was shielded by an 8- to 12-in. thickness of lithiated paraffin bricks and a 6- to 8-in. thickness of lead. This was necessary in order to reduce to a minimum the background in the spectrometer resulting from gamma rays which did not enter the spectrometer along its collimator.

The gamma-ray scintillation spectrometer employed in this experiment was of the multiple-crystal type developed for use at the BSF.[6,7] While difficult to operate, this spectrometer provides a reasonably unique response characteristic. This implies that there exists a fairly straightforward relationship between the voltage spectrum of pulses obtained from the spectrometer and the energy spectrum of photons giving rise to these pulses. Such a unique response is virtually required in the case of the study of complicated spectra. This condition was not met by any single scintillation crystal of available size.

[6] F. C. Maienschein, *Multiple-Crystal Gamma-Ray Spectrometer*, ORNL-1142 (July 3, 1952).

[7] T. A. Love, R. W. Peelle, and F. C. Maienschein, *Electronic Instrumentation for a Multiple-Crystal Gamma-Ray Scintillation Spectrometer*, ORNL-1929 (Oct. 25, 1955).

Measurements of the gamma-ray spectrum were made while the fuel loop was rotated. The observed counting rates were a function of time after the activation of the rotating belt was begun. In principle they would also be a function of the time T required for the belt to complete one revolution.

In order to determine the contribution to the spectrum by background gamma rays (i.e., those not emitted from that section of the fuel loop directly in front of the spectrometer collimator), spectral measurements were made with the fuel stationary and with a large lead plug filling the collimator opening. Spectral measurements were not started until some time after the rotating rig had been operating at full power. This allowed most of the fission-product nuclides to approach their equilibrium value. Loop rotation periods T between 1.2 and 2.5 sec were used for a total of four spectral measurements.

Results and Discussion

Although a complete analysis is not yet available, there is no apparent variation either in shape or in intensity of the spectrum as the rotation period is changed. A typical spectrum shown in Fig. 16.2 is representative of the gamma radiation from the fuel loop about 3 hr after the beginning of the activation.

The shape of the spectrum is arrived at after a determination of the efficiency of the detector as a function of photon energy. The normalization of the spectrum depends on additional factors such as the solid angle of the gamma-ray collimator used, the thermal-neutron flux impinging upon the reactor side of the loop, and the percentage utilization of this flux for the fission process. The curve presented in Fig. 16.2 represents a rapid evaluation of these factors. A more complete evaluation of the data will also include the calculation of the statistical errors on the points shown. These errors are considerable for measurements at the higher energies, and it is expected that they will adequately explain the scatter of the experimental data points. A correction procedure should also be applied to take into account the residual spread of response inherent in the gamma-ray spectrometer used. Application of this correction should tend to reduce the measured yield at the lowest energies.

In addition to the experimental errors noted above, systematic errors arising from experimental bias must be considered. Bias against both the long-lived and very short-lived fission-product gamma-ray emitters is known to exist in the results given here. The bias against long half lives arises from the failure to operate the fuel belt for an infinitely long time prior to spectral determinations. The bias against the very short half lives comes from the inability to operate the fuel belt with very short rotation periods.

The probability that the radiation from a given nuclide will be detected is[8]

$$f(\lambda) = \frac{\sinh(\beta\lambda T/2)}{\beta \sinh(\lambda T/2)}(1 - e^{-\lambda\tau}) ,$$

where

λ = decay constant of the nuclide,
T = length of time required for a fuel-belt rotation,
β = fraction of the circumference of the fuel belt which is under thermal-neutron irradiation at any given instant,
τ = period of time during which the fuel belt is rotated with neutron irradiation prior to the time of measurement of the photon spectrum.

It will be noted that $f(\lambda)$ is nearly unity whenever

$$\frac{1}{\tau} \ll \lambda \ll \frac{1}{T} .$$

For this experiment $f(\lambda) \geqq 0.85$ for half lives between 0.35 sec and 1 hr. From the known characteristics of individual gamma-ray emitters it would be possible to correct the measured spectrum for the bias against the long-half-life emitters. No correction can be made for the unknown short period gamma-ray emitters.

The fission-product photon energy spectrum shown in Fig. 16.2 was integrated between 0.36 and 5.8 Mev to obtain an average of 4.8 Mev per fission over the intervening energy interval. In addition to any error dependent upon the failure to remove experimental bias, an estimated probable error of ±20% is assigned to these averages and to the normalization of the experimental spectrum. This estimated error is largely caused by uncertainties in the true fission rate in the uranium of the fuel plates.

[8]This formula assumes that all the radioactive nuclides are born at the time of fission.

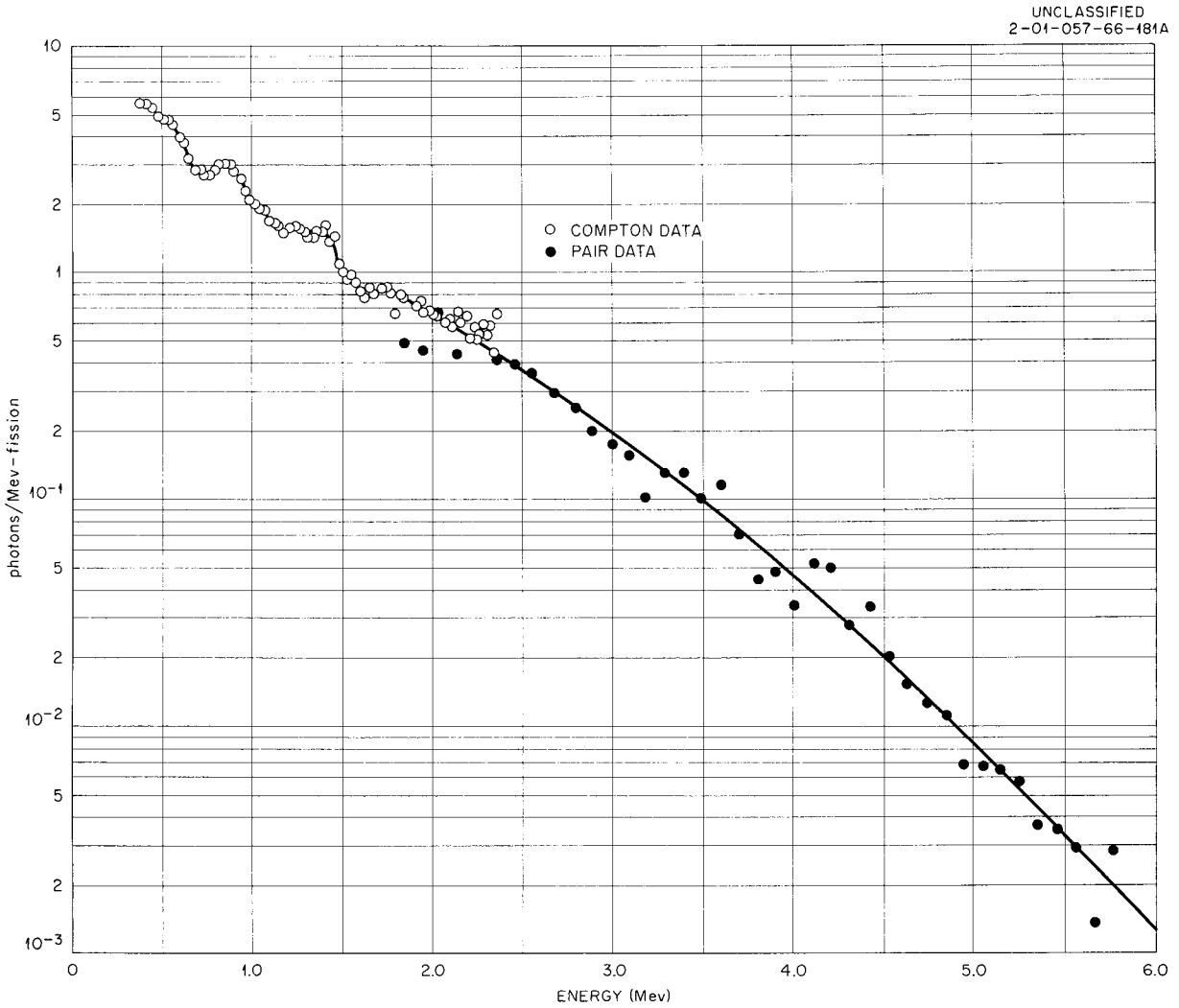

Fig. 16.2. Typical Spectrum of Fission-Product Gamma Rays from a Rotating Fuel Belt.

17. TIME AND ENERGY SPECTRA OF FISSION-PRODUCT GAMMA RAYS MEASURED AT SHORT TIMES AFTER URANIUM SAMPLE IRRADIATIONS

W. Zobel T. A. Love

As described in the preceding chapter, two methods for measuring the spectrum of short-lived fission-product gamma rays have been employed. In this chapter the results of the experiment utilizing method 2 are discussed. This experiment consisted of two parts. In the first part the detailed time dependence of relatively large photon energy groups was studied, while in the second part detailed energy spectra were measured at different times after fission.

Experimental Apparatus

Both parts of the experiment required essentially the same equipment. It was necessary to introduce a U^{235} sample into a known neutron flux, irradiate it for a measured period of time, remove it from the flux, and transport it to the detector. The equipment used for these operations consisted of the fast pneumatic tube[1] at the ORNL Graphite Reactor, a multiple-crystal gamma-ray spectrometer,[2,3] and associated electronic equipment. The spectrometer was moved to the reactor, while the electronic equipment remained at the BSF, an arrangement which necessitated some changes in the electronics. These changes, together with other modifications necessary for this experiment, are described in Chap. 50 of this report.

For the time-dependence study, samples of enriched uranium weighing about 2, 7, or 15 mg were irradiated in the reactor for periods varying from 0.8 to 32 sec. The irradiation time depended to some extent on the time region under investigation, and the combination of irradiation time and sample size was chosen so as to keep the resulting counting rate within manageable limits. In addition, an attempt was made to keep the irradiation time smaller than, or equal to, the waiting period between irradiation and counting. This condition could be fulfilled in all but three cases. The energy range to be investigated (0.28 to 5.0 Mev) was divided into six intervals, with one interval being covered by both the Compton (two-crystal) and the pair (three-crystal) spectrometers. The experiment covered the time range from 1.25 to 1600 sec after fission, where fission was presumed to have taken place at the mid-point of the irradiation interval. Energy calibration of the spectrometer was carried out in the usual manner before and after each run, using several sources as shown in Table 17.1. The time analyzer, that is, the multichannel analyzer converted from energy analysis to time analysis, was calibrated before and after each run by use of a 60-cycle pulser. The efficiency of the spectrometer as a function of photon energy was determined with the aid of sources whose absolute strengths were measured in the high-pressure ion chamber of the ORNL Radioisotopes Control Laboratory. The total efficiency of the spectrometer rather than the peak efficiency was used in the calculations.

TABLE 17.1. GAMMA-RAY SOURCES USED FOR CALIBRATION OF THE BSF SPECTROMETER

Source	Gamma-Ray Energy (Mev)
Hg^{203}	0.279
Na^{22}	0.511, 1.277
Zn^{65}	1.114
F^{20}	1.63
Zr^{90*}	2.30
Na^{24}	1.368, 2.754
ThC''	2.615
N^{16}	6.13

For the energy spectra study, samples of enriched uranium weighing about 2, 7, 15, or 32 mg were irradiated for periods ranging from 1 to 64 sec. Combinations of sample weight and bombarding time were chosen for the same criteria as in the first part. Energy spectra, covering the

[1] Designed by E. C. Campbell, Physics Division.

[2] F. C. Maienschein, *Multiple-Crystal Gamma-Ray Spectrometer*, ORNL-1142 (July 3, 1952).

[3] T. A. Love, R. W. Peelle, and F. C. Maienschein, *Electronic Instrumentation for a Multiple-Crystal Gamma-Ray Scintillation Spectrometer*, ORNL-1929 (Oct. 25, 1955).

range from 0.28 to 5.4 Mev, were taken at ten different times after fission, defined as above. Calibration and efficiency determinations of the spectrometer were also performed in the same manner described above.

Results and Discussion

A preliminary, and rather crude, analysis of the experiment has been performed. The data were corrected for counting losses due to the inherent dead-time of the equipment. These losses were determined experimentally. The corrected counts per channel were divided by the counting time, the total sample weight, the efficiency of the spectrometer, the energy interval per channel, the bombarding time, and the number of fissions per milligram of U^{235} per second. All these quantities are obvious and were easily obtained, except the last two. The number of fissions can be calculated from the sample weight and the thermal-neutron flux. The sample, on its way into and out of the reactor, moved in a region of varying flux. Since a detailed flux pattern over this region was not available, it was decided to measure an "effective" thermal-neutron flux. This effective thermal-neutron flux was obtained by exposing bare and cadmium-covered gold foils at the time of each run and computing the flux from the cadmium difference. The effective bombarding times were obtained in a similar manner by exposing gold foils for the nominal bombarding times used in the experiment and calculating the effective bombarding times from the activities so obtained.

The results of the time-dependence study are plotted in Fig. 17.1. Figures 17.2 and 17.3 present the results of the energy-spectra study. No errors have yet been computed for the points on these curves. Crossplots of the results of the two studies are shown in Figs. 17.4 and 17.5. It is evident that the agreement is quite good.

The results of each part of the experiment were integrated numerically to give the number of photons and the total fission-product gamma-ray energy released per fission in the energy range from 0.28 to 5.0 Mev and in the time interval from 1.25 to 1600 sec after fission. The number of photons per fission was found to be 2.92 in the time-dependence study and 2.81 in the energy-spectra study. The energy per fission was found to be 3.23 and 3.22 Mev, respectively, for the two studies. Pending a more complete analysis these numbers must carry an estimated error of $\pm 25\%$.

The results of this experiment may be compared with the results of the experiment discussed in Chap. 16; however, it should be borne in mind that systematic differences exist in the evaluation of the data in the two experiments. In particular, the spectrometer efficiency used to evaluate the moving-fuel-belt experiment was the peak efficiency rather than the total efficiency as used here. Owing to the nonuniqueness of the response of the spectrometer it is felt that neither of the methods will really give the correct answer, although the results presented in this chapter should constitute a lower limit, and those in Chap. 16 should represent an upper limit.

Further work leading toward a refinement of the method of analysis is in progress.

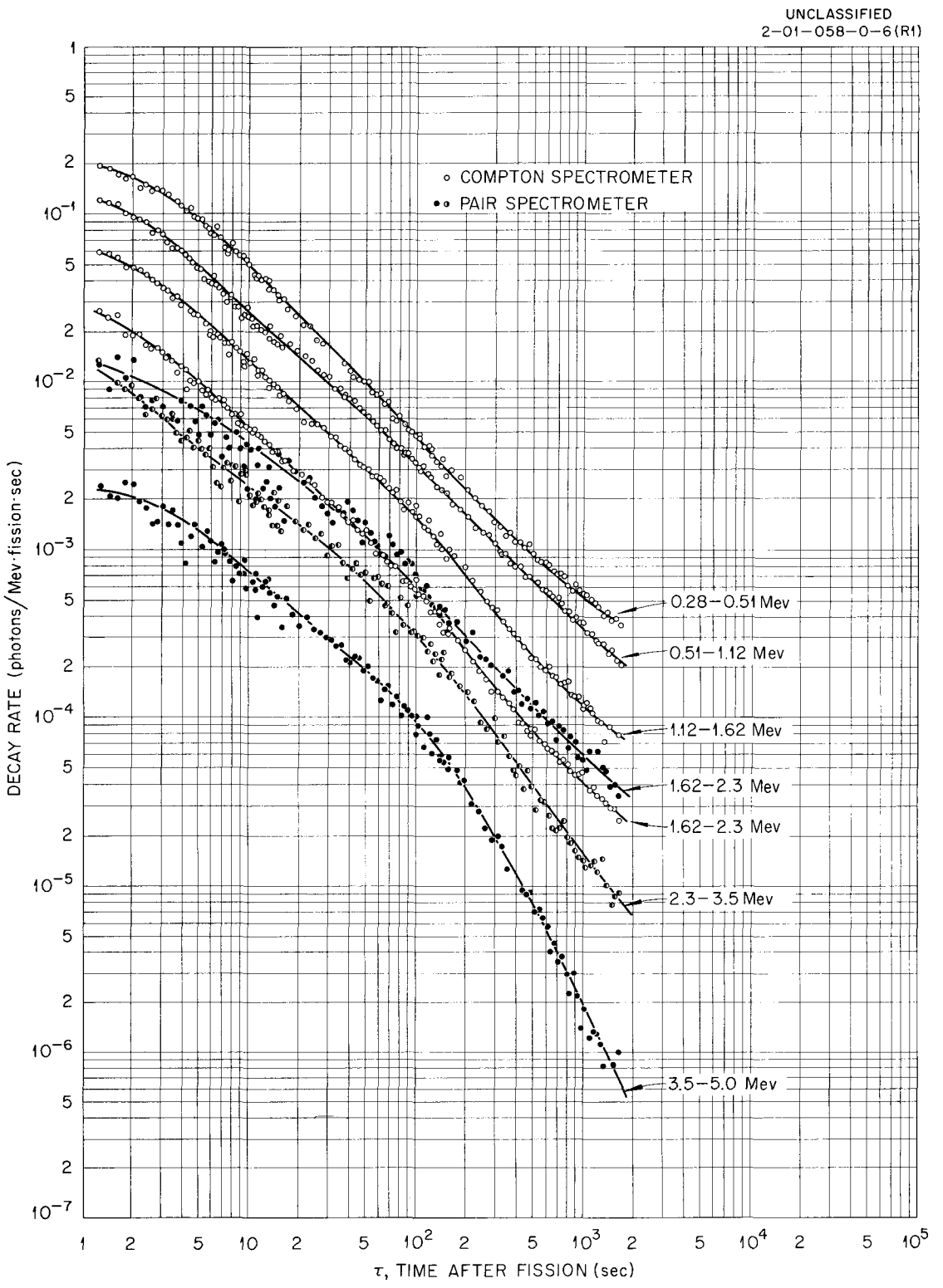

Fig. 17.1. Fission-Product Gamma-Ray Decay Rates as a Function of Time After Fission for Six Photon Energy Groups.

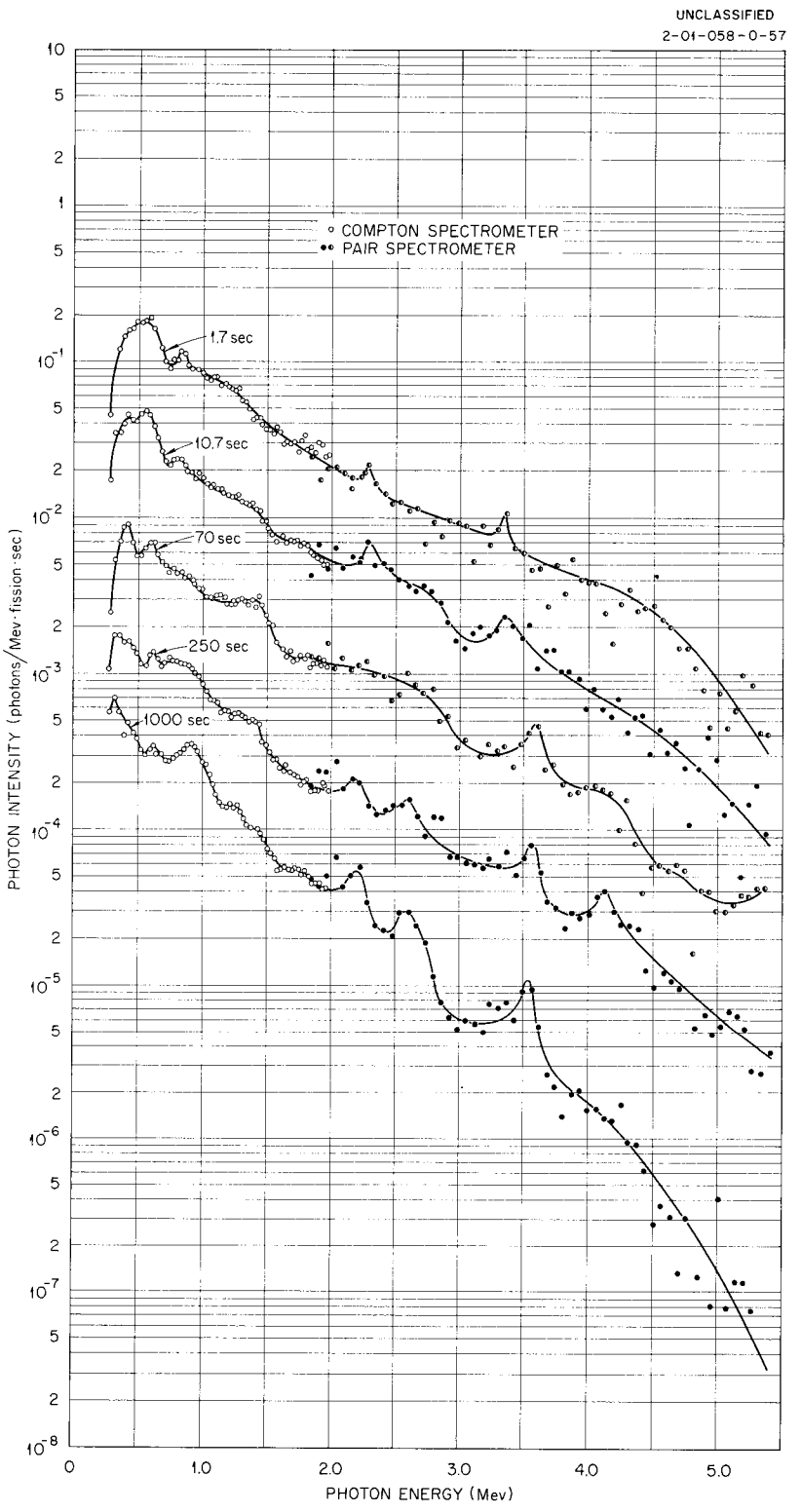

Fig. 17.2. Fission-Product Photon Energy Spectrum at 1.7, 10.7, 70, 250, and 1000 sec After Fission.

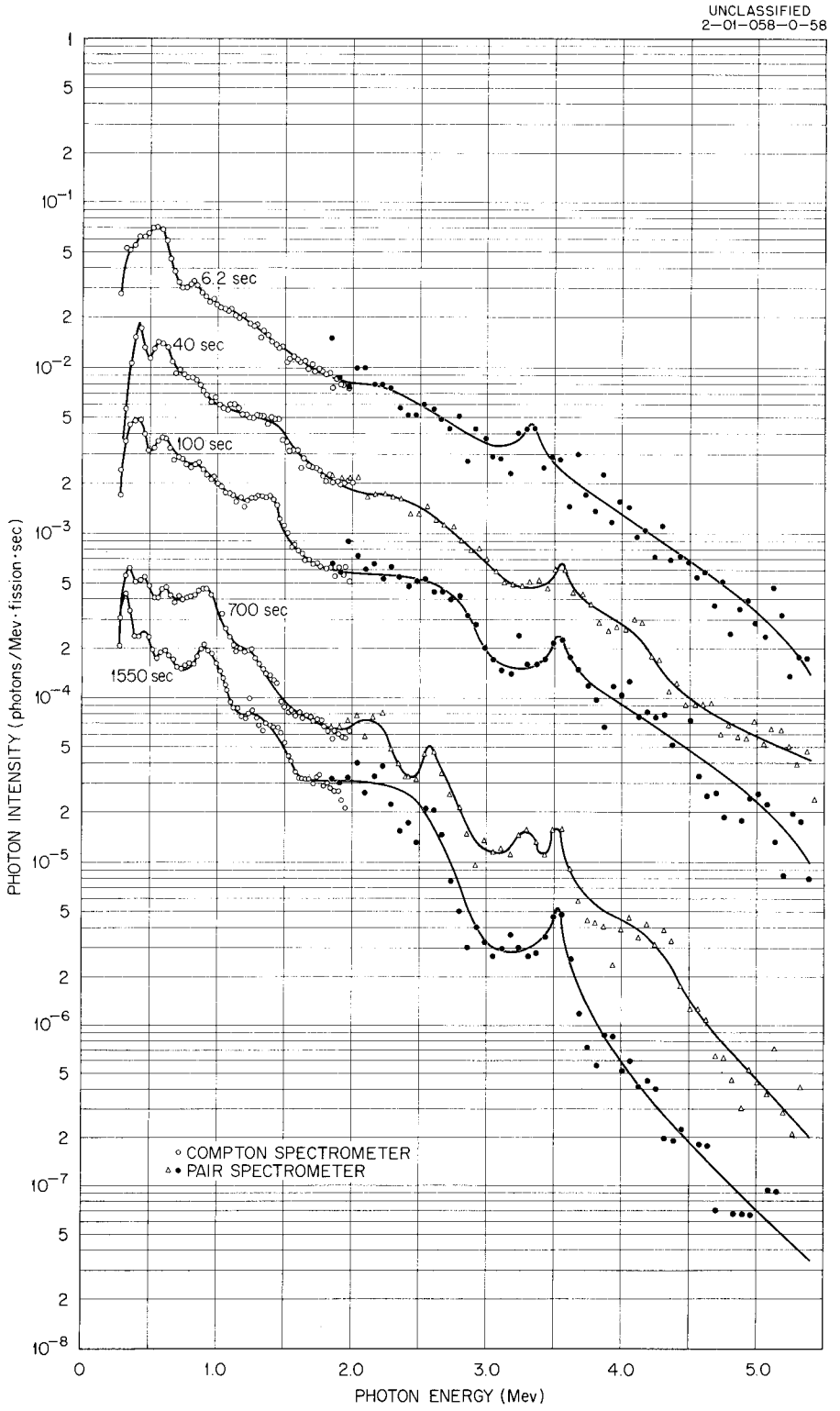

Fig. 17.3. Fission-Product Photon Energy Spectrum at 6.2, 40, 100, 700, and 1550 sec After Fission.

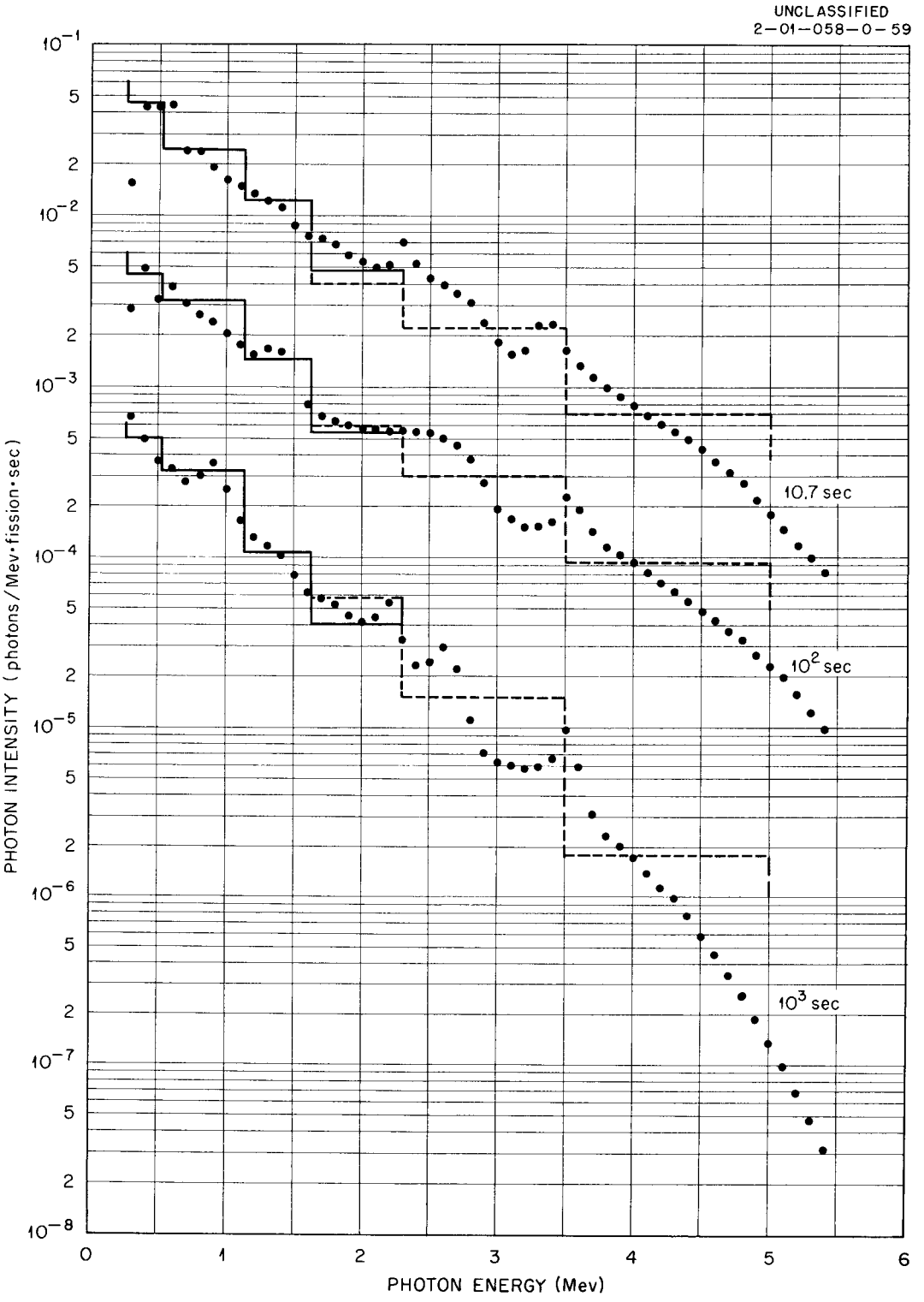

Fig. 17.4. Fission-Product Photon Energy Spectrum with Superimposed Spectrum from Time Decay Study.

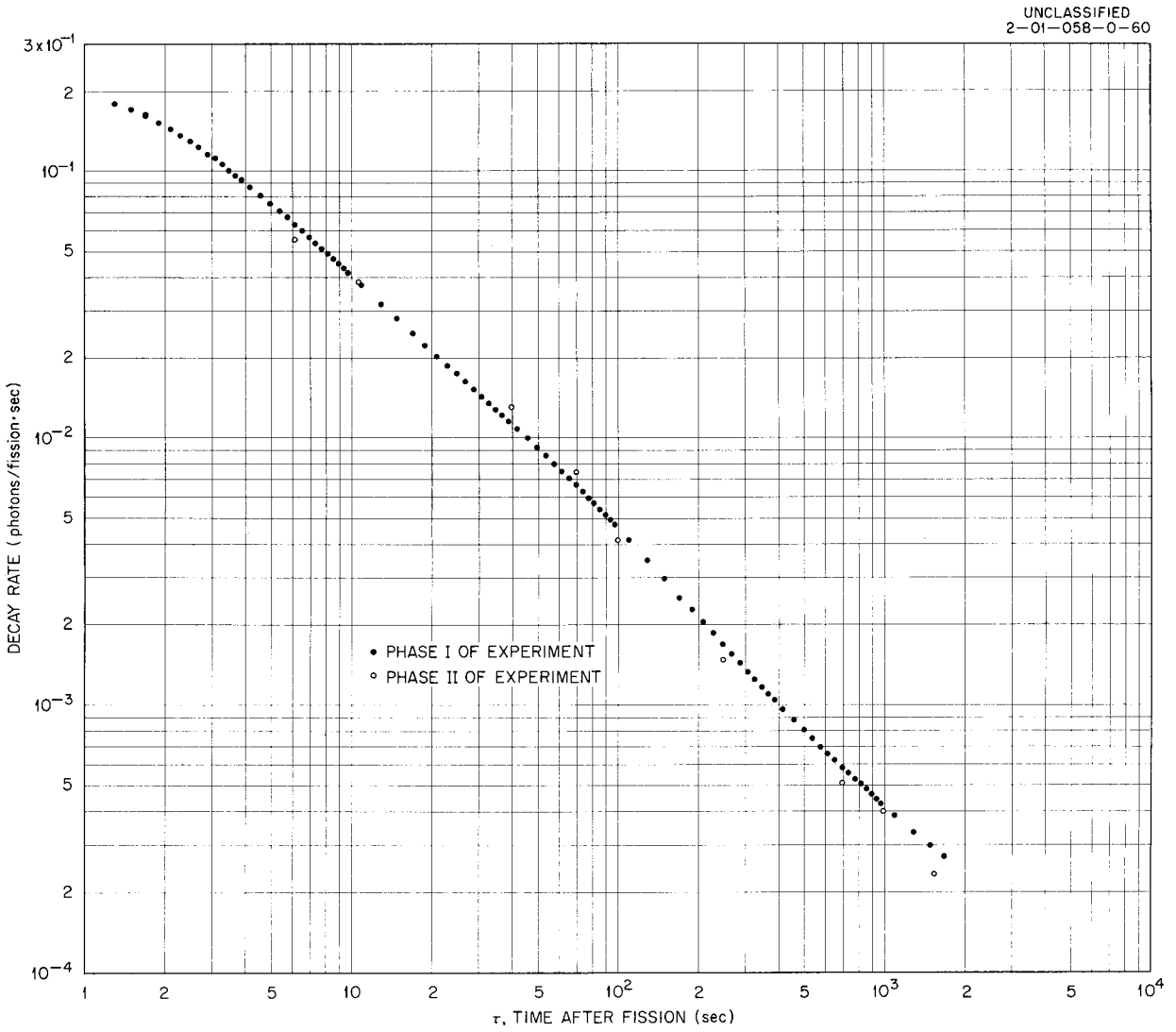

Fig. 17.5. Decay Rate of Fission-Product Gamma Rays for 0.28- to 5.0-Mev Energy Range with Superimposed Points from Energy Spectra Study.

18. THERMAL-NEUTRON FISSION CROSS SECTIONS OF Pu^{239} AND Pu^{240}

W. W. Pratt[1] F. J. Muckenthaler E. G. Silver

The thermal-neutron fission cross sections for Pu^{239} and Pu^{240} have been measured by a method in which these constants are compared with the corresponding constants for U^{235}. The measurements were made with the aid of a double fission chamber (Fig. 18.1) placed in the neutron beam emerging from hole 57 in the ORNL Graphite Reactor. One section of the fission chamber, called "the monitor chamber," contained a deposit of U^{235} which served to monitor the beam. The other section, called "the comparison chamber," contained a deposit of either U^{235} or the plutonium isotope to be investigated. The ratio of the number of fission pulses counted with the plutonium deposit in the comparison chamber to the number of fission pulses counted with the U^{235} deposit in the comparison chamber, each referred to a given number of pulses in the monitor chamber, was used to deduce the ratio of the fission cross section of the plutonium isotope to the fission cross section of U^{235}.

All the isotopes employed were deposited on nickel foils $\frac{3}{4}$ in. in diameter and 0.002 in. thick. The surface density of the deposits was approximately 100 $\mu g/cm^2$, and the diameter of the deposit was approximately 0.5 in. These foils were placed in pairs back-to-back in the fission chamber, which was a $1\frac{1}{4}$-in.-ID aluminum cylinder with 0.031-in.-thick walls. On each side of the pair of foils was an aluminum plate 0.020 in. thick and $\frac{3}{4}$ in. in diameter. These plates formed the collecting electrodes. The distance between a collecting electrode and the foil was $\frac{1}{8}$ in. The foils and collecting electrodes were held in place by a system of aluminum rings and a polyethylene spacer. The two foils in a pair were in electrical contact with each other and were connected to a negative 500-v regulated power supply. A gas mixture of tank argon plus 3% CO_2 was allowed to flow through the chamber at an approximate rate of 0.1 ft^3/hr. The pressure in the chamber was maintained at 15 psig.

Three types of foils were used: U^{235} foils, Pu^{239} foils, and Pu^{240} foils. The composition of each is given in Table 18.1. The number of atoms present on each foil was determined by counting the alpha-particle decay[2] and making use of the isotope abundances, the half lives of alpha decay of the isotopes present, and the known efficiency of the alpha-particle counter. At least five of each of the foil types were made available initially. The amount of material present on each foil was established within the tolerances given below:

U^{235} foil	0.9% (by weight)
Pu^{239} foil	1.6% (by alpha count)
Pu^{240} foil	1.9% (by alpha count)

These numbers are due to uncertainties in counter efficiencies and half lives; they do not include alpha-counting statistics ($\leq 1\%$) which are accounted for elsewhere.

Foils of U^{235}, Pu^{239}, and Pu^{240} were placed in an alternating sequence in the comparison chamber, and a U^{235} foil remained in the monitor chamber.

[1]Pennsylvania State University.

[2]The alpha particle counting was carried out by F. Moore, Analytical Chemistry Division.

TABLE 18.1. ISOTOPIC ANALYSIS OF U^{235}, Pu^{239}, AND Pu^{240} FOILS

Isotope	Amount in Foil (%)
U^{235} Foils	
U^{234}	0.048 ± 0.006
U^{235}	99.806 ± 0.015
U^{236}	0.062 ± 0.006
U^{238}	0.084 ± 0.006
Pu^{239} Foils	
Pu^{239}	99.796 ± 0.006
Pu^{240}	0.191 ± 0.001
Pu^{241}	<0.01
Pu^{242}	Negligible
Pu^{240} Foils	
Pu^{239}	12.200 ± 0.113
Pu^{240}	87.172 ± 0.055
Pu^{241}	0.583 ± 0.085
Pu^{242}	0.044 ± 0.038

For each foil in the comparison chamber 20 measurements were made. Each measurement consisted in observing the number of pulses counted in the comparison chamber per 65,536 pulses counted in the monitor chamber. A measurement of the alpha-particle counting rate was made in an alpha counter of standard geometry both before and after exposure in the fission chamber to ensure that none of the deposit was lost. The statistical precision for each group of counts was <0.5%.

For each foil a cadmium ratio was determined by comparing the number of pulses counted in the

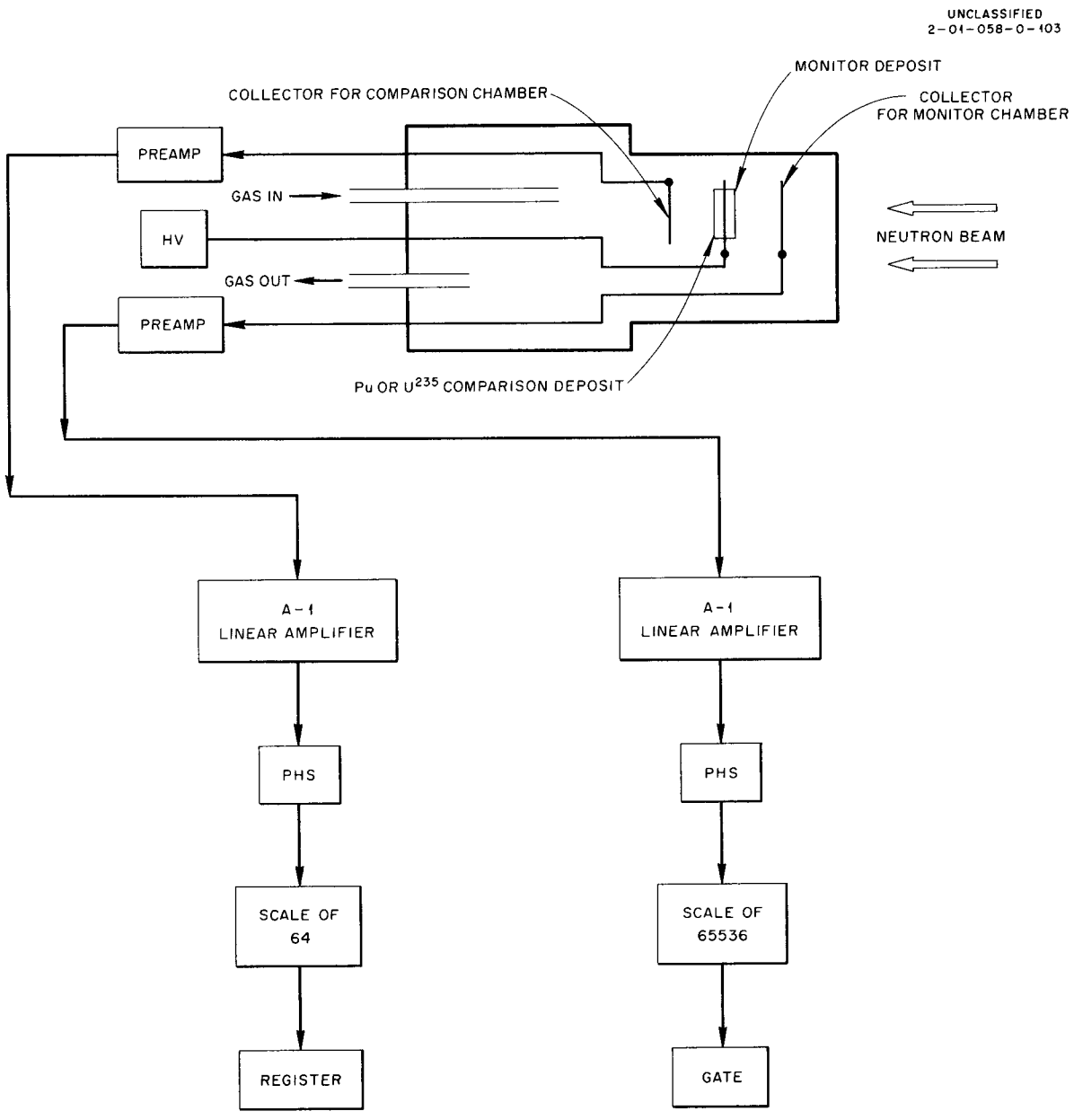

Fig. 18.1. Experimental Apparatus Used for the Measurement of the Thermal-Neutron Fission Cross Sections of Pu^{239} and Pu^{240}.

cadmium-shielded comparison chamber with the number in an unshielded chamber. The observed cadmium ratios were:

U^{235} foil	25.3 ± 0.3
Pu^{239} foil	23.1 ± 0.4
Pu^{240} foil	22.6 ± 2.0

The fission cross sections of the plutonium isotopes, averaged over the neutron energy spectrum of the beam below the cadmium cutoff, were obtained by comparing the cadmium differences (total counts in unshielded chambers minus total counts in the shielded detector for the specified isotope) for Pu^{239} foils and Pu^{240} foils with the cadmium difference for U^{235} foils. In the case of the Pu^{239}, the foils of which were essentially pure Pu^{239}, the cross section was determined by the equation,

$$\frac{\sigma^{49}}{\sigma^{25}} = \frac{N_c^{49}/N_a^{49}}{N_c^{25}/N_a^{25}} , \tag{1}$$

where

σ^{49}, σ^{25} = average fission cross sections for Pu^{239} and U^{235}, respectively,

N_c^{49}, N_c^{25} = cadmium differences for Pu^{239} and U^{235} foils, respectively,

N_a^{49}, N_a^{25} = number of atoms of the Pu^{239} or U^{235} isotope on the foil.

The fission cross section for Pu^{240}, the foils of which contained appreciable amounts of Pu^{239} and Pu^{241}, was obtained from the corresponding relation:

$$\frac{\sigma^{40}}{\sigma^{25}} = \frac{N_c^{40}/N_a^{40}}{N_c^{25}/N_a^{25}} - \left(\frac{N_a^{41}}{N_a^{40}}\right)\frac{\sigma^{41}}{\sigma^{25}} - \left(\frac{N_a^{49}}{N_a^{40}}\right)\frac{\sigma^{49}}{\sigma^{25}} , \tag{2}$$

where the terms for the respective isotopes have the same significance as in Eq. 1.

The results of the measurements gave the following cross-section ratios averaged over the spectrum of neutrons in the beam hole:

$$\frac{\sigma^{40}}{\sigma^{25}} = 0.0070 \pm 0.0154 ,$$
$$\frac{\sigma^{49}}{\sigma^{25}} = 1.725 \pm 0.027 . \tag{3}$$

It was, of course, necessary to adjust these values for temperature. The temperature of neutrons from this beam hole had been previously estimated to be 495°K by use of a $1/v$ absorber.[3]

In general, the measured cross section can be defined as

$$\sigma = \frac{\int_0^{0.5\,\mathrm{ev}} n(E)\,\sigma(E)\,dE}{\int_0^{0.5\,\mathrm{ev}} n(E)\,dE} , \tag{4}$$

where

$n(E)$ = neutron flux distribution as a function of neutron energy,

$\sigma(E)$ = cross section for neutrons of energy E,

and 0.5 ev is taken to be the "cadmium cut-off." If $\sigma(E)$ is defined as $\sigma_0 f(E)$, where $\sigma_0 = \sigma$ (2200 m/sec), and it is assumed that the spectrum is a Maxwellian distribution at 495°K, then $\sigma = \sigma_0 F$, where

$$F = \frac{\int_0^{0.5\,\mathrm{ev}} Ee^{-E/kT} f(E)\,dE}{\int_0^{0.5\,\mathrm{ev}} Ee^{-E/kT}\,dE} . \tag{5}$$

The function $f(E)$ was obtained from BNL-325,[4] and values of F were computed for the isotopes at a temperature of 495°K as follows:

$$F^{25} = 0.633 ,$$
$$F^{49} = 0.885 ,$$
$$F^{40} = 0.694 .$$

The cross sections were then determined as follows:

$$\sigma_0^{49} = \frac{\sigma^{49}}{\sigma^{25}}\,\frac{F^{25}}{F^{49}}\,\sigma_0^{25} ,$$

$$\sigma_0^{40} = \frac{\sigma^{40}}{\sigma^{25}}\,\frac{F^{25}}{F^{40}}\,\sigma_0^{25} ,$$

[3] L. D. Roberts, Physics Division, private communication.

[4] D. J. Hughes and J. A. Harvey, *Neutron Cross Sections*, BNL-325 (July 1, 1955).

where

$$F^{25}/F^{49} = 0.715 ,$$

$$F^{25}/F^{40} = 0.913 .$$

The value given by the Brookhaven Neutron Cross Section Compilation Group[4] for σ_0^{25} was 580 ± 8 barns. Using this value in the above equations yielded:

$$\sigma^{49} = 715 \pm 15 \text{ barns} ,$$

$$\sigma^{40} = 3.7 \pm 8 \text{ barns} .$$

The determination of the flux from hole 57 was accomplished by measuring a $1/v$ absorber. With the assumption that the neutrons were of Maxwellian energy distribution, the temperature appears to be 495°K. The use of this result to deduce the cross section of another element for 2200-m/sec neutrons is then dependent on the assumption of Maxwellian distribution, and this uncertainty is accentuated for the case of a non-$1/v$ absorber, as was used in this experiment. Because of this uncertainty, another experiment is contemplated in which the graphite thermal column at the BSF will be used, for which the flux should more certainly be Maxwellian.

19. NUMBER OF NEUTRONS RELEASED PER THERMAL FISSION OF Pu^{241}

G. deSaussure E. G. Silver

The number of neutrons released per thermal fission of Pu^{241} ($\bar{\nu}^{41}$) has been measured by several investigators.[1-5] Prior to the initiation of this experiment, the results of two other experiments were known. A group at Argonne National Laboratory had reported[1] a value of 2.91 ± 0.10, and an experiment at ORNL[2] had resulted in a value 3.30 ± 0.23. In view of the discrepancy between the two, it was decided to repeat the latter experiment with improved instrumentation. In the discussion below this experiment is described, and the results are compared both with earlier and with later measurements.

Description of Experiment

In the experiment the number of neutrons produced per thermal fission in plutonium samples introduced in the beam of neutrons from hole 57 of the ORNL Graphite Reactor was compared with the number produced in uranium samples. From this ratio, the value of $\bar{\nu}^{41}$ could be determined by comparison with the published value[6] of $\bar{\nu}^{25}$. The plutonium samples were prepared by F. Moore,[7] and the uranium samples were supplied by R. Greene[8] of the Oak Ridge Gaseous Diffusion Plant. The samples were deposited on nickel foils ¾ in. in diameter and 0.002 in. thick. Each deposit was ½ in. in diameter and 100 $\mu g/cm^2$ in thickness. The isotopic compositions of the samples, as determined by alpha-particle counting one week after the samples were prepared, are listed in Table 19.1. The foils were introduced into a small double fission chamber, of which they formed the electrodes, and fast neutrons released by the foils were detected by a pair of 5-in.-dia Hornyak buttons bound to the faces of 5-in.-dia Dumont photomultiplier tubes. (Hornyak buttons are disks

[1] A. H. Jaffey *et al.*, *Thermal Neutron Fission Cross Section of Pu^{241}*, ANL-5397 (Jan. 3, 1956); A. H. Jaffey, C. T. Hibdon, and R. Sjoblom, *Thermal Neutron ν for Pu^{241}*, ANL-5396 (March 31, 1955).

[2] W. W. Pratt, Pennsylvania State University, and F. J. Muckenthaler, Oak Ridge National Laboratory, private communication.

[3] D. E. McMillan *et al.*, *A Measurement of Eta and Other Fission Parameters for U^{233}, Pu^{239}, and Pu^{241} Relative to U^{235} at Sub-Cadmium Neutron Energies*, KAPL-1464 (Dec. 15, 1955).

[4] V. I. Kalashnikova *et al.*, *Conference of the Academy of Sciences of the USSR on the Peaceful Uses of Atomic Energy* (English Translation), USAEC Report PT-I, p 123 (1956).

[5] J. E. Sanders, *J. Nuclear Energy* 2, 247 (1956).

[6] D. J. Hughes and J. A. Harvey, *Heavy Element Cross Sections*, addendum to *Neutron Cross Sections*, BNL-325 (July 1955).

[7] Analytical Chemistry Division; the isotopes had been separated by the Electronuclear Research Division.

[8] Isotopes Standards Section, Uranium Measurements Group.

TABLE 19.1. ISOTOPIC ANALYSES OF Pu^{241} AND U^{235} SAMPLES

Isotope	Amount in Foil (wt %)
Pu^{241} Sample	
Pu^{241}	49.20
Pu^{240}	25.27
Pu^{239}	24.76
Pu^{242}	0.77
U^{235} Sample	
U^{235}	99.8
U^{233}	<0.2
U^{234}	Trace
U^{238}	Trace

of a Lucite-ZnS mixture. Fast neutrons collide with protons in the Lucite, and the recoiling protons in the ZnS produce scintillations that are detected by the photomultiplier. These buttons are described in detail in Chap. 49.)

The pulses of the fission chamber were amplified through a preamplifier and an A-1 amplifier. The bias on the pulse-height selector of the fission chamber was set so as to discriminate against individual alpha particles. The proper pulse-height-selector setting was found on the plateau of a curve of counting rate plotted as a function of the pulse-height-selector setting. The pulses from the pulse-height selector were recorded with a scaler and a register.

The pulses from the two photomultipliers were amplified through a pair of preamplifiers and an A-1 amplifier. An attempt was made to discriminate against pulses caused in the Hornyak buttons by gamma rays. (These pulses are much smaller than most pulses due to fast neutrons.) This was done by plotting the logarithm of the number of counts, with a strong Cs^{137} gamma-ray source close to the detector, as a function of the pulse-height setting. This plot is a very steep, straight line. The pulse-height-selector setting was so chosen that the gamma-ray counting rate due to the Cs^{137} source was smaller by a factor of about 1000 than the normal counting rate of the Hornyak buttons when the beam of neutrons was on. However, the possibility that gamma-ray pileup or that gamma rays of very high energies might have been detected was not excluded. The pulses from the pulse-height selector of the detector amplifiers were recorded by a scaler and a register.

The pulses from the pulse-height selectors of the fission chamber and detector amplifiers were also sent through a coincidence circuit with about a 1-μsec resolution time. A variable delay was inserted between the neutron detector and the coincidence circuit. The coincidence rate vs delay time was plotted. The delay corresponding to the maximum coincidence rate was chosen to measure the number of neutrons in coincidence with fission. When the pulses from the Hornyak buttons were delayed more than about 1.5 μsec, the coincidence rate became independent of additional delay. This constant rate (lower by about a factor of 20 than the rate at the peak of the coincidence rate vs delay curve) was treated as a constant background of accidental coincidences and subtracted from the number of measured coincidences. Its magnitude was slightly larger than the accidental coincidence rate calculated from the presumed resolving time of the coincidence circuit.

Most of the difficulties associated with this experiment were related to variations in the sensitivity of the Hornyak buttons. The sensitivity changes rapidly with the high voltage on the photomultiplier and with the ambient temperature. Furthermore, since the counting rate at the pulse-height selector of the amplifier changes rapidly with the pulse-height setting, the counting rate varies with changes in the amplification. The high-voltage supply, a very stable Hamner supply, was monitored during each run by balancing the voltage against a standard cell. The amplification of the amplifier and preamplifier was frequently checked with a pulse generator of standard amplitude, and the runs were made at night when the temperature and the line voltage in the reactor building were more constant. Nevertheless, successive determinations of the number of fast neutrons per fission varied by about 2%, whereas the statistical variation should not have exceeded 0.1%. Those variations were attributed to temperature variations in the Hornyak buttons, and an attempt is now being made to correct this for future measurements by enclosing the detectors in a temperature-controlled box.

Results of the Experiment

The ratio of the number of neutrons per fission in the plutonium foils (n^{Pu}) to the number of neutrons per fission in the uranium foils (n^{U}) was 1.28 ± 0.01. For the interpretation of this result, it was assumed that fission neutrons from Pu^{239}, Pu^{241}, and U^{235} have the same probability of being recorded by the Hornyak button. This assumption is justified, since the efficiency of the Hornyak button has been shown to change very little with neutron energy (see Chap. 49), and the fission spectra of these three isotopes are almost identical.[9] Only the prompt neutrons were detected, since delayed neutrons are eliminated by the coincidence technique. However, the delayed neutrons would be such a small fraction of the total number of neutrons emitted (0.75% for U^{235}) that they could not appreciably change the ratio. An attempt was made to subtract any effect associated with fission produced by epicadmium neutrons by measuring the cadmium ratios for n^{Pu} and n^{U}. But when a cadmium foil is placed in the beam, n^{Pu} and n^{U} are not significantly above background. Thus the ratio n^{Pu}/n^{U} refers to fission caused by subcadmium neutrons. It is usually assumed that over this energy region ν is independent of the energy of the neutron causing the fission.

The ratio $\bar{\nu}^{41}/\bar{\nu}^{25}$ is obtained from the following relation:

$$\frac{\bar{\nu}^{41}}{\bar{\nu}^{25}} = \frac{n^{Pu}}{n^{U}} + \left(\frac{n^{Pu}}{n^{U}} - \frac{\bar{\nu}^{49}}{\bar{\nu}^{25}}\right)\frac{N_a^{49}}{N_a^{41}}\,\frac{\bar{\sigma}^{49}}{\bar{\sigma}^{41}} ,$$

where

$\bar{\nu}^{25}$ = number of neutrons released per thermal fission of U^{235}

= 2.46 ± 0.03 (ref 6),

$\bar{\nu}^{49}$ = number of neutrons released per thermal fission of Pu^{239},

N_a^{49}, N_a^{41} = number of atoms of Pu^{239} and Pu^{241} in the samples,

$\bar{\sigma}^{49}$, $\bar{\sigma}^{41}$ = fission cross sections of Pu^{239} and Pu^{241} averaged over the spectrum of subcadmium neutrons from hole 57 of the ORNL Graphite Reactor.

[9] N. Nereson, *Phys. Rev.* 88, 823 (1952).

The contributions of Pu^{240} and Pu^{242} were considered to be negligible, since their thermal-neutron fission cross sections are very small.

It was felt that the most accurate determination of the ratio $\bar{\nu}^{49}/\bar{\nu}^{25}$ was determined by McMillan *et al.*,[3] who reported a value of 1.251 ± 2.1%.

The ratio N_a^{49}/N_a^{41} was determined, by the isotopic composition of the samples, to be 0.519. A correction for the decay of Pu^{241} was included.

Little is known about the spectrum of neutrons from hole 57, and it is difficult to obtain the exact value of $\bar{\sigma}^{49}/\bar{\sigma}^{41}$. However, since the ratio $\bar{\nu}^{41}/\bar{\nu}^{25}$ is very insensitive to the ratio $\bar{\sigma}^{49}/\bar{\sigma}^{41}$ a value reported by McMillan *et al.*[3] for a subcadmium neutron beam probably quite different from that of hole 57 was used. The value is 1.515/1.666 = 0.909.

The results for this experiment then are:

$$\frac{\bar{\nu}^{41}}{\bar{\nu}^{25}} = 1.29 \pm 0.05 ,$$

$$\bar{\nu}^{41} = 3.17 \pm 0.12 .$$

The error was calculated by assigning a 2% error to the determination of n^{Pu}/n^{U}. This is much larger than the error expected on the basis of statistics (0.1%), but it corresponds to the discrepancy between successive measurements of the ratio. The importance of the errors associated with the poor knowledge of $\bar{\sigma}^{49}/\bar{\sigma}^{41}$ and $\bar{\nu}^{49}/\bar{\nu}^{25}$ could be greatly reduced by working with samples with a smaller N_a^{49}/N_a^{41} ratio. The experiment will be repeated with such foils as soon as samples of better isotopic enrichment are available.

Comparison of Results with Other Values

All the reported values of ν^{41} are summarized in Table 19.2. The value of ν^{41} = 2.91 ± 0.10 reported by the group[1] at Argonne was the result of measured ratios of $\nu^{41}\sigma^{41}/\nu^{25}\sigma^{25}$, $\nu^{41}\sigma^{41}/\nu^{23}\sigma^{23}$ (23 is the symbol for U^{233}), and $\nu^{41}\sigma^{41}/\nu^{49}\sigma^{49}$. The value of σ^{41} used in these ratios was their measured value of 1100 ± 30 barns (at 2200 m/sec), which was obtained by assuming that σ^{41} followed the $1/v$ law. (No corrections were made for self-absorption in their sample and for the fact that their spectrum was not Maxwellian.) This value of σ^{41} is higher than the one reported in the BNL-325 addendum[6] (σ^{41} = 950 barns). If the later value of the BNL-325 addendum is used, the value of ν^{41} becomes 3.37.

TABLE 19.2. VALUES OF ν^{41}/ν^{25} AND ν^{41} REPORTED BY VARIOUS INVESTIGATORS

Investigator	ν^{41}/ν^{25}	ν^{41}
deSaussure and Silver	1.29 ± 0.05	3.17 ± 0.12
Pratt and Muckenthaler		3.30 ± 0.23
Jaffey *et al.*		2.91 ± 0.10
		(3.27)*
Kalashnikova *et al.*	1.24 ± 0.01	
McMillan *et al.*	1.305 ± 3.1%	
Sanders	1.192 ± 0.011	

*Corrected for later value of σ^{41} published in BNL-325 addendum.

By a method very similar to the one used in this chapter (coincidence method) a USSR group[4] has measured a value of $\nu^{41}/\nu^{25} = 1.24 \pm 0.01$, which agrees (within the experimental error quoted) with the value obtained here.

The group[3] at KAPL determined (from careful reactivity and activation measurements) a value of $\nu^{41}/\nu^{25} = 1.305 \pm 3.1\%$, which is also in good agreement with this measurement.

Sanders[5] reported a value $\nu^{41}/\nu^{25} = 1.192 \pm 0.011$ determined by the coincidence method. This value is lower than all the other measurements, and the discrepancy remains unexplained.

It is felt that the experiment at ORNL is precise in two respects. First, the coincidence method, by counting the relative number of neutrons emitted in coincidence with fission, does not require the exact knowledge of the fission cross section and the energy spectrum of the thermal neutrons causing the fission. Second, the Hornyak button, because its records fast neutrons directly, allows for the use of very rapid coincidence circuits (with resolution time of the order of microseconds). The British and Russian groups that have used the coincidence technique have used thermal-neutron detectors, and, because they had to wait for the fission neutrons to thermalize, they had to use much longer resolution times (of the order of milliseconds). This greatly increased their background counts.

20. FISSION NEUTRON SPECTRUM OF U^{233}

K. M. Henry M. P. Haydon

In order to establish, if possible, the validity of the fission neutron spectrum of U^{233} as determined by measurements with the proton-recoil neutron spectrometer,[1] the spectrum has also been measured with nuclear photographic plates. The experimental conditions for this measurement were similar to those for the earlier measurement. The camera[2,3] in which the plates were mounted was placed in the same spectrometer box. The same U^{233} source (1.62 g of U^{233} plated on ten 3-in.-dia aluminum disks) was placed on the end of a flared conical collimator, the opposite end of which was attached to the spectrometer box. The source end of the collimator was positioned close to the BSF thermal column (the two were actually separated by a small air wedge), and the axis of the collimator-box assembly was tilted 17 deg with respect to a perpendicular to the thermal column. The thermal column itself consisted of 5 in. of lead and 3 ft of carbon. A schematic of the experimental arrangement is shown in Fig. 20.1.

Two measurements were made. In the first, both the radiation from the U^{233} source and the background radiation from the thermal column were detected. In the second test only the background was measured. During each test six 3-in.-long Ilford C2 nuclear photographic plates were exposed in the camera for a 25-min period while the BSR was operated at a power of 20 kw. The plates were mounted radially on the side of the cylindrical camera at a 10-deg angle to the beam

[1] K. M. Henry and M. P. Haydon, *The Fission Neutron Spectrum of U^{233}*, ORNL CF-55-4-22 (April 22, 1955).

[2] J. L. Meem and E. B. Johnson, *A Nuclear Plate Camera for Fast Neutron Spectroscopy at the Bulk Shielding Facility*, AECD-3266 (Sept. 14, 1951).

[3] M. P. Haydon, E. B. Johnson, and J. L. Meem, *Measurement of the Fast Neutron Spectrum of the Bulk Shielding Reactor Using Nuclear Plates*, ORNL CF-53-8-146 (Aug. 31, 1953).

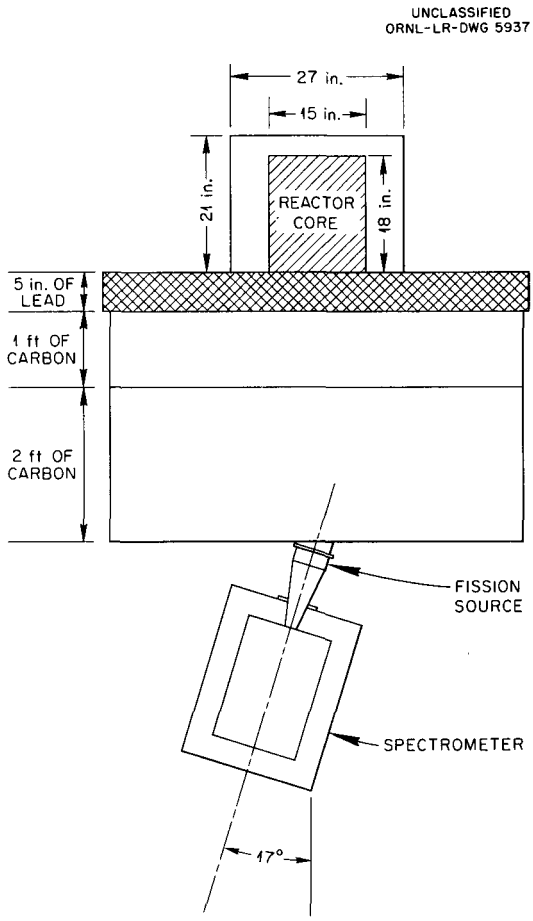

Fig. 20.1. Experimental Arrangement for the BSF Measurement of the Fission Neutron Spectrum of U^{233}.

axis. Three plates received protons from a 5-mil (12.95 mg/cm^2) polystyrene radiator which was placed in the collimated beam; the three remaining plates were shielded from the radiator protons by a platinum absorber so that they only recorded extraneous events such as water scatter, which would constitute the camera background.

After normal photographic processing, the 12 plates were scanned, every 0.2 mm, with a Lietz Ortholux research microscope, using oil immersion and 1350X magnification, over the central 60 mm of their 3-in. length in swaths 75 μ wide. The track densities on the plates varied from 120 tracks/cm^2 in the first test to 29 tracks/cm^2 in the second test.

As the proton tracks were discriminated, evaluated, and measured, they were tallied into groups corresponding in range to predetermined neutron energy intervals as outlined by Rosen[4] and also by Allred and Armstrong.[5] These calculations include the correction for the radiator thickness. The proton-range values were read from a graph plotted from the experimental results of Rotblat[6] as tabulated in LA-1510.[5]

The number of neutrons in each energy interval corresponding to the number of protons divided by the *n-p* cross section at that energy is plotted in Fig. 20.2. The statistical error formula is the same as that used earlier.[3] The energy error was also computed in the same manner as before,

[4] L. Rosen, *Nucleonics* 11(7), 32, esp 38 (1953).

[5] J. C. Allred and A. H. Armstrong, *Laboratory Handbook of Nuclear Microscopy*, LA-1510 (Feb. 1953).

[6] J. Rotblat, *Nature* 167, 550 (1951).

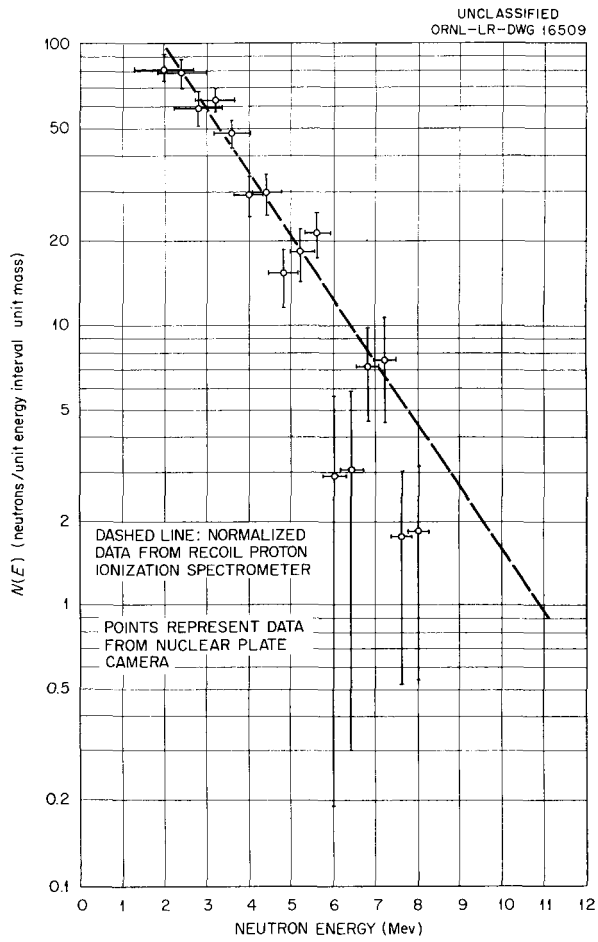

Fig. 20.2. Fission Neutron Spectrum of U^{233} (0.4-Mev Intervals).

although the actual radiator correction was revised in accordance with the work of Evans[7] at Los Alamos.

The large statistical errors were due to the presence of a very large background. The major reason for the unusually large background was probably the small size of the U^{233} source, which required a large incident flux to produce a usable fission rate.

[7]J. E. Evans, *Fast Neutron Spectra from the Water Boiler*, LA-1395 (March 1951).

The dashed curve in Fig. 20.2 shows the shape of the spectrum previously obtained with the proton-recoil spectrometer.[1] The two curves are normalized in the low-energy region. The shapes of the spectra agree well within the combined limits of error. The statistical errors for the spectrometer data are about one-half as large as those obtained with the plates.

Another experiment is planned in which the proton-recoil spectrometer will be used to examine a much larger ($\sim$200 g) U^{233} source.

21. FAST-NEUTRON SPECTRUM OF A 117-curie Po-Be SOURCE

K. M. Henry

Since Po-Be sources are used to calibrate fast-neutron dosimeters, the fast-neutron spectrum of such sources should be known. The spectra of several sources have previously been measured with the BSF proton-recoil spectrometer.[1,2] Recently, an additional measurement was made with the proton-recoil spectrometer for a source (PN-105)[3] that had a large source intensity which permitted better statistical accuracy than was previously possible with reasonable counting times. This source also had a larger physical size and different container material (steel instead of nickel), which it was felt might influence the spectrum.

The source was constructed by distilling polonium into beryllium powder.[3,4] The material was encased in a cold-rolled-steel jacket which had an inside diameter of 0.84 in. and an inside length of 0.84 in. The outside diameter was 1.03 in. and the outside length was 1.03 in. The casing was plated with a 0.02-in.-thick nickel covering to form a right circular cylinder 1.05 in. in diameter by 1.05 in. high. The source contained 117 curies of polonium and 7.2 g of beryllium, which gave a specified emission of 2.99×10^8 neutrons/sec for a neutron efficiency of 88.9%.

The neutron intensity of the source was such that for a dose rate of 35 neutrons$\cdot$cm$^{-2}\cdot$sec^{-1} (limitation set by Health Physics Division) the source would have had to be positioned in the center of a circle 27 ft in diameter. Since an area this size could not be conveniently obtained, the source and the spectrometer were positioned within a cave (20- by 30-in. base, 25 in. high, 20-in.-thick walls) of lithiated paraffin as a shield. No modifications were made in either the equipment or operating technique of the proton-recoil neutron spectrometer[3] for this run.

No evidence of temperature instability was observed by the spectrometer, although the temperature outside the neutron shield varied as much as 20° F. The resulting neutron spectrum (Fig. 21.1) agrees within a statistical deviation with the spectra previously obtained with this spectrometer.[2] It is believed probable that the lowest energy values are influenced by neutron scatter within the cave.

[1]R. G. Cochran and K. M. Henry, *A Proton Recoil Type Fast-Neutron Spectrometer*, ORNL-1479 (April 20, 1953).

[2]R. G. Cochran and K. M. Henry, *Rev. Sci. Instr.* **26**, 757 (1955).

[3]PN-105 Source Fabrication Records (Sept. 2, 1955), J. Gillette.

[4]*Isotopics* 3(2), USAEC, Superintendent of Documents, Washington, D.C., April 1953.

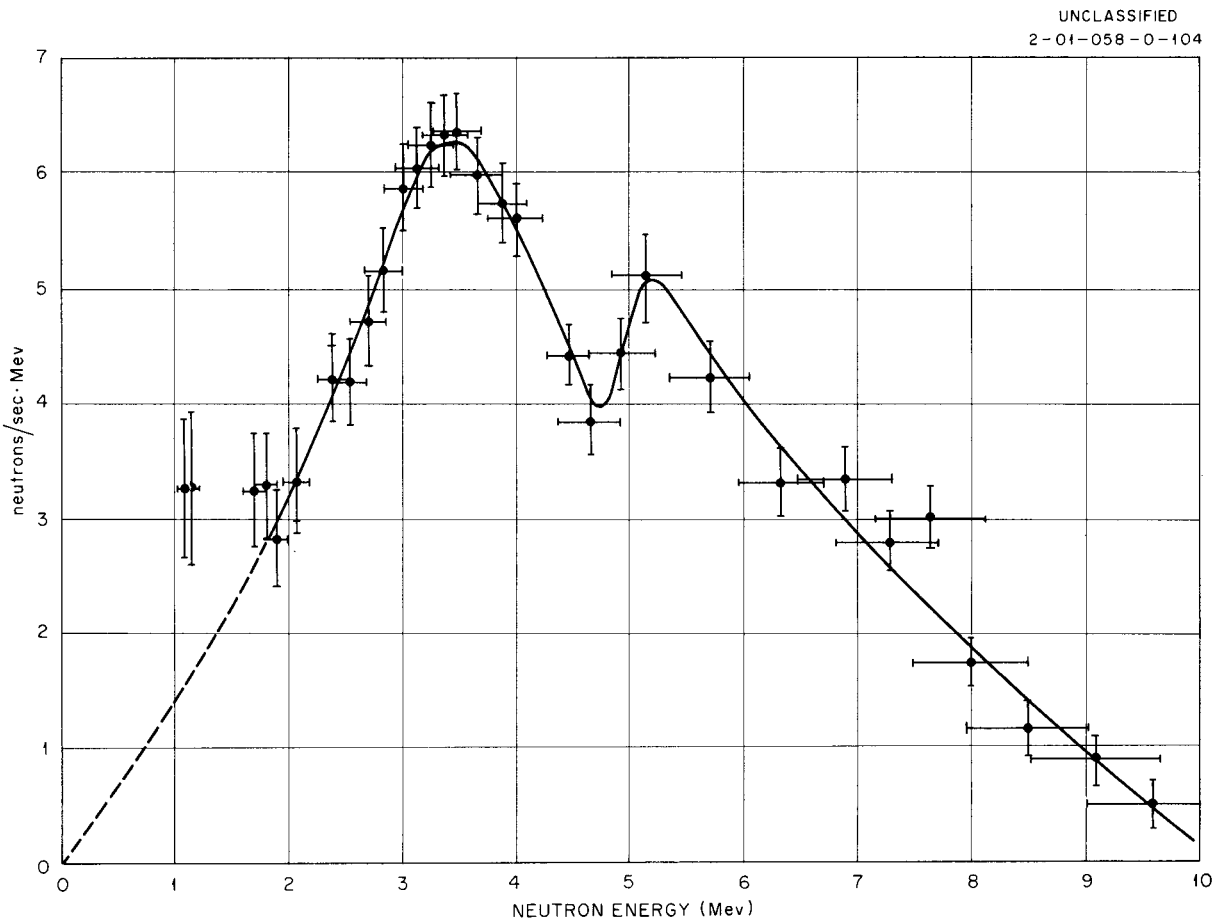

Fig. 21.1. Spectrum of Fast Neutrons from a 117-curie Po-Be Source.

Part IV

REACTOR THEORY

22. REFLECTOR SAVINGS METHOD FOR ESTIMATING FLUXES IN A FULLY REFLECTED REACTOR

M. L. Nelson

Group equations for a fully reflected reactor have not been satisfactorily solved except in one dimension. Such one-dimensional problems may be readily solved by analytical or numerical techniques. In particular, the infinite slab and infinite cylinder have been coded for the Oracle in the three-group, three-region (3G3R) program. These one-dimensional solutions may now be used to estimate the solutions for the case of a fully reflected cylinder or parallelepiped.

For a cylindrical reactor with a core of radius r and half-height h, a lateral reflector of thickness R, and end reflectors of thickness H, an estimate of the multiplication constant k is determined by the repetitive process described below.

First, the problem of a reactor with a core of radius r and an arbitrarily chosen half-height h_0, a lateral reflector of thickness R, and *bare ends* is considered. This reactor has a multiplication constant k_0' which can be computed, for example, by the 3G3R code. Next, the radius r_0 of a completely bare reactor with a half-height h_0 and a multiplication constant k_0' can be determined. The difference $(r_0 - r)$ is the reflector savings of the lateral reflector for the cylinder with bare ends, half-height h_0, and a multiplication constant k_0'.

The next step is to consider a laterally bare reactor with end reflectors of thickness H and a core of radius r_0 and half-height h. This reactor has a multiplication constant k_0'' which can be determined by the 3G3R code. The half-height h_1 of a completely bare reactor with a radius r_0 and a multiplication constant k_0'' can then be determined. The difference $(h_1 - h)$ is the reflector savings of the end reflector for the laterally bare cylinder.

By replacing h_0 with h_1, another multiplication constant, k_1', and another radius, r_1, can be determined. Replacing r_0 with r_1 yields k_1'' and h_2. This process is repeated, and the sequences thus generated seem to converge, to limits independent of the initial choice of h_0, and with

$$\lim k_n'' = \lim k_n' .$$

Calling this common limit k^* and defining

$$r^* = \lim r_n , \quad h^* = \lim h_n ,$$

gives the results listed in Table 22.1.

TABLE 22.1. PARAMETERS OF CYLINDRICAL REACTORS

Core Radius	Core Half-Height	Reflector Thickness		Multiplication Constant
		Lateral	End	
r	h	R	H	k
r^*	h^*	0	0	k^*
r	h^*	R	0	k^*
r^*	h	0	H	k^*

It is thought that k^* is a reasonably good estimate of k and that the product of the fluxes in the two reactors listed last is an estimate of the flux of the fully reflected reactor. The case of a fully reflected parallelepiped is handled in the obviously analogous manner.

An Oracle program which applies this method (incorporating the 3G3R) has been prepared and proved. It will be used to estimate multiplication constants and fluxes for various loadings of the Oak Ridge Research Reactor (ORR). In fact, the method has been applied to the ORR, using the Oracle with the 3G3R and performing the iterations by hand.

The quality of the estimates yielded by the process described, their alleged uniqueness, just which reactor problems they solve, and their relation to the case of the fully reflected reactor constitute an interesting and useful investigation.

23. ESTIMATION OF RESONANCE INTEGRALS

L. Dresner

Many new experimental data on neutron resonances have recently become available.[1] Regularities have been observed in certain average resonance parameters, namely, $\overline{\Gamma_n^0}/D^*$, the ratio of the average reduced neutron width to the average level spacing between resonances of the same spin and parity, and $\overline{\Gamma_\gamma}/D^*$, the ratio of the average radiative width to the average level spacing between resonances of the same spin and parity. These regularities should make possible an interpolation of these parameters to nuclei not studied experimentally. Knowledge of the average resonance parameters makes possible the calculation of the corresponding resonance integral, a quantity which is important in calculating critical masses, the effect of poisons on reactors, the resonance activation of reactor materials, etc. Hence, it should be possible to estimate resonance integrals for nuclei for which little or no resonance data are available; this conjecture is investigated below in some detail.

For nuclei in which the resonance integral is due to the cumulative contributions of many nearly equal resonances, it is given by

$$(1)\quad \int \sigma_a \frac{dE}{E} = \frac{1.3 \times 10^6}{E_1} \left(\frac{2\pi\overline{\Gamma_\gamma}}{D^*}\right) \frac{\beta - \log(1+\beta)}{\beta^2} \text{ barns},$$

where

σ_a = neutron radiative capture cross section,

$\beta = \overline{\Gamma_\gamma}/\overline{\Gamma_n^0}\ \sqrt{E_1}$,

$\overline{\Gamma_\gamma}$ = average radiative neutron width,

$\overline{\Gamma_n^0}$ = average reduced neutron width,

E = neutron energy,

E_1 = energy of the first resonance in electron volts.

For heavy (A greater than ~100) nonmagic nuclei, Eq. 1 is virtually independent of $\overline{\Gamma_\gamma}/D^*$.

For high energies the radiative capture cross section can be written[2] as

$$(2)\quad \sigma_a = \pi(R + \lambda\!\!\!^-)^2 \frac{2\pi\overline{\Gamma_\gamma}}{D^*},$$

where R is the nuclear radius and $\lambda\!\!\!^-$ is the neutron wavelength divided by 2π. For several nuclei, namely, In^{115}, Sb, I^{127}, Au^{197}, and Th^{232}, the radiative capture cross section is known as a function of energy[3] and can be used to determine the energy dependence of $2\pi\overline{\Gamma_\gamma}/D^*$. Figure 23.1 is a plot of $2\pi\overline{\Gamma_\gamma}/D^*$ vs neutron energy for these nuclei. It is roughly constant with energy in the energy range in which Eq. 2 is valid, confirming the theoretical expectation[2] that Γ_γ varies as D^*. This fact justifies treating $2\pi\overline{\Gamma_\gamma}/D^*$ as a constant in the integration; $2\pi\overline{\Gamma_\gamma}/D^*$ can also be found as a function of mass number by using measured values of the radiative capture cross section for fission neutrons (effective neutron energy = 1 Mev).[4] Figure 23.2 is a plot of $2\pi\overline{\Gamma_\gamma}/D^*$ vs A calculated in this way, and several points calculated from direct measurements of resonance parameters[1] are included. The good agreement between the resonance values of $2\pi\overline{\Gamma_\gamma}/D^*$ and the high-energy value again indicates the energy independence of $2\pi\overline{\Gamma_\gamma}/D^*$. It can be seen that $2\pi\overline{\Gamma_\gamma}/D^*$ rises until A is ~100 and remains roughly constant for 100 less than ~A less than ~200, except for sharp drops in the vicinity of closed-shell nuclei.

According to the continuum theory of nuclear reactions,[2] $2\pi\overline{\Gamma_n^0}/D^* = 8.8 \times 10^{-4}\ ev^{-1/2}$. According to Feshback *et al.*,[5] $2\pi\overline{\Gamma_n^0}/D^*$ should have peaks at A = 11, 55, and 155 at values several times the continuum-theory value and valleys between the peaks where it falls to only a fraction of the continuum-theory value. Carter *et al.*[6] compared these theories with experimental values and found that $2\pi\overline{\Gamma_n^0}/D^*$ does peak at $A \sim 155$ but that the experimental peak is lower than the theoretical peak and that the experimental wings are higher than the theoretical wings.

---

[1] F. G. P. Seidl *et al.*, *Phys. Rev.* 95, 476 (1954).

[2] J. M. Blatt and V. F. Weisskopf, *Theoretical Nuclear Physics*, Wiley, New York, 1952.

[3] *Neutron Cross Sections*, AECU-2040 (May 15, 1952).

[4] D. J. Hughes, *Pile Neutron Research*, Addison-Wesley, Cambridge, Mass. (1953).

[5] H. Feshbach, C. E. Porter, and V. F. Weisskopf, *Phys. Rev.* 96, 448 (1954).

[6] R. S. Carter *et al.*, *Phys. Rev.* 96, 113 (1954).

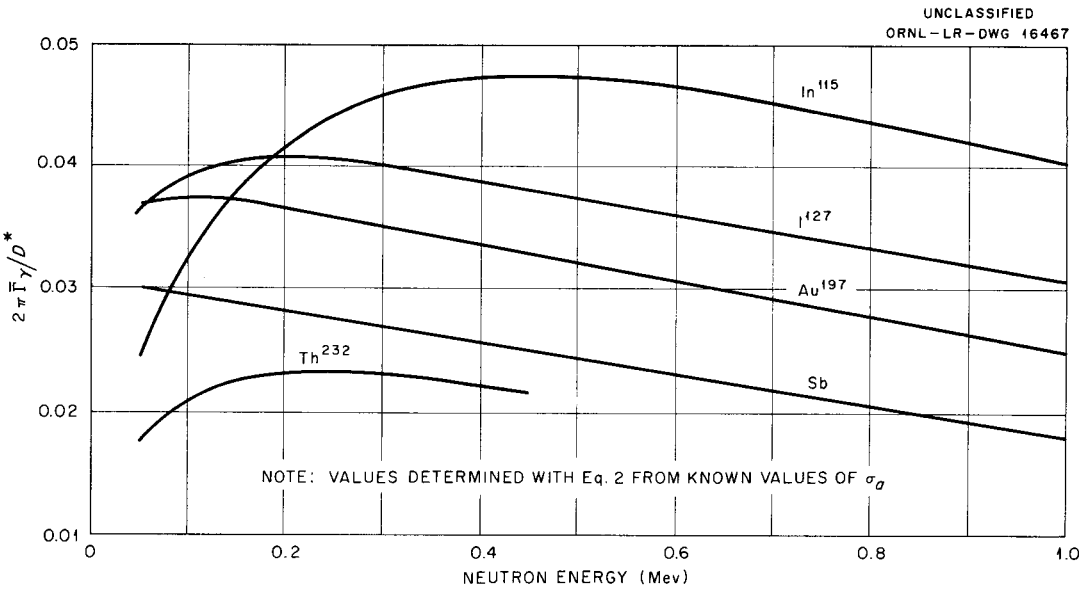

Fig. 23.1. $2\pi\overline{\Gamma}_\gamma/D^*$ as a Function of Neutron Energy for Several Nuclei.

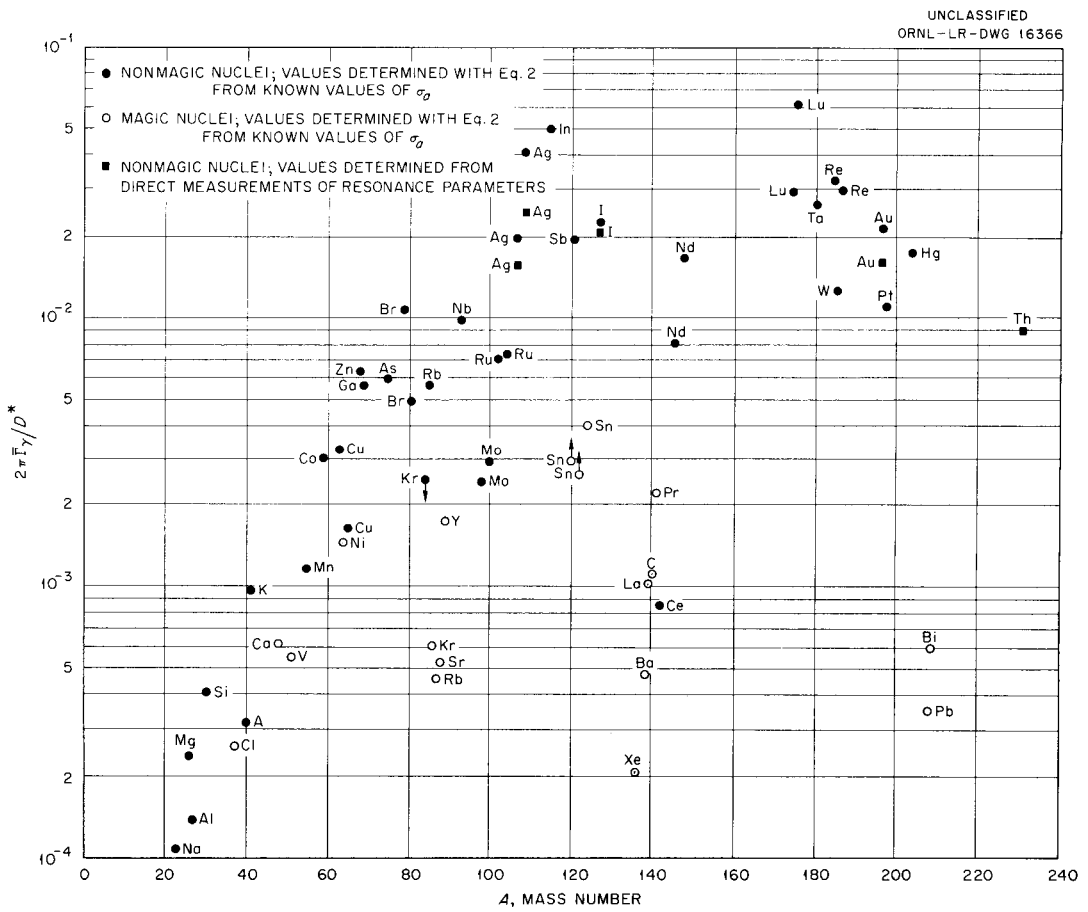

Fig. 23.2. $2\pi\overline{\Gamma}_\gamma/D^*$ as a Function of Mass Number.

The condition for validity of the statistical theory is that the resonance integral be due to the cumulative effect of many resonances. If, as is the case for Au^{197}, the resonance integral is due mainly to one large resonance, the statistical theory fails. If this one resonance occurs at least several widths from thermal energy, as is often the case, the resonance integral can be related to the thermal radiative capture cross section. It is easily shown that the ratio of the resonance integral to the radiative capture cross section at energy kT is given by

$$(3) \qquad \frac{\int \sigma_a \, dE/E}{\sigma_a(kT)} = \frac{2\pi(kT)^{1/2} E_0^{1/2}}{\Gamma} ,$$

where Γ is the total width of the resonance and E_0 the resonance energy.

In Table 23.1 a comparison is made between the value of the resonance integral derived from Eq. 1 and the experimentally known value for nuclei for which $2\pi\overline{\Gamma_\gamma}/D^*$, $2\pi\overline{\Gamma_n^0}/D^*$, and E_1 are experimentally known. Agreement is within 50% in all cases, indicating that the statistical fluctuations, together with experimental uncertainties, are no more than ~50%.

When the resonance integral is due to a single large resonance at least several widths from thermal energies, Eq. 3 should be an extremely good approximation. In Table 23.2 resonance integrals estimated from Eq. 3 are compared with experimentally known resonance integrals for nuclei for for which Γ, E_0, and $\sigma_a(kT)$ are experimentally known and in which the resonance integral is due to one large resonance. Agreement should have been very good; the fact that it is not is taken to

TABLE 23.1. COMPARISON BETWEEN RESONANCE INTEGRALS ESTIMATED BY THE STATISTICAL METHOD AND EXPERIMENTAL RESONANCE INTEGRALS FOR SEVERAL NUCLEI FOR WHICH $2\pi\overline{\Gamma_\gamma}/D^*$, $2\pi\overline{\Gamma_n^0}/D^*$, AND E_1 ARE KNOWN

Nucleus	$\frac{2\pi\overline{\Gamma_\gamma}}{D^*} \times 10^3$	$\frac{2\pi\overline{\Gamma_n^0}}{D^*} \times 10^3$ (ev$^{-1/2}$)	E_1 (ev)	Resonance Integrals (barns)	
				Experimental	Estimated
$_{47}Ag^{107}$	20[a]	0.31[b]	16.6[c]	98.3[d]	82
$_{53}I^{127}$	23[a]	0.75[b]	20.5[c]	119[d]	150
$_{73}Ta^{181}$	27[a]	0.63[b]	4.29[e]	517[d]	335[f]
$_{75}Re^{187}$	31[a]	0.57[b]	4.40[g]	275[d]	310
$_{90}Th^{232}$	9.4[c]	0.50[b]	22.1[c]	67.3[b]	83
$_{92}U^{238}$	9.7[i]	1.0[i]	6.6[i]	240[d]	290[j]

[a] D. J. Hughes, *Pile Neutron Research*, p 110–111, Addison-Wesley, Cambridge, Mass., 1953.

[b] R. S. Carter *et al.*, *Phys. Rev.* **96**, 113 (1954).

[c] F. G. P. Seidl *et al.*, *Phys. Rev.* **95**, 746 (1954).

[d] D. J. Hughes, *op. cit.*, p 139.

[e] R. Christensen, *Phys. Rev.* **92**, 702 (1953).

[f] V. E. Pilcher, D. J. Hughes, and J. A. Harvey, *Bull. Am. Phys. Soc.* **30**, 11 (1955), report $\overline{\Gamma_n^0}/D^* = 1.8 \times 10^{-4}$ ev$^{-1/2}$; the corresponding estimated resonance integral is 555 barns.

[g] E. Melkonian, W. W. Havens, and L. J. Rainwater, *Phys. Rev.* **92**, 702 (1953).

[h] R. Macklin and H. Pomerance, *Proceedings of the International Conference on the Peaceful Uses of Atomic Energy*, vol 5, p 96, United Nations, New York, 1956.

[i] L. M. Bollinger, *et al.*, *Bull. Am. Phys. Soc.* **29**(7), 8 (1954).

[j] R. Macklin and H. Pomerance, *op. cit.*, report 278 barns for the resonance integral of U^{238}; J. A. Harvey *et al.*, (*Phys. Rev.*, to be published) report $\overline{\Gamma_n^0}/D^* = 1.2 \times 10^{-4}$ ev$^{-1/2}$ for U^{238}, giving an estimated resonance integral of 244 barns.

TABLE 23.2. COMPARISON BETWEEN RESONANCE INTEGRALS ESTIMATED FROM Eq. 3 AND EXPERIMENTAL RESONANCE INTEGRALS FOR SEVERAL NUCLEI FOR WHICH Γ_γ, E_0, AND $\sigma_a(kT)$ ARE EXPERIMENTALLY KNOWN AND IN WHICH THE RESONANCE INTEGRAL IS DUE TO ONE LARGE RESONANCE

Nucleus	$\Gamma_\gamma \cong \Gamma$ (mv)	E_0 (ev)	$\sigma_a(kT)$ (barns)	Resonance Integrals (barns)	
				Experimental	Estimated
$_{45}Rh^{103}$	155[a]	1.26[a]	150[b]	589[c]	1080
$_{47}Ag^{109}$	159[a]	5.21[a]	84[b]	1213[d]	1206
$_{49}In^{115}$	100[a]	1.46[a]	1.45[b]	2580[c]	1752
$_{72}Hf$	43[a]	1.08[a]	115[b]	1400[c]	2778[e]
$_{75}Re^{185}$	90[a]	2.18[a]	100[b]	1061[c]	1630[f]
$_{77}In^{191}$	100[g]	0.64[g]	960[b]	3270[c]	7680[b]
$_{77}Ir^{193}$	150[g]	1.27[g]	130[b]	1213[c]	976[b]
$_{79}Au^{197}$	150[a]	4.91[a]	94[b]	1300[c]	1390

[a]D. J. Hughes and J. A. Harvey, *Nature* 173, 942 (1954).

[b]D. J. Hughes, *Pile Neutron Research*, p 356, Addison-Wesley, Cambridge, Mass., 1953.

[c]*Ibid.*, p 139.

[d]C. O. Muelhause, S. P. Harris, and G. E. Thomas, *Phys. Rev.* 79, 11 (1950).

[e]D. J. Hughes and J. A. Harvey, *Nature* 173, 942 (1954), identify the 1.08 state as belonging to Hf^{177}; B. T. Feld, *Table of Neutron Resonance Constants*, NYO-3078 (Aug. 28, 1953), reports that Γ_γ = 120 mv for this level, which would lead to an estimated resonance integral of 995 barns.

[f]G. Igo, *Bull. Am. Phys. Soc.* 30, 10 (1955), reports 49 mv for this level; the corresponding resonance integral is 3000 barns.

[g]B. T. Feld, *op. cit.*

[h]According to Feld, *op. cit.*, the various data reported for these nuclei do not agree particularly well; H. H. Landon, *Bull. Am. Phys. Soc.* 30, 10 (1955), confirms the isotropic assignments of these levels and reports $\Gamma_\gamma = 75$ and 86 mv, respectively, for them; the corresponding estimated resonance integrals are 10,200 and 1700 barns.

indicate rather sizable errors in at least some of the experimental data.

In the region where A is greater than $\sim$100, $2\pi\overline{\Gamma_\gamma}/D^* \sim 0.02$ for nonmagic nuclei, and $2\pi\overline{\Gamma_n^0}/D^* \sim 5 \times 10^{-4}$ to 10×10^{-4} $ev^{-1/2}$. The value of the resonance integral as a function of E_1 calculated from Eq. 1 is plotted in Fig. 23.3 for several choices of the nuclear parameters. The close agreement of curve A with curve B and curve C with curve D indicates that the value of the resonance integral is an insensitive function of $2\pi\overline{\Gamma_\gamma}/D^*$ when $A \geqq 100$. Included in the plot, as individual points, are the experimental resonance integrals of Table 23.1 as a function of the experimental values of E_1. In general, the experimental values fall within a factor of 2 of the values predicted by curves A and B, with the exception of Hf^{180}, where the factor is 3.

The following conclusions concerning the estimation of resonance integrals can now be made:

1. Heavy nuclei, $A \geqq 100$, nonmagic, statistical theory: These resonance integrals are virtually independent of $2\pi\overline{\Gamma_\gamma}/D^*$. They can be estimated, when E_1 is known, within a factor of 2 from Fig. 23.3.

2. Heavy nuclei, $A \geqq 100$, nonmagic, one-level theory: For these nuclei, Eq. 3 is in principle a very good approximation. The accuracy of estimation of the resonance integral is given by the accuracy of estimation of Γ_γ.

3. Light nuclei, $A \leqq 50$. These nuclei are $1/v$ absorbers, as is well known. The resonance integral above cadmium resonance is half the thermal absorption cross section.

4. Intermediate nuclei, $50 \leqq A \leqq 100$, nonmagic, statistical theory: One serious disagreement of

estimate and experiment occurs among four nuclei tested.

5. Intermediate nuclei, $50 \leqq A \leqq 100$, nonmagic, one-level theory: In general, the total width Γ is not given, even approximately, by the radiative width. In the absence of some data for determining Γ, little can be said about the resonance integral. For three nuclei examined for which E_0, Γ, and $\sigma_a(kT)$ are known experimentally, agreement was poor in two cases. However, the experimental data on which the comparison is based are not too reliable.

6. Magic and near-magic nuclei: In general, magic nuclei behave as though they were lighter than they are. For example, Y^{89} and Pr^{141} exhibit $1/v$ absorption, while $Tl^{203,205}$ exhibits large level spacings characteristic of light nuclei. These nuclei can be treated by the methods outlined above, subject to the same restrictions as heretofore mentioned.

This paper has been published in detail in the open literature.[7]

[7] L. Dresner, *J. Nuc. Energy* 2, 118 (1955).

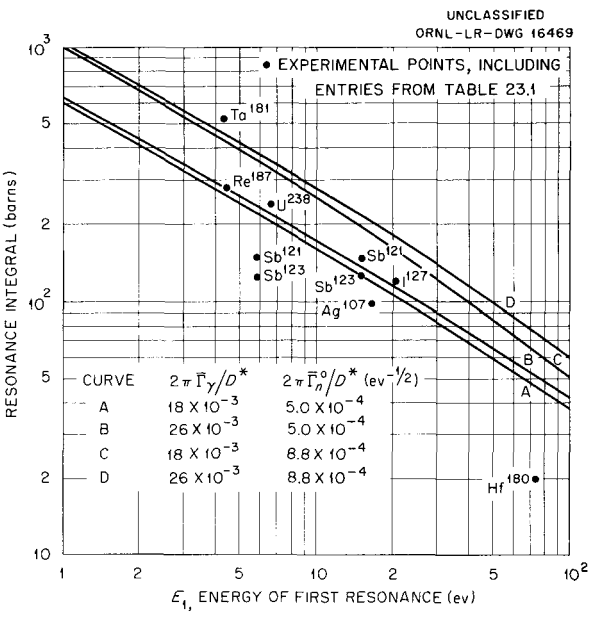

Fig. 23.3. Resonance Integral (According to the Statistical Theory) as a Function of Energy of First Resonance for Nonmagic Nuclei with $A \geqq 100$.

24. HOMOGENEOUS EFFECTIVE RESONANCE INTEGRALS OF U^{238} AND Th^{232}

L. Dresner

In a homogeneous medium the effective resonance integral of a resonance line can be written in terms of the resonance parameters as[1]

$$(1) \qquad \left(\int \sigma_a \frac{dE}{E}\right)_{\text{eff}} = \frac{\sigma_p \Gamma_\gamma}{E_0} J(\xi,\beta) \ ,$$

where

$$(2) \qquad J(\xi,\beta) = \int_0^\infty \frac{\psi(\xi,x)}{\psi(\xi,x) + \beta} dx \ .$$

The following definitions apply to Eqs. 1 and 2:

σ_a = resonance absorption cross section,

σ_p = energy-independent scattering cross section,

E = neutron energy,

E_0 = resonance energy,

Γ_γ = radiative width of the resonance,

ξ = ratio of the natural to the Doppler width,

β = ratio of the potential scattering cross section to the total cross section at resonance,

$\psi(\xi,x)$ = Doppler broadened line shape defined by

$$(3) \qquad \psi(\xi,x) = \frac{\xi}{2\sqrt{\pi}} \int_{-\infty}^{+\infty} \frac{\exp\left[-\xi^2/4\,(x-y)^2\right]}{1+y^2} dy \ ,$$

where x is the energy measured from exact resonance in units of the half-width. The function $J(\xi,\beta)$ has been tabulated by the Oracle, to an accuracy of ~1%, for

$$\xi = 0.1\ (0.1)\ 1.0 \quad \text{and} \quad \beta = 2^k \times 10^{-5} \ ,$$

where $k = 0, 1, \ldots, 31$. The results are given in Table 24.1 and also in Figs. 24.1 and 24.2. As can be shown from the properties of $\psi(\xi,x)$,

$$(4) \qquad J(\xi,\beta) \longrightarrow \frac{\pi/2}{[\beta(1+\beta)]^{1/2}} \text{ as } \begin{cases} \xi \longrightarrow \infty \ (T \longrightarrow 0°K) \\ \beta \longrightarrow 0 \ (\sigma_p \longrightarrow 0) \\ \beta \longrightarrow \infty \ (\sigma_p \longrightarrow \infty) \end{cases} .$$

This limit corresponds to a vanishing thermal correction to the effective resonance integral. The curve J vs β for $\xi = 1.0$ is virtually identical with $\pi/2[\beta(1+\beta)]^{-1/2}$, indicating that when the natural width exceeds the Doppler width the effective resonance integral has its unbroadened value.

The computed values of $J(\xi,\beta)$ were applied to the calculation of the effective resonance integral as a function of σ_p for $T = 0$ and 300°K for U^{238} and Th^{232}. For resonances for which the resonance parameters have been measured,[2] the effective resonance integral was calculated directly from Eq. 1. For the remaining, high-energy, unresolved resonances a statistical estimate was made. Finally, a $1/v$ contribution was included. The results[3] are shown in Table 24.2 and plotted in Fig. 24.3. In U^{238}, agreement of the $T = 300°K$ curve with experiment is seen to be excellent; in Th^{232} the agreement is seen to be good except for ThO_2. The experimental point for ThO_2, however, is probably incorrect.[3]

It is interesting to note the considerable contribution to the effective resonance integral that is made by the unresolved resonances at low σ_p (e.g., at σ_p less than ~200 barns). In this range their contribution is enhanced by the strong self-shielding of the low-energy, resolved resonances. In U^{238} at 300°K, for example, for low σ_p, the unresolved resonances contribute about one-third as much as the resolved resonances; in Th^{232} for

[1] E. P. Wigner *et al.*, *J. Appl. Phys.* **26**, 260 (1955).

[2] D. J. Hughes and J. A. Harvey, *Neutron Cross Sections*, BNL-325 (July 1, 1955).

[3] Experimental values of the effective resonance integrals are also plotted and are taken from the paper of R. Macklin and H. Pomerance, "Resonance Capture Integrals," *Proceedings of the International Conference on the Peaceful Uses of Atomic Energy*, vol 5, p 96, United Nations, New York, 1956.

TABLE 24.1. THE FUNCTION $J(\xi,\beta)$ FOR $\xi = 0.1\ (0.1)\ 1.0$ AND $\beta = 2^k \times 10^{-5}$

k	$J(\xi,\beta)$									
	$\xi = 0.1$	$\xi = 0.2$	$\xi = 0.3$	$\xi = 0.4$	$\xi = 0.5$	$\xi = 0.6$	$\xi = 0.7$	$\xi = 0.8$	$\xi = 0.9$	$\xi = 1.0$
0	4.979(2)*	4.970(2)	4.969(2)	4.968(2)	4.968(2)	4.968(2)	4.967(2)	4.967(2)	4.967(2)	4.967(2)
1	3.532	3.517	3.514	3.513	3.513	3.513	3.513	3.513	3.513	3.513
2	2.514	2.491	2.487	2.485	2.485	2.484	2.484	2.484	2.484	2.484
3	1.801	1.767	1.761	1.759	1.758	1.757	1.757	1.757	1.757	1.757
4	1.307	1.257	1.248	1.245	1.244	1.243	1.243	1.243	1.242	1.242
5	9.667(1)	8.993(1)	8.872(1)	8.831(1)	8.812(1)	8.802(1)	8.796(1)	8.792(1)	8.790(1)	8.788(1)
6	7.355	6.501	6.335	6.278	6.252	6.238	6.230	6.225	6.221	6.218
7	5.773	4.777	4.562	4.485	4.450	4.430	4.419	4.412	4.407	4.403
8	4.647	3.589	3.328	3.230	3.183	3.158	3.143	3.133	3.126	3.121
9	3.781	2.759	2.471	2.354	2.297	2.265	2.245	2.232	2.223	2.217
10	3.045	2.153	1.867	1.741	1.675	1.638	1.614	1.598	1.587	1.579
11	2.367	1.676	1.423	1.301	1.235	1.194	1.168	1.151	1.138	1.129
12	1.730	1.268	1.074	9.718(0)	9.119(0)	8.739(0)	8.484(0)	8.304(0)	8.174(0)	8.077(0)
13	1.164	9.081(0)	7.815(0)	7.087	6.629	6.322	6.107	5.950	5.833	5.744
14	7.172(0)	6.014	5.342	4.914	4.624	4.419	4.268	4.154	4.066	3.997
15	4.088	3.658	3.371	3.169	3.022	2.911	2.826	2.759	2.706	2.663
16	2.204	2.067	1.966	1.889	1.829	1.781	1.743	1.712	1.687	1.666
17	1.148	1.109	1.078	1.053	1.033	1.016	1.002	9.904(−1)	9.805(−1)	9.722(−1)
18	5.862(−1)	5.757(−1)	5.671(−1)	5.599(−1)	5.539(−1)	5.488(−1)	5.445(−1)	5.408	5.376	5.348
19	2.963	2.936	2.913	2.894	2.877	2.863	2.851	2.840	2.831	2.823
20	1.490	1.483	1.477	1.472	1.468	1.464	1.461	1.458	1.455	1.453
21	7.468(−2)	7.452(−2)	7.437(−2)	7.424(−2)	7.413(−2)	7.403(−2)	7.395(−2)	7.388(−2)	7.381(−2)	7.375(−2)
22	3.739	3.735	3.732	3.728	3.726	3.723	3.721	3.719	3.718	3.716
23	1.871	1.870	1.869	1.868	1.868	1.867	1.867	1.866	1.866	1.865
24	9.358(−3)	9.356(−3)	9.355(−3)	9.352(−3)	9.350(−3)	9.349(−3)	9.348(−3)	9.346(−3)	9.345(−3)	9.344(−3)
25	4.680	4.680	4.679	4.679	4.678	4.678	4.678	4.677	4.677	4.677
26	2.340	2.340	2.340	2.340	2.340	2.340	2.340	2.340	2.340	2.340
27	1.170	1.170	1.170	1.170	1.170	1.170	1.170	1.170	1.170	1.170
28	5.851(−4)	5.851(−4)	5.851(−4)	5.851(−4)	5.851(−4)	5.851(−4)	5.851(−4)	5.851(−4)	5.851(−4)	5.851(−4)
29	2.925	2.926	2.926	2.926	2.926	2.926	2.926	2.926	2.926	2.926
30	1.463	1.463	1.463	1.463	1.463	1.463	1.463	1.463	1.463	1.463
31	7.314(−5)	7.314(−5)	7.315(−5)	7.315(−5)	7.315(−5)	7.315(−5)	7.314(−5)	7.314(−5)	7.314(−5)	7.314(−5)

*Numbers in parentheses are powers of 10, which multiply the entry next to which they stand and all unmarked entries below it.

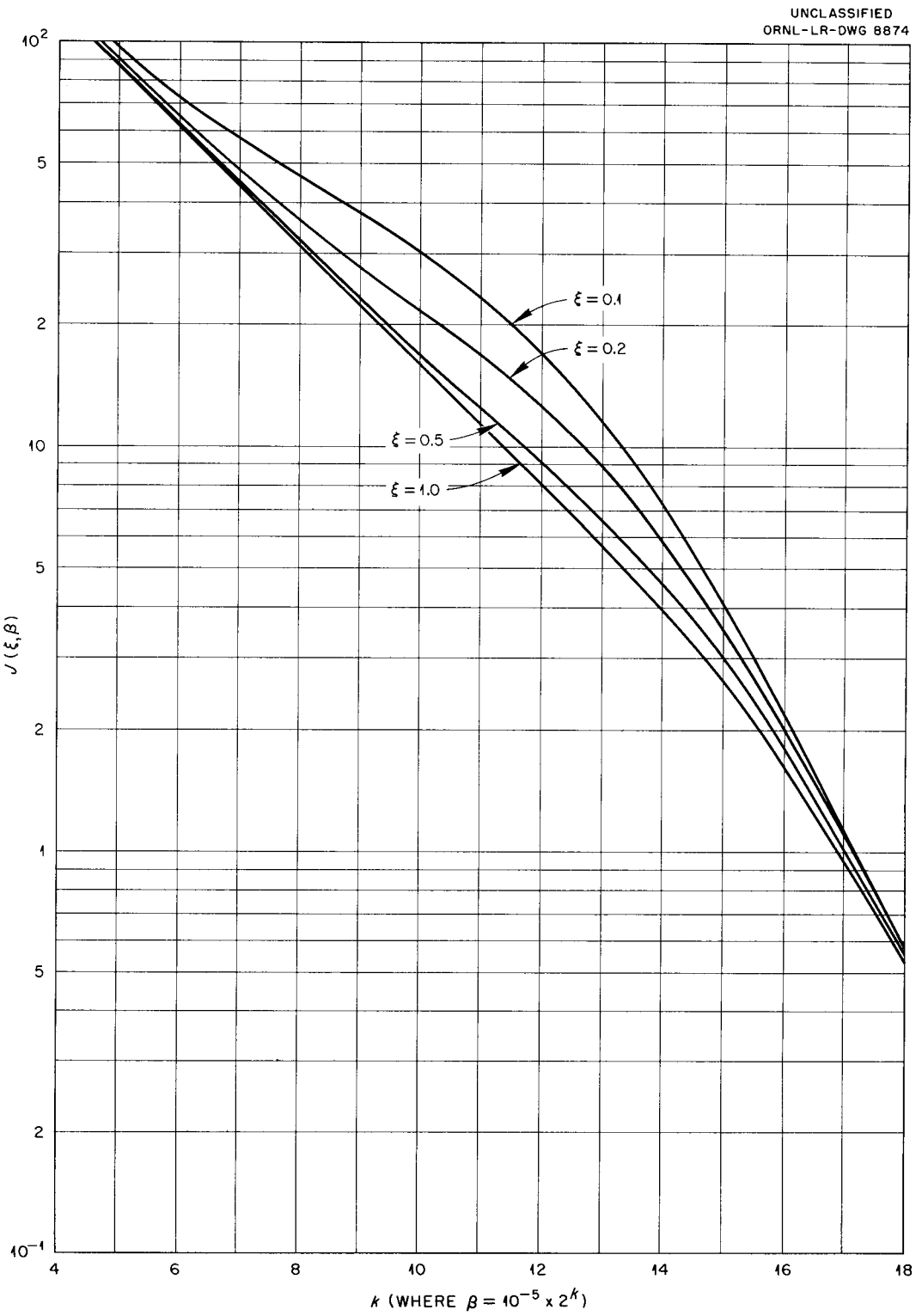

Fig. 24.1. $J(\xi,\beta)$ **vs** k **for** $0.1 \leqq \xi \leqq 1.0$.

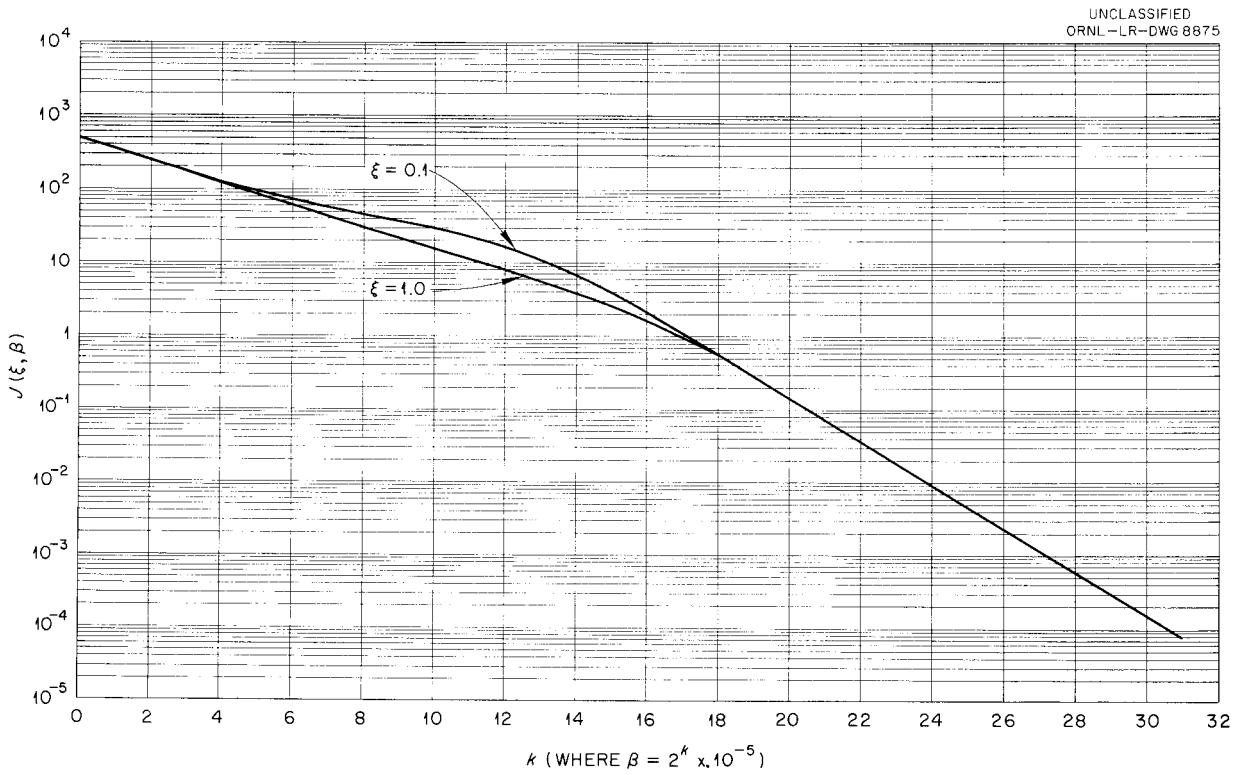

Fig. 24.2. $J(\xi,\beta)$ **vs** k **for** ξ **= 0.1 and 1.0.**

the same temperature and σ_p the contributions are about equal. Calculations of the effective resonance integral which omit the Doppler effect will always be underestimates. In U^{238} at $\sigma_p = 20$ and 2000 barns the underestimate will be ~15%, while at $\sigma_p = 200$ barns the underestimate will be ~30%. In Th^{232} the corresponding values are, respectively, ~25 and ~40%.

Similar calculations have been performed to obtain the temperature coefficient of the effective resonance integrals of the pure U^{238} and Th^{232} metals. In the range 20 to 600°C the temperature coefficients are 1.0 and 1.5% per 100°C, respectively. These numbers are subject to about a 15% variation around the stated values, owing to some uncertainties in the constants used in the calculation. Some experimental values for comparison are contained in Table 24.3.

The preceding calculations were based on the theory of Wigner *et al.*,[1] a condition of which is that the width of the resonance line be narrow compared with the average logarithmic energy loss per collision. In mixtures with considerable moderator scattering this condition is fairly well fulfilled. In pure U^{238} metal, however, the condition is not met in the lowest resonances. The contribution of these resonances can be calculated by adapting the well-known solution of the slowing-down problem with constant ratio, η, of scattering to total cross section[4] to the case of slowly varying η. Then the contribution of a resonance to the effective resonance integral is

$$(5) \quad \left(\int \sigma_a \frac{dE}{E}\right)_{\text{eff}} = \sigma_p \int_{\text{res}} \lambda(E) \frac{dE}{E} \quad ,$$

[4] A. M. Weinberg and L. C. Noderer, *Theory of Neutron Chain Reactions*, ORNL CF-51-5-98, vol I (May 15, 1951); H. Hurwitz, Jr., has also given a similar solution on the slowing-down problems which leads to Eq. 5 (see, for example, H. Soodak, F. Adler, and E. Greuling, chap. 1.3, p 370–71, *Reactor Handbook*, Technical Information Service, AEC, 1955).

where $\lambda(E)$ is a solution of the transcendental equation

$$(6) \qquad 1 + \lambda = \eta \frac{1 - \alpha^{1+\lambda}}{1 - \alpha} .$$

Here $\alpha = [(A - 1)/(A + 1)]^2$, where A is the mass number of the moderator. As shown in Eq. 7, λ can be expanded as a power series in $1 - \eta$ around $\eta = 1$:

$$(7) \quad -\lambda = \frac{1 - \eta}{\xi} + \frac{\xi - \gamma}{\xi}(1 - \eta)^2 + \ldots ,$$

where

$$\xi = 1 + \frac{\alpha \ln \alpha}{1 - \alpha} ,$$

$$\gamma = 1 - \frac{1}{2} \frac{\alpha(\ln \alpha)^2}{(1 - \alpha)\,\xi} .$$

TABLE 24.3. TEMPERATURE COEFFICIENTS OF THE RESONANCE INTEGRALS IN URANIUM AND THORIUM METALS IN THE RANGE 0 TO 600°C

Metal	Temperature Coefficient (% per 100°C)
U^{238}	1.0 ± 0.2[a]
	1.74 ± 0.20[b]
	2.1[c]
Th^{232}	2.2[a]

[a]G. Rodeback, *Sodium Graphite Reactor Quarterly Progress Report*, NAA-SR-1347 (Oct. 1, 1955).
[b]M. V. Davis, *Resonance Capture of Neutrons by Uranium Cylinders*, HW-37766 (Aug. 18, 1955).
[c]E. Creutz *et al.*, *J. Appl. Phys.* **26**, 276 (1955).

TABLE 24.2. CALCULATED CONTRIBUTIONS TO THE EFFECTIVE RESONANCE INTEGRALS OF U^{238} AND Th^{232}

Nucleus	Temperature (°K)	σ_p (barns)	Contribution of Resolved Resonances (barns)	Contribution of Unresolved Resonances (barns)	$1/v$ Contribution (barns)	Effective Resonance Integral (barns)
U^{238}	0	20	7.9	1.7	1.4	11.0
		200	24	4.8	1.4	30
		2000	74	11	1.4	86
	300	20	8.1	3.0	1.4	12.5
		80	17	6.6	1.4	25
		200	27	9.4	1.4	38
		2000	86	12	1.4	99
Th^{232}	0	20	3.7	2.2	3.5	9.4
		200	12	6.3	3.5	22
		2000	33	14	3.5	51
	300	20	4.0	4.0	3.5	11.5
		80	8.9	8.6	3.5	21.0
		200	15	12	3.5	31
		2000	42	20	3.5	66

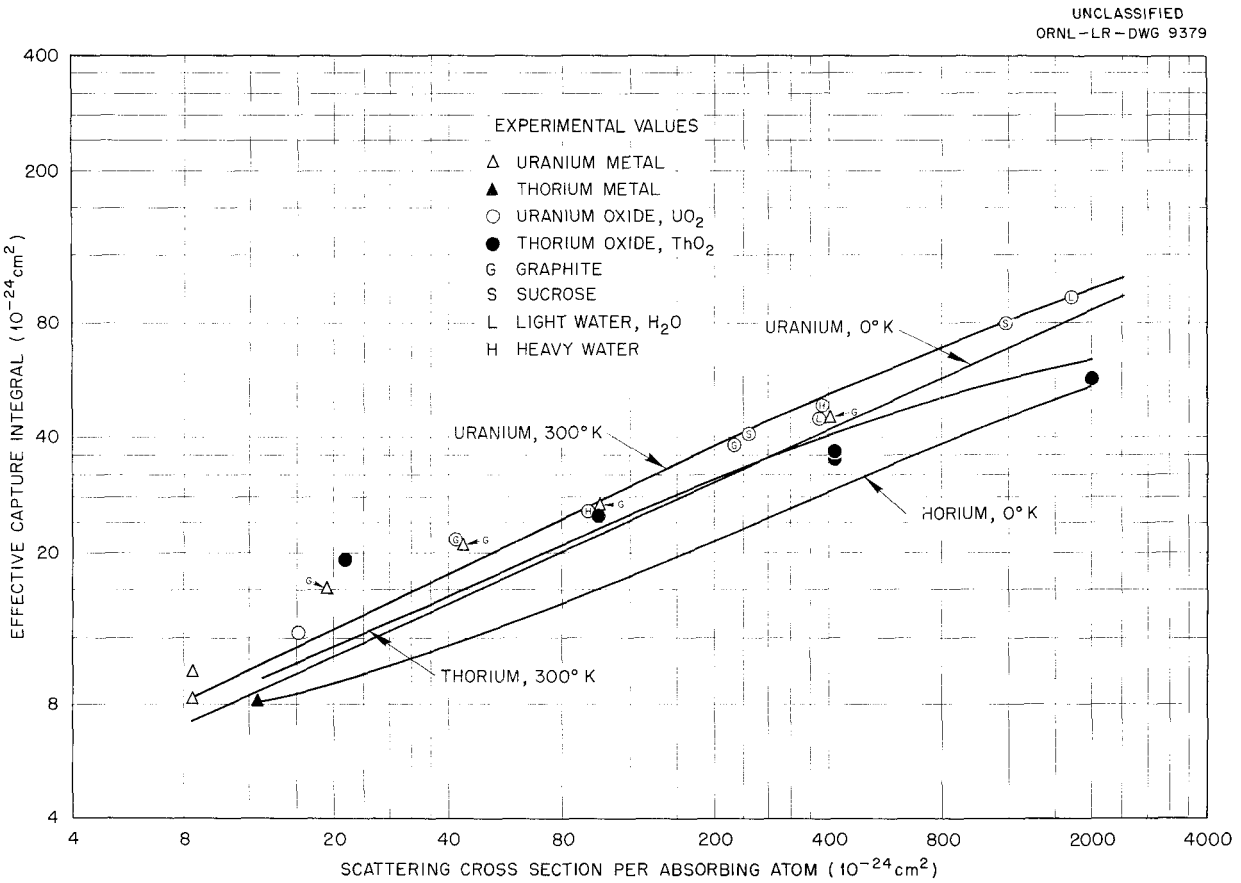

Fig. 24.3. Effective Resonance Capture Integrals of U^{238} and Th^{232} Diluted with Other Materials.

In terms of the cross sections, λ is $-\Sigma_a/\xi\Sigma_t$ and $-\Sigma_a/(\xi\Sigma_s + \gamma\Sigma_a)$ to first and second orders, respectively, in $1 - \eta$. These are the Wigner and Goertzel-Greuling approximations.[5] Figure 24.4 presents $\xi\lambda$ vs η in various approximations.

The contributions of the 6.7- and 21.0-ev resonances were calculated numerically from Eq. 5, with the correct Doppler broadened line shape appropriate to T = 300°K being used.[6] The contributions of the 37-, 67-, 104-, and 192-ev resonances can be calculated by using $\lambda = -\Sigma_a/(\xi\Sigma_s + \gamma\Sigma_a)$ (Goertzel-Greuling approximation), since η is greater than ~0.5 for all of them. In this case the Doppler broadened contribution can also be written in terms of the function $J(\xi,\beta)$. Finally, all other resolved resonances are thin enough to be treated by Wigner's theory. The unresolved resonances have η values close to 1 and again can be treated by Wigner's theory. Their contribution was statistically estimated as before. The results of these calculations are presented in Table 24.4. Multiple collisions in the lowest uranium resonances increase the effective resonance integral about 1.5 barns (20%) over the value computed with the one-collision, narrow-resonance theory. According to Macklin and Pomerance,[3] the best experimental value of the effective resonance integral is, without the $1/v$ contribution, 10.2 barns, with an uncertainty of about 15%. This value is somewhat high in comparison with the calculated values.

Portions of this paper were published previously.[7]

[5] H. Soodak, F. Adler, and E. Greuling, chap. 1.3, p 365 *ff.* in *Reactor Handbook*, Technical Information Service, AEC, 1955.

[6] M. E. Rose *et al.*, *A Table of the Integral . . .*, WAPD-SR-506 (Oct. 1954).

[7] L. Dresner, *Nuc. Sci. Eng.* 1, 68 (1956); L. Dresner, *The Effective Resonance Integral of U^{238} Metal*, ORNL-2101 (July 19, 1956).

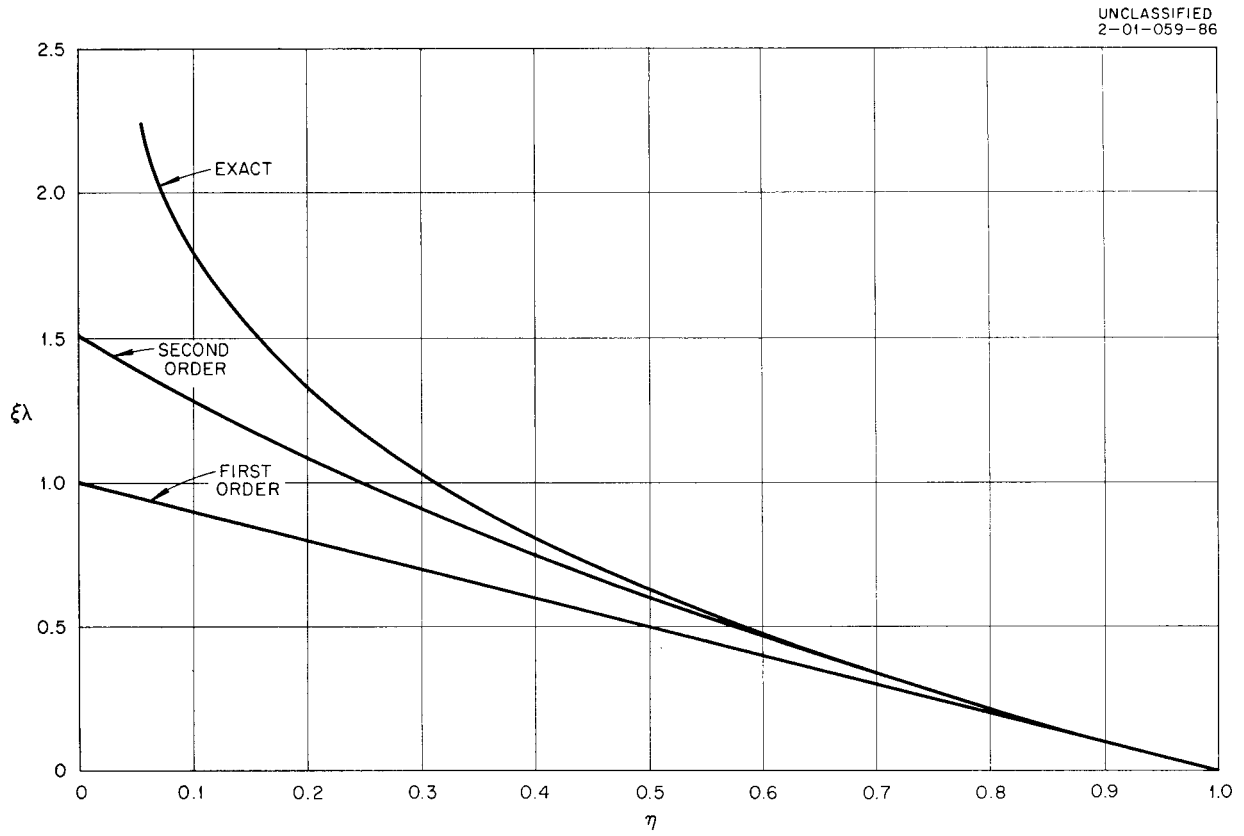

Fig. 24.4. $\xi\lambda$ vs η in Various Approximations for A = 238.

TABLE 24.4. CONTRIBUTIONS TO THE EFFECTIVE RESONANCE INTEGRAL OF PURE U^{238} METAL AT T = 300°K

	Contribution (barns)	
	Wigner's Theory	Theory Corrected for Wide Resonances
6.7-ev resonance	2.7	3.9
21.0-ev resonance	1.0	1.3
Remaining resolved resonances	1.7	1.8
Unresolved resonances	1.7	1.7
$1/v$ contribution	1.4	1.4
Total	8.5	10.1

25. EFFECT OF GEOMETRY ON RESONANCE NEUTRON ABSORPTION

L. Dresner

According to the theory of Wigner[1] the geometric dependence of the effective resonance integral is entirely given by

$$(1)\quad \left(\int \sigma_a \frac{dE}{E}\right)_{\text{eff}} = A\left[\frac{1}{d} + \frac{1}{d_s} C(\bar{l})\, \frac{m}{4\sigma_p}\left(\frac{K}{J}\right)\frac{S}{M}\right],$$

where

σ_a = resonance absorption cross section,

E = neutron energy,

A = effective resonance integral appropriate to an infinite homogeneous medium,

d = volume disadvantage factor,[2]

d_s = surface disadvantage factor,[2]

$\bar{l}$ = average chord length of the fuel lump ($= 4V/S$),

V/S = volume-to-surface ratio,

m = mass per absorbing nucleus,

σ_p = potential scattering cross section,

S/M = surface-to-mass ratio of the fuel lump,

$C(\bar{l}) = \dfrac{2}{1 + \sqrt{1 + (N\sigma_p \bar{l})^{-1}}}$ and corrects for neutrons which enter the lump surface but do not collide in the lump,

N = number of absorbing atoms per unit volume.

The terms K and J are defined respectively by

$$(2)\quad K = \int_0^\infty \left(\frac{\psi}{\psi + \beta}\right)^2 dx\,, \qquad J = \int_0^\infty \frac{\psi}{\psi + \beta}\, dx\,,$$

where $\psi(\xi,x)$ is the resonance line shape given by

$$(3)\quad \psi(\xi,x) = \frac{\xi}{2\sqrt{\pi}} \int_{-\infty}^{+\infty} \frac{\exp[-\xi^2/4(x-y)^2]}{1+y^2}\, dy\,,$$

ξ is the ratio of the natural to the Doppler width, β is the ratio of the potential scattering cross section to the total cross section *at resonance*, and x is the energy measured from exact resonance in units of the half-width. Figure 25.1 shows a plot of K/J vs β for $\xi = 0.1$, 0.3, and ∞. The latter value corresponds to $\psi(\xi,x) = (1 + x^2)^{-1}$, the natural line shape, for which $K/J = [2(1+\beta)]^{-1}$; $\xi \sim 0.3$ for the lowest resonances of uranium and $\beta \sim 10^{-3}$. Since the main contribution to the surface as well as to the volume absorption comes from the lowest resonances, the value of K/J appropriate for Eq. 1 is probably quite close to the natural line-shape value of $\frac{1}{2}$ for small β.

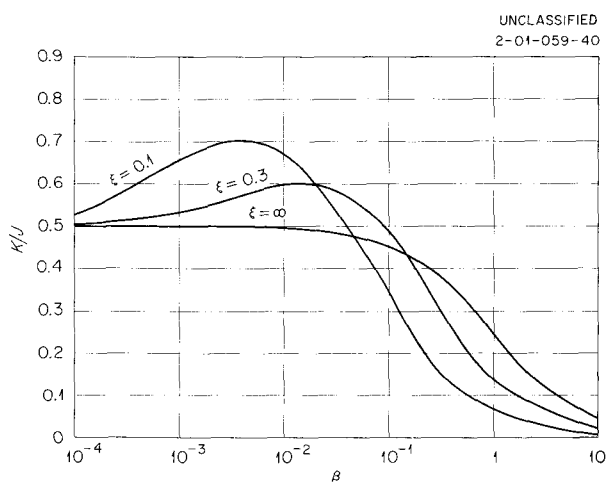

Fig. 25.1. K/J **as a Function of** β **for** $\xi = 0.1$, **0.3, and** ∞.

Using the natural line-shape value of K/J, namely, $\frac{1}{2}$, the bracket in Eq. 1, which represents the theoretical dependence of the effective resonance integral on geometry, was compared with experiment for uranium. The experimental dependence on geometry was determined for uranium metal from the activation experiments of Creutz *et al.*,[3] the activation experiments of Risser *et al.*,[4] the pile

[1] E. P. Wigner *et al.*, *J. Appl. Phys.* **26**, 260 (1955).

[2] See, for example, M. M. Shapiro, chap. 1.5, p 480 *ff.* in *Reactor Handbook*, Technical Information Service, AEC, 1955.

[3] E. Creutz, H. Jupnik, and T. Snyder, *Effect of Geometry on Resonance Absorption of Neutrons by Uranium*, C-116 (June 1942); E. Creutz *et al.*, *J. Appl. Phys.* **26**, 271 (1955).

[4] J. R. Risser *et al.*, ORNL-958 (1951). (Classified).

oscillator experiments of Untermyer,[5] and the lattice analyses of Davey.[6] The experiments of Creutz *et al.*[3] also provided information on the geometric dependence of the resonance integral for U_3O_8 and a U_3O_8-C mixture. Figure 25.2 shows the comparison between theory and experiment in a typical case.

The following conclusions can be drawn from these considerations: In the first place, if $\beta \ll 1$ and the Doppler broadening is slight, then $K/J \sim \frac{1}{2}$, irrespective of the details of the resonance structure. In this event, the geometric dependence of the resonance integral is *independent* of the details of resonance structure (widths, energies). Therefore, comparison of theory and experiment can provide a check on the theory independent of the uncertainties in resonance structure.

The comparison between theory and experiment led in every case to the conclusion that Wigner's theory overestimates the surface absorption. Arbitrarily reducing the surface absorption to 0.6 of the value given in Eq. 1 produced better agreement for lumps whose average chord length, $\bar{l}$, was greater than 5 mm. These conclusions may apply, *ceteris paribus*, to other materials, for example, thorium, independently of the details of resonance structure.

[5] S. Untermyer, *Resonance Absorption of Uranium Rods*, ANL-4350 (1949).

[6] W. G. Davey, AERE RP/R 1842 (1955). (Confidential Atomic).

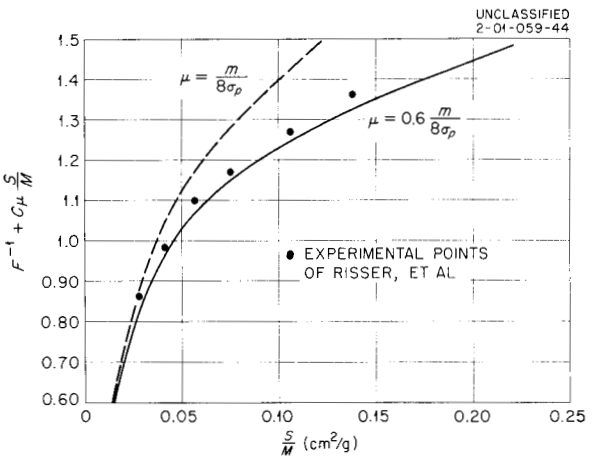

Fig. 25.2. Dependence of the Effective Resonance Integral on Geometry.

To test this last conclusion Eq. 1 was compared with experimental variations of the effective resonance integral of thorium derived from danger coefficient measurements of Untermyer and Eggler.[7] Again the reduction in the theoretical surface absorption by a factor of 0.6 improved agreement with experiment. Hence, with this reduction noted, Eq. 1 seems to reproduce the experimental variation in the effective resonance integral with geometry fairly well.

[7] S. Untermyer and C. Eggler, *Resonance Integral of Thorium Metal Lumps*, ANL-4596 (1951).

26. CALCULATION OF NEUTRON RADIATIVE CAPTURE CROSS SECTIONS

L. Dresner

Several attempts[1] have been made to estimate fission-product poisoning in the intermediate energy range (10^3 to 10^6 ev) by using the following expression for the radiative capture cross section, σ_a:

$$(1) \quad \sigma_a = \pi\lambda\!\!\!^{-2}\left(\frac{2\pi\Gamma_\gamma}{D^*}\right)\frac{\Gamma_n}{\Gamma_n + \Gamma_\gamma}\left(1 + \frac{R^2}{\lambda\!\!\!^{-2}}\right) ,$$

where

$\lambda\!\!\!^{-}$ = neutron wavelength divided by 2π,

Γ_γ, Γ_n = average low-energy radiative and neutron widths, respectively,

D^* = average spacing of resonance levels of the same spin and parity,

R = nuclear radius.

According to Margolis[2] an expression for σ_a based on the statistical theory of the nucleus is

$$(2) \quad \sigma_a = \frac{\pi\lambda\!\!\!^{-2}}{2(2I+1)}\left(\frac{2\pi\Gamma_\gamma}{D^*}\right)\sum_{l=1}^{\infty}\sum_{J}\frac{(2J+1)\,\epsilon^J_{jl}\,T_l(E)}{\left(\frac{2\pi\Gamma_\gamma}{D^*}\right) + \sum_{l'=0}^{\infty}\epsilon^J_{jl'}\,T_{l'}(E)} ,$$

where I is the spin of the target nucleus, $l\hbar$ and $l'\hbar$ are the neutron orbital angular momenta, $J\hbar$ is the total angular momentum of the compound nucleus, $T_l(E)$ is the nuclear penetrability defined by Blatt and Weisskopf,[3] and ϵ^J_{jl} is a symbol defined by Hauser and Feshbach[4] as

$$(3) \quad \epsilon^J_{jl} = 2 \text{ for } |J - l| \leqq I \pm \tfrac{1}{2} \leqq J + l$$
$$= 1 \text{ for } |J - l| \leqq I + \tfrac{1}{2} \text{ or } I - \tfrac{1}{2} \text{ but not both} \leqq J + l$$
$$= 0 \text{ otherwise} .$$

Equation 2 as written ignores the competition of inelastic scattering with compound elastic scattering, although Eq. 2 may be generalized to include it. For nuclei with $I = 0$, Eq. 2 takes the simpler form

$$(4) \quad \sigma_a = \pi\lambda\!\!\!^{-2}\left(\frac{2\pi\Gamma_\gamma}{D^*}\right)\sum_{l=0}^{\infty}\frac{(2l+1)\,T_l(E)}{T_l(E) + (2\pi\Gamma_\gamma/D^*)} .$$

The low-energy limit of Eq. 2 is

$$(5a) \quad \sigma_a = \pi\lambda\!\!\!^{-2}\left(\frac{2\pi\Gamma_\gamma}{D^*}\right)\frac{\Gamma_n}{\Gamma_n + \Gamma_\gamma} ,$$

while the high-energy limit is

$$(5b) \quad \sigma_a = \pi(R + \lambda\!\!\!^{-})^2\left(\frac{2\pi\Gamma_\gamma}{D^*}\right) .$$

Equation 5b was derived by Bethe.[5] These limits are the same as the low- and high-energy limits of Eq. 1.

Equation 4 can be approximated rather well by the formula

$$(6) \quad \sigma_a = \pi\lambda\!\!\!^{-2}\left(\frac{2\pi\Gamma_\gamma}{D^*}\right) L(L+1) ,$$

where L is a solution of

$$\ln\Gamma(L + \tfrac{1}{2}) = \tfrac{1}{2}\ln\left(\frac{2D^*}{\Gamma_\gamma}\sqrt{\frac{E}{E+V}}\right) + L\ln\left(\frac{R^2}{2\lambda\!\!\!^{-}}\right),$$

in which Γ is the usual gamma function, E is the neutron energy, and V is the nuclear well depth.

In Fig. 26.1 are presented the results of calculations made for the radiative capture cross section

[1] A. M. Weinberg, *Proceedings of the International Conference on the Peaceful Uses of Atomic Energy*, vol 3, p 19, United Nations, New York, 1955; H. Hurwitz, Jr., and P. Greebler, KAPL-1449 (1955).

[2] B. Margolis, *Phys. Rev.* 88, 327 (1952).

[3] J. Blatt and V. F. Weisskopf, *Theoretical Nuclear Physics*, chap. 8, Wiley, New York, 1952.

[4] H. Hauser and H. Feshbach, *Phys. Rev.* 87, 366 (1952).

[5] H. A. Bethe, *Phys. Rev.* 57, 1125 (1940).

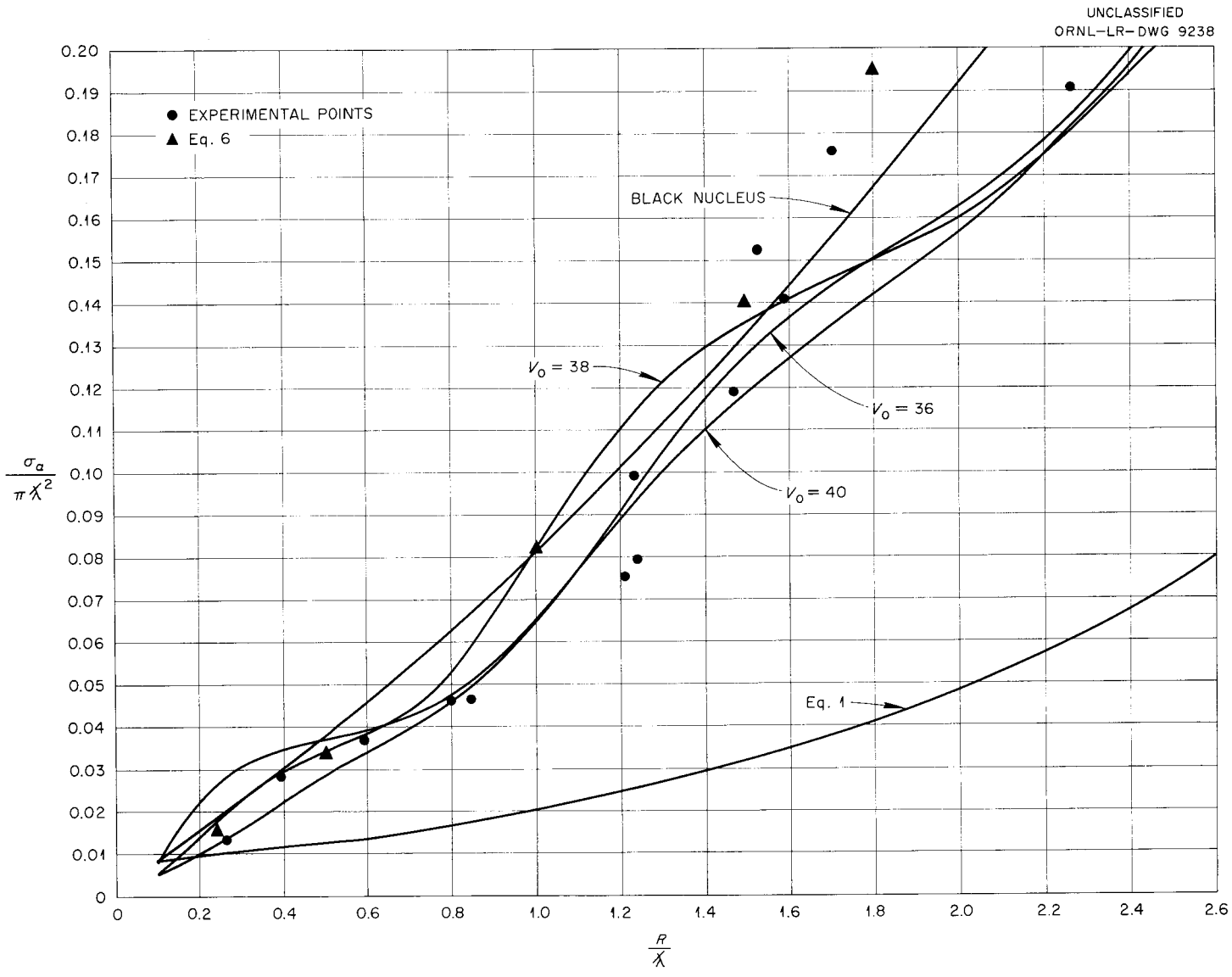

Fig. 26.1. $\sigma_a/\pi\lambda\!\!\!^{-2}$ **vs** $R/\lambda\!\!\!^{-}$ **for** U^{238}.

of U^{238}. In accordance with reported resonance data, $2\pi\Gamma_\gamma/D^*$ was chosen as 0.01. In three of the calculations made with Eq. 5, the penetrabilities, $T_l(x)$, were calculated from the "cloudy crystal ball" model with $\xi = 0.03$ and $V_0 = 36$, 38, and 40 Mev, respectively. In the fourth calculation the "black nucleus" model was used, again with $V_0 = 36$ Mev. The circles are experimental points.[6] All the calculated curves agree quite well with the points. The curves calculated with the cloudy crystal ball show oscillatory behavior, attributable to giant resonances, which is also present in the experimental points. Agreement on this point, however, is merely qualitative. For the purpose of reactor calculations the black nucleus model is entirely adequate for obtaining radiative capture cross sections.

Included on the plot is a calculation of σ_a by use of Eq. 1; $(2\pi\Gamma_n/D^*)\ E^{-1/2}$ was chosen as 0.75×10^{-3} $ev^{-1/2}$, in accordance with the data reported by Hughes and Harvey.[6] Finally included on the plot are some points (triangles) calculated with Eq. 6. These points agree quite well with the exact curve calculated from the black nucleus model and Eq. 5. The curve calculated from Eq. 1, on the other hand, lies considerably below the experimental points. Moreover, at $x = 6$, which corresponds to about 9 Mev in U^{238}, the ratio of Eq. 5 (or Eq. 6) to Eq. 1 is still ~3:1. Hence Eq. 1 considerably underestimates the contributions of neutrons with $l > 0$ to the absorption cross section.

Two general conclusions can be drawn: (1) the use of Eq. 1 in estimating fission-product poisoning leads to serious underestimates, and (2) the use of Eq. 5 and black nucleus penetrabilities (or Eq. 6) leads to good agreement between calculated and experimental values of σ_a.

Another version of this paper was published previously.[7]

[6] D. J. Hughes and J. A. Harvey, *Neutron Cross Sections*, BNL-325 (1955).

[7] L. Dresner, *Nuc. Sci. Eng.* 1, 103 (1956).

27. THE ORACLE THREE-GROUP, THREE-REGION REACTOR CODE

W. E. Kinney G. Heilborn

The Oracle reactor code which accommodates the largest number of groups and regions at present is the three-group, three-region (3G3R) reactor code. With it, slabs, cylinders, and spheres at 52 space points can be calculated by using diffusion theory and group transfer cross sections. Thin shells are allowed between regions.

Since the publication of a description[1] of the code, changes have been made so that the degree of convergence may be specified, and the multiplication constant and convergence test number are punched only upon convergence and not upon each iteration. A normalization and edit program has been written which normalizes the fluxes of the code to the largest flux, averages the fluxes spatially for each group and region, computes currents at interfaces, and plots and prints the results on the curve plotter. A typical plot of the flux as a function of a reactor radius is shown in Fig. 27.1.

UNCLASSIFIED
ORNL-LR-DWG. 16573

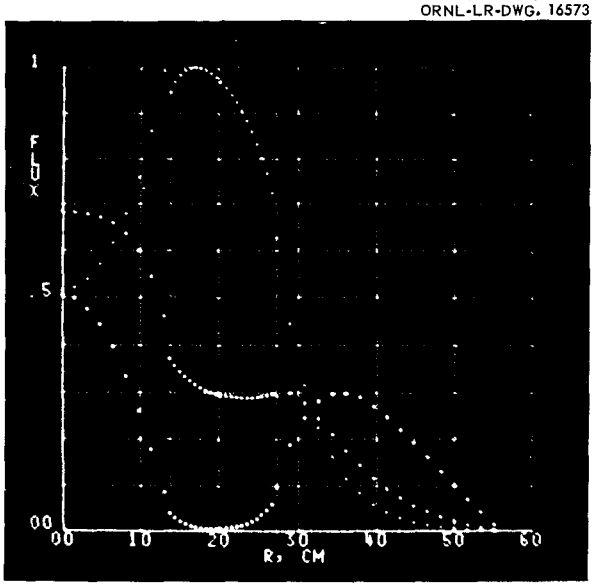

Fig. 27.1. Typical Oracle Plot of the Flux in a Reactor as a Function of Reactor Radius.

[1] R. R. Bate, L. T. Einstein, and W. E. Kinney, *Description and Operating Manual for the Three Group, Three Region Reactor Code for Oracle*, ORNL CF-55-1-76 (Jan. 1955).

28. MULTIGROUP CALCULATIONS FOR A MULTIREGION REACTOR

W. E. Kinney
R. R. Coveyou
J. G. Sullivan
B. J. Garrick[1]

A program designated as "Corn Pone" has been initiated to develop a multigroup code for the Oracle which will be used to calculate the parameters of a multiregion reactor. Equations resulting from a consistent P_1 approximation to the Boltzmann equation are incorporated in the code. The theory of Corn Pone and a description of the properties of the code are given below.

Theory of Corn Pone

P_1 Equations. – A P_1 approximation to the Boltzmann equation yields for one space variable,

$$(1)\quad \tfrac{1}{3}\nabla_0\phi_0(r,u) + \sum_n \tau_n(u)\,\phi_1(r,u) = \sum_n \int_0^u \phi_1(r,u')\,\sigma_n(u')\,K_{1_n}(u'\to u)\,du' \quad ,$$

$$(2)\quad \nabla_1\phi_1(r,u) = S(r,u) - \sum_n \tau_n(u)\,\phi_0(r,u) + \sum_n \int_0^u \phi_0(r,u')\,\sigma_n(u')\,K_{0_n}(u'\to u)\,du' \quad .$$

The boundary conditions are

$$(3)\quad \begin{aligned} &(a)\ \phi_0(r,0) = 0 \ ,\\ &(b)\ \phi_1(r,0) = 0 \ ,\\ &(c)\ \phi_1(0,u) = 0 \ ,\\ &(d)\ \phi_0 \text{ continuous} \ ,\\ &(e)\ \phi_1 \text{ continuous} \ ,\\ &(f)\ \text{either } \phi_0(R,u) = 0 \text{ or } j\text{-}(R,u) = 0 \ , \end{aligned}$$

where

$$\nabla_0 = \frac{\partial}{\partial r} \ ,$$

$$\nabla_1 = \frac{\partial}{\partial r} + \frac{g}{r} \ (g = 0,\ 1,\ 2 \text{ for a slab, cylinder, or sphere, respectively}),$$

r = distance from the origin,

u = lethargy,

τ_n = macroscopic total cross section for element n,

σ_n = macroscopic scattering cross section for element n,

ϕ_0 = flux,

ϕ_1 = current,

$K_n(u'\to u) = \tfrac{1}{2}K_{0_n}(u'\to u) + \tfrac{3}{2}K_{1_n}(u'\to u)\,\mu_n$
scattering kernel for element n,

---

[1]Oak Ridge School of Reactor Technology.

μ_n = cosine of the scattering angle in the laboratory system for element n,

j^- = partial current in negative direction,

R = outer boundary of reactor.

Defining the slowing-down densities

$$Q_n(r,u) = \int_0^u \phi_0(r,u')\,\sigma_n(u')\,du' \int_u^\infty K_{0_n}(u' \to u'')\,du'' \quad , \tag{4}$$

$$P_n(r,u) = \int_0^u \phi_1(r,u')\,\sigma_n(u')\,du' \int_u^\infty K_{1_n}(u' \to u'')\,du'' \quad , \tag{5}$$

and using Goertzel-Greuling synthetic kernels (see ref 2)

$$\begin{aligned} K_0(u' \to u) &= \frac{\xi}{\gamma^2}\, e^{-(u-u')/\gamma} + \left(1 - \frac{\xi}{\gamma}\right)\delta(u - u') \ , & u \geqq u' \ , \\ &= 0 \ , & u < u' \ , \end{aligned} \tag{6}$$

$$\begin{aligned} K_1(u' \to u) &= \frac{\eta}{\rho^2}\, e^{-(u-u')/\rho} + \left(\bar{\mu} - \frac{\eta}{\rho}\right)\delta(u - u') \ , & u \geqq u' \ , \\ &= 0 \ , & u < u' \ , \end{aligned} \tag{7}$$

where

$$\xi = \bar{u} \ ,$$

$$\gamma = \frac{\overline{u^2}}{2\xi} \ ,$$

$$\eta = \overline{u\mu} \ ,$$

$$\rho = \frac{\overline{u^2\mu}}{2\eta} \ ,$$

gives

$$\gamma_n \frac{\partial}{\partial u} Q_n(r,u) + Q_n(r,u) = \xi_n \sigma_n(u)\,\phi_0(r,u) \quad , \tag{8}$$

$$\rho_n \frac{\partial}{\partial u} P_n(r,u) + P_n(r,u) = \eta_n \sigma_n(u)\,\phi_1(r,u) \quad . \tag{9}$$

For some elements it will be reasonable to say that

$$\frac{\partial}{\partial u} Q_n(r,u) = -\alpha_n(u)\,\phi_0(r,u) \tag{10}$$

and/or that

$$\frac{\partial}{\partial u} P_n(r,u) = -\beta_n(u)\,\phi_1(r,u) \quad , \tag{11}$$

---

[2]Note that Eqs. 6 and 7 are exact for hydrogen, since, in that case, $\xi = 1$, $\gamma = 1$, $\bar{\mu} = 2/3$, $\eta = 4/9$ and $\rho = 2/3$.

where

α_n = macroscopic absorption cross section for element n,

$\beta_n = \tau_n - \bar{\mu}_n \sigma_n$.

Elements to which Eqs. 10 and 11 apply will be designated as class A; those to which Eq. 11 only applies will be designated as class B; and those to which neither Eq. 10 nor Eq. 11 applies will be designated as class C. Substitution into Eqs. 1 and 2 from Eqs. 8, 9, 10, and 11 gives

$$(12)\quad \tfrac{1}{3}\nabla_0\phi_0(r,u) + \sum_{A,B}\left[\beta_n(u) + \eta_n \frac{d}{du}\sigma_n(u) + \rho_n \frac{d}{du}\beta_n(u)\right]\phi_1(r,u) + \sum_{C}\left[\beta_n(u) + \frac{\eta_n}{\rho_n}\sigma_n(u)\right]\phi_1(r,u) + \sum_{A,B}\left[\eta_n\sigma_n(u) + \rho_n\beta_n(u)\right]\frac{\partial}{\partial u}\phi_1(r,u) - \sum_{C}\frac{1}{\rho_n}P_n(r,u) = 0 ,$$

$$(13)\quad \nabla_1\phi_1(r,u) - S(r,u) + \sum_{A}\left[\alpha_n(u) + \xi_n \frac{d}{du}\sigma_n(u) + \gamma_n \frac{d}{du}\alpha_n(u)\right]\phi_0(r,u) + \sum_{A}\left[\xi_n\sigma_n(u) + \gamma_n\alpha_n(u)\right]\frac{\partial}{\partial u}\phi_0(r,u) + \sum_{B,C}\left[\alpha_n(u) + \frac{\xi_n}{\gamma_n}\sigma_n(u)\right]\phi_0(r,u) - \sum_{B,C}\frac{1}{\gamma_n}Q_n(r,u) = 0 ,$$

where the summations run over the indicated classes.

Lethargy Integration. – The lethargy range is broken into i groups, and ϕ_0, ϕ_1, Q, and P are assumed to vary linearly with lethargy over a group. Then, for example,

$$(14)\qquad \frac{1}{U_i}\int_{u_i}^{u_{i+1}} \sigma(u)\,\phi_0(r,u)\,du = {}^{*}\sigma(u_i)\,\bar{\phi}_0(r,u_i) + \sigma^{*}(u_i)\,\phi_0(r,u_i) ,$$

where

$$^{*}\sigma(u_i) = \frac{1}{U_i^2}\int_{u_i}^{u_{i+1}} \sigma(u)\,2(u - u_i)\,du ,$$

$$\sigma^{*}(u_i) = \frac{1}{U_i^2}\int_{u_i}^{u_{i+1}} \sigma(u)\,(u_{i+1} + u_i - 2u)\,du ,$$

$U_i = u_{i+1} - u_i$,

u_i = lower lethargy limit of group i ,

u_{i+1} = upper lethargy limit of group i ,

$\bar{\phi}_0(r,u_i)$ = average, or mid-point flux of group i .

Integrating Eqs. 12 and 13 over group i and dividing by U_i leads to

$$\nabla_0 \bar{\phi}_0(r,u_i) + A(u_i)\,\bar{\phi}_1(r,u_i) + B(r,u_i) = 0 \quad , \tag{15}$$

$$\nabla_1 \bar{\phi}_1(r,u_i) = -C(u_i)\,\bar{\phi}_0(r,u_i) + D(r,u_i) \quad , \tag{16}$$

where

$$A(u_i) = 3\left\{\sum_n {}^*\beta_n(u_i) + \sum_{A,B} \frac{2}{U_i}\left[\eta_n{}^*\sigma_n(u_i) + \rho_n{}^*\beta_n(u_i)\right] + \sum_C \frac{2\eta_n}{2\rho_n + U_i}\,{}^*\sigma_n(u_i)\right\} ,$$

$$B(r,u_i) = G(u_i)\,\phi_1(r,u_i) - 3\sum_C \frac{2}{2\rho_n + U_i}\,P_n(r,u_i) \quad ,$$

$$G(u_i) = 3\left(\sum_n \beta_n^*(u_i) + \sum_{A,B} \frac{2}{U_i}\left\{\eta_n\left[\sigma_n^*(u_i) - \sigma_n(u_i)\right] + \rho_n\left[\beta_n^*(u_i) - \beta_n(u_i)\right]\right\} + \right.$$

$$\left. + \sum_C \frac{2\xi_n}{2\rho_n + U_i}\,\sigma_n^*(u_i)\right) ,$$

$$C(u_i) = \sum_n {}^*\alpha_n(u_i) + \sum_A \frac{2}{U_i}\left[\xi_n{}^*\sigma_n(u_i) + \gamma_n{}^*\alpha_n(u_i)\right] + \sum_{B,C} \frac{2\xi_n}{2\gamma_n + U_i}\,{}^*\sigma_n(u_i) ,$$

$$D(r,u_i) = -I(u_i)\,\phi_0(r,u_i) + \bar{S}(r,u_i) + \sum_{B,C} \frac{2}{2\gamma_n + U_i}\,Q_n(r,u_i) \quad ,$$

$$I(u_i) = \sum_n \alpha_n^*(u_i) + \sum_A \frac{2}{U_i}\left\{\xi_n\left[\sigma_n^*(u_i) - \sigma_n(u_i)\right] + \gamma_n\left[\alpha_n^*(u_i) - \alpha_n(u_i)\right]\right\} +$$

$$+ \sum_{B,C} \frac{2\xi_n}{2\gamma_n + U_i}\,\sigma_n^*(u_i) \quad .$$

Operating on Eq. 15 with ∇_1 on the left and substituting from Eq. 16 results in

$$\frac{\partial^2}{\partial r^2}\,\bar{\phi}_0(r,u_i) + \frac{g}{r}\,\frac{\partial}{\partial r}\,\bar{\phi}_0(r,u_i) - \delta(u_i)\,\bar{\phi}_0(r,u_i) + \tag{17}$$

$$+ \frac{\partial}{\partial r}\,B(r,u_i) + \frac{g}{r}\,B(r,u_i) + A(u_i)\,D(r,u_i) = 0 \quad ,$$

where $\delta(u_i) = A(u_i)\,C(u_i)$. If the reactor is to be a parallelepiped or a finite cylinder, geometric buckling may be added to $\delta(u_i)$.

Thermal Group. – The equations for the thermal group are

$$\tfrac{1}{3}\nabla_0\phi_0^{th}(r) + \phi_1^{th}(r)\sum_n \bar{\tau}_n - \sum_n P_n^{th}(r) = 0 \quad , \tag{18}$$

(19) $$\nabla_1 \phi_1^{th}(r) = S^{th}(r) - \phi_0^{th}(r) \sum_n \bar{\alpha}_n + \sum_n Q_n^{th}(r) \quad ,$$

where $\bar{\tau}$ and $\bar{\alpha}$ indicate averages over a Maxwell-Boltzmann distribution and $P^{th}(r)$ and $Q^{th}(r)$ are slowing-down densities at the top, in lethargy, of the epithermal group.

Spatial Integration. – Taking difference approximations to first, second, and third derivatives, good to order h^4, where h is the lattice spacing, results in the following difference equation at space point k:

(20) $$P_k \Omega_{k+1} - Q_k \Omega_k + R_k \Omega_{k-1} + S_k = 0 \quad ,$$

where, for a group and a region,

$$P_k = \frac{1}{2} + \frac{gh}{4r} + \frac{g(g-2)}{24} \frac{h^2}{r^2} - \frac{g(g-2)}{48} \frac{h^3}{r^3} - \frac{\delta h^2}{24} - \frac{\delta h^3 g}{48r} \quad ,$$

$$Q_k = 1 + \frac{g(g-2)}{12} \frac{h^2}{r^2} + \frac{5}{12} \delta h^2 \quad ,$$

$$R_k = \frac{1}{2} - \frac{gh}{4r} + \frac{g(g-2)}{24} \frac{h^2}{r^2} + \frac{g(g-2)}{48} \frac{h^3}{r^3} - \frac{\delta h^2}{24} + \frac{\delta h^3 g}{48r} \quad ,$$

$$\begin{aligned} S_k = & -\frac{h}{48} B_{k+2} + hB_{k+1} \left\{ \frac{7}{24} + \frac{gh}{12r} \left[1 + \frac{h}{4r} (g-2) \right] \right\} + \\ & + hB_k \frac{gh}{r} \left[\frac{1}{3} + \frac{1}{24} \frac{h^2}{r^2} (2-g) \right] + hB_{k-1} \left\{ -\frac{7}{24} + \frac{gh}{12r} \left[1 - \frac{h}{4r} (g-2) \right] \right\} + \\ & + \frac{h}{48} B_{k-2} + A \left[\frac{h^2}{24} \left(1 + \frac{gh}{2r} \right) D_{k+1} + \frac{5}{12} h^2 D_k + \frac{h^2}{24} \left(1 - \frac{gh}{2r} \right) D_{k-1} \right] \quad , \end{aligned}$$

Ω_k = flux at space point k.

Assuming

(21) $$\Omega_k = \Gamma_k \Omega_{k+1} + \Delta_k \quad ,$$

it follows that

(22) $$\Gamma_k = \frac{P_k}{Q_k - R_k \Gamma_{k-1}} \quad ,$$

(23) $$\Delta_k = \frac{R_k \Delta_{k-1} + S_k}{Q_k - R_k \Gamma_{k-1}} \quad ;$$

Γ_0 and Δ_0 are computed to satisfy Eq. 3c, and all the Γ_k's and Δ_k's are then calculated from Eqs. 22 and 23. The flux at one space point beyond the outer boundary is then

computed to satisfy Eq. 3*f*, and all the fluxes are calculated from Eq. 21. The terms P_k, Q_k, R_k, and S_k take special forms to satisfy Eqs. 3*d* and 3*e* at interfaces.

General Method of Solution. – A source constant in fissionable regions and zero elsewhere is assumed for the first iteration. Equation 20 is solved for each group, and a source for the next iteration is computed. The initial and computed sources are compared to determine the multiplication constant k. The new source is divided by k to force steady state, and another iteration is started. The process is continued until convergence of k, source, or thermal flux.

Properties of Corn Pone

Reactor Properties. – Corn Pone will be a one-dimensional calculation in which the critical parameters of parallelepipeds, cylinders, or spheres will be computed. Either zero flux or zero return current may be the outer boundary condition. There may be i groups and j regions with the following restrictions:

$$i < \sim 400$$

$$j < 128$$

$$ij < \sim 4000$$

Region Properties. – A region is defined as that part of the reactor over which material concentrations are constant. All the 44 elements and alloys available may appear in each region, and four of these may be special elements of class B or C (see above). Each region has its own epithermal and thermal groups. The region lattice spacing, b, is chosen by the code such that

$$(a) \qquad \Sigma_{max} b < 1 \ ,$$

$$(b) \qquad bN = t \ ,$$

where

Σ_{max} = maximum cross section,
t = region thickness,
N = smallest integer under restriction a.

Scattering Kernels. – In addition to the scattering kernels of Eqs. 6 and 7 there will be available

$$(24) \quad \begin{cases} (a) \quad K_0(u' \to u) = \xi\delta'(u - u') + \delta(u - u') & \text{(Fermi)} \ , \\ (b) \quad K_0(u' \to u) = \dfrac{1}{\xi} e^{-(u-u')/\xi} \ , \qquad u \geqq u' & \text{(Wigner)} \ , \\ \qquad\qquad\qquad = 0 \ , \qquad u < u' & \end{cases}$$

$$
(25)\quad
\begin{aligned}
&(a) \qquad K_1(u' \to u) = \bar{\mu}\delta(u - u') \ , \\
&(b) \qquad K_1(u' \to u) = \eta\delta'(u - u') + \bar{\mu}\delta(u - u') \ , \\
&(c) \qquad K_1(u' \to u) = \frac{1}{\eta} e^{-(u-u')/\eta} + (\bar{\mu} - 1)\ \delta(u - u') \ , \qquad u \geqq u' \ , \\
&\qquad\qquad\qquad\quad = 0 \ , \qquad\qquad\qquad\qquad\qquad\qquad\qquad\qquad u < u' \ .
\end{aligned}
$$

Equation 25*c* is included for completeness even though it is expected to be unstable, since $\eta < 0$ for mass > 1. The Goertzel-Selengut approximation may be obtained by applying Eq. 25*a* to all elements, Eq. 24*b* to all elements except hydrogen, and Eq. 6 to hydrogen.

Output. – Initial conditions, k, and the convergence criterion will be printed for every case. The following may be printed if desired:

1. sources,
2. absorptions, escapes, and fissions for each group and region,
3. any or all fluxes.

Status of Corn Pone

Corn Pone will have four major parts: (1) group constant preparation routine, (2) reactor constant preparation routine, (3) integration routine, and (4) edit routine. Flowsheets have been drawn for parts 1, 2, and 3. Most of the code for parts 1 and 2 has been written.

29. ORACLE MASTER CROSS-SECTION TAPE

R. R. Bate[1] J. H. Marable J. W. Niestle[1]

In order to solve a wide range of reactor problems on the Oracle it is necessary that cross sections be readily available to the machine. For this purpose preparation of a permanent master cross-section magnetic tape which stores the various microscopic cross sections of the elements as a function of energy has been initiated.

The cross sections, or the logarithms of the cross sections, are recorded on the master tape with the corresponding lethargy values. The lethargies are chosen in such a way that the logarithms of the cross sections (or the cross sections themselves) may be assumed to be linear in the lethargy intervals between the recorded points. Whenever the data have been available, or whenever reasonable extrapolation or interpolation has been possible, the data have been recorded from 10^8 to 10^{-4} ev. The negative of the lethargy [$u = \ln (100 \text{ Mev}/E)$] has been recorded in place of the lethargy whenever such estimations have been made.

In addition to cross-section data, the masses and concentrations of the isotopes are stored on the master cross-section tape. A particular cross section is completely identified by three numbers: the atomic number of the element, a code number specifying the isotope or mixture of isotopes, and another code number specifying the type of cross section. A program exists which punches out on paper tape desired cross sections at constant lethargy intervals.

In order to find errors which may have arisen in the processing of the data, an edit program has been written with which a continuous curve of each cross section is plotted on the Oracle. Photographs of these plots may easily be compared with the original cross-section curves from which the data were taken. The practicability of this procedure has already been demonstrated. Whenever possible the data have been independently processed by two people. A program to compare these two sets of data in order to find any major discrepancies is being written.

The total and fission cross-section data[2] are now on the master tape, or are on paper tape ready to be loaded into the machine and written onto the master tape. Since absorption and scattering cross-section data are scarce, a program has been coded to calculate absorption cross sections on the basis of a black absorbing model of the nucleus.

[1]U.S. Army.

[2]D. J. Hughes and J. A. Harvey, *Neutron Cross Sections*, BNL-325 (1955); M. D. Golberg *et al.*, BNL-250 (1954). (Secret).

30. MONTE CARLO MASTER CROSS-SECTION TAPE

R. R. Bate[1] J. H. Marable J. W. Niestle[1]

As an adjunct to the master cross-section tape described above, a second Monte Carlo master cross-section tape has been prepared. This tape has the same basic nuclear information as the master tape itself, but in greater detail and, hence, with a lesser capacity in the number of elements. The arrangement of the cross sections (and other data) on this tape is made with regard to fast access and rapid use in Monte Carlo problems, although it is possible that it can be used profitably for other types of problems. Each cross section for each element is stored in groups which range over a factor of 2 in energy, while within the group the cross sections are given at 64 points equally spaced in energy. This is done so that the range of energies covered by each block is measured by a constant lethargy change, while, within the block, the address in the memory of the cross section desired can be found by a simple linear transformation of the energy for which the cross section is desired. The types of data which can be stored on this tape are total cross sections, scattering cross sections, fission cross sections, mean cosines of scattering angles, etc.

[1]U.S. Army.

31. A PROGRAM COMPILER FOR THE ORACLE

R. R. Bate[1] M. E. LaVerne

In the preparation of the complex Oracle codes which are being designed and written, the need for versatile assembly routine capable of integrating specially written codes with a required selection of standard routines from the subroutine libraries has become apparent. Such a routine, designated as the "Compiler," has been designed and coded. The Compiler has now been in operation for some months and has proved to be a valuable aid to programmers in the preparation of problems for the Oracle.

Terminology used in this report conforms, in general, to the standards in the *Glossary of the Association for Computing Machinery.*[2] Further discussion of the utility for a compiling routine accompanied by an adequate library of subroutines may be found in the *Manual for the Oracle.*[3]

Desirable Characteristics of a Program Compiler

During the course of the logical design of the Compiler a number of features desirable in a good compiling routine were considered for inclusion. A list of such features includes the following:

1. The coding system should be simple and natural.
2. The Compiler should be able to determine what subroutines are needed and to select them automatically from a large library.
3. Cross references between subroutines should be possible without troublesome hand computation of addresses.
4. Needed permanent constants should be automatically selected by the Compiler from a large list.
5. Allocation of storage should be done by the Compiler automatically.
6. Fast storage space should be used economically.
7. A directory of the location of subroutines, permanent constants, and storage should be produced by the Compiler.
8. The record of the final routine should be complete and compact; some flexibility in form should be permitted to allow for personal preferences.
9. Automatic checks should be made at several stages of the compilation to guard against typing and coding errors.
10. If a routine exceeds fast storage capacity it should be separated automatically into segments of the most efficient length.

In the programing of the present Compiler all the above characteristics, except 9 and 10, in part, were incorporated. A number of safeguards against typing errors were included, but automatic checking of coding errors could be done in only the most rudimentary fashion and probably would not have been worth the trouble. A feasible solution to the problem of cross references between subroutines located in different segments of a routine was not found. Hence, as a compromise, this Compiler is limited to compiling one segment of a routine at a time and providing for intersegment storage, with the necessary segmentation and communication among segments being provided by the programmer.

Description of the Compiler System

Every routine is divided into a number of pieces of pseudo codes called "hunks," each in relative coding. Complete cross referencing of hunks is possible, using either or both of two systems: full cross-hunk referencing, in which extra words are used in the pseudo code; and shorthand cross-hunk referencing from, and to, five special hunks, in which extra words are not used. These special hunks may also be referred to by means of the full cross-hunk reference.

Temporary storage is provided for subroutines, and intersegment storage is provided for routines that exceed fast storage and must be split into manageable segments.

Necessary permanent constants are selected automatically from a standard list of 4096 constants.

The Compiler coding system embraces both normal routines and interpretive routines of the three-address and single-address types.

---

[1] U.S. Army.

[2] *Glossary of the Association for Computing Machinery*, Assn. for Computing Machinery Committee on Nomenclature, G. M. Harper, Chairman (June 1954).

[3] M. R. Arnette, *Manual for the Oracle*, sec 5, ORNL CF-53-12-2 (Dec. 1953).

The Hunk Key. – In order to identify a hunk and completely specify its composition a key appears at the beginning of each hunk. The hunk key consists of a hunk number followed by a set of key words specifying the number and type of words appearing in each section of the hunk. These groups of words appear, of course, in the same order as their corresponding key words. On paper tape the key consists of nine words, and on magnetic tape, five, each word being given as a hexadecimal integer.

A paper-tape hunk key contains the following words, in order:

h	Hunk number
v	Variable words to be decoded and oriented
x	Extra words for sentinels and cross-hunk references
c	Constants to be stored unconverted
d	Decimal fractions to be converted
e	Decimal integers to be converted
f	Decimal 8-32 floating-point numbers to be converted
g	Decimal 40-40 floating-point number pairs to be converted
z	Zero words to be provided at the end of the routine

Only five key words are required on magnetic tape because all conversions have been performed, and those numbers identified by c, d, e, f, and g may be lumped together as just constants. The magnetic-tape key is, then, as follows:

h	Hunk number
v	Variable words
$\bar{v}$	Variable plus extra words
$\bar{c}$	Constants ($\bar{c} = c + d + e + f + 2g$)
z	Zero words

The hunk number contains, as an integral part, an indicator that specifies whether the hunk is a normal or interpretive routine and whether it operates on one or more single-address or three-address words.

Subroutine Entries. – Subroutine entries are effected by means of a word of pseudo code in which appear, in order:

1. a sentinel, indicating that the word is a subroutine entry,
2. the relative address of the word to which entry is to be made in the subroutine together with an indication of whether the entry is to the left or right of the word,
3. the subroutine number (hunk number).

If the subroutine is of the interpretive type, with a list of words to be interpreted, the list must follow immediately after the subroutine entry. This list is terminated with a sentinel, an extra word in the pseudo code, in order for the Compiler to determine where the interpreted words end.

The final routine sometimes requires that one of the addresses in the last interpreted word be increased by 800 (hexadecimal) in order to signal the end of the list to the routine. The sentinel also indicates to the Compiler which address of the preceding word is to be so treated.

Cross-Hunk References. – In the full cross-hunk references a special symbolic address replaces the normal relative address in the word, referring to a word in another hunk, and an extra word is inserted by the programmer into the pseudo code after the word containing the symbolic address. If two or three cross-hunk references are made in the same word, two or three extra words are inserted, respectively, in the same order as the references are made. The extra words describe the relative addresses and the hunks referred to.

In the shorthand cross-hunk references the references to frequently used hunks may be shortened by using five special hunks to which reference may be made by replacing the normal relative address in the word, referring to a special hunk by the sum of that hunk number and the relative address referred to in the hunk. The special hunks may also, of course, be referred to by means of the full cross-hunk reference.

Word Locations. – Some complication in specifying the location of a word arises from the presence of the extra words that appear intermingled with the variable words of a hunk before compilation, but are squeezed out when a routine is assembled. The following four means of specifying a word location must be carefully distinguished:

1. absolute address (the fast storage location of a word in the assembled routine),
2. hunk relative address (the location of a word relative to the zeroth word of its hunk in an

assembled routine – note that extra words are not counted),

3. hunk position (the location of a word relative to the zeroth word of its hunk, counting both ordinary and extra words),
4. hunk-tape position (the location of a word on paper tape relative to the zeroth word of its hunk, counting both ordinary and extra words – this may differ from the hunk position because of typing errors).

The last two means of specifying word location are used in correcting typed hunks.

Temporary Storage, Intersegment Storage, Permanent Constants. – References to temporary or intersegment storage and to permanent constants are made through the use of three special hunks (different from those mentioned under "Cross-Hunk References"). Either full or shorthand cross-hunk references may be employed.

Space provided in the final routine for temporary storage is enough to accommodate all the storage positions from the initial through the largest reference to the temporary storage hunk. Similarly, space left for intersegment storage will accommodate all the positions from the initial through the largest reference to the intersegment storage hunk. The length of, and hence the largest reference to, the intersegment storage hunk must be the same in all segments of the routine. Note that these storage hunks do not physically exist, since all that is required is space in the final routine.

Only those permanent constants explicitly referred to in a routine will be selected from the permanent constants hunk and inserted in that routine. The permanent constants hunk, containing 4096 constants, is specially and permanently stored with the Compiler on magnetic tape.

Break Points. – Break points may be inserted in a routine by any of three methods at the programmer's disposal: (1) a paper tape may be used which specifies, for each word in which one or more break points is to be inserted, the hunk number, the relative address of the word in the hunk, and the portion or portions of the word in which a break point is wanted; (2) the full cross-hunk reference may be utilized for this purpose by increasing the relative address in the extra word by 800 (hexadecimal); (3) the usual break-point indication may be used in a protected address.

Special Rules. – The following special rules apply to protected addresses, reference to absolute addresses, and selection of hunks:

1. Protected addresses are those in stop, shift, hunt, and curve-plotter instructions. Such addresses are not changed by the Compiler unless the symbolic address referred to under "Cross-Hunk References" appears, in which case the usual change specified by a cross-hunk reference is made.

2. Absolute addresses may be referred to in the pseudo code by means of a full cross-hunk reference to hunk number OCFFF. The relative address portion of the extra word is inserted unchanged by the Compiler in place of the symbolic address appearing in the pseudo code.

3. Only those hunks will appear in the final routine that are referred to in the basic hunk or in other hunks directly or indirectly called for by the basic hunk. No hunk will appear more than once, regardless of the number of references to it.

Arrangement of the Final Routine. – The initial address of the basic hunk of a routine may be specified by the programmer, but all other addresses in the routine are automatically assigned by the Compiler. The final arrangement in the fast storage is as follows:

1. space from beginning of a fast storage to beginning of basic hunk (generally vacant and unassigned),
2. basic hunk,
3. hunks obtained from the programmer's private library,
4. hunks obtained from the Compiler public library,
5. permanent constants obtained from the Compiler list of permanent constants,
6. temporary storage (generally vacant and, at most, irrelevant),
7. space from end of temporary storage to beginning of intersegment storage (vacant and unassigned),
8. intersegment storage to end of fast storage.

32. MONTE CARLO CALCULATION OF NEUTRON AGE IN WATER

R. R. Coveyou

An Oracle code using the Monte Carlo method has been prepared to compute neutron ages and certain other reactor parameters in mixtures of scatterers and absorbers. This code has been used to compute the age of neutrons from fission spectrum to indium resonance in water and to examine the effect on the age of certain modifications in the input parameters. The motivation for this work was furnished by the well-known discrepancy between the experimental and the computed values of this constant.

If the slowing down and diffusion of neutrons issuing from a plane isotropic monochromatic source in an infinite homogeneous mixture are expressed in terms of the Boltzmann equation, if the Fourier transform of this equation with respect to the space coordinate is taken and this transform, in turn, is expanded in powers of the transform variable, and if the angular distribution is expanded in Legendre polynomials, the following coupled integral equation is obtained:

$$D_{nl}(u) = \sum_i D_{nl}(u')\,\psi_i(u')\,K_{il}(u' \longrightarrow u)\,du' + \delta_{n0}\delta_{l0}\,\delta(u) + \lambda(u)\left[\frac{n(l+1)}{2l+1}\,D_{n-1,l+1}(u) + \frac{nl}{2l+1}\,D_{n-1,l-1}(u)\right] , \tag{1}$$

where

$D(z,u,\mu)$ = collision density at z due to neutrons of lethargy u and direction cosine μ,

$$\tilde{D}(\omega,u,\mu) = \int_{-\infty}^{\infty} e^{i\omega x}\,D(x,u,\mu)\,dx = \sum_{n=0}^{\infty}\frac{(i\omega)^n}{n!}\sum_{l=0}^{\infty}\left(\frac{2l+1}{2}\right)D_{nl}(u)\,P_l(\mu) ,$$

$\lambda(u)$ = mean free path for a neutron of lethargy u,

$\psi_i(u)$ = probability that a neutron of lethargy u will be scattered by a nucleus of element i (or, more generally, by a scattering process of type i),

$K_i(u' \longrightarrow u,\mu_0)$ = probability that a neutron of lethargy u', scattered by a nucleus of element i, will assume lethargy u and be scattered with scattering cosine μ_0

$$= \sum_{l=0}^{\infty}\left(\frac{2l+1}{2}\right)K_{il}(u' \longrightarrow u)\,P_l(\mu_0) .$$

It is noted that, with the conditions stated,

1. $D_{nl}(u) \equiv 0$ if $n < l$ or if $n + l$ is odd,
2. $D_{n0}(u)/D_{00}(u)$ is the nth spatial moment of the collision density at lethargy u,
3. the moments of this plane source problem yield the point source moments by

$$\langle r^n \rangle \text{ point} = (n+1)\,\langle |z|^n \rangle \text{ plane} .$$

The equations which suffice to fix the second moment are:

$$D_{00}(u) = \sum_i \int D_{00}(u')\,\psi_i(u')\,K_{i0}(u' \longrightarrow u)\,du' + \delta(u) , \tag{2}$$

$$D_{11}(u) = \sum_i \int D_{11}(u')\,\psi_i(u')\,K_{i1}(u' \longrightarrow u)\,du' + \frac{\lambda(u)}{3}\,D_{00}(u) , \tag{3}$$

(4) $D_{20}(u)$

$$= \sum_i \int D_{20}(u')\, \psi_i(u')\, K_{i0}(u' \longrightarrow u)\, du' + \\ + 2\lambda(u)\, D_{11}(u) \ .$$

It is this set of equations which is the basis of the procedure. Consider a neutron born with zero lethargy. Its first flight is terminated by a scattering with a nucleus i with probability $\psi_i(0)$, or by absorption with probability $1 - \sum_i \psi_i(u)$. If it survives and is scattered by nucleus i, then it assumes lethargy u, with probability $K_{i0}(0 \longrightarrow u_1)$. The neutron continues in this way until it is absorbed or its lethargy passes beyond the range of interest. Then the behavior of an ensemble of such neutrons is governed by Eq. 2.

Now, consider two parameters of the neutron history, labeled D_{11} and D_{20} and computed by the following rules:

1. initially, $D_{11} = D_{20} = 0$,
2. at each collision, D_{11} is increased by the amount $\lambda(u)/3$,
3. at each scattering, D_{11} is multiplied by

$$K_{i1}(u' \longrightarrow u)\, [K_{i0}(u' \longrightarrow u)]^{-1} \ ,$$

4. at each collision, D_{20} is increased by $2\lambda(u)\, D_{11}$.

Then the computations will have the following properties:

1. The expected values of D_{11} and D_{20} at lethargy u are just $D_{11}(u)$ and $D_{20}(u)$, respectively.
2. For elastic collisions, the quotient in rule 3 is just the scattering cosine.
3. If a large number of neutrons is followed from source to terminal lethargy, a history at that collision which throws the neutron across the terminal lethargy being completed, then the average of D_{20} over such histories is an estimate of the second spatial moment of the slowing-down distribution at the terminal lethargy.
4. In the interpretation of results care must be taken to distinguish between the quantity computed here (τ_q in the notations of Hurwitz and Zweifel[1]) and the quantity τ_N which is sometimes computed and is, usually, that measured in an experiment. (The quantity τ_N is computed from the second moment of the flux at the detection lethargy and is slightly larger.)

In the actual code, further refinements are made which increase the efficiency of the calculation greatly. For instance, the calculation can be so arranged that no square root, logarithm, exponential, or trigonometric function need be calculated (at least, for elastic scattering). That the method as so far explained is already more efficient than a straightforward Monto Carlo, which is used to compute the position of the neutron, is seen from the following considerations. The method used could start from a consideration of the squared distance traveled by a neutron throughout its history. Close examination of the expression for this quantity shows that the path lengths and the azimuths of scattering angles can be averaged analytically, and the result is the procedure given here. (Historically, this is the way it was designed.) But, with the quantities averaged out, there disappears also the variance of the estimate springing from the variability of these quantities.

The method is capable of further refinement and extension to higher spatial moments, and, indeed, can be made to yield almost all parameters necessary to describe the behavior of fast neutrons (resonance escape probability, fast fission effect, removal and transfer cross sections, fast lifetimes, etc.). A code is being designed to exploit these possibilities.

[1] H. Hurwitz, Jr., and P. F. Zweifel, *Slowing Down of Neutrons by Hydrogenous Moderators*, KAPL-1269 (Feb. 10, 1955).

33. NUMERICAL INTEGRATION OF THE ONE-VELOCITY BOLTZMANN EQUATION

J. H. Marable

Approximate solutions of the transport equation for one-velocity neutrons may be found by means of a program which has been coded for the Oracle. These solutions are found by a numerical integration technique. The number of space points allowed is essentially unlimited, and the number of regions of solid angle (indicating the velocity direction of the neutron) may range through the even numbers from 2 to 20, inclusive.

There can be but one homogeneous and isotropic medium, and this must have either plane or spherical symmetry. The outer boundary condition is that of a bare reactor; that is, no neutrons enter the medium through its external surface.

There are two types of problems which can be solved by means of this program: (1) the eigenvalue problem associated with a critical system and (2) the problem of the flux distribution resulting from an arbitrary isotropic source of neutrons. In both types the scattering of neutrons need not be assumed to be isotropic.

---

34. SOME REMARKS ON THE SLOWING DOWN OF NEUTRONS IN HYDROGEN

T. A. Welton[1] L. C. Biedenharn[2]

A unique feature of hydrogenous moderators is that a neutron can lose all its energy in a single collision with a hydrogen atom, which rules out any straightforward use of the Fermi age theory. A very convenient and ingenious amalgam of the Fermi age theory for the heavy elements and an approximate non-age theory for hydrogen has been suggested by Goertzel and Selengut.[3] Their technique, called "the G-S approximation," is subject to a basic criticism in that it neglects, in the hydrogen moderation, the strong correlation of the energy loss of the neutron with angle. The usual P_1 approximation in the Boltzmann equation is already sufficient to handle this complication. Hence it is of interest to compare the predictions of the two theories in order to investigate the effect of neglecting the energy loss–angle correlation.

The discussion is confined to the case of pure hydrogen as regards the slowing-down action. It is possible in this case to calculate the age exactly in the P_1 approximation. This is compared with the G-S results. Attention is paid to both the second moment of the flux and the second moment of the slowing-down density. A large part, although not all, of the difference between the two results is due to the much longer first flight in the G-S approximation. This is due to the appearance of $\Sigma_{TR} = \frac{1}{3}\Sigma$ rather than Σ itself in the expression for first flight. Numerical comparisons have been presented[4] for the case of constant hydrogen cross section and for the observed n-p scattering cross section.

---

[1]Physics Division.

[2]The Rice Institute.

[3]G. Goertzel, *Criticality of Hydrogen Moderated Reactors*, TAB-53 (July 1950); D. Selengut, private communication to G. Goertzel.

[4]L. C. Biedenharn and T. A. Welton, *Some Remarks on the Slowing Down of Neutrons in Hydrogen*, ORNL-2107 (Aug. 10, 1956).

35. NEUTRON SLOWING DOWN BY HYDROGEN IN THE CONSISTENT P_1 APPROXIMATION

A. Simon

It is customary to use the age-diffusion approximation in calculating the criticality of systems which do not contain hydrogen. When hydrogen is present, however, it is clear that this method is inappropriate, since the age-diffusion theory assumes continuous slowing down, while the neutron can actually lose all its energy in a hydrogen collision. This situation has been partially remedied by the introduction of the Goertzel-Selengut (G-S) method,[1] which in effect makes use of the correct distribution of energy loss suffered by a neutron in a collision with a proton but neglects the correlation between energy loss and angle of scattering. The scattering by the heavier elements is treated in the same fashion as in the age-diffusion approximation.

The neglect of energy-angle correlation in the G-S theory has at least one well-known consequence in that the predicted age in hydrogen, with the heavier elements considered as non-slowing-down, is incorrect.[2] On the other hand, it is equally well known that when the energy-angle correlation is included in a consistent manner, the age is then given correctly.[3] Since the starting point of all these approximation methods is the P_1 approximation to the Boltzmann equation, and since the energy-angle correlation in hydrogen may be included in a consistent manner, this last method is often referred to as the consistent P_1 approximation.

In the preceding paper Biedenharn and Welton[4] have used the P_1 equations to obtain an expression for the age in pure hydrogen. In many reactor applications, however, higher moments of the neutron density play an important role. Hence it is of interest to obtain solutions for the slowing-down density itself in the P_1 approximation. Such solutions have been obtained[5] for two special cases. One of these is for pure hydrogen with zero absorption ($\Sigma_A^H = 0$), hydrogen having a $1/v$ scattering cross section ($\Sigma_S^H \sim 1/v$). The second is for all cross sections constant.

These results may be compared with the corresponding result for the slowing-down density in the G-S theory.[2] The results for the $1/v$ case are illustrated in Fig. 35.1. Here B is the buckling of the flux and q the slowing-down density. Note that the initial slope, which is the age, is larger for the G-S theory. However, the slowing-down density ultimately becomes smaller in the P_1 theory and even becomes negative for sufficiently large

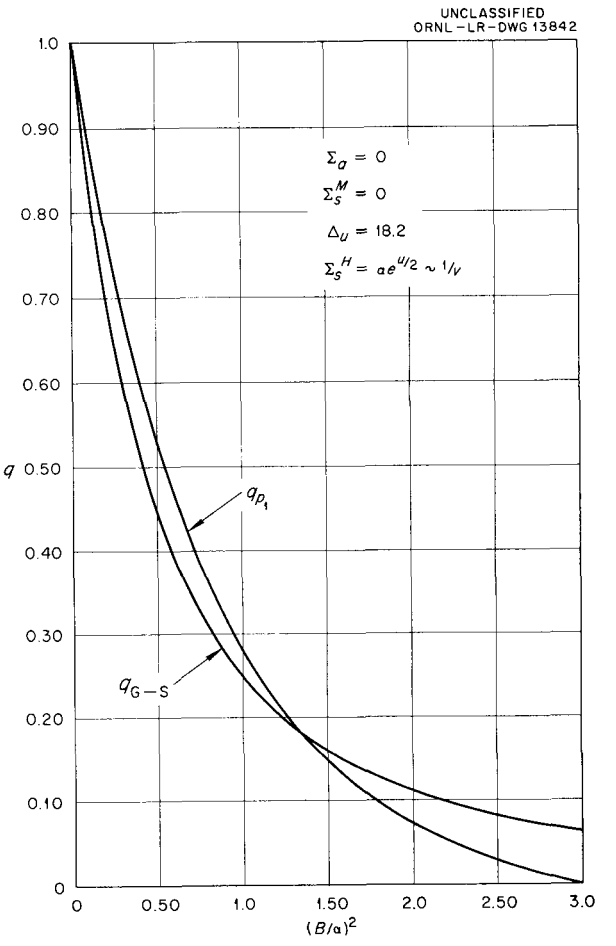

Fig. 35.1. Variation of Slowing Down with Buckling for the $1/v$ Case.

[1] G. Goertzel, *Criticality of Hydrogen Moderated Reactors*, TAB-53 (July 1950); D. Selengut, private communication to G. Goertzel.

[2] H. Hurwitz, Jr., and P. F. Zweifel, *Slowing Down of Neutrons by Hydrogenous Moderators*, KAPL-1269 (Feb. 10, 1955).

[3] R. E. Marshak, *Revs. Mod. Phys.* 19, 201 (1947).

[4] L. C. Biedenharn and T. A. Welton, *Some Remarks on the Slowing Down of Neutrons in Hydrogen*, ORNL-2107 (Aug. 10, 1956).

[5] A. Simon, *Neutron Slowing Down by Hydrogen in the Consistent P_1 Approximation*, ORNL-2098 (July 5, 1956).

buckling. This last effect may be understood by realizing that the neutron flux becomes highly singular in angle for large bucklings. Furthermore, the important contribution to the slowing down is then made by neutrons which have suffered large-angle collisions. If an attempt is made to fit a singular function with only two spherical harmonics, the resulting fit is usually negative in the backward direction. For example, the expression of a delta function in spherical harmonics is

$$\delta(\theta) \cong \frac{1}{2}(1 + 3\cos\theta)$$

and is negative in the backward direction.

A typical result for the case of all cross sections constant is shown in Fig. 35.2. The first flight is no longer important in determining the age, and, hence, the initial slopes are almost identical. Differences between the P_1 and G-S results are only seen at large bucklings.

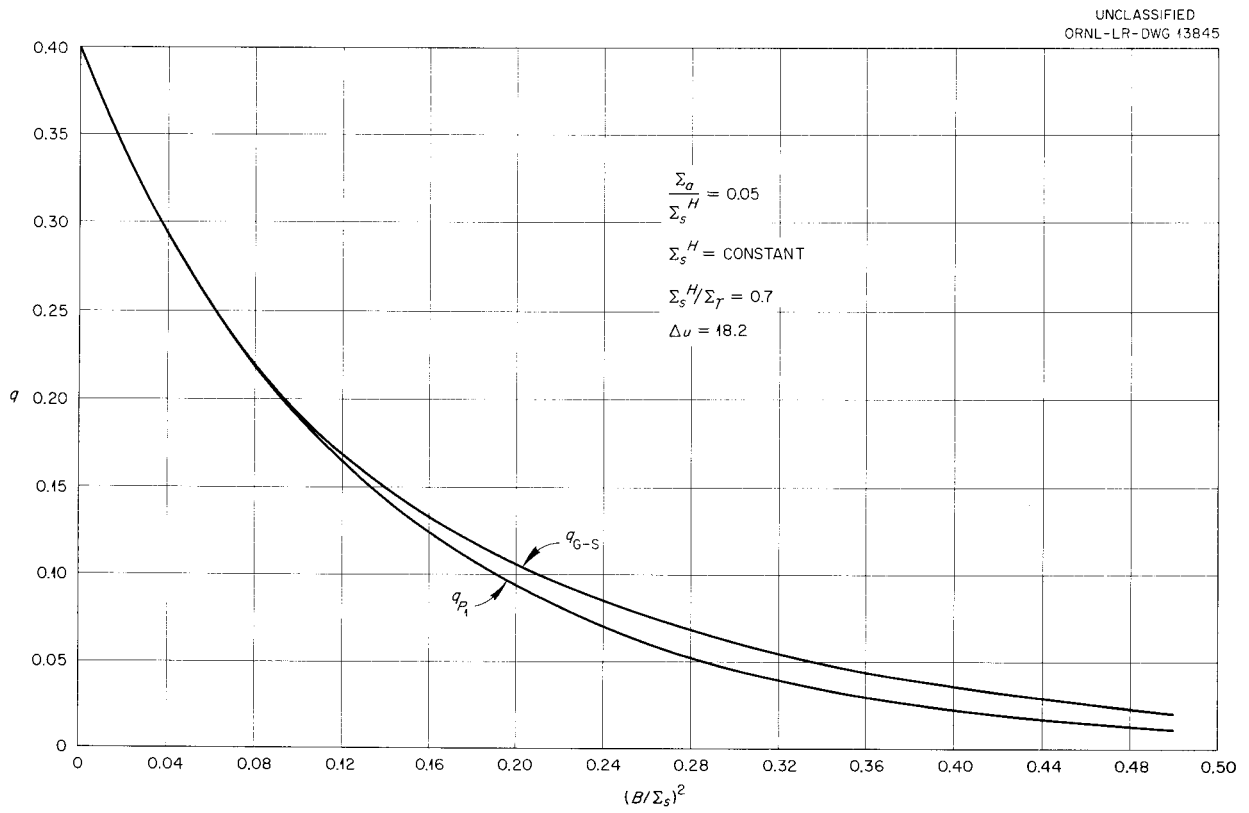

Fig. 35.2. Variation of Slowing Down with Buckling When All Cross Sections Are Constant.

Part V

SHIELDING RESEARCH

36. ATTENUATION BY WATER OF THE FAST-NEUTRON DOSE RATE FROM THE BSR

T. V. Blosser

The first fast-neutron dose attenuation measurement was made in the water of the BSF in 1951. Since that time there has been considerable additional development of neutron dosimeters. Also, since the maximum power level of the BSR has been increased by a factor of 100, measurements can now be made through larger water thicknesses. Therefore, a new set of fast-neutron dose measurements was made in the water at various distances (up to 180 cm) from the north face of loading No. 33 of the BSR (5 by 6 element loading, see Fig. 4.1 of Chap. 4).

To obtain measurements out to 180 cm from the reactor, three types of Hurst dosimeters[1,2] (phantom, absolute, and three-section) and two sizes of Hornyak buttons[3] (see also, Chap. 49) were used. The Hornyak buttons were 2 in. in diameter, one being $^3/_{16}$ in. thick and the other 1 in. thick.

Instrument Calibration

The gamma-ray response for each detector was determined by placing it in a known gamma-ray field and discriminating at a level which excluded gamma-ray pulses at the levels shown in Table 36.1.

The response of each detector to neutrons, at its listed gamma-ray discrimination level, was determined by placing the counter in a known neutron flux from a Po-Be source. In the case of the Hornyak buttons the response to neutrons was used as a check for consistency of the equipment. When measurements were made in the water, the Hornyak button dose data were normalized to a Hurst-type dosimeter.

[1] G. S. Hurst, R. H. Ritchie, and H. N. Wilson, *Rev. Sci. Instr.* **22**, 981 (1951).

[2] G. S. Hurst, *Brit. J. Radiol.* **27**, 353 (1954).

[3] W. F. Hornyak, *Rev. Sci. Instr.* **23**, 264 (1952).

TABLE 36.1. UPPER LIMIT OF GAMMA-RAY DISCRIMINATION LEVELS OF NEUTRON DETECTORS

Detector	Gamma-Ray Field (ergs per gram of tissue per hour)
Phantom Hurst dosimeter	1400
Absolute Hurst dosimeter	400
Three-section Hurst dosimeter	500
1-in.-thick Hornyak button	3700
$^3/_{16}$-in.-thick Hornyak button	3700

The absolute Hurst-type dosimeter was used to compare the previous Po-Be source calibration result with that of the neutron dose in terms of the strength of an alpha source (Pu^{239}). The alpha particles were admitted to the active volume of the counter (determined by means of field tubes) by removing the source cover with the external electromagnet. The response of the counter to alpha particles, neutrons, and gamma rays is shown in Fig. 36.1. The alpha-particle integral pulse-height curve showed that 109 v corresponds to the mean range for this particular wire size and ethylene filling. If this point is taken as 5.14 Mev, the energy of the alpha particles, the instrument can be calibrated in terms of particle energy (Mev) as follows:

$$D = \frac{RCf}{g_{ethylene}} A_n ,$$

where

D = dose (ergs per gram of tissue per second),

R = ratio of the energy of the alpha particle to to the mean range pulse height (Mev/v),

C = 1.60×10^{-6} ergs/Mev,

f = 0.69, a correction factor to take into account that a gram of ethylene absorbs more energy in a given neutron flux than a gram of tissue in the same flux, that is, response per gram of tissue divided by response per gram of ethylene,

g = weight of material (g),

A_n = area of neutron integral pulse-height curve (v/sec).

From the values for the energy of the alpha particle and pulse height at mean range, as given above, $R = 0.0473$ Mev/v for the absolute dosimeter. The mass of ethylene gas for the filling used was

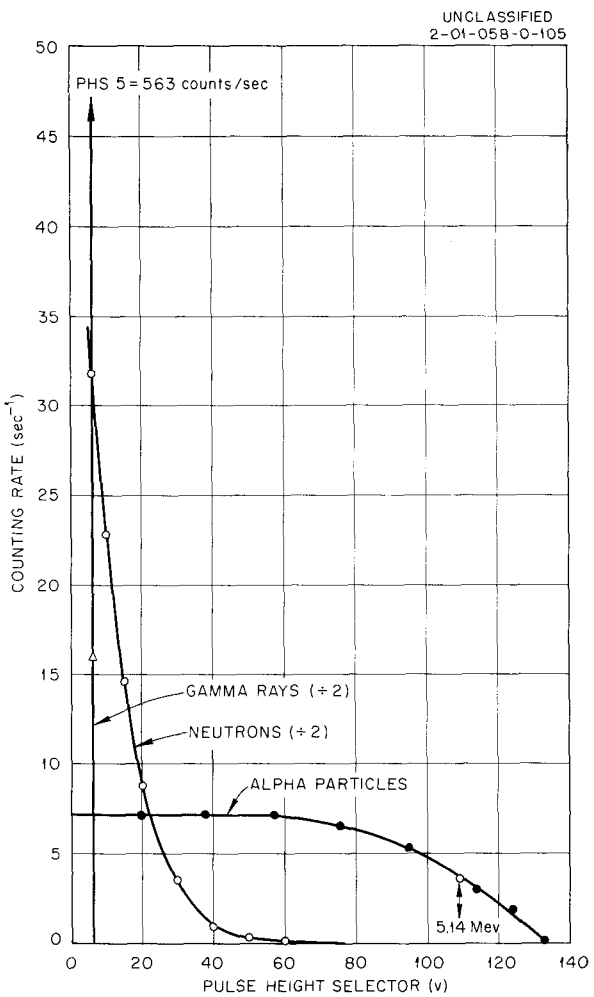

Fig. 36.1. Response of Absolute Hurst Dosimeter to Sources of Alpha Particles, Neutrons, and Gamma Rays.

0.064 g at STP. Solving for D,

$$D = (8.16 \pm 0.7) \times 10^{-7} A_n \text{ (ergs per gram of tissue per second)} \div \text{(v/sec)} \quad .$$

The calibration of the absolute dosimeter by use of a Po-Be source was performed in air. For this purpose the dose resulting from single neutron collisions was calculated for the previously measured neutron spectrum.[4] On comparing this expected dose with the actual instrument response, A_n, a calibration factor is obtained, giving for the dose:

$$D = (8.92 \pm 0.9) \times 10^{-7} A_n \text{ (ergs per gram of tissue per second)} \div \text{(v/sec)} \quad .$$

The agreement with the alpha-source calibration is well within the combined limits of error.

Determination of Centers of Detection[5]

For measurements made in air, the distance from a source to a detector can be approximated rather closely by measuring to the geometric center of the detector. However, this is not true in the case of the 1-in.-thick Hornyak button, which is thick with respect to both the length of a proton recoil and a characteristic attenuation length for the light of scintillation in the medium.

Therefore, for the Hornyak button the center of detection in air was determined experimentally by making observations of the counting-rate variation with distance from the detector to the neutron source. The distances covered were from 20 to 120 cm, and the center of detection was determined to be very near the button-phototube interface. This scheme was also applied to the Hurst dosimeter.

When making measurements in a medium such as water, the center of detection of any detector is uncertain owing to the unknown angular distribution of the neutron flux. For these water measurements the phantom dosimeter, which has a radius of 0.45 cm, was used as a standard, and the larger detectors were normalized to it.

Experimental Procedure and Results

Prior to the measurements the reactor was operated at high powers (100 kw and 1 Mw), and thus the large fission-product gamma-ray dose, which affects neutron detector operation, limited the closest approach to the reactor. Since the neutron-to-gamma-ray ratio decreases rapidly with distance, a 1.5-in.-thick lead slab was placed 40 to 50 cm

[4] B. F. Whitmore and W. B. Baker, *Phys. Rev.* 78, 799 (1950).

[5] H. E. Hungerford, *Center of Detection Calculations for Neutron Counters and Ion Chambers*, ORNL CF-51-5-177 (May 14, 1951).

from the reactor, when needed, to attenuate the gamma-ray flux.

Plots of the fast-neutron dose measured in the water along the reactor center line are shown in Fig. 36.2 in terms of ergs per gram of tissue. Previously, fast-neutron data were reported in rep units (roentgen equivalent physical); 1 rep is equivalent to 93 ergs. The dashed curve in Fig. 36.2 is from the 1951 measurements,[6] which are 10 to 12% lower than the current data. The 1951 data have been corrected for the latest calibration of the reactor power[7] and for the change in the nitrogen cross-section data[1,2] used in determining values for the dose curve due to single neutron collisions in tissue.

There is a separation between the 1951 and the 1956 data, which increases slowly beyond 120 cm. At the last point of the 1951 measurements (160 cm) this total separation is 20 to 25%. It is known that for distances past 100 cm the photoneutrons produced from the deuterium in water become detectable in the thermal-neutron flux measurements. During the 1951 measurements a larger lead thickness (3 in.) was used to shield out the gamma-ray flux, which would also reduce the neutron dose.

When a comparison is made with data for the Ground Test Reactor (GTR) at Convair[8] (dotted curve in Fig. 36.2), agreement in the absolute magnitude is indicated to within approximately 16%. This deviation is not surprising because of the geometrical differences in reactor configurations. The GTR loading was a 5 by 7 element loading with the four corners missing. The shapes of the two curves agree very well in the region of overlap.

[6] R. G. Cochran and H. E. Hungerford, *Fast Neutron Dosimeter Measurements for Experiment 1 in the Bulk Shielding Facility*, ORNL CF-51-5-61 (May 7, 1951).

[7] J. L. Meem, E. B. Johnson, and H. E. Hungerford, ORNL CF-53-5-21 (May 12, 1953) (Secret).

[8] E. W. Hessee, CVAC-238T (April 20, 1955) (Secret).

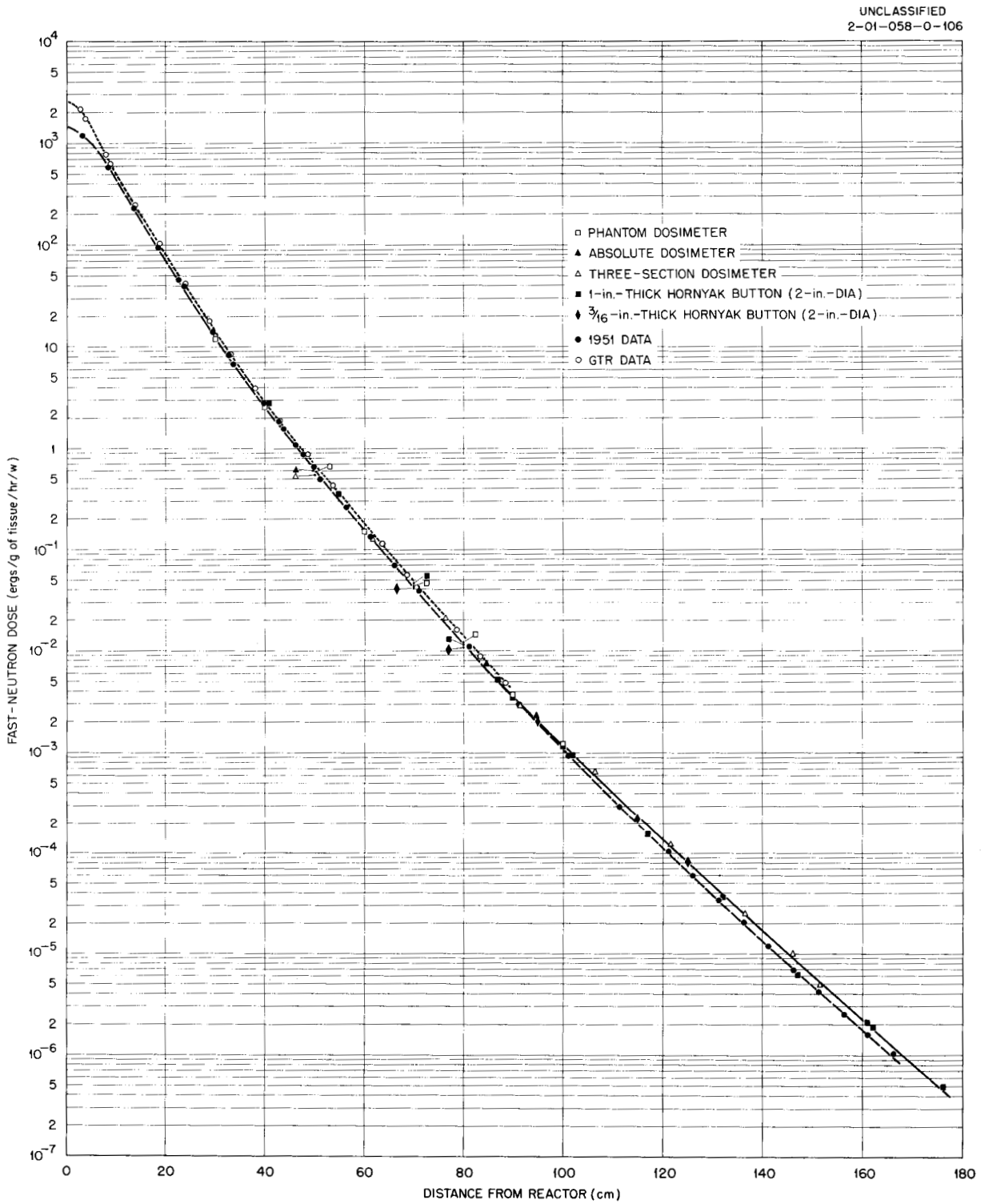

Fig. 36.2. Attenuation by Water of the Fast-Neutron Dose Rate from the BSR.

37. STUDY OF NUCLEAR AND PHYSICAL PROPERTIES OF THE ORNL GRAPHITE REACTOR SHIELD

T. V. Blosser
G. W. Bond[1]
L. A. Lee[1]
D. T. Morgan[1]
J. F. Nichols[1]
T. O. P. Speidel[1]
D. W. Vroom[1]
M. A. Welt[1]
R. C. Reid[1]
A. B. Reynolds[1]

Since the construction of the ORNL Graphite Reactor 12 years ago, the concrete shield around the reactor has been subjected to intensive radiation. Since there is no experimental information about the structural and nuclear durability of concrete for such long exposures to a fission source, an experiment was initiated to investigate the properties of the concrete in this reactor shield.

The shield of the ORNL Graphite Reactor is 7 ft thick and consists of three sections of concrete. The inner foot adjacent to the graphite lattice and the outer foot are composed of ordinary Portland concrete. Sandwiched between these 1-ft sections of ordinary concrete is a 5-ft thickness of barytes-haydite concrete. The water content of the barytes-haydite is roughly twice that of the ordinary concrete and its density is slightly greater. A 1-in.-thick layer of asbestos separates the shield from the graphite lattice, and thin coatings of water-proofing tar separate the ordinary concrete from the barytes-haydite concrete.

In order to determine the neutron and gamma-ray attenuation properties of the concrete, a $4\frac{5}{8}$-in.-dia hole was drilled through the shield in increments of either 1 or $\frac{1}{2}$ ft at the center of the south face of the reactor. The gamma-ray and fast-neutron doses and the thermal-neutron flux were determined as a function of shield thickness by measuring these doses after each incremental drilling. The method of taking attenuation data as the drilling proceeded was adopted to ensure that the shield between reactor and detector was undisturbed. Other experiments to measure in-place shielding have failed because the hole was first drilled and then filled with plugs, the measurements being made between plug sections. Leakage around the plugs was in each case excessive. In the present experiment, concrete plugs were placed behind all gamma-ray and neutron detectors (i.e., between the detector and the outside edge of the shield) in order to obtain a shield medium as nearly homogeneous as possible. Compressed air rather than water was used to cool the diamond core drill in order to prevent the introduction of water into the drilling region.

Gamma-ray dose rate measurements were made with a 50-cc ionization chamber and a gamma-sensitive film. The results of both methods are presented in Fig. 37.1. At each drilling depth, measurements were also made while the detector was moved outward from the bottom of the hole. These measurements are represented in Fig. 37.1 by the curves extending to the right of the dose curve for the bottom of the hole. After the third drilling (shield thickness = 4 ft), the graphite plugs in the experimental holes adjacent to the holes being drilled for this experiment were

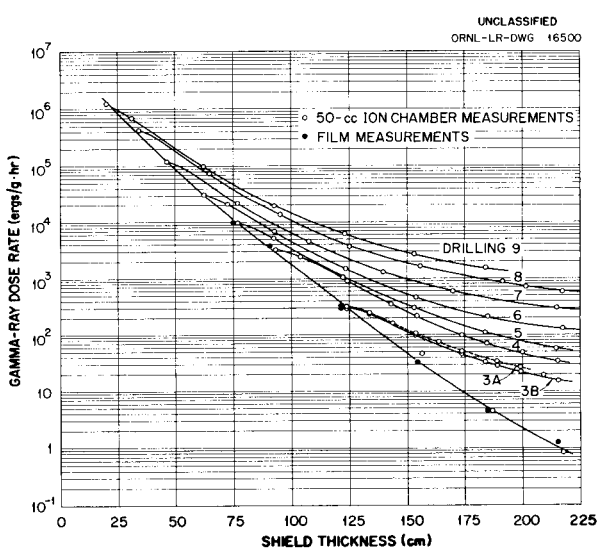

Fig. 37.1. Gamma-Ray Dose Rate as a Function of the Shield Thickness of the ORNL Graphite Reactor.

[1]MIT Engineering Practice School, Gaseous Diffusion Plant, Oak Ridge, Tennessee.

removed and replaced by close-fitting concrete plugs. Measurements for drilling 3A, represented by the dashed curve in Fig. 37.1, were made before the graphite plugs were removed; measurements for drilling 3B were made after the graphite plugs were replaced by concrete plugs.

Fast-neutron dose rates were measured with a Hurst dosimeter, with the response to gamma rays biased out. In order to permit biasing out the intense gamma-ray field present for shield thicknesses less than 3 ft, measurements were made at reduced power levels, and the results were normalized to a power level of 3500 kw.

The results of the fast-neutron dose measurements, with the detector in the same positions as for the gamma-ray measurements, are presented in Fig. 37.2. The plots of two of the measurements, curves 1 and 2 in Fig. 37.2, have irregular shapes with relation to the other traverses. The data for curve 1 were taken while the graphite plugs mentioned above were located in neighboring experimental holes. The other traverse at this shield thickness was made after the graphite plugs were replaced by concrete plugs. At the time that the measurements for curve 2 were taken, an exceptionally high background was encountered which seriously affected the calibration of the dosimeter. This high background was caused by radiation, from a nearby experimental hole, resulting from the temporary replacement of the concrete plugs with an experimental graphite plug during a normal Monday shutdown.

Thermal-neutron flux measurements were made with bare and cadmium-covered gold and indium foils. Gold foils were used for measurements at shield thicknesses of 4 ft and less, and indium foils were used for thicknesses of 7 to 1.5 ft. The results of these measurements are presented in Fig. 37.3.

Chemical and physical properties of the concrete which was removed during the drillings are being determined, but the complete results are not yet available. The temperature gradient through the shield will also be measured by inserting into the hole a 7-ft-long concrete plug in which 12 thermocouples will be embedded 1 to 15 in. apart. In addition, fast-neutron spectral measurements will be made. The entire experiment will be reported in a topical report.[2]

[2] T. V. Blosser *et al.*, *Study of Nuclear and Physical Properties of the ORNL Graphite Reactor Shield*, ORNL-2195 (to be published).

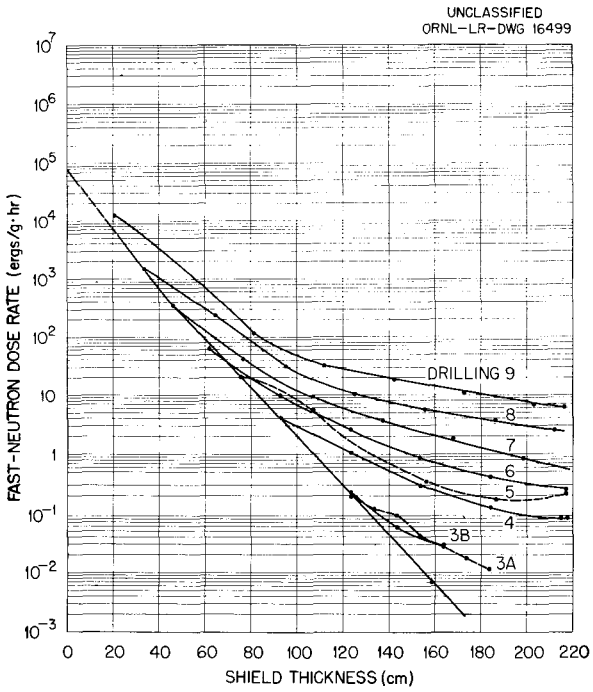

Fig. 37.2. Fast-Neutron Dose Rate as a Function of the Shield Thickness of the ORNL Graphite Reactor.

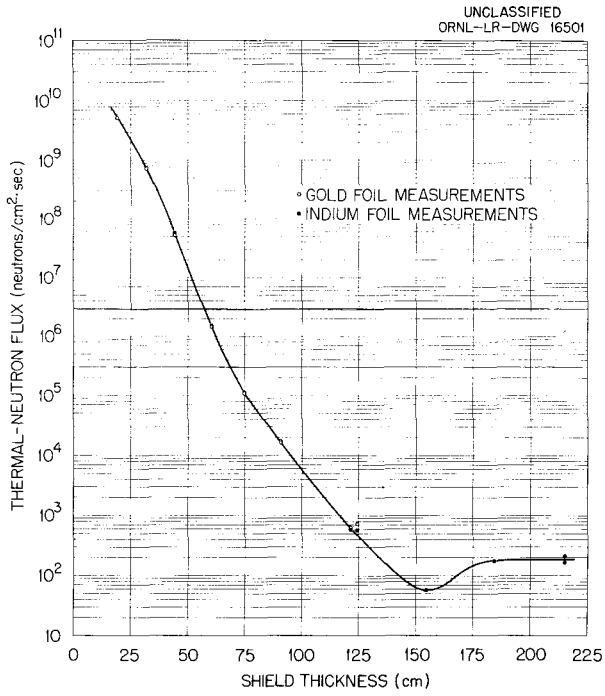

Fig. 37.3. Thermal-Neutron Flux as a Function of the Shield Thickness of the ORNL Graphite Reactor.

38. RADIATION ATTENUATION CHARACTERISTICS OF STRUCTURAL CONCRETE

J. M. Miller

The physical properties of the various types of concrete have been discussed in several publications,[1] as well as the attenuation by various concretes of radiation from radioactive sources.[2,3] However, there have been no measurements of the attenuation by concrete of radiation from a fission source. Since the shields of many stationary reactors will probably be made of concrete, a series of tests to determine the radiation attenuation characteristics of structural concrete have been performed at the LTSF.

Experimental Procedure

The LTSF is a 7 × 7 × 11 ft tank of water which acts as a "lid" to a 32 × 28 in. hole through the 7-ft-thick concrete shield of the ORNL Graphite Reactor. There is a 28-in.-dia uranium converter plate, or source plate, at the outside of the hole. This plate consists of a rectangular array of natural uranium slugs (1.1 in. in diameter and 4 in. long), which are activated by thermal neutrons from the reactor, thus producing a fission source.

The concrete-shield configurations were placed near the source in the water of the LTSF. They consisted of 2-in.-thick concrete slabs, 56 in. high by 64 in. wide, in various arrangements (see Fig. 38.1 and Table 38.1). The slabs were painted with Amercote to prevent them from absorbing water during the experiment. The analysis of the concrete, which had an average density of 2.39, is given in Table 38.2.

All the experiments were performed in a steel tank which was positioned in the LTSF so that one side of the tank was as close as possible to the source plate. An aluminum window in the source side of the tank suppressed the production of capture gamma rays in the steel.

The water content in each configuration is shown in Table 38.3. The thickness of the configurations given in the table extended from the slab side of the aluminum window to the slab side of the water behind the concrete. There were spaces between some of the slabs when they were placed in adjacent positions because some of them were bowed.

Measurements of the attenuation of the fast-neutron dose rate, thermal-neutron flux, and gamma-ray dose rate were made along the source axis in the water beyond the concrete. A Hurst dosimeter[4] was used to measure the fast-neutron dose

[1] Most of these publications are included in a bibliography by T. G. Linxweiler, *Concretes for Radiation Shielding; A Bibliography*, HW-24071 (April 9, 1952).

[2] E. J. Callan, *J. Am. Concrete Inst.* **50**, 17 (Sept. 1953).

[3] B. E. Foster, *J. Am. Concrete Inst.* **50**, 45 (Sept. 1953).

[4] G. S. Hurst and R. H. Ritchie, *A Count-Rate Method of Measuring Fast Neutron Tissue Dose*, ORNL-930 (Jan. 30, 1951).

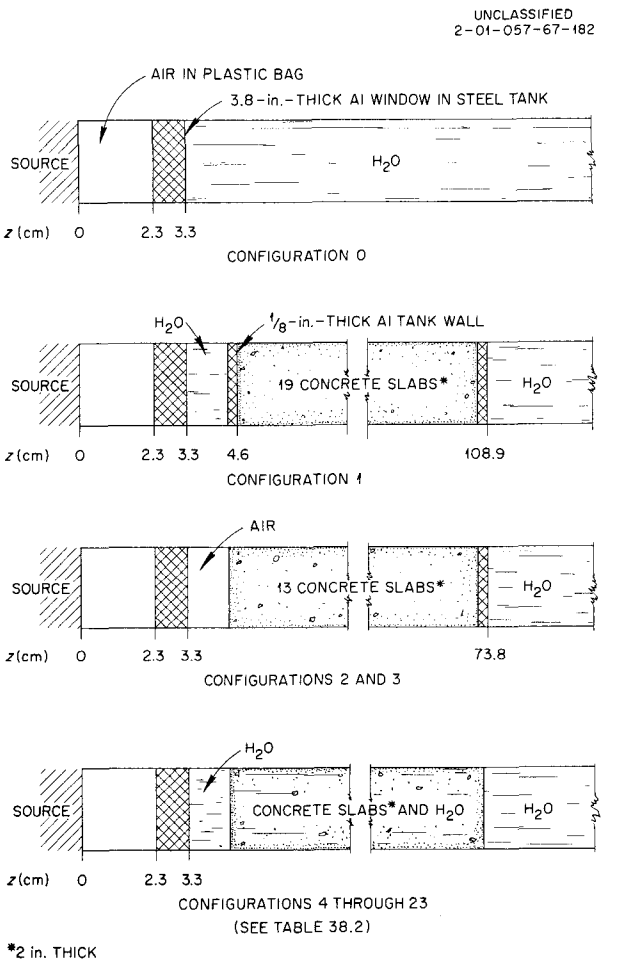

Fig. 38.1. Concrete Configurations Tested at the LTSF.

TABLE 38.1. DESCRIPTION OF CONCRETE CONFIGURATIONS TESTED AT LTSF*

Configuration No.	Description
0	A water-filled steel tank with $\frac{3}{8}$-in.-thick Al window on the source wide was placed in the water of the LTSF; the 2.3-cm space between the Al window and the source was filled with air contained in a plastic bag
1	An Al tank ($\frac{1}{8}$-in.-thick walls) filled with 19 dry 2-in.-thick concrete slabs was placed inside the steel tank; the $\frac{3}{8}$-in. space between the Al window of the outer tank and the Al wall of the inner tank was filled with water
2	13 dry 2-in.-thick concrete slabs were placed inside the steel tank; the $\frac{3}{8}$-in. space between the Al wall and the first slab was filled with air; the water-filled Al tank was positioned behind the concrete
3	Same as configuration 2 except concrete slab section was flooded with water
4	Same as configuration 3 except Al tank was removed
5	Same as configuration 4 but with $\frac{1}{8}$-in.-thick water gaps between slabs
6	Same as configuration 4 but with $\frac{1}{2}$-in.-thick water gaps between slabs
7	Same as configuration 4 but with $\frac{1}{4}$-in.-thick water gaps between slabs
8	2 adjacent slabs in water-filled steel tank
9	4 adjacent slabs in water-filled steel tank
10	Same as configuration 8 but 6 slabs were used
11	Same as configuration 8 but 8 slabs were used
12	Same as configuration 8 but 12 slabs were used
13	Same as configuration 8 but 16 slabs were used
14	Same as configuration 8 but 19 slabs were used
15	Same as configuration 8 but 22 slabs were used
16	2 adjacent slabs followed by $\frac{1}{2}$-in.-thick water followed by 2 adjacent slabs followed by $\frac{1}{2}$-in. water gap, etc. for a total of 22 slabs
17	Same as configuration 16 except for a total of 20 slabs
18	Same as configuration 16 except for a total of 18 slabs
19	Same as configuration 16 except for a total of 16 slabs
20	Same as configuration 16 except for a total of 12 slabs
21	Same as configuration 16 except for a total of 8 slabs
22	Same as configuration 16 except for a total of 6 slabs
23	Same as configuration 16 except for a total of 4 slabs

*See also, Fig. 38.1.

TABLE 38.2. CHEMICAL ANALYSIS OF THE CONCRETE TESTED AT THE LTSF

Density = 2.39 g/cm^3; analyses based on three samples

Constituent	Concentration (wt %)	Constituent	Concentration (wt %)
Loss on ignition	25.32	K	0.18
Insoluble residue*	30.51	Ca	24.33
SO_3	0.73	Mg	2.40
SiO_2	30.63	H	0.83
Fe_2O_3	1.57	C	4.92
Al_2O_3	6.68	O	46.7
P	0.31	Al	3.54
Mn	0.11	Si	14.3
CO_3	24.62	S	0.29
H_2O**	7.48	Fe	1.10
Na	0.45		

*Insoluble in HCl.

**Includes water of hydration.

rate. Thermal-neutron flux measurements were made with a 12½-in. BF_3 counter,[5] as well as with two fission chambers (3-in.- and ½-in.-dia U^{235} plates). The gamma-ray dose rate measurements were made with a 900-cc graphite-lined ionization chamber.[6]

Effective Removal Cross Section

The macroscopic neutron removal cross section Σ_R was calculated, from which the mass attenuation coefficient $\Sigma_R/\rho = (3.6 \pm 0.2) \times 10^{-2}$ cm^2/g was obtained. This value is in good agreement with $\Sigma_R/\rho = 3.7 \times 10^{-2}$ cm^2/g (Table 38.4), which was obtained by taking the sum of the products of the per cent by weight of each element (obtained from the chemical analysis) and the mass attenuation coefficient (obtained from a graph of Σ_R/ρ as a function of the mass of the element[7]).

[5] B. B. Rossi and H. H. Staub, *Ionization Chambers and Counters; Experimental Techniques*, McGraw-Hill, New York, 1949.

[6] L. H. Ballweg and J. L. Meem, *A Standard Gamma-Ray Ionization Chamber for Shielding Measurements*, ORNL-1028 (July 9, 1951).

[7] G. T. Chapman and C. L. Storrs, *Effective Neutron Removal Cross Sections for Shielding*, ORNL-1843, p 26 (Sept. 19, 1955).

The macroscopic removal cross section of concrete was derived from the following formula:[7]

$$\frac{D_1(z)}{D_2(z+t)} = \frac{\lambda_1}{\lambda_2}\left(\frac{z+t}{z}\right)^2\left(1 - \frac{a^2 t}{4\lambda z(z+t) - a^2 z}\right)e^{\Sigma_R t},$$

where

$D_1(z)$, $D_2(z+t)$ = doses as measured without and with the concrete inserted,

a = radius of the circular source (cm),

λ_1 = relaxation length in water alone (cm),

λ_2 = relaxation length in water behind sample (cm),

λ = average of λ_1 and λ_2,

z = source-detector distance without concrete sample (84 cm),

t = thickness of concrete (66 cm),

Σ_R = macroscopic removal cross section.

The limit of error was deduced from uncertainties in the quantities used in the above formula.

TABLE 38.3. WATER THICKNESSES IN CONCRETE SHIELDING CONFIGURATIONS

Configuration No.	Thickness (cm)	Number of Slabs	Water Thickness (cm)			Other Materials (cm)
			In Slabs*	Between Slabs	Total	
1	105.6	19	7.2	0.0	7.6	0.6 Al, ~7 air
2	70.5	13	4.9	0.0	4.9	0.3 Al, ~4 air
3	70.5	13	4.9	3.2	9.1	0.3 Al
4	71.3	13	4.9	4.2	10.1	
5	74.3	13	4.9	7.2	13.1	
6	86.5	13	4.9	19.4	25.3	
7	78.0	13	4.9	10.9	16.8	
8	11.3	2	0.8	0.1	1.9	
9	22.4	4	1.5	1.4	3.9	
10	33.7	6	2.3	2.2	5.5	
11	45.8	8	3.0	4.2	8.2	
12	66.6	12	4.6	4.4	10.0	
13	89.6	16	6.1	7.3	14.4	
14	106.0	19	7.2	8.5	16.7	
15	123.8	22	8.3	10.9	20.2	
16	135.7	22	8.3	22.8	32.1	
17	122.8	20	7.6	20.0	28.6	
18	109.6	18	6.8	17.1	24.9	
19	97.5	16	6.1	15.2	22.3	
20	73.0	12	4.6	11.0	16.6	
21	50.6	8	3.0	9.0	13.0	
22	36.9	6	2.3	5.4	8.7	
23	24.3	4	1.5	3.0	5.5	

*Includes water of hydration.

Discussion

The purpose of this investigation was to determine the effect of the water content on ordinary concrete neutron attenuation and, to a limited extent, its effect on gamma-ray attenuation. In Fig. 38.2 is shown the thermal-neutron flux at each of two fixed distances (15 and 30 cm) behind various thicknesses of concrete in water. Figure 38.3 shows the same data for the case in which water is permitted to remain between the slabs ($\frac{1}{2}$ in. of water to 4 in. of concrete). From analyses of these two cases it is evident that the usual removal cross section data are adequate for predicting the added attenuation of the water.

Figure 38.4 shows directly, from measurements in water behind slabs spaced closely together and at various separation distances, that the fast-neutron dose rate is constant for a given total concrete thickness. This indicates that the location of the water in the shield, that is, in the concrete or behind it, is immaterial.

Figure 38.5 shows that the penetration of capture gamma rays is reduced by the addition of water, but not by a large factor. Figure 38.6 shows the attenuation of gamma rays by various thicknesses of concrete.

TABLE 38.4. CALCULATION OF FAST-NEUTRON REMOVAL ATTENUATION COEFFICIENT FOR DRY ORDINARY CONCRETE

Element	Concentration (wt %)	Σ_R/ρ (cm^2/g)*	Wt %·Σ_R/ρ (10^{-2} cm^2/g)
O	46.7	3.72×10^{-2}	1.74
S	0.29	2.77×10^{-2}	0.01
Si	14.3	3.01×10^{-2}	0.43
Fe	1.10	2.14×10^{-2}	0.02
Al	3.54	2.92×10^{-2}	0.10
P	0.31	2.83×10^{-2}	0.01
Mn	0.11	2.02×10^{-2}	0.00
C	4.92	4.07×10^{-2}	0.20
H	0.83	5.98×10^{-1}	0.50
Na	0.45	3.41×10^{-2}	0.02
K	0.18	2.47×10^{-2}	0.00
Ca	24.32	2.43×10^{-2}	0.59
Mg	2.40	3.33×10^{-2}	0.08
		Total	3.70

*Values of the neutron removal cross section, Σ_R, are taken from ORNL-1843 (see ref 7).

This experiment will be reported more completely in an ORNL topical report.[8]

[8] J. M. Miller, *Radiation Attenuation Characteristics of Structural Concrete*, ORNL-2193 (in press).

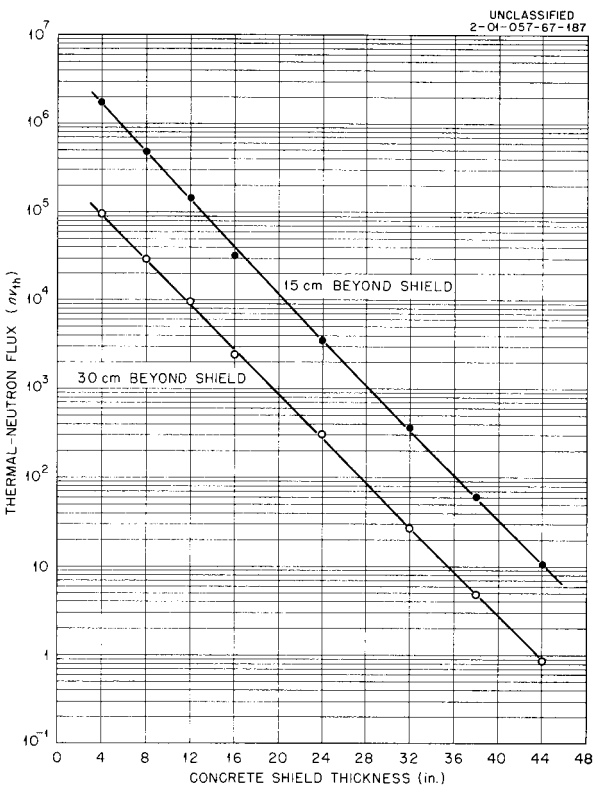

Fig. 38.2. Thermal-Neutron Flux in Water Beyond Various Thicknesses of a Concrete Shield.

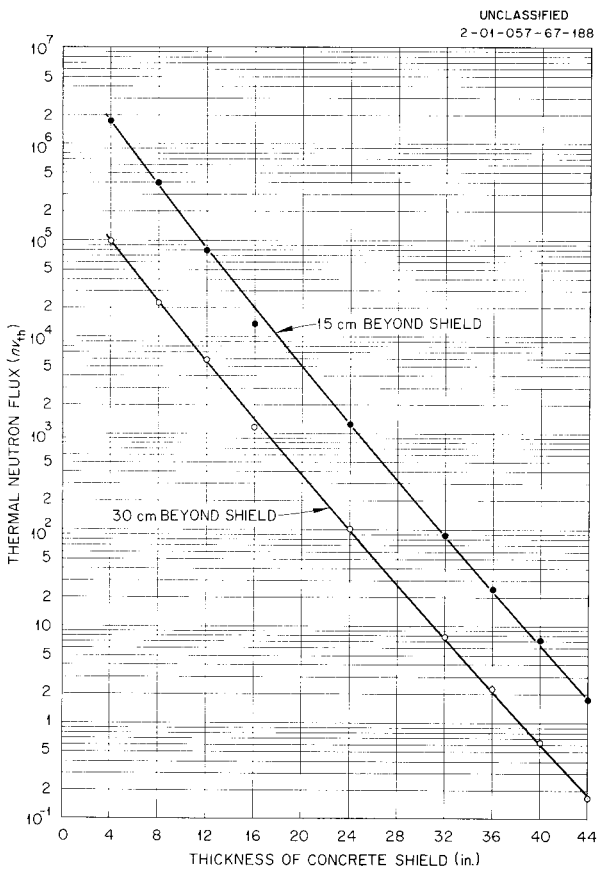

Fig. 38.3. Thermal-Neutron Flux in Water Beyond Various Thicknesses of a Concrete Shield in Which a ½-in.-thick Water Gap Follows Each 4-in. Thickness of Concrete.

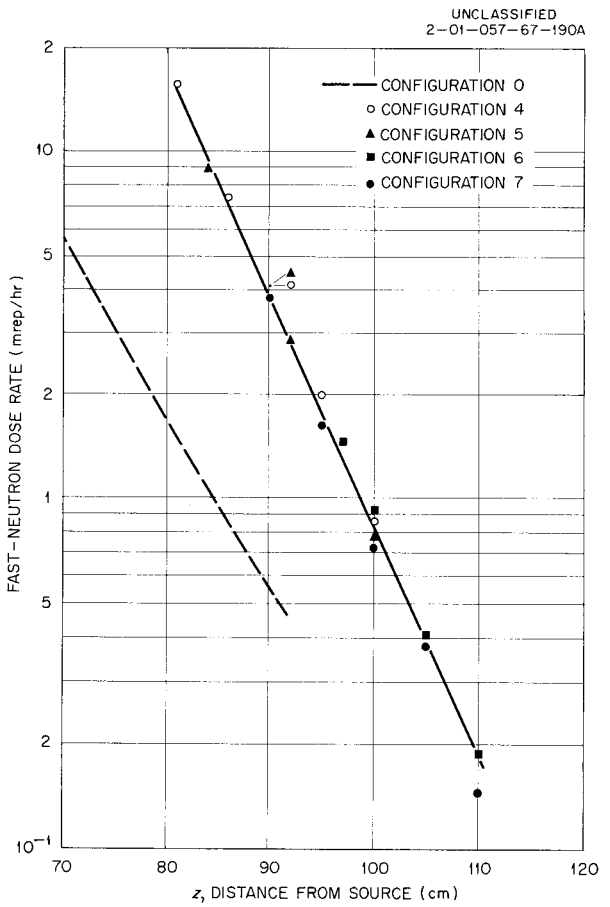

Fig. 38.4. Fast-Neutron Dose Rates in Water Beyond Configurations 4, 5, 6, and 7.

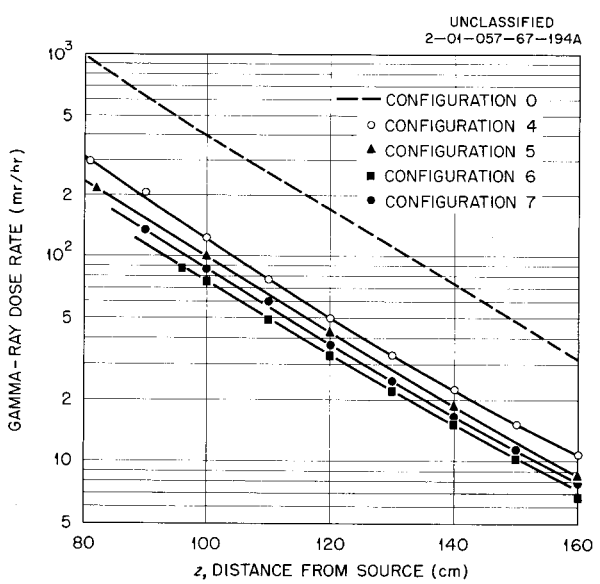

Fig. 38.5. Gamma-Ray Dose Rates in Water Beyond Configurations 4, 5, 6, and 7.

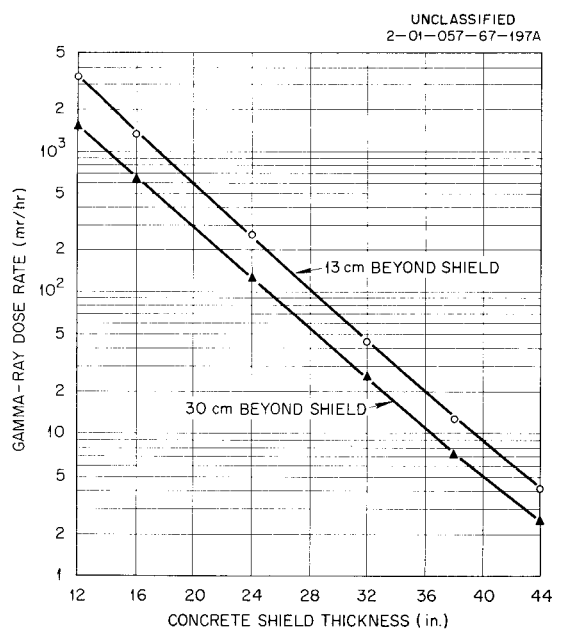

Fig. 38.6. Gamma-Ray Dose Rates Beyond Configurations 8, 9, 10, 11, 12, 13, 14, and 15.

39. NEW LID TANK SHIELDING FACILITY SOURCE PLATE

D. R. Otis[1]

The LTSF at the ORNL Graphite Reactor is used to study the shielding properties of proposed shield configurations. The neutron and gamma radiation is obtained from a "source plate" containing U^{235}, which absorbs thermal neutrons that issue from a hole in the reactor shield and which, in turn, emits a fission spectrum of neutrons and gamma rays.

The first LTSF source plate (SP-1) was installed in 1949. During the last few years it became apparent that a source plate of a different design would be an improvement in several respects. Consequently, a new source plate (SP-2) was installed in September 1955. This new plate represents an improvement over SP-1 in that (1) the power is greater, (2) the geometry more nearly approaches the ideal disk shape, and (3) the self-absorption of the source and the source power can be more accurately calculated.

The new source consists of a circular disk of enriched uranium (20.8% U^{235} and 79.2% U^{238}) 28 in. in diameter and 0.06 in. thick. An exploded assembly is shown in Fig. 39.1. An interesting feature of this design is the inclusion of a spiral-wound electric heater and temperature gages to aid in the power calibration of the source plate.

An extensive series of tests was made to establish the strength of the new source. Three independent methods were used, each involving the measurement of a different fundamental property of the fission reaction. The three methods can be described as follows:

1. measurement of the total number of thermal neutrons captured within the source plate,
2. measurement of the rate of neutron production within the source,
3. measurement of the energy dissipation in the source.

The number of thermal neutrons captured in the source was determined by using gold-wire measurements to infer the thermal-neutron current incident upon the source and by using a cross-sectional mockup of the source plate assembly to determine the fraction of the current absorbed in the source. This method yielded a source strength of 1.60×10^{11} fissions/sec $\pm$ 9%.

The rate of neutron production within the source was determined from measurements of the thermal-neutron flux throughout the LTSF water. From these data, the number of neutrons absorbed within the water was calculated. The fraction of source neutrons absorbed within the water was estimated, and this was divided into the calculated number of neutrons absorbed. The resulting source strength was 1.73×10^{11} fissions/sec $\pm$ 13.5%.

The energy dissipation was estimated by comparing the transient temperature response of the source-plate assembly for two conditions of heating: (1) heating by fission power (normal operation) and (2) heating by electric power, using the electric heater shown in Fig. 39.1. The source strength based upon the temperature measurements was 1.63×10^{11} fissions/sec $\pm$ 6%.

The results from the three different methods were averaged according to a system in which the result from each method was weighted with the inverse square of the absolute error. The resulting average source strength was 1.62×10^{11} fissions/sec $\pm$ 5%. This can be interpreted as

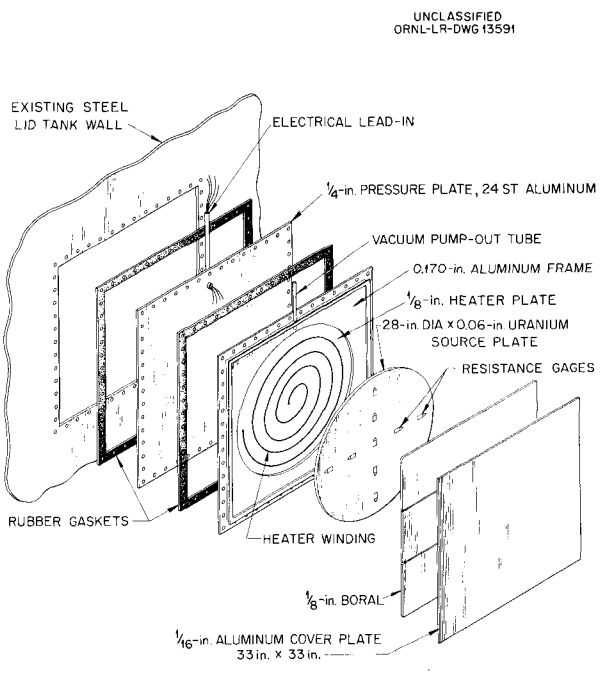

Fig. 39.1. The SP-2 LTSF Source-Plate Assembly.

[1]Convair, San Diego.

5.18 ± 0.26 w of power[2] for a reactor whose energy dissipation is 200 Mev/fission. Since the source-plate area is 3980 cm^2, the unit source strength is then 1.30×10^{-2} w/cm^2. All estimated errors represent a 68% confidence level.

The attenuation of the source radiation by the source-plate assembly can be accounted for by an "effective leakage factor." This factor attempts to correct dose measurements made behind shield configurations for the effect of the absorption of the source-plate assembly. For gamma rays, then, the effective leakage factor is 0.88 if it is assumed that 3-Mev photons emitted nearly normal to the source plate surface are most important behind shield configurations. If the attenuation of fission neutrons by the source-plate assembly is calculated, using effective removal cross sections, the resulting effective leakage factor is 0.94.

All LTSF data taken with SP-2 will be normalized to 1 w by dividing by 5.18. Therefore, correction should be applied if the energy dissipation in the reactor under consideration differs from 200 Mev/fission. The effective leakage factors will not be incorporated into the reported data, since they are applicable only to measurements behind shield configurations. It was deemed advisable to allow the designer the option of using the above leakage factors or of using his own.

[2]The power calibration tests were completed in March 1956, and a preliminary estimate of 5.5 ± 0.5 w was reported in May 1956, at the First Semiannual ANP Shielding Information Meeting, May 7–8, 1956, by W. J. McCool and D. R. Otis; see also, papers I-G and I-H in the minutes of the meeting, ORNL-2115 (May 7, 1956) (Classified).

40. DETERMINATION OF THE EFFECTIVE POWER OF THE OLD LID TANK SOURCE PLATE (SP-1)

J. Smolen[1]

After installation of the new source plate, SP-2 (see Chap. 39), at the LTSF, the effective power of the old source plate, SP-1 (see Fig. 40.1), could be determined by multiplying the power of SP-2 (5.18 w ± 5%) by a neutron leakage factor (0.94) and dividing by an effective power ratio of the two plates. The power ratio was determined by comparing thermal-neutron measurements in the LTSF water as a function of distance from the two sources.

The measurements which were compared (Fig. 40.2) were taken with foils of gold and indium and also with ½- and 3-in. fission chambers. The responses of the fission chambers, excluding a constant used to convert the observed counts per minute to flux, have shown good stability and repeatability over an extended period. The foil measurements would normally be the most absolute; however, the gold and indium foil measurements[2] of thermal neutrons from SP-1 were made in early 1950, and details of the calibrations are unknown. The present methods of foil calibration would not necessarily yield comparable results.

The observed ratio of measurements with fission detectors is, however, in fair agreement with the ratio obtained from foil measurements at distances of 10 to 60 cm from the source-plate surface. Agreement is excellent for measurements at distances from 40 to 60 cm, yielding a ratio of 2.7. Between 10 and 30 cm the fission-detector measurements gave a ratio of about 3.2, and the foil measurements gave a ratio of about 2.9. (The character of the flux distribution between 0 and 10 cm is largely due to differences in construction of the source-plate assemblies. The SP-2 assembly produces a large flux depression at the source-plate surface created by a boron curtain between the uranium source disk and its 1/16-in.-thick aluminum cover plate. The boron curtain in the SP-1 assembly was covered with a ½-in.-thick lead slab.)

On the basis of these measurements an effective SP-2/SP-1 power ratio of 2.9 ± 10% was used in the determination of the power of SP-1. The results indicated a power of 1.7 w, with an estimated error of ±11%.

[1]Pratt & Whitney Aircraft.

[2]C. E. Clifford, *Measurements of Neutron and Gamma Distribution in 100% Water from a 28 in. Diameter Fission Source*, ORNL CF-50-1-153 (Feb. 1, 1950).

UNCLASSIFIED
2-01-057-0-286

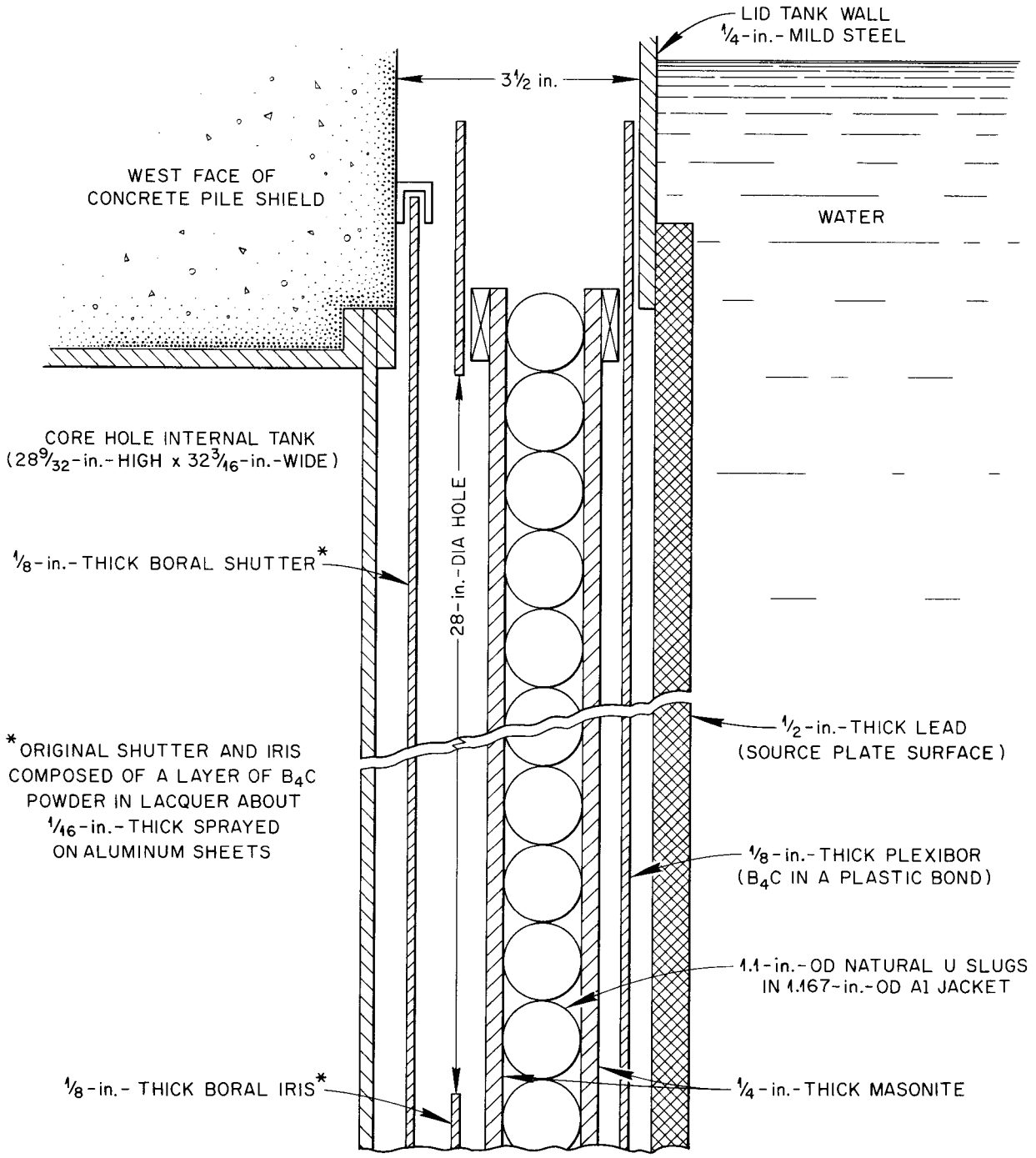

Fig. 40.1. The SP-1 LTSF Source-Plate Assembly.

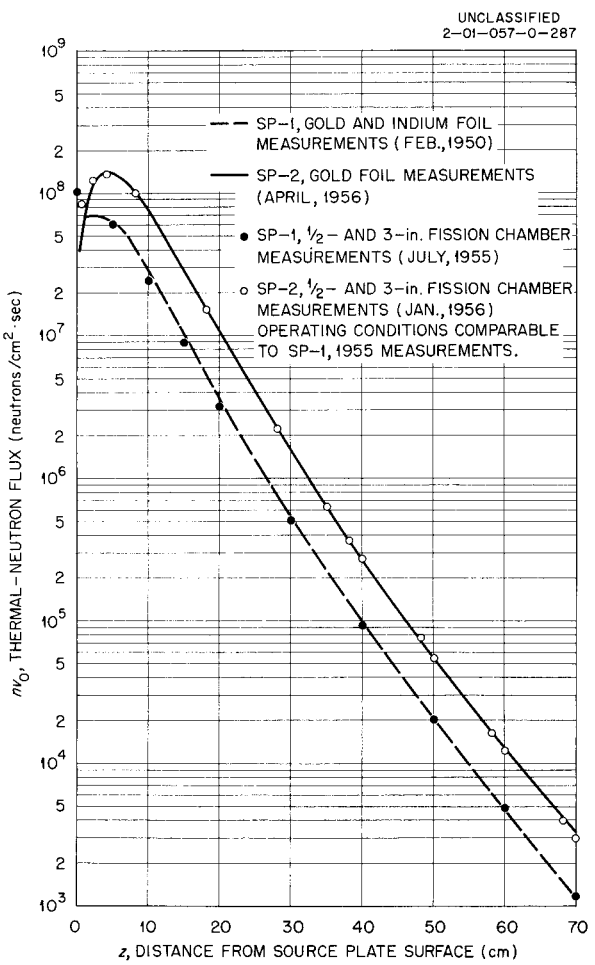

Fig. 40.2. Comparison of the Thermal-Neutron Flux in the Water of the LTSF with Source Plates SP-1 and SP-2.

A comparison of gamma-ray dose rate measurements in the LTSF water as a function of distance from the two sources (Fig. 40.3) yields a ratio of about 4.0 ± 8%. This larger ratio, as compared with the ratio of the thermal-neutron curves, is attributed to the higher self-absorption of photons in the SP-1 assembly. The gamma-ray leakage factor of SP-2 has been calculated[3] to be about 0.88 for 3-Mev gamma rays. The leakage of

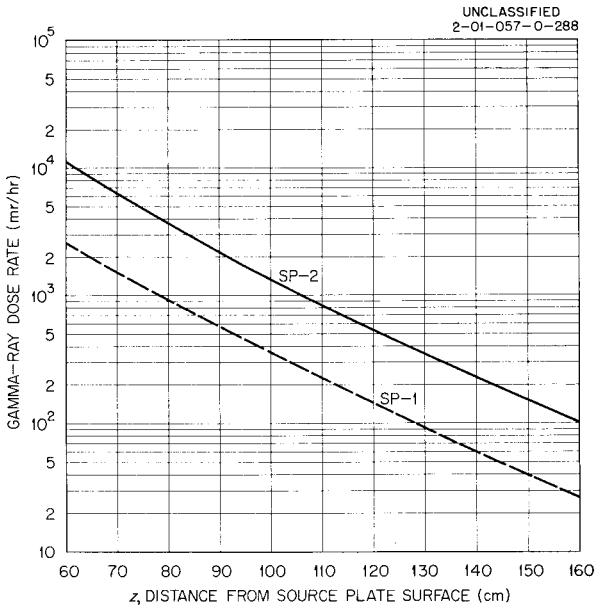

Fig. 40.3. Comparison of the Gamma-Ray Dose Rate in the Water of the LTSF with Source Plates SP-1 and SP-2.

photons from SP-1 is obviously less because of self-absorption in the uranium slugs and absorption by the ½-in.-thick lead cover plate. Also observable from Fig. 40.3 is a slight hardening of the gamma-ray spectrum from SP-1 because of low-energy photon absorption in the source-plate assembly.

The gamma-ray dose rates observed in the water are comprised of a primary and a secondary component. The magnitude of the secondary component, consisting of 2.23-Mev photons from thermal-neutron captures by hydrogen, is proportional to the thermal-neutron flux. Therefore, the effective power of SP-1 cannot be directly determined by the gamma-ray emission by applying the ratio of the observed dose rates from SP-2 and SP-1.

[3] J. Smolen, *The Lid Tank Shielding Facility at Oak Ridge National Laboratory, Part II. Determination of the Fission Rate of the Source Plate* (to be published).

41. EFFECTIVE NEUTRON REMOVAL CROSS SECTIONS OF CARBON AND OXYGEN IN CONTINUOUS MEDIA

D. K. Trubey G. T. Chapman

Thermal-neutron flux measurements at the LTSF in media of water, oil, and a sugar-water solution have been used to calculate the neutron removal cross sections of carbon and oxygen distributed in continuous media. The oil (G-E 10-C insulating oil) was assumed to be CH_2 and had a density of 0.876 g/cm^3. The sugar solution (density = 1.312 ± 0.001 g/cm^3) contained 64.2 wt % sugar ($C_{12}H_{22}O_{11}$), which gave 0.354 g/cm^3 of carbon and a hydrogen and oxygen density that was 96% of that of plain water.

The measurements in the sugar solution and in water were compared to obtain the removal cross section for carbon in a distributed medium. Since the sugar solution contained almost as much hydrogen and oxygen as does plain water and contained them in the same ratio, the effect of the water could be estimated and subtracted. Then by comparing measurements in oil and water and using the distributed carbon cross section, the oxygen cross section was determined. The resulting cross sections were 0.72 ± 0.05 barn for carbon[1] and 0.92 ± 0.05 barn for oxygen. It is interesting to note that these values are somewhat less than those previously published[2] (0.81 ± 0.05 barn for carbon and 0.99 ± 0.10 for oxygen). The earlier values were obtained with a thick sample adjacent to the source plate. This value for oxygen has a large uncertainty partly because the sample was an oxygen compound. It is not clear that the distributed cross section is really less (due to the experimental uncertainty), but if it is, the difference seems to be small.

The calculational procedures used to determine these cross sections will be published in a separate report.[3]

[1] The value of 0.750 barn, reported by D. K. Trubey, *ANP Quar. Prog. Rep. Sept. 10, 1954*, ORNL-1771, p 164, esp 165, was computed with no geometric correction.

[2] G. T. Chapman and C. L. Storrs, ORNL-1843 (Aug. 31, 1955).

[3] D. K. Trubey and G. T. Chapman, *The Effective Neutron Removal Cross Sections of Carbon and Oxygen in Continuous Mediums*, ORNL-2197 (to be published).

42. THEORY OF THE $C^{13}(\gamma,n)C^{12}$ REACTION

E. Guth G. deSaussure

During shielding measurements of the attenuation of neutrons in oil and sugar water,[1] a background of neutrons was observed which was attributed to the (γ,n) reaction of C^{13}. At that time the experimental cross section was not known, and it was decided to apply a calculational model as used successfully by Guth and Mullin for the $Be^9(\gamma,n)Be^8$ reaction.[2] In this model a valence neutron moves in the field of a core, namely, the Be^8 or the C^{12} nuclei. However, before this model was applied, Cook and Telegdi[3] reported an experimental determination of the photodisintegration cross section of C^{13} as a function of energy, using the betatron. While this work is necessarily very inaccurate close to the threshold, it improves in accuracy rapidly with increasing energy. On the basis of the Cook-Telegdi work, an almost quantitative calculation of the neutron background observed in the shielding tests was made (see Chap. 43, this report). Although this explained the neutron background in the experiment, the theoretical work on this model was pursued somewhat further. Looking at the inverse reaction, the capture of gamma rays by C^{12}, it was concluded that in contrast with the case of $Be^9(\gamma,n)Be^8$,

[1] G. T. Chapman *et al.*, *Measurements of an Effective Neutron Cross Section of Lithium at the Lid Tank Shielding Facility*, ORNL CF-54-11-3 (Nov. 2, 1954); see also, Chap. 41 in this report.

[2] E. Guth and C. J. Mullins, *Phys. Rev.* **76**, 234, esp 239 and 682 (1949).

[3] B. C. Cook and V. L. Telegdi, private communication.

the $C^{13}(\gamma,n)C^{12}$ reaction does not show resonance right above the threshold. This essential difference causes the $C^{13}(\gamma,n)C^{12}$ cross section to become much smaller (by about a factor of 10 at least) than the corresponding $Be^9(\gamma,n)Be^8$ cross section. Further details will be obtained experimentally[4] by use of a single-energy gamma-ray source.

[4]Work to be done by H. B. Willard, Physics Division.

43. ESTIMATION OF PHOTONEUTRONS FROM C^{13}

D. K. Trubey

Measurements of thermal-neutron flux in the presence of high-energy gamma rays in liquid media containing hydrogen, or carbon and hydrogen, indicate that photoneutrons comprise a large fraction of the total thermal-neutron flux at large distances from the neutron source. The evidence for this is a change in slope of the flux plotted as a function of distance from the neutron source. At large distances, the slope is characteristic of gamma-ray attenuation in the medium rather than of neutron attenuation. For example, the estimated deuterium photoneutron flux has been shown to be nearly equal to the total measured flux in the pool of the BSF at distances from the reactor of about 2 m or greater.[1] More recently, the photoneutron process has been observed to be important at closer distances in media containing carbon than was the case in pure water.[2] This is attributed chiefly to the (γ,n) reaction in C^{13} induced by the high-energy capture gamma rays from an Inconel plate adjacent to the source plate of the LTSF.[3] Verification, however, was not possible until recently determined values of the cross section for the reaction were available.

Figure 43.1 shows data obtained at the LTSF by using a medium of G-E 10-C insulating oil. The insertion of a bismuth slab in the oil reduced the gamma rays sufficiently that photoneutrons were effectively eliminated without any other observable effect. In order to verify that the process in question was indeed responsible, estimations of the expected flux due to photoneutrons were added to the measured flux values obtained while the gamma rays were suppressed. The result was equal to the measured total flux within the experimental uncertainty (Fig. 43.2). The cross section for the $C^{13}(\gamma,n)C^{12}$ reaction was taken from the data of Cook and Telegdi,[4] and the cross section for the $H^2(\gamma,n)H^1$ reaction was taken from *The Reactor Handbook*.[5]

Most of the gamma rays which produce neutrons in C^{13} (the dominant process in the experiment) at large distances are very energetic (over 5 Mev). Thus the gamma rays from the fission process in the source plate were neglected in the calculation, and only capture gamma rays from the Inconel circular plate were considered. A simple spectrum of source energies (five groups) was computed from the known thermal-neutron flux at the location of the $\frac{1}{8}$-in.-thick, 28-in.-dia Inconel plate, the absorption cross section of the elements in the Inconel, and estimations[6] of the capture gamma-ray distribution. For energies above 7 Mev, the binding energy of the nucleus was the energy assumed. It was also assumed that the attenuation of both the neutron and gamma-ray fluxes in the Inconel was negligible. The gamma-ray flux for each group was then computed at various distances by multiplying the source strength by the attenuation factor for an isotropic plane circular source in an infinite medium and adding a built-up flux obtained from

[1]J. M. LaRue *et al.*, ORNL CF-51-8-290 (Aug. 24, 1951).

[2]G. T. Chapman *et al.*, *Measurements of an Effective Neutron Cross Section of Lithium at the Lid Tank Shielding Facility*, ORNL CF-54-11-3 (Nov. 2, 1954); see also, chap. 41 in this report.

[3]That this is the responsible reaction was first suggested by H. Goldstein of NDA.

[4]B. C. Cook and V. L. Telegdi, private communication to E. Guth, January 1956; the $C^{13}(\gamma,n)C^{12}$ cross section has been calculated by G. deSaussure and E. Guth (see chap. 42 of this report).

[5]J. F. Hogerton and R. C. Grass (eds.), *The Reactor Handbook*, vol 1, p 473, Technical Information Service, AEC, 1955.

[6]P. Mittleman, *Gamma Rays Resulting from Thermal Neutron Capture*, NDA-10-99 (Oct. 6, 1953).

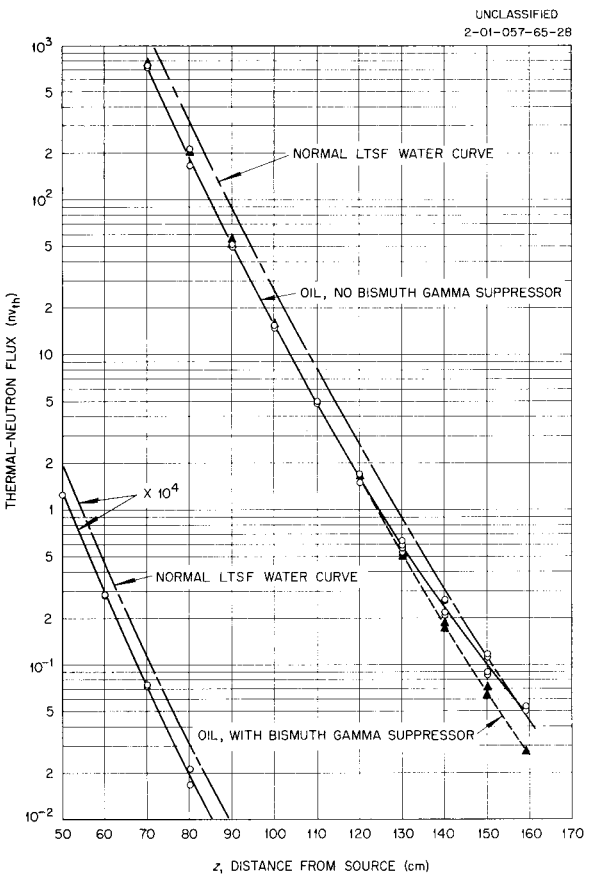

Fig. 43.1. Thermal-Neutron Flux in Oil With and Without Bismuth Slab to Suppress Photoneutron Production.

higher groups. This built-up flux was computed from published differential energy spectra in water.[7] The method used for this calculation will be published in a separate report.[8]

The photoneutron thermal flux may be computed from the following relation:

$$\phi_{th}(z)\,\Sigma_a = \sum_{E=0}^{\infty} \Gamma(z,E)\,\Sigma_p(E) \ ,$$

where

ϕ_{th} = photoneutron thermal flux,

Σ_a = macroscopic thermal-neutron absorption cross section in the medium,

[7] H. Goldstein and J. E. Wilkins, Jr., *Calculations of the Penetration of Gamma Rays. Final Report*, NYO-3075 (June 30, 1954).

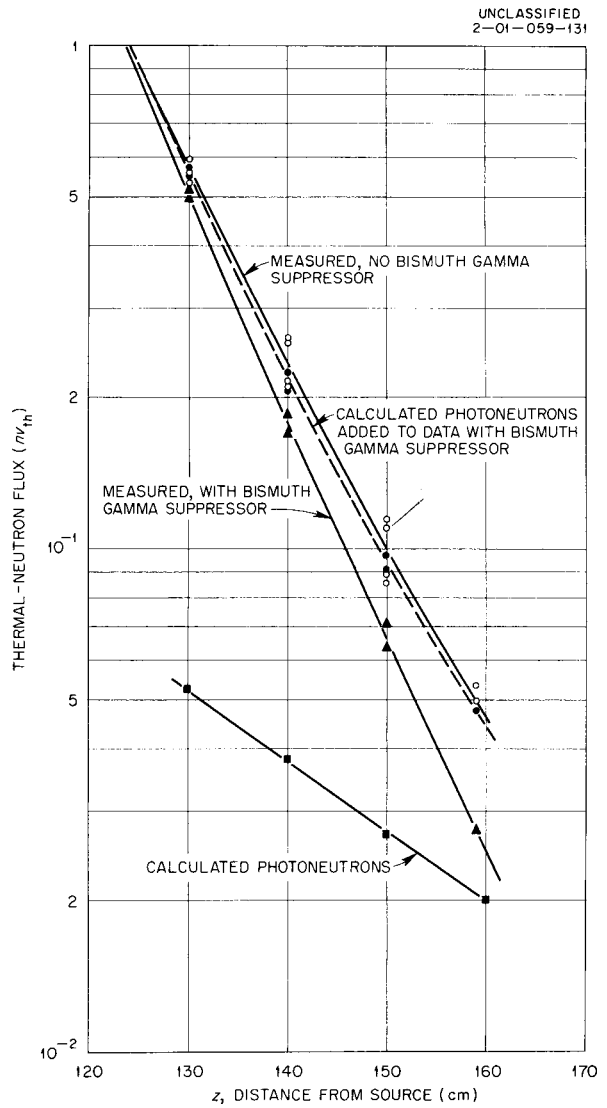

Fig. 43.2. Measured and Calculated Thermal-Neutron Flux in Oil Showing Measured and Calculated Components.

$\Gamma(z,E)$ = photon flux of energy E at z distance from the source

$$= \Gamma(0,E)\left\{\frac{E_1(\mu z) - E_1\left[\mu z\sqrt{1+(a^2/z^2)}\right]}{2}\right\} +$$

+ built-up group,

[8] D. K. Trubey, *Estimation of Photoneutrons from* C^{13}, ORNL-2200 (to be published).

$$E_1(\mu z) = \int_{\mu z}^{\infty} \frac{e^{-y}}{y}\, dy \quad ,$$

μ = linear total absorption coefficient for gamma rays of energy E,

a = radius of the source (both LTSF source plate and Inconel plate),

z = distance from the source,

$\Sigma_p(E)$ = photoneutron production macroscopic cross section for gamma rays of energy E.

The justification for this equation is presented elsewhere.[8] It is apparent that it is correct if migration of neutrons can be neglected. This is permissible in this case because neutrons are attenuated very rapidly, as compared with gamma rays.

---

44. ENERGY AND ANGULAR DISTRIBUTION OF GAMMA RADIATION FROM A Co^{60} SOURCE AFTER DIFFUSION THROUGH MANY MEAN FREE PATHS OF WATER

R. W. Peelle F. C. Maienschein
T. A. Love

Considerable efforts have been expended[1] to calculate the details of the intensity distribution of gamma rays which penetrate or diffuse through media whose linear dimensions are large compared with an interaction mean free path for the photons involved. Difficulty arises in the calculations because of the complexity of the scattering process. The calculational problem tends to be more severe for absorbers consisting of elements of low atomic number, where Compton scattering is the most important effect, and for penetrations which correspond to many mean free paths of the primary radiation.

The most trusted calculations available at this time are "moments method" calculations resulting from a combined National Bureau of Standards and Nuclear Development Associates computing program.[1-4] These calculations, supposed to be valid for an infinite homogeneous medium, have provided the energy spectrum of the energy flux, integrated over all solid angles for an isotropic detector. Further integration has been performed to obtain various significant buildup factors. The dose buildup factors obtained from the moments method calculations have been compared favorably with dose measurements obtained in water[1,5] as a function of detector separation distance from a Co^{60} point source. Dose rate checks have also been made in media of iron[6,7] and lead,[7] confirming the results of these calculations. Hayward[8] measured the electron spectrum observed in an anthracene crystal when it was placed in a water medium at various distances from a Co^{60} point source. This experiment agreed with a special moments method calculation designed for testing the experimental results. These integral experiments have been interpreted as substantiating the general validity of the results of the moments method calculational program.

In order to further test the results of either this calculational approach or of any future computations, it has seemed that calculated energy and angle spectra should be subjected to experimental scrutiny, since the agreement with experiment of the calculated buildup factors may be fortuitous. Such a detailed study has been reported by Whyte[9] for a medium of concrete terminated at the point of detection and with detector angles up to 60 deg.

---

[1] L. V. Spencer and U. Fano, *Phys. Rev.* 81, 464 (1951); see also, L. V. Spencer and U. Fano, *J. Research Nat. Bur. Standards* 46, 446 (1951).

[2] L. V. Spencer and F. Stinson, *Phys. Rev.* 85, 662 (1952).

[3] U. Fano, *J. Research Nat. Bur. Standards* 51, 95 (1953).

[4] H. Goldstein and J. E. Wilkins, Jr., *Calculations of the Penetration of Gamma Rays. Final Report*, NDA-15C-41 or NYO-3075 (June 30, 1954).

[5] G. R. White, *Phys. Rev.* 80, 154 (1950).

[6] L. A. Beach, R. B. Theus, and W. R. Faust, *Phys. Rev.* 92, 355 (1953).

[7] C. Garrett and G. N. Whyte, *Phys. Rev.* 95, 889 (1954).

[8] E. Hayward, *Phys. Rev.* 86, 493 (1952).

[9] G. N. Whyte, *Can. J. Phys.* 33, 96 (1955).

Whyte's integrated and normalized results are in good agreement with those of the moments method, but no attempt was made to obtain an absolute normalization of the results.

An experiment has been performed at ORNL to determine the energy and angle spectrum of the energy flux from a point isotropic Co^{60} source in an effectively infinite medium of water. Spectra were obtained for several detector observation angles for each of two source-detector separation distances. These spectra are compared with the available calculated spectra for the same cases.

Experimental Procedure

A double-crystal Compton scintillation spectrometer[10–12] was used in this experiment because of its reasonably unique response to incident monoenergetic gamma rays. Figure 44.1 shows the geometry of the spectrometer and the source as suspended in the pool of water at the BSF. Although the term "detector angle" implies that the spectrometer was repositioned throughout the experiment, in practice the source was actually moved by means of a swinging arm pivoted just above the end of the spectrometer collimator, as determined by a plumb. This source could then be set so that the detector angle θ had any value between 0 and 90 deg, while maintaining a constant source-detector separation. The spectrometer was positioned about 10 ft from the sides and bottom of the BSF pool and about 15 ft from the water surface.

Two Co^{60} sources were used during the course of this experiment, one having a strength of approximately 100 curies and the other approximately 195 mc. The 195-mc source was calibrated against a small (1-mc) source whose strength was known to within about 3% (as the result of measurements with a calibrated high-pressure ionization

[10] F. C. Maienschein, *Multiple Crystal Gamma-Ray Spectrometer*, ORNL-1142 (April 14, 1952).

[11] F. Maienschein and T. Love, *Nucleonics* 12(5), 6 (1954).

[12] T. A. Love, R. W. Peelle, and F. C. Maienschein, *Electronic Instrumentation for a Multiple-Crystal Gamma-Ray Scintillation Spectrometer*, ORNL-1929 (Oct. 3, 1955).

UNCLASSIFIED
ORNL—LR—DWG 16471

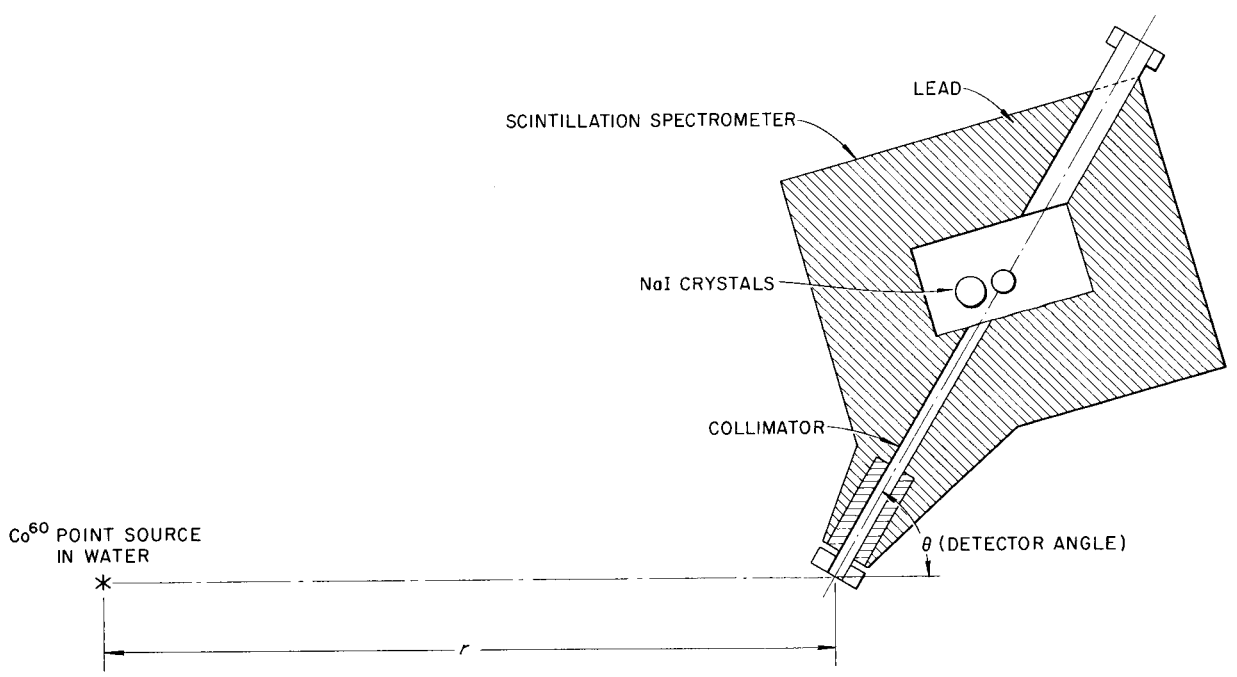

Fig. 44.1. Geometry for the Gamma-Ray Spectrometer and Co^{60} Source.

chamber[13]). The ratio between the 195-mc and the 1-mc sources was obtained by counting and dosimetry techniques. The 195-mc source was also sent to the National Bureau of Standards for a dose calibration; the results were corrected approximately for degradation. The 100-curie source was calibrated against the 195-mc source. Table 44.1 shows the strengths of the sources used, the methods of calibration, and the precision to which they are believed to be known. For the calibration by detector responses through 90- and 140-cm thicknesses (r) of water, pure exponential attenuation was assumed with little error because of the smallness of the solid angle accepted by the spectrometer ($\sim 2.2 \times 10^{-3}$ steradians).

Figure 44.2 shows typical pulse-height response data of the double-crystal spectrometer to several sources. The uniqueness of response is not so good as that reported by Whyte,[9] presumably because of the fact that Whyte used a superior detector geometry. The spectral sensitivity of the spectrometer, divided by the gamma-ray energy, is shown in Fig. 44.3. Only the approximately gaussian peaks of the experimental response functions are counted in determining this curve. The basic efficiency curve was taken from an earlier report,[10] except for a change of absolute normalization based upon the instrument response to the 1-mc Co^{60} source.

[13]This high-pressure chamber was used through the courtesy of E. I. Wyatt's group in the Analytical Chemistry Division.

Energy spectra were obtained for a number of detector angles (θ) between 0 and 90 deg at each of two penetration distances (90 and 140 cm). Background spectra, corresponding to the detection of photons which penetrated the walls of the lead spectrometer shield, were obtained by repeating each run with a 6-in.-long lead plug filling the nose of the collimator. Table 44.2 shows a summary of all the sets of experimental parameters studied. It should be noted that measurements obtained for scattering angles between ±3 deg are strongly affected by the angular aperture of the collimator.

Method of Analysis of the Data

Calculation of the Corrected Yields. – The raw pulse-height distributions, observed experimentally

TABLE 44.2. SUMMARY OF PARAMETER SETS STUDIED IN EXPERIMENTAL ATTENUATION MEASUREMENTS

Source Strength, S (d/sec)	Separation Distance, r (cm)	Scattering Angle, θ (deg)
0.72×10^{10}	90	0, ±2, 4, 10
3.8×10^{12}	90	15, 30, 50, 70, 90
	140	0, ±2, 4, 10, 30, 60, 90

TABLE 44.1. STRENGTHS OF THE TWO Co^{60} SOURCES

Source	Method of Calibration	Source Strength, S (d/sec)	
		Calibrated	Used in Data Analysis
195 mc	Against 1-mc source	$0.72 \times 10^{10} \pm 5\%$	$0.72 \times 10^{10} \pm 4\%$
	NBS dose calibration	$0.73 \times 10^{10} \pm 4\%$	
	Response of Compton spectrometer; $r = 90$ cm, $\theta = 0$	$0.71 \times 10^{10} \pm 8\%$	
100 curies	Response of Compton spectrometer; $r = 140$ cm, $\theta = 0$	$4.2 \times 10^{10} \pm 8\%$	$3.8 \times 10^{12} \pm 8\%$
	Response of Compton spectrometer; $r = 90$ cm, $\theta = 10$ deg, as compared with response to 195-mc source	$3.8 \times 10^{10} \pm 7\%$	

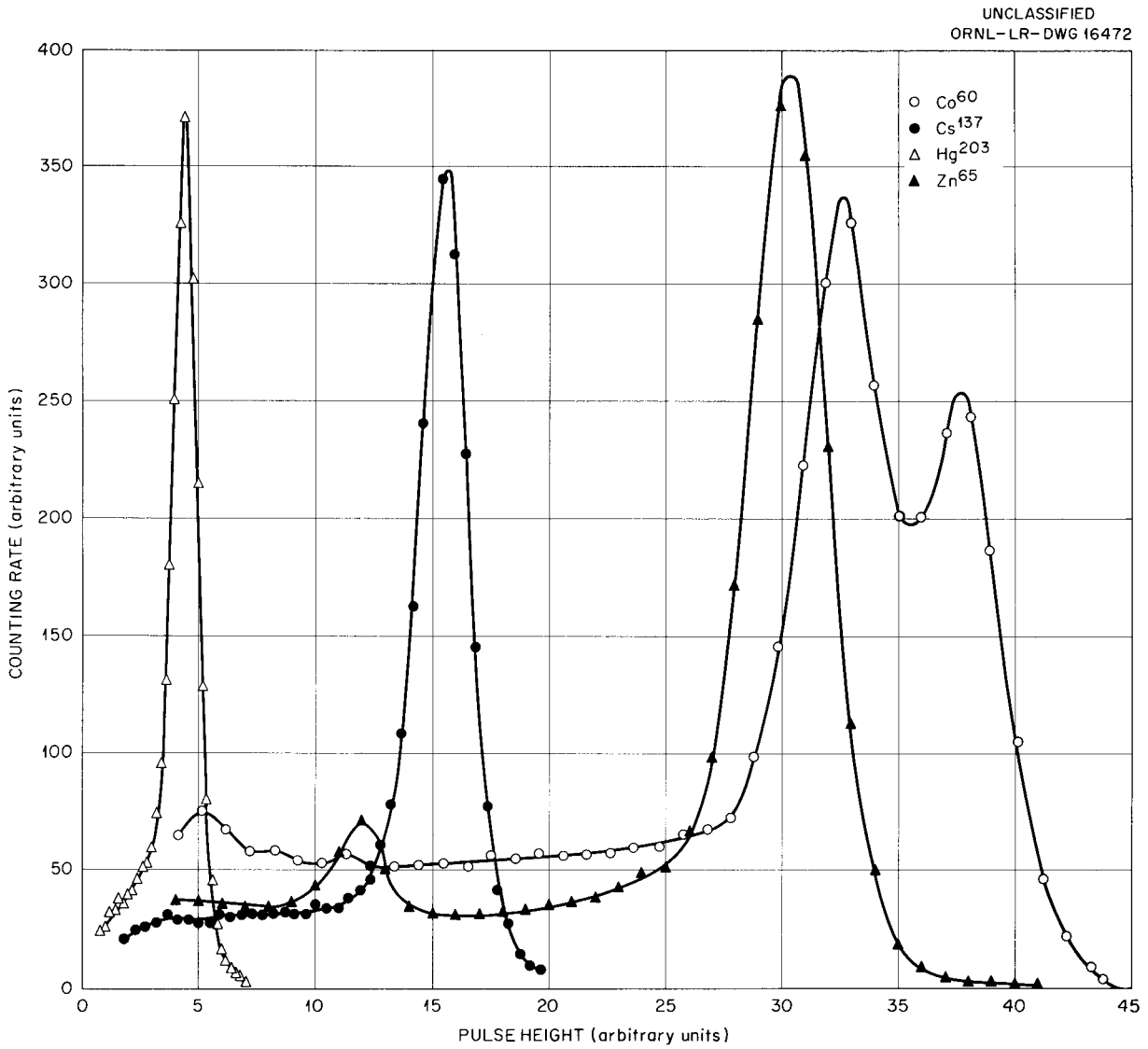

Fig. 44.2. Response of the Compton Spectrometer to Monoenergetic Gamma Rays. Arbitrarily normalized pulse-height spectra are shown on the same relative energy scale for radioisotope sources placed at the nose of the spectrometer collimator. The sources used were Hg^{203} (280 kev), Cs^{137} (662 kev), Zn^{65} (1.12 Mev), and Co^{60} (1.17 and 1.33 Mev).

in terms of counting rate per pulse-height channel, must be subjected to the following corrections in order to obtain the experimental photon number spectrum (photons·Mev^{-1}·sec^{-1}·cm^{-2}):

1. The pulse-height scale must be converted to a photon energy scale.
2. The observed yield per pulse-height interval must be converted to pulses per photon energy interval.
3. Correction must be made for the detection efficiency of the spectrometer as a function of energy.
4. Correction should be made for the nonuniqueness of the response of the spectrometer.

These corrections are all straightforward except the last one. The need for this correction arises from the fact that a beam of monoenergetic gamma

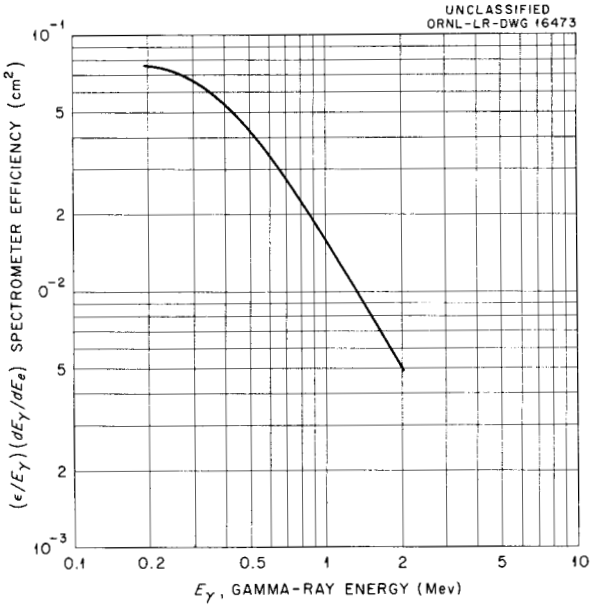

Fig. 44.3. Spectral Efficiency of the Compton Spectrometer, (ϵ/E_γ) (dE_γ/dE_e) (cm^2/Mev). This function, when multiplied by the differential photon energy flux, I, at the end of the collimator and by the collimator solid angle, yields the counting rate observed per unit of absorbed electron energy E_e in the central crystal of the Compton spectrometer. This curve is based on the efficiency curve previously reported (see ref 10) and upon the spectrometer geometry.

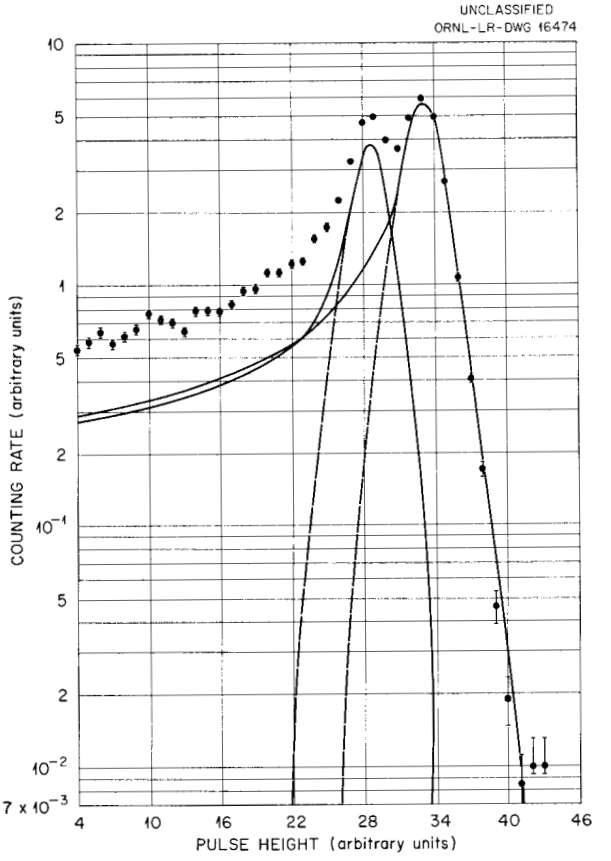

Fig. 44.4. Decomposition of the Observed Co^{60} Spectrum into Peaks Corresponding to the Two Source Energies (θ = 0 deg, r = 140 cm). The points indicate the pulse-height spectrum observed experimentally. The solid lines indicate the responses which would have been expected if individual sources of 1.17 and 1.33 Mev had been used. The dashed lines indicate the extension of gaussian resolution functions. The combined spectrum, corrected for spectrometer nonuniqueness, would consist of the sum of the two gaussian resolution functions shown.

rays incident upon the spectrometer are represented at the spectrometer output by a distribution of pulses of a different size, as shown in Fig. 44.2. The experimental results presented here have been corrected only for the "tail" corresponding to gamma rays near the original energies of 1.17 and 1.33 Mev.

Figure 44.4 shows the manner in which the experimental response function for θ = 0 deg and r = 140 cm was separated into two components supposed to correspond to the discrete source energies of 1.17 and 1.33 Mev. The spectral shapes of Fig. 44.4 were then applied to data for larger angles in order to obtain the desired photon number spectrum.

Figure 44.5 shows the nonuniqueness subtraction made for a measurement at θ = 4 deg and r = 140 cm. The normalized response functions are shown fitted to the humps arising at photon energies of 1.17 and 1.33 Mev. The experimental points at lower energies are shown before and after subtraction of the tails corresponding to these humps. There were three aspects of the nonuniqueness problem which are not considered in the method described above:

1. An estimate of the errors arising from the continuous nature of the high-energy section of the scattered photon spectrum was made by observing the effect upon the estimated nonuniqueness correction of splitting the region above

1.1 Mev into more than the two groups corresponding to the original source gamma rays. Separate tail subtractions were made for each of these energy groups, using interpolated monoenergetic response functions. In the cases where this alternate technique was used, the change at any point of the resulting photon spectrum was less than the known statistical uncertainties in the original pulse-height spectrum.

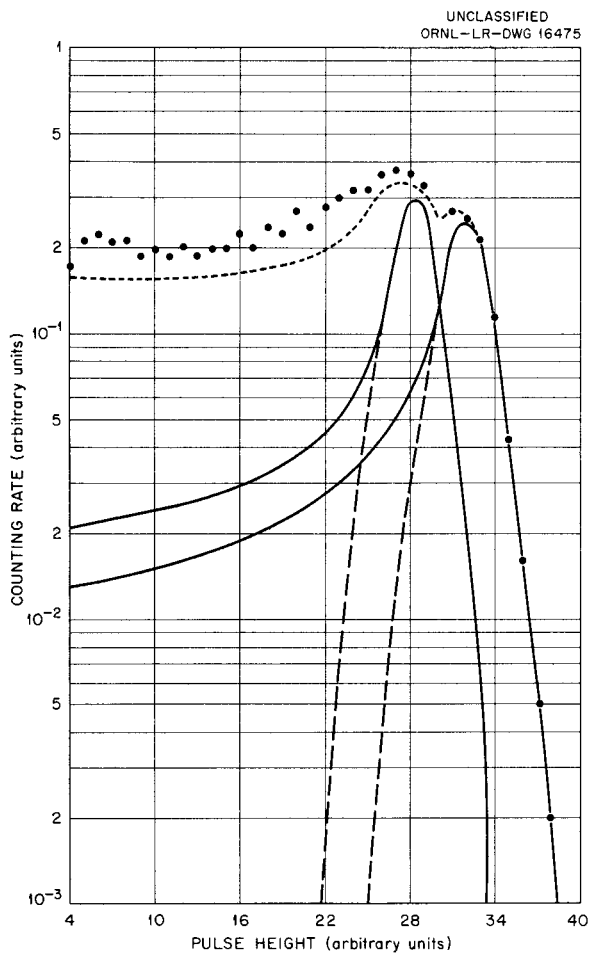

Fig. 44.5. Nonuniqueness Correction of the Pulse-Height Spectrum Observed at θ = 4 deg, r = 140 cm. The points indicate the pulse-height spectrum observed experimentally. The solid curves are the same shape as those in Fig. 44.4, but here they are normalized to fit the high-energy portion of the experimental spectrum shown. The dashed lines represent extensions of the normal resolution functions. Nonuniqueness corrections were made by subtracting from the experimental spectrum the area between the solid and dotted curves for both the 1.17- and 1.33-Mev peaks. The dotted line is the final corrected curve. It was this curve that was used to derive the photon number spectrum observed by the spectrometer.

2. Reasonably good instrument response curves were available for three gamma-ray energies, but corrections were made only for the primary energies of the Co^{60} source, since the calculations were made by hand. The error induced in the photon number spectrum by the failure to subtract a tail corresponding to portions of the measured spectrum below 1 Mev has been estimated crudely for the points at the lowest measured energy (0.25 Mev). At these points, where the relative error from this source should be a maximum, estimated errors range between 5 and 15% (the error leads to the acceptance of too large a flux value), increasing as the pulse-height distribution becomes more flat. These estimates were made by assuming an analytical form for the true spectrum and for the energy dependence of the "peak-to-total" ratio. The peak-to-total ratio consists of the total number of counts in the peak of the distribution divided by all the observed counts down to zero pulse height.

3. The width of the resolution function at the peak of the spectrometer response was completely ignored in the analysis presented here. This is felt to have no appreciable effect upon the results.

Determination of the Energy Flux. – The energy spectrum of the photon energy flux, I, is given by the relation:

$$I(r,E_0,E,\theta) = \frac{EN(r,E_0,E,\theta)}{S\Omega} \ (\mathrm{cm}^{-2}\cdot\mathrm{steradian}^{-1}) ,$$

where

r = source-detector separation distance (cm); the detector is consistently considered to be located at the nose of the spectrometer collimator (see Fig. 44.1);

E_0 = source photon energy, equal to 1.17 and 1.33 Mev for each source disintegration;

E = energy of the observed scattered photon, or, more precisely, the photon energy corresponding to the observed pulse height (Mev);

θ = detector angle (see Fig. 44.1);

$N(r,E_0,E,\theta)$ = experimental number of photons per second per unit energy interval per unit collimator area for specified r and θ values;

S = absolute source strength (d/sec);

Ω = magnitude of the sensitive solid angle as determined by the spectrometer collimator (steradians).

Results and Discussion

Presentations of data for gamma-ray penetration are normally given in terms of the dimensionless function:

$$4\pi r^2 e^{\mu r} I(r,E_0,E,\theta) \quad ,$$

where μ is the total absorption coefficient (cm^{-1}) at energy E_0. This quantity is convenient, since it is dimensionless and the magnitude is near unity. The results presented here are in terms of this function, where μ has been taken as 0.0612 cm^{-1} for water, and the energy and the angle spectrum of the energy flux are normalized to one disintegration yielding a 1.33- and a 1.17-Mev photon.

Figure 44.6 shows the angle and the energy spectral results obtained for r = 90 cm, and Fig. 44.7 gives those for r = 140 cm. All the data shown except those for θ = 0 and 2 deg are directly significant from the point of view of gamma-ray diffusion. The θ = 0 deg data are representative only of the attenuation in water, geometrical factors, and the resolution of the spectrometer.

Discussion of Errors. – The representative errors shown on the curves of Figs. 44.5 and 44.6 are expressive of only the statistical errors of counting. Other random errors do not influence the shape of the energy flux spectra shown. Such random errors, so called because their algebraic orientation is unknown, are summarized in Table 44.3. These errors, if combined according to sums of squares, amount to a total random error in the normalization of the curves of about 12%.

In addition to these normalization errors, there exist difficulties which influence the shape of the resulting spectra. A 5 to 15% nonuniqueness error at the lower energies has already been described. An uncertainty of about 15% is estimated to result from lack of exact knowledge of the efficiency of this spectrometer as a function of energy. This uncertainty is largely the result of the assumption of a relative spectral response unchanged from earlier experiments. The efficiency as a function of energy was not tested during the experiment here described.

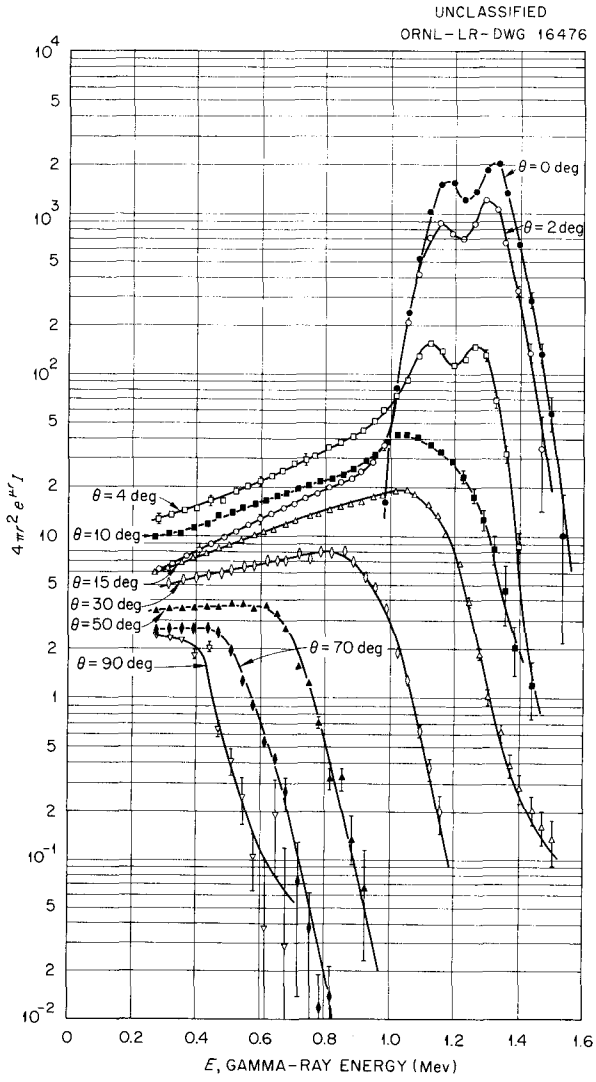

Fig. 44.6. Energy and Angle Spectrum of Energy Flux for a Co^{60} Source; r = 90 cm. The energy spectrum of the energy flux is shown for nine different detector angles as labeled. The energy flux is presented after multiplication by $4\pi r^2 e^{\mu r}$ in order to present a dimensionless quantity. The data for angles less than 30 deg have been smoothed out in the region below the peak by the process of nonuniqueness correction illustrated in Fig. 44.5. The errors shown represent counting statistics.

The energy scale of the quoted results, both relative and absolute, has an estimated standard deviation of about 2%.

Comparison of Experimental Results for Water and Concrete Media. – Figure 44.8 shows that the results obtained in this experiment for 5.5 mean free paths (mfp) of water agree favorably with those for 5.6 mfp of concrete.[14] The concrete experiment extended only to θ = 60 deg. Only the shapes of the curves in Fig. 44.8 may be compared, since Whyte's results were not absolutely normalized.

[14] G. N. Whyte, *Can. J. Phys.* 33, 96 (1955).

Comparison of Experimental and Calculated Results for a Water Medium. – No calculated results are presently available for energy spectra for given detector angles. In the paragraphs below are discussed two comparisons which can be made by manipulation of the data of Figs. 44.6 and 44.7.

TABLE 44.3. ESTIMATED STANDARD DEVIATIONS FOR THE ERRORS INDUCED IN THE FINAL RESULTS

Origin of Error	Estimated Standard Deviation in Final Result (%)
Measurement of r	7
Detected photon energy	1
Source strength	8
$\bar{\epsilon}_{avg}\Omega$, average efficiency times spectrometer solid angle	7

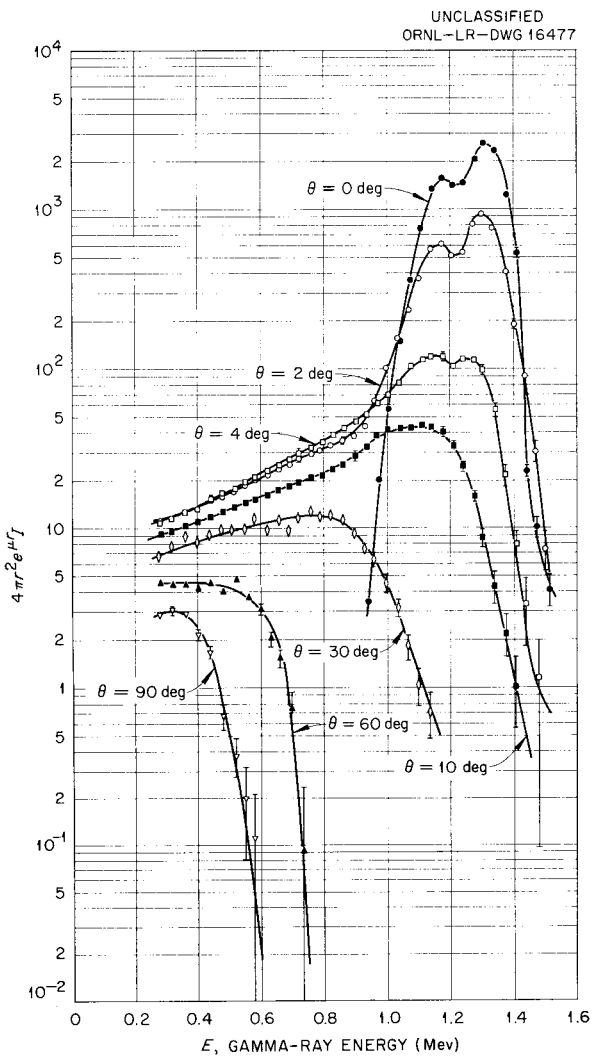

Fig. 44.7. Energy and Angle Spectrum of Energy Flux for a Co^{60} Source; r = 140 cm. The energy spectrum of the flux is shown for seven detector angles. For further discussion, see the caption of Fig. 44.6.

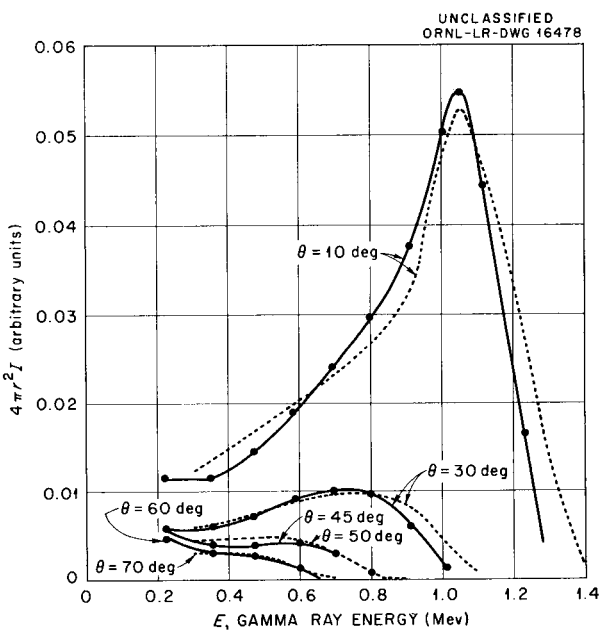

Fig. 44.8. Comparison of Experimental Data (Dashed Line) for 5.5 mfp (90 cm) of Water with Data for 5.6 mfp of Concrete. These two sets of data were normalized at 30 deg, since Whyte's data were not absolute.

Angle spectra are available for three scattered photon energies from Co^{60} in water in the early calculation of Spencer and Stinson,[15] who used hand calculations of only a few moments. In Fig. 44.9, cross-plots of the data of Figs. 44.6 and 44.7 are compared with the results of Spencer and Stinson. There is wide disagreement between the results, especially in the magnitude. If the experimental data were reduced by a factor of 2, the shapes would be in good agreement for 0.256 and 0.365 Mev.

[15] L. V. Spencer and F. Stinson, *Phys. Rev.* **85**, 662 (1952).

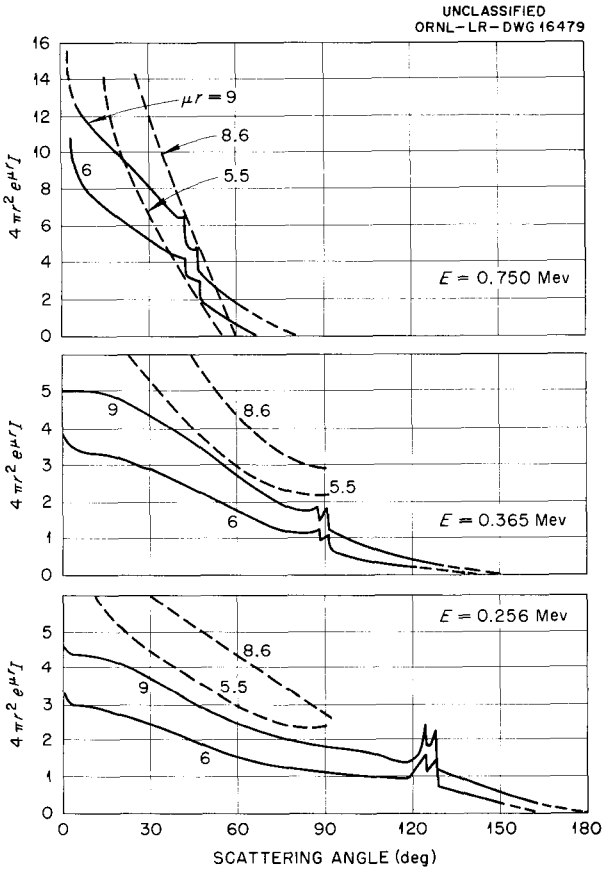

Fig. 44.9. Comparison of Experimental Data for Water with Calculated Data for Water. Three separate graphs are shown for each of three values of the scattered gamma-ray energy, E. The values shown on each curve refer to the number of mean free paths for 1.33-Mev radiation in water (μ = 0.0612 cm^{-1}). The experimental data (dashed lines) disagree with calculations (solid lines) by an almost constant factor of 2 for 0.256 and 0.365 Mev. The disagreement is not so uniform for the 0.75-Mev data.

Goldstein and Wilkins[16] present the energy spectra of the energy flux for Co^{60} gamma radiation in water as integrations over all solid angles of the differential spectra. To compare these calculated results with experiment it was necessary to perform an integration of the experimental results over the detector angle. Since only a few scattering angles were measured, interpolations were made for angles between those measured. The errors in the angle integrals induced by the interpolation could be $\sim$20%. Experimental observations were not possible for detector angles larger than 90 deg, although at scattered energies of less than 0.5 Mev, larger angles are important to the integration. Extrapolations were made for larger angles in all cases, but uncertainties of about 30% can exist for the lowest energies plotted. In addition, at energies above 1 Mev it was necessary to avoid, by extrapolation, effects of detector energy and angle resolution. This last factor is capable of introducing additional uncertainties of $\sim$20% in the integration at the highest energies.

In Fig. 44.10 the results of such integrations are compared with the calculations of Goldstein and Wilkins.[16] It is seen that there again exists a discrepancy of about a factor of 2 in integrated intensity, along with a very considerable difference in shape. The latter may be strongly influenced by the problems of the hand integration, but it is not likely that this error will account for the disagreement between the experiment and theory.

Conclusions

A considerable discrepancy in absolute magnitude seems to exist between the results of this experiment and those of calculational programs which have previously seemed to yield good results when compared with dose measurements. This discrepancy cannot be explained on the basis of known experimental uncertainties. However, when the experiment was performed it was not expected that absolute intensity results would be presented.

[16] H. Goldstein and J. E. Wilkins, Jr., *Calculations of the Penetration of Gamma Rays. Final Report*, NDA-15C-41 or NYO-3075 (June 30, 1954).

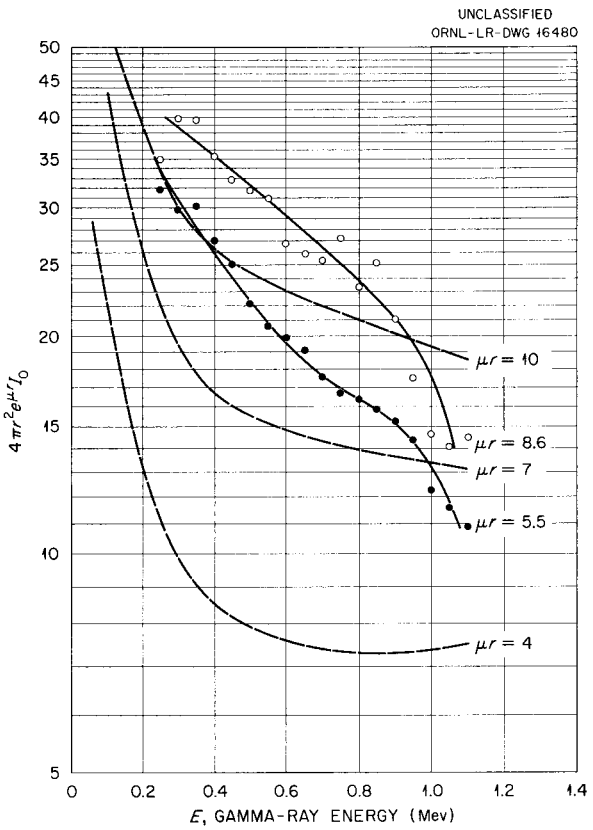

Fig. 44.10. Comparison of the Experimental Differential Energy Flux After Integration Over Angle (Solid Lines) with Calculated Values (Dashed Lines). The values shown for the various curves refer to the number of mean free paths for 1.33-Mev radiation in water ($\mu = 0.0612$ cm^{-1}).

The shapes of the experimental spectra, after rough integration over detector angle, do not appear to agree with the calculated results of the moments method. However, this comparison of spectral shape cannot be made fairly until calculations have produced energy spectra directly comparable with experiment.

As mentioned previously, the experimental results presented agreed with those for concrete.[14] It is to be noted that Whyte's integration over the angle of his normalized experimental data agreed in shape with the calculations of Goldstein and Wilkins. The only obvious explanation for this is that Whyte's data extended to only 60 deg, while this experiment extended to 90 deg. Further, in the integration presented in Fig. 44.10, significant contributions for angles >90 deg were present for energies <0.5 Mev. These contributions were estimated on the basis of crude extrapolations.

It is planned that when additional suitable equipment becomes available, a more careful and complete experiment of this type will be performed. Both spectral and dose measurements will be made under similar conditions to improve the usefulness of the data.

This paper is to be published as a separate topical report.[17]

[17] R. W. Peelle, F. C. Maienschein, and T. A. Love, *Energy and Angular Distribution of Gamma Radiation from a Co^{60} Source After Diffusion Through Many Mean Free Paths of Water*, ORNL-2196 (to be published).

45. ENERGY AND ANGULAR DISTRIBUTION OF AIR-SCATTERED NEUTRONS FROM A MONOENERGETIC SOURCE

C. D. Zerby

A calculation of the energy and the angular flux distribution of air-scattered neutrons is being made by using the Monte Carlo method. The problem analysis is complete, and coding for calculation on the Oracle is near completion.

The source of neutrons can be taken as an isotropic point source or a unit surface source located in a sphere. The neutrons emitted from the surface can have an angular distribution about the normal given by

$$P(\theta) = A \cos^n \theta ,$$

where

$P(\theta)$ = probability of emission per unit solid angle, in a direction inclined at an angle θ with the normal, per unit area,

θ = angle with respect to the normal,

A = normalizing constant,

n = 0, 1, 2, ...

The neutron angular flux distribution and the energy spectrum at several angle intervals will be determined at various points in space. The surface source can have any orientation and location with respect to the points at which the flux will be determined.

The cross sections being used were taken from a previous report[1] and include the complete resonance structure. The scattering will be taken as isotropic in the center-of-mass system.

Although the fluxes will be determined for monoenergetic neutron sources, it will be possible to construct the flux for sources emitting neutrons with any angular distribution and energy spectrum by superposition of the resulting data.

For comparison with previous approximate analytic calculations, the energy and the angular distribution of single, double, triple, and all other multiply scattered neutrons will be recorded separately.

[1] *Neutron Cross Sections*, AECU-2040 (May 15, 1952).

46. ENERGY ABSORPTION RESULTING FROM GAMMA RADIATION INCIDENT ON A MULTIREGION SHIELD WITH SLAB GEOMETRY

S. Auslender[1]

The code of a Monte Carlo calculation of energy penetration and deposition resulting from transport gamma radiation in a shield of slab geometry has been used in a parametric study of a two-region lead-water shield. The code utilizes straightforward sampling techniques except for a doubling technique operating on the unscattered flux.

For the parametric study the radiation was 1-Mev gamma rays incident on the slab at 0°, 60°, 70° 32′, and 75° 31′. The first region of the slab was composed of water 1.5 mfp thick at the initial gamma-ray energy, and the second region was composed of lead 0.5 mfp thick. Preliminary results of the calculation are shown in Figs. 46.1 through 46.4. The dashed lines are a fit by eye to the data. The large rate of change of heat deposition near the front surface of the lead can be explained by the rapid absorption, in the lead, of the low energy.

The coding has been extended to calculate energy flux and tissue dose rate as well as energy deposition. Figures 46.5 through 46.9 are plots of the buildup factor for the dose rate, due to the gamma rays that have penetrated the slab, as a function of the composition of the slab. The buildup factor is defined as

$$B_r \equiv \frac{D}{D_0 e^{\mu_0 r \sec \theta}} ,$$

[1] Pratt & Whitney Aircraft.

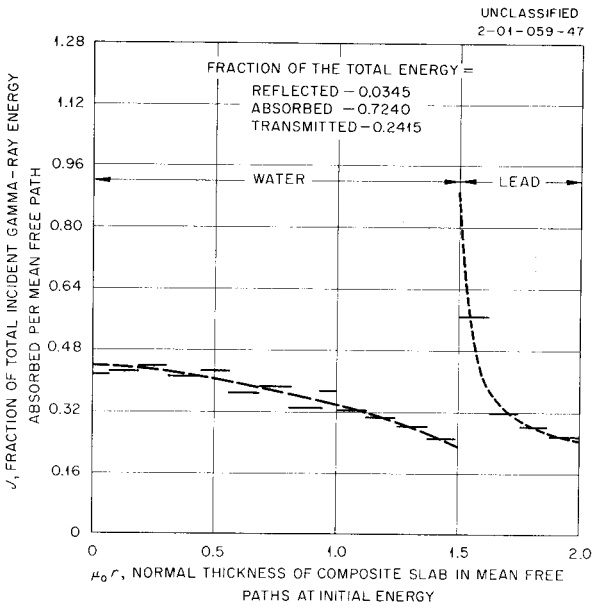

Fig. 46.1. Fraction of Energy from 0-deg Incident Gamma Rays Absorbed in a Water-Lead Slab.

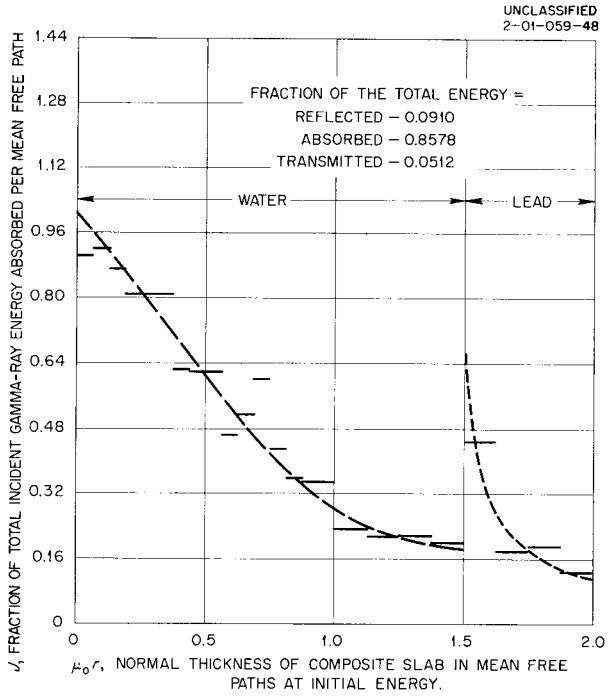

Fig. 46.2. Fraction of Energy from 60-deg Incident Gamma Rays Absorbed in a Water-Lead Slab.

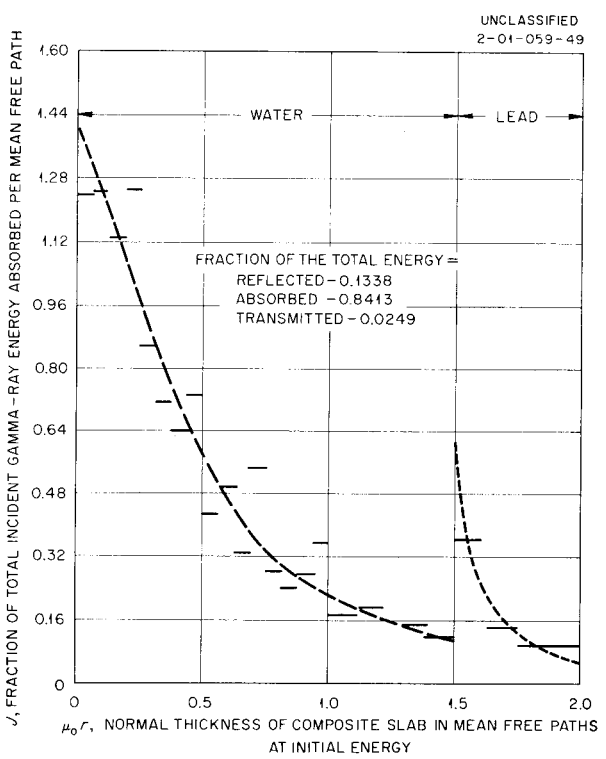

Fig. 46.3. Fraction of Energy from 70° 32′ Incident Gamma Rays Absorbed in a Water-Lead Slab.

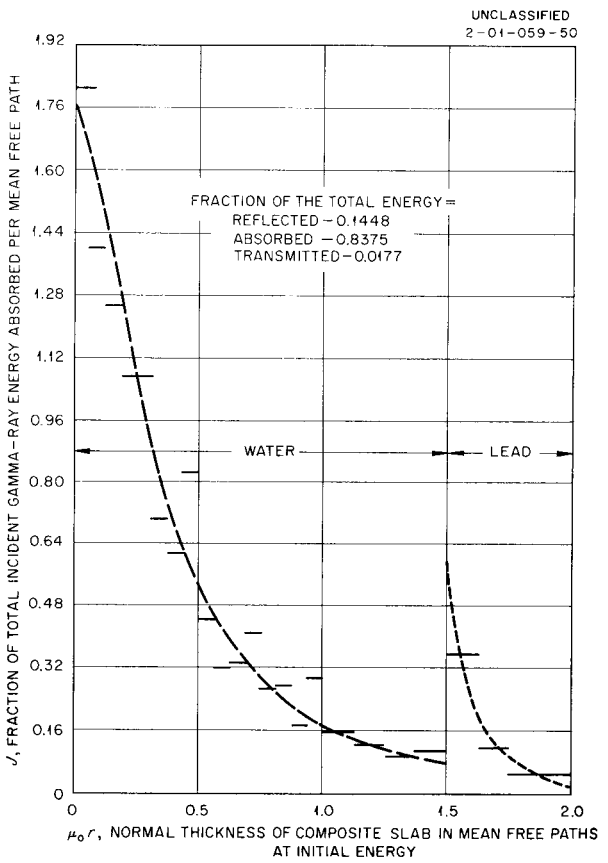

Fig. 46.4. Fraction of Energy from 75° 31′ Incident Gamma Rays Absorbed in a Water-Lead Slab.

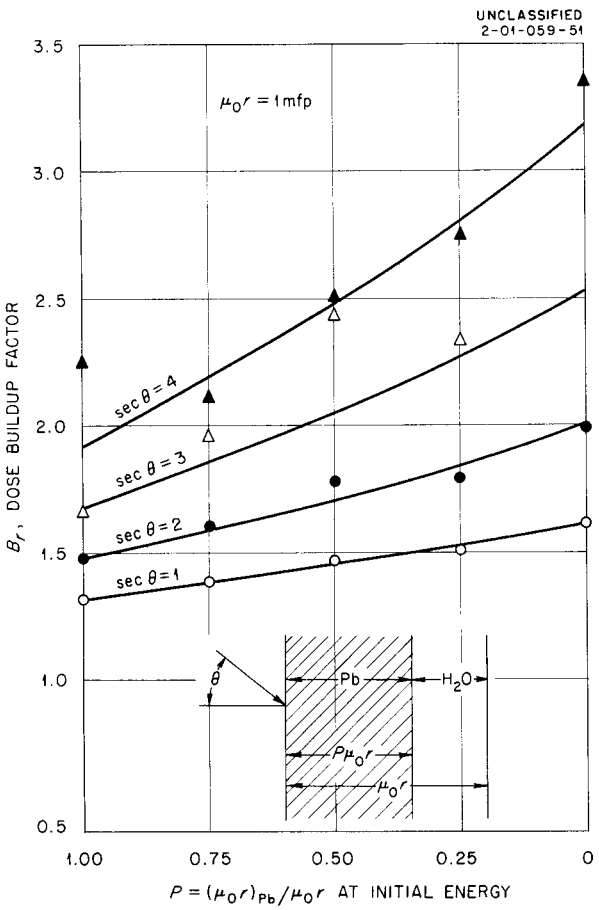

Fig. 46.5. Buildup Factor for Dose Rate in a Lead-Water Shield Resulting from 3-Mev Incident Photons from a Plane, Monodirectional Source.

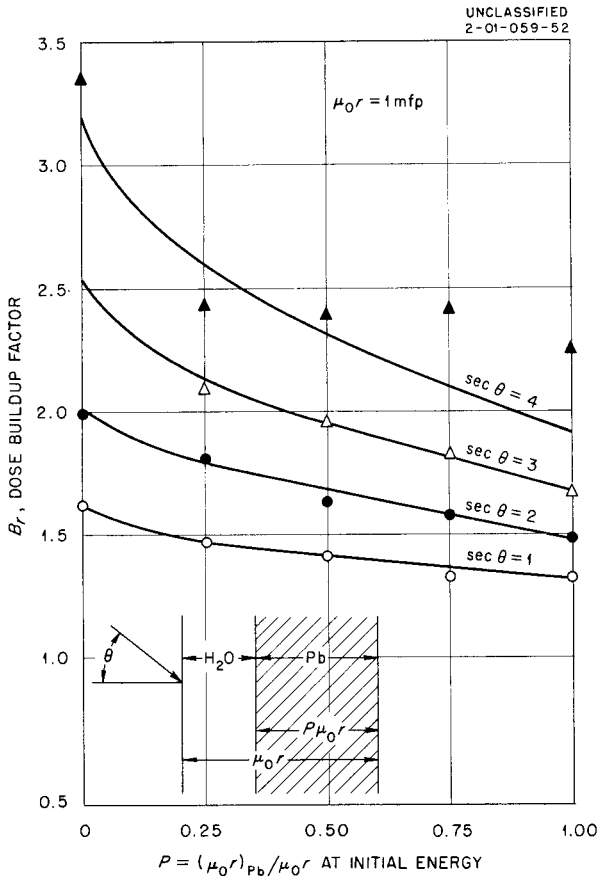

Fig. 46.6. Buildup Factor for Dose Rate in a Water-Lead Shield Resulting from 3-Mev Incident Photons from a Plane, Monodirectional Source.

where

D = calculated dose rate (mr/hr),

D_0 = dose rate with the source unchanged but with the slab missing,

$\mu_0 r \sec\theta$ = oblique thickness of the slab in mean free paths at the source energy.

The composition of the slab is denoted by P and defined as

$$P \equiv \frac{\text{thickness of lead (mfp)}}{\text{thickness of entire slab (mfp)}} \quad \text{(at the source energy)}$$

$$= \frac{(\mu_0 r)_{Pb}}{\mu_0 r} ,$$

where

$$\mu_0 r \equiv (\mu_0 r)_{Pb} + (\mu_0 r)_{H_2O} .$$

Figures 46.5, 46.7, and 46.9 are for shields with the lead in front of the water, and Figs. 46.6 and 46.8 are for water in front of lead. The sources for Figs. 46.5 through 46.8 are plane monodirectional. The source for Fig. 46.9 is a surface source having a $\cos^n\theta$ angular distribution, where θ is measured from the normal to the surface.

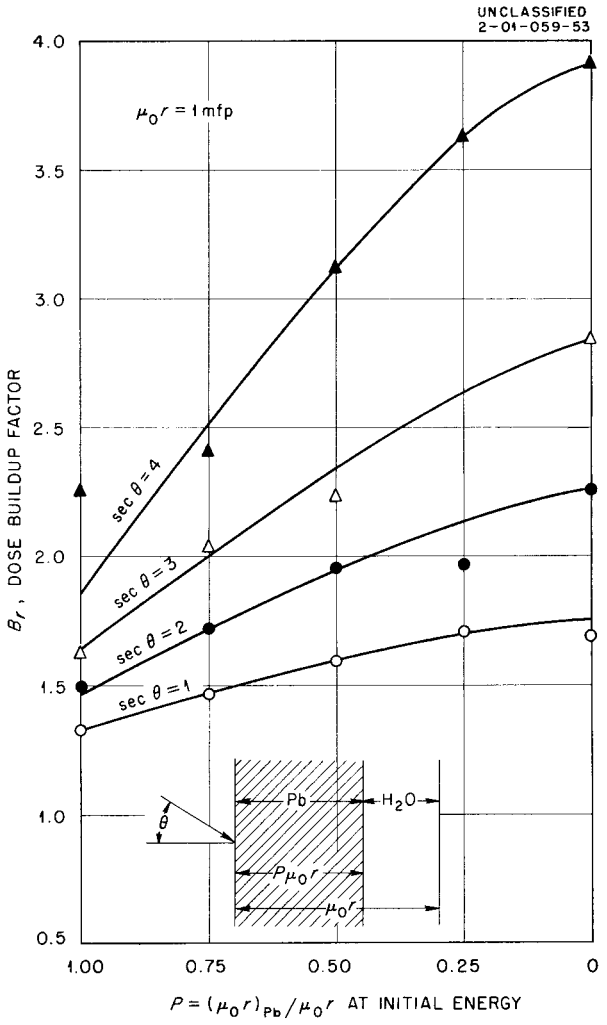

Fig. 46.7. Buildup Factor for Dose Rate in a Lead-Water Shield Resulting from 1-Mev Incident Photons from a Plane, Monodirectional Source.

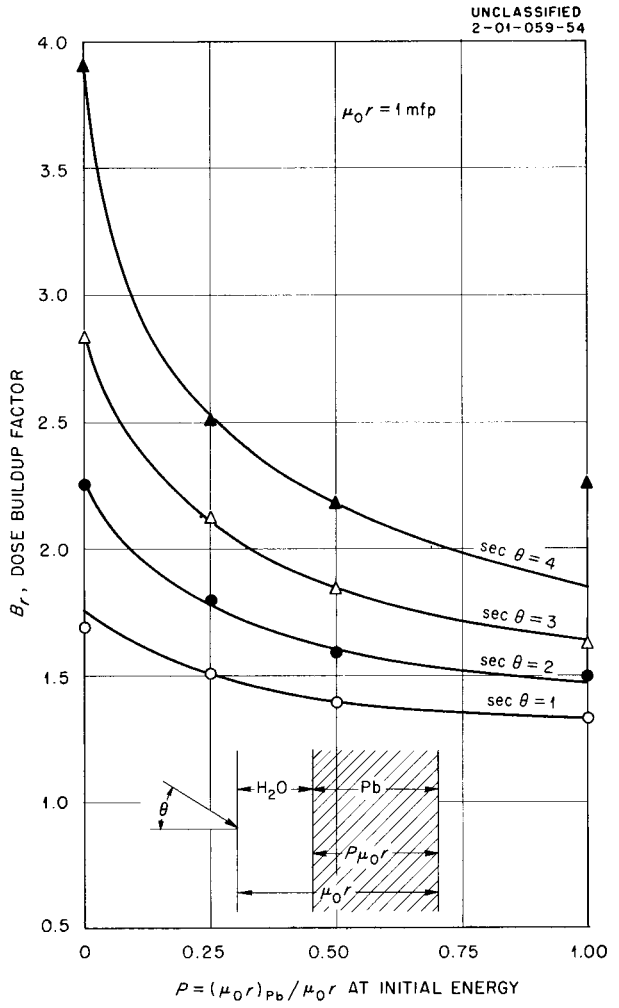

Fig. 46.8. Buildup Factor for Dose Rate in a Water-Lead Shield Resulting from 1-Mev Incident Photons from a Plane, Monodirectional Source.

This source is normalized to one gamma ray per unit area of surface per 2π steradians (in the forward direction):

$$1 = \int_{2\pi} S(\Omega)\, d\Omega \ ,$$

$$S(\Omega) = \frac{n+1}{2\pi} \cos^n \theta \ .$$

When $n = 0$, the source is isotropic. For $n = \infty$, the source is plane monodirectional and normal to the surface.

It is obvious from the figures that lead is more effective in stratified slab shields when it is placed behind a good scatterer such as water.

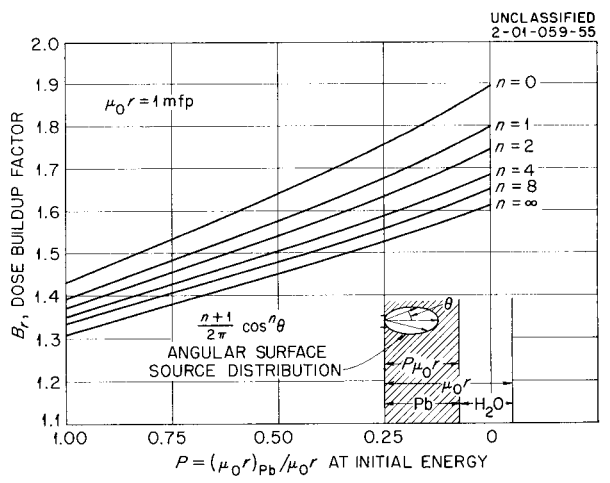

Fig. 46.9. Buildup Factor for Dose Rate in a Lead-Water Shield Resulting from 3-Mev Incident Photons from a Plane Cos^n θ Surface Source.

This is especially true for the lower source energies. The explanation is fundamentally the same as for the large energy deposition rate in the front edge of the lead when it is behind water. The scatter in the answers is, of course, due to the method of solution. Since the answers are estimates of the correct answer, any one problem may be calculated several times, each time with a new set of random numbers. If this is done, the average of the several estimates can be accepted as the answer, and a standard deviation can be calculated for it.

47. MONTE CARLO STUDY OF THE GAMMA-RAY ENERGY FLUX, DOSE RATE, AND BUILDUP FACTORS IN A LEAD-WATER SLAB SHIELD OF FINITE THICKNESS

S. Auslender[1]

The gamma-ray energy flux, dose rate, and buildup factors in a lead-water shield of finite thickness have been calculated by a Monte Carlo method. The calculations included 1-, 3-, and 6-Mev photons incident on the slab, both along a normal and at an angle of 60 deg. The buildup factors for energy and dose obtained in this calculation were compared with those obtained by use of the moments method[2] for monoenergetic, plane monodirectional sources normally incident upon a semi-infinite, homogeneous medium. The thicknesses of the lead-water shield in centimeters and in mean free paths for the various incident gamma-ray energies are given in Table 47.1.

The normalized energy flux for the 3-Mev photons is plotted in Fig. 47.1, as a function of the normal

[1] Pratt & Whitney Aircraft.

[2] H. Goldstein and J. E. Wilkins, Jr., *Calculations of the Penetration of Gamma Rays. Final Report*, NYO-3075 (June 30, 1954).

TABLE 47.1. NORMAL THICKNESSES OF A LEAD-WATER SLAB SHIELD

Region	Thickness			
	cm	mfp		
		1 Mev	3 Mev	6 Mev
Pb	11.58	9.089	5.654	5.878
H_2O	35.81	2.542	1.382	0.996
Total	47.39	11.631	7.036	6.874

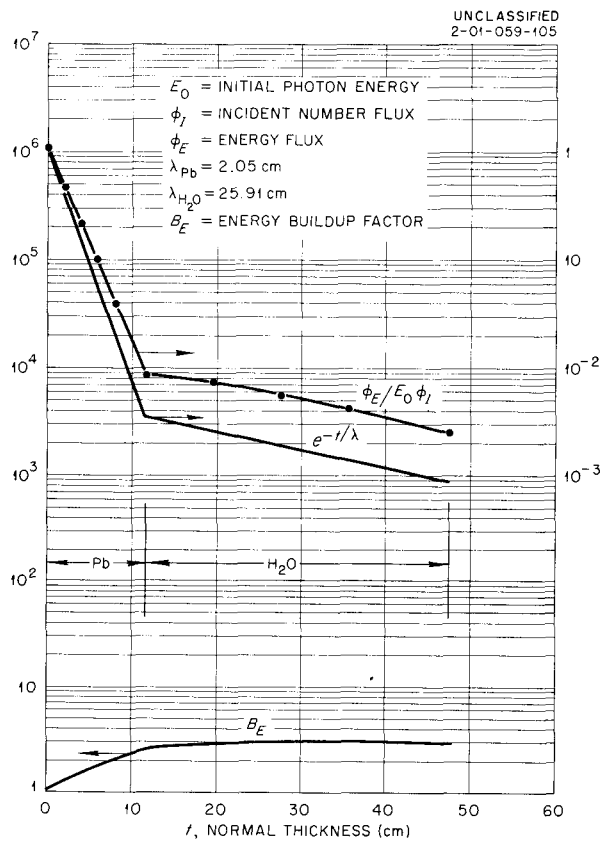

Fig. 47.1. Gamma-Ray Energy Flux and Energy Buildup Factor as a Function of the Normal Thickness (cm) of a Finite Lead-Water Slab Shield: 3-Mev Normally Incident Photons.

thickness of the shield in centimeter units. The uncollided energy flux, normalized to unity at the initial boundary, is also plotted. The third curve in the figure is the energy buildup factor, B_E, which is the ratio of the two energy flux curves:

$$B_E \equiv \frac{\phi_E/E_0\phi_I}{e^{-t/\lambda}} \equiv \frac{\phi_E}{E_0\phi_I e^{-t/\lambda}} ,$$

where

ϕ_E (Mev·cm^{-2}·sec^{-1}) = energy flux at the point of interest in the shield,

E_0 (Mev/γ) = initial photon energy,

ϕ_I (γ's·cm^{-2}·sec^{-1}) = number flux incident on shield,

t (cm) = distance between the initial boundary and the point of interest in the shield,

λ (cm) = relaxation length,

$e^{-t/\lambda}$ = uncollided energy flux at the point of interest.

In a similar manner the normalized dose rate and the dose buildup factor, B_r, are plotted in Figs. 47.2 and 47.3 for 3-Mev photons incident on the slab at 0 and 60 deg, respectively. Here,

$$B_r \equiv \frac{D/\phi_I}{D_0 e^{-t\sec\theta/\lambda}/\phi_I} \equiv \frac{D}{D_0 e^{-t\sec\theta/\lambda}} ,$$

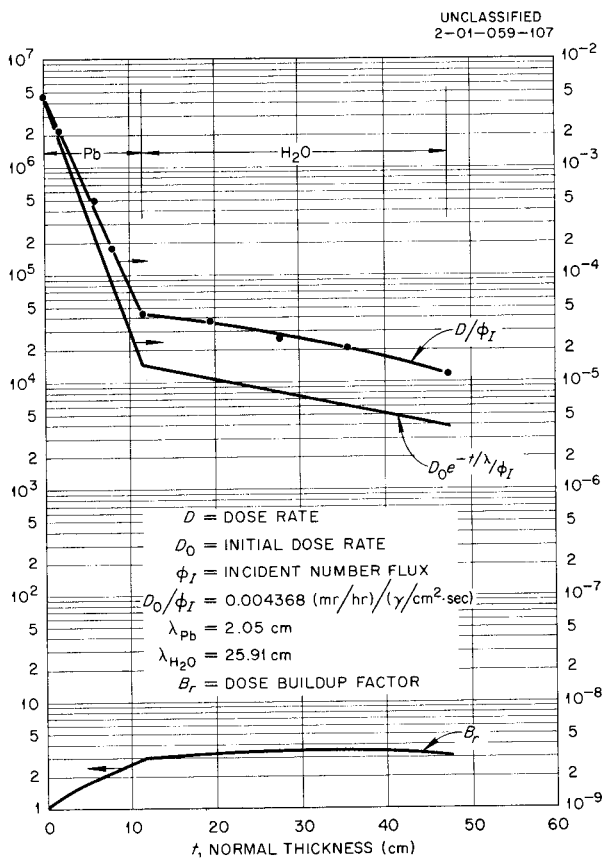

Fig. 47.2. Gamma-Ray Dose Rate and Dose Buildup Factor as a Function of the Normal Thickness (cm) of a Finite Lead-Water Slab Shield: 3-Mev Normally Incident Photons.

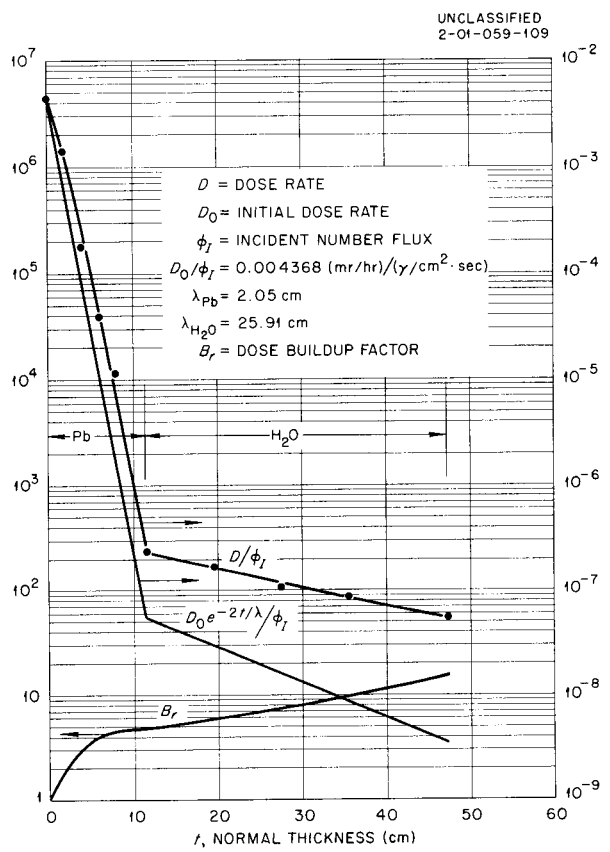

Fig. 47.3. Gamma-Ray Dose Rate and Dose Buildup Factor as a Function of the Normal Thickness (cm) of a Finite Lead-Water Slab Shield: 3-Mev Photons Incident at a 60-deg Angle.

where

D (mr/hr) = dose rate (tissue) at the point of interest,

D_0 (mr/hr) = dose rate (tissue) of the uncollided incident photons at the initial boundary,

θ = angle of incident radiation (deg).

The energy buildup factor as a function of oblique thickness, in mean free paths, for normally incident photons is presented in Fig. 47.4. The dose buildup factors as a function of the oblique thickness are given in Figs. 47.5 and 47.6 for photons normally incident and for 60-deg incident photons, respectively. Data from the results of the moments method solution[2] are also plotted for purposes of comparison, although it must be remembered that those calculations were for infinite homogeneous media and are not directly comparable with the present calculations for a finite two-region slab. The calculations for lead do agree reasonably well for the first few relaxation lengths, where the effects stemming from the dissimilarity of the slabs should be least.

This investigation will be reported in greater detail elsewhere.[3]

[3] S. Auslender, *A Monte Carlo Study of the Gamma-Ray Energy Flux, Dose Rate, and Buildup Factors in a Lead-Water Slab Shield of Finite Thickness*, ORNL-2194 (in press).

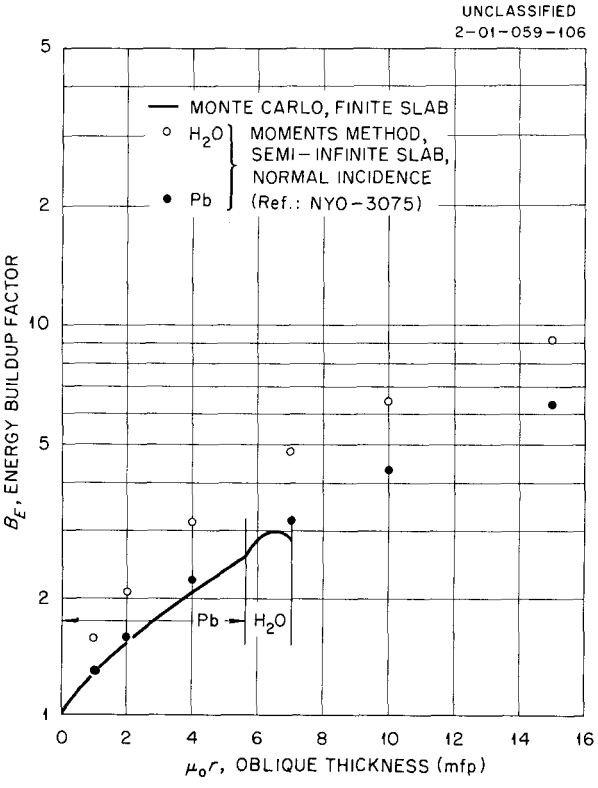

Fig. 47.4. Gamma-Ray Energy Buildup Factor as a Function of the Oblique Thickness (mfp) of a Finite Lead-Water Slab Shield: 3-Mev Normally Incident Photons.

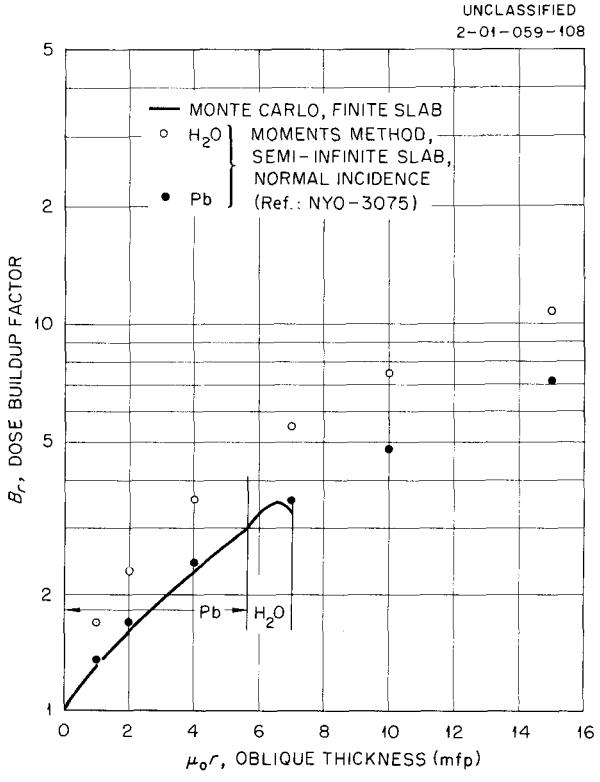

Fig. 47.5. Gamma-Ray Dose Buildup Factor as a Function of Oblique Thickness (mfp) of a Lead-Water Slab Shield: 3-Mev Normally Incident Photons.

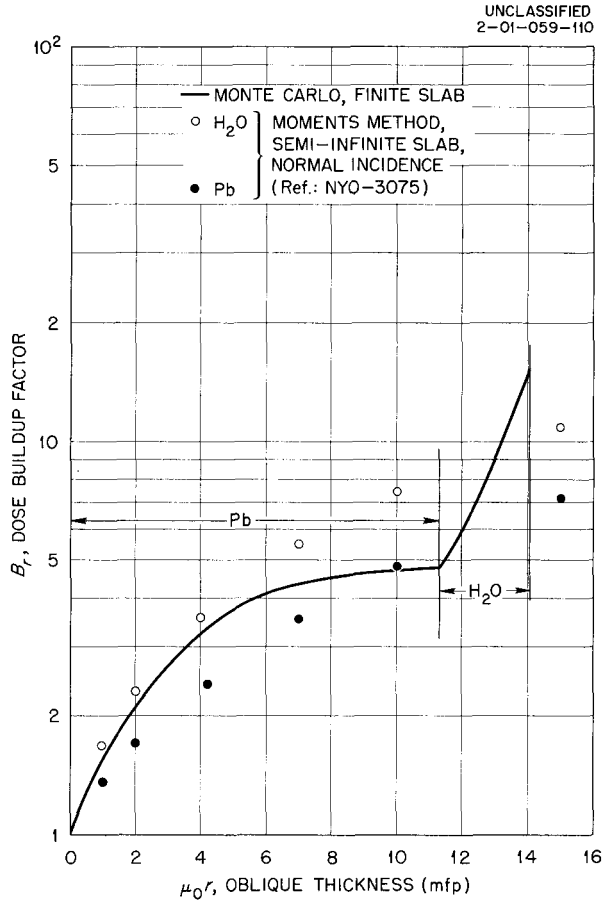

Fig. 47.6. Gamma-Ray Dose Buildup Factor as a Function of Oblique Thickness (mfp) of a Finite Lead-Water Slab Shield: 3-Mev Photons Incident at a 60-deg Angle.

Part VI

RADIATION DETECTOR DEVELOPMENT

48. FAST-NEUTRON SPECTROMETER DEVELOPMENT

R. B. Murray

A knowledge of the energy spectrum of fission neutrons, after they penetrate various thicknesses of shielding material, is of considerable importance in a shield design program. Measurements of such spectra have been handicapped in the past because of the lack of an efficient, fast-neutron spectrometer which would record spectra directly; the measurements were made previously by employing the laborious technique of counting tracks in nuclear emulsions. The development of such an instrument presents a difficult problem in that: (1) it is necessary to measure a *continuous* spectrum over the region from 1 to 12 Mev; (2) the neutron source may be widely distributed in space, as in the case of a reactor and shield; and (3) fission neutrons are accompanied by an enormous background of gamma rays of high energy.

A proton-recoil, fast-neutron spectrometer has been designed and successfully used at the Bulk Shielding Facility by Cochran and Henry.[1] This instrument is limited in its usefulness, however, by the inherently low detection efficiency of a radiator-absorber type of spectrometer. In view of this fact, a fast-neutron spectrometer program has continued with the hope of developing a more sensitive instrument which can be used to extend the previous measurements.

The types of spectrometers which have been considered for this purpose are (1) proton-recoil spectrometers, and (2) those in which the total energy released in a neutron-induced nuclear reaction is measured. In the proton-recoil instrument the detection efficiency is usually small, since it is necessary to collimate the incoming neutron beam as well as the recoil protons. In this respect the second type of instrument is to be preferred, since nearly isotropic detection can be realized in a proportional counter or scintillation crystal containing the target nucleus.

A survey of nuclear reactions which might serve as a basis for a neutron spectrometer indicates that the number of possible reactions is very small. The $He^3(n,p)H^3$ reaction (Q = 0.77 Mev) has been used[2] in a proportional counter for neutron spectroscopy in the region between thermal energies and 1.2 Mev. The pulse-height spectrum from monoenergetic neutrons of energy E_n contains not only a peak from the (n,p) reaction at $E_n + Q$, but also a continuous distribution below $\frac{3}{4}E_n$, arising from elastically scattered He^3 recoils. The pulse-height distribution arising from a fission spectrum of neutrons would then be a very complex one, and its interpretation would necessitate a detailed knowledge of the reaction and scattering cross sections, information which is not available at the present time.

The $Li^6(n,\alpha)H^3$ reaction (Q = 4.78 Mev) has been employed as a neutron detector in various lithium-containing phosphors; some attempts have been made to measure fast-neutron spectra with lithium-loaded photographic emulsions. This reaction seems to be most applicable to the problem at hand by virtue of its high Q, since competing nuclear reactions are endothermic with Q values of about −2.5 Mev.

Other nuclear reactions which might conceivably be used to measure fast-neutron energies generally give rise to several groups of pulses from a monoenergetic neutron source as a result of branching of the reaction. For example, the $B^{10}(n,\alpha)Li^7$ reaction goes to the ground state and first excited state of Li^7 with Q values of 2.78 and 2.30 Mev, respectively.

The two spectrometers now being considered are a proton-recoil instrument and an LiI(Eu) scintillation spectrometer. Both spectrometers are discussed below.

Proton-Recoil Spectrometer

In the absence of a nuclear reaction which can be immediately utilized, attention has been devoted to the various types of proton-recoil spectrometers in the hope of realizing a greater detection efficiency than in the previous instrument.[1] Such an improvement is to be found, in principle, in a spectrometer designed and constructed at the Laboratory by Johnson and

[1] R. G. Cochran and K. M. Henry, *Rev. Sci. Instr.* **26**, 757 (1955).

[2] R. Batchelor, R. Aves, and T. H. R. Skyrme, *Rev. Sci. Instr.* **26**, 1037 (1955).

Trail.[3] A diagram of this instrument is shown in Fig. 48.1.

In practice, the neutron beam is collimated along the horizontal direction and impinges on a thin polyethylene radiator which is mounted in one of several apertures in the radiator wheel. Those recoil protons which emerge in the forward direction are detected by a triple coincidence in the two proportional counters and the NaI crystal. A triple coincidence signal opens the gate to a multichannel analyzer which records the pulse height from the scintillation counter. This pulse height is a direct measure of the neutron energy after correction has been made for the proton energy loss in the proportional counters. Several radiators, of various thicknesses, can be accommodated in the radiator wheel, so that a given spectral region can be examined with a radiator of optimum thickness. Field tubes in the proportional counters restrict the sensitive volume to the upper half-plane, so that spurious events in the lower half of the counters will not register. A more detailed description of the construction and operation of this instrument is available elsewhere.[3]

The efficiency of this spectrometer is greater than that of a radiator-absorber type[1] in two respects: (1) it is possible to cover a wide spectral region with the use of a multichannel analyzer rather than only one narrow energy interval at a time; (2) in a given energy interval, all recoil protons emitted in the forward direction are detected and analyzed, whereas in the radiator-absorber spectrometer only a fraction of the protons having the proper energy and direction are detected. This fraction depends on the relative thicknesses of the radiator and the detector.

In view of the substantial increase in efficiency possible with the crystal spectrometer, an instrument of this type is being constructed and

[3] C. H. Johnson and C. C. Trail, *Rev. Sci. Instr.* **27**, 468 (1956).

UNCLASSIFIED
ORNL-LR-DWG 10816

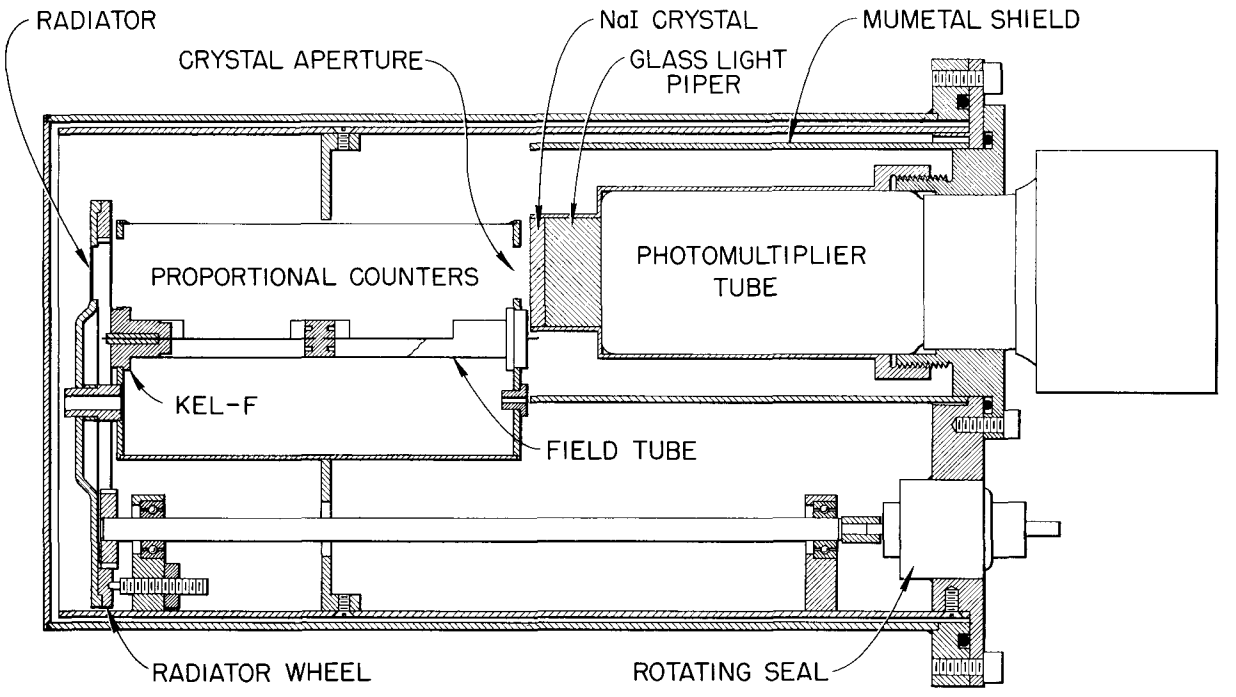

Fig. 48.1. Schematic Diagram of Proton-Recoil Spectrometer.

will be tested at the BSF. The principal uncertainty in its usefulness is the fact that high counting rates can be anticipated, especially in the scintillation counter, from the intense gamma-ray background. It is hoped, however, that the use of a thin crystal and fast coincidence techniques will permit satisfactory operation with a reactor as the neutron source. All the mechanical and electronic components of the spectrometer have been constructed and assembled. The spectrometer is currently in the stage of preliminary operation and testing. It will be checked out and calibrated with monoenergetic neutrons from the Van de Graaff generator prior to any attempt to measure a fission spectrum.

LiI(Eu) Scintillation Spectrometer

The scintillation response of LiI(Eu) crystals to neutrons is due to the $Li^6(n,\alpha)H^3$ reaction (Q = 4.78 Mev); the reaction products in slowing down and stopping excite the crystal, causing radiation of light which can be detected by a conventional photomultiplier arrangement. Analysis of the photomultiplier pulse-height spectrum provides a measure of the total energy released in the crystal, and hence of the energy of the incoming neutron.

There are several advantages offered by an LiI(Eu) crystal being used as the detecting element in a fast-neutron spectrometer: (1) the crystal is an isotropic detector, so that a neutron collimator need not be used to define the direction of the incident neutron; (2) the crystal is small (e.g., 1 in. in diameter and $\frac{1}{8}$ in. thick), making possible spectral measurements at a "point"; (3) the detection efficiency is orders of magnitude greater than that afforded by proton-recoil spectrometers; and (4) pulses from gamma rays below about 4.7 Mev fall below the thermal peak and can thus be biased out. The difficulties which may be encountered are: (1) the crystals may respond to high-energy gamma rays; (2) the energy resolution for fast neutrons is rather broad; and (3) the crystals are hygroscopic and must be maintained in a moisture-free environment.

The detection efficiency for crystals of Li^6I as a function of neutron energy is shown in Fig. 48.2. The shape of the curve is determined entirely by the energy dependence of the $Li^6(n,\alpha)H^3$ cross section. Thin crystals (2 mm in thickness) are normally used in this work to minimize the gamma-ray detection efficiency; the pulse-height spectra obtained from 10-mm-thick crystals are quite similar to those from 2-mm-thick crystals.

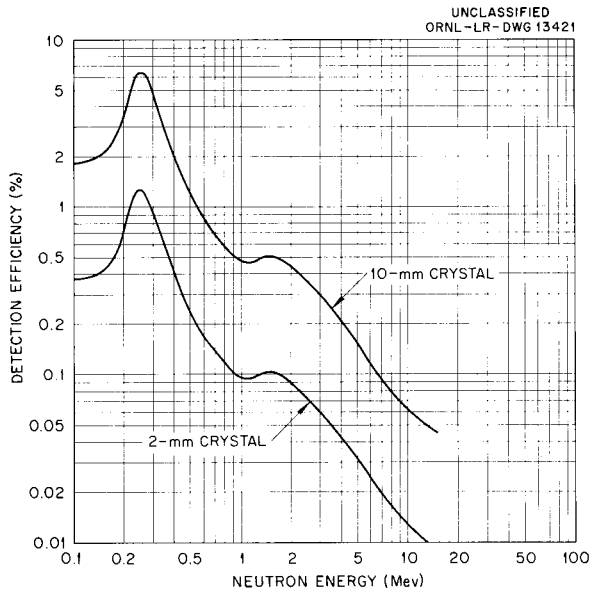

Fig. 48.2. Detection Efficiency of Li^6I as a Function of Neutron Energy.

In order to examine the properties of LiI(Eu) as a fast-neutron spectrometer, it is necessary to bombard a crystal with fast neutrons of a single energy and observe the resulting pulse-height spectrum. Monoenergetic neutrons in the energy region from 0.63 to 14.9 Mev were obtained from the (p,t), (d,d), and (d,t) reactions, using gas targets. The incident particle was accelerated by the ORNL 2.5-Mev Van de Graaff generator. The pulse-height spectra shown in Figs. 48.3, 48.4, and 48.5 are from a 2-mm-thick crystal of Li^6I containing 0.025 mole % europium activator, with incident neutrons of energies 0.63, 1.57, and 5.79 Mev, respectively. These spectra were obtained with the crystal at room temperature. In every case the large thermal-neutron peak arises from neutrons degraded in energy by scattering from the walls, floor, etc. The magnitude of this peak is due to the very large cross section for the (n,α) reaction at thermal energies. In these spectra it is seen that the fast-neutron peak appears as a broad and "rectangular" band, rather than the sharp Gaussian shape of the thermal-neutron peak. This behavior is tentatively ascribed to a difference in the scintillation efficiency

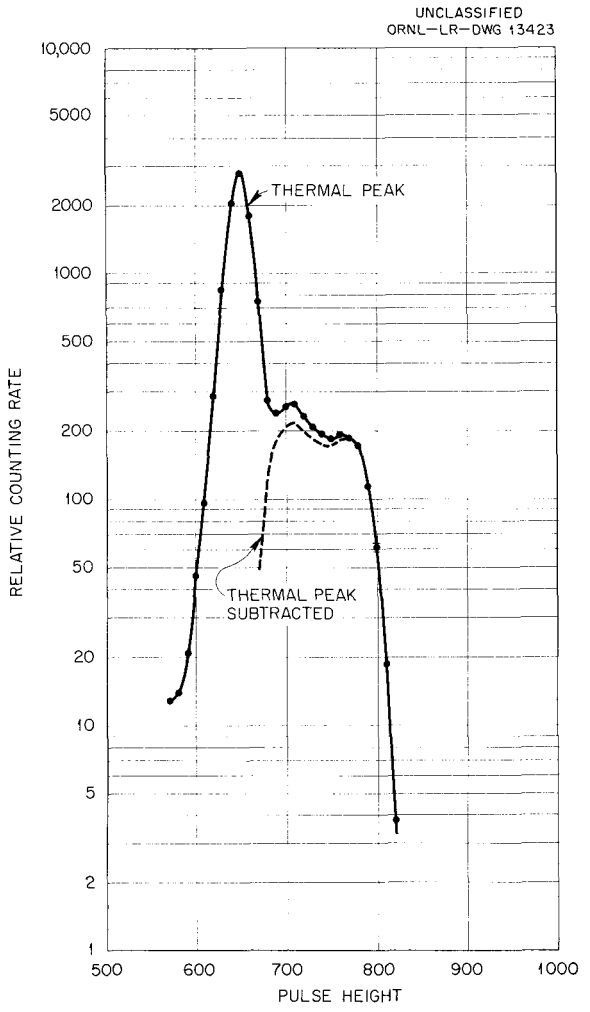

Fig. 48.3. Scintillation Respose of an Li^6I (0.025% Eu) Crystal (24-mm-dia × 2-mm-thick) to 0.63-Mev Neutrons.

of LiI(Eu) for the alpha and the triton at room temperature. For the fast-neutron-induced reaction both the alpha and triton have a range of energies available to them, since the energy division between the reaction products depends upon their angular distribution. For very slow (thermal) neutrons, however, the energy distribution between the alpha and the triton is uniquely specified.

Figure 48.6 shows the pulse-height spectrum from 5.79-Mev neutrons on an 8-mm-thick crystal of Li^7I(Eu). This may be compared with Fig. 48.5 [5.79-Mev neutrons on Li^6I(Eu)], in which a large fast-neutron peak occurs. No evidence of a fast-neutron peak was observed in the Li^7 crystal.

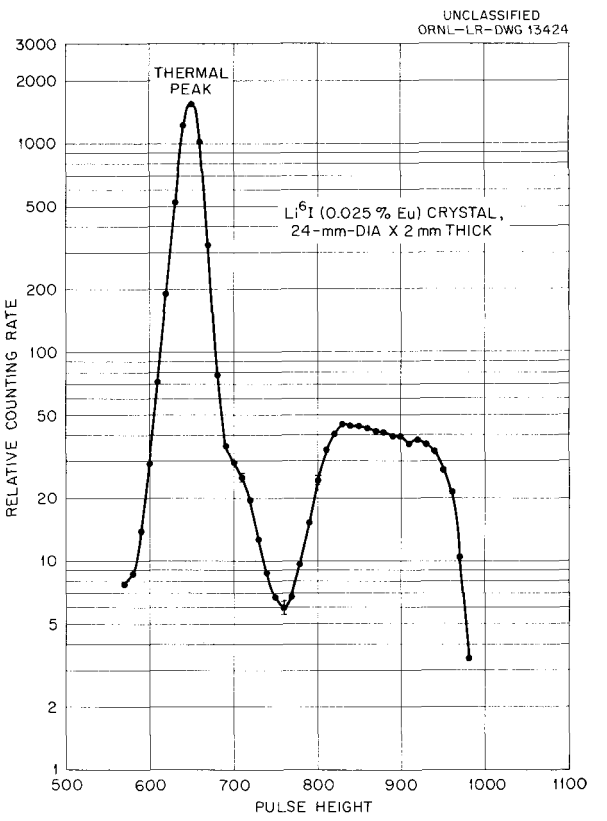

Fig. 48.4. Scintillation Response of an Li^6I (0.025% Eu) Crystal (24-mm-dia × 2-mm-thick) to 1.57-Mev Neutrons.

The small thermal-neutron peak in Fig. 48.6 is due to a trace of Li^6 impurity. The continuous background in both Figs. 48.5 and 48.6 arises from the penetration of the deuteron beam through a thin nickel foil in the gas target which is used for the (d,d) reaction. This background can be isolated (and subtracted) from the fast-neutron spectrum simply by removing the deuterium gas from the target. It should be noted that this continuum is not the result of 5.79-Mev neutrons on the crystal.

One of the major difficulties in measuring the fast-neutron spectrum from a fission source or reactor is the large background of high-energy gamma rays. The availability of the separated isotopes Li^6 and Li^7 leads to the possibility of a simple technique for eliminating the gamma-ray contribution to an observed fast-neutron pulse-height spectrum. This might be done by recording the spectrum from both an Li^6 and an Li^7 crystal;

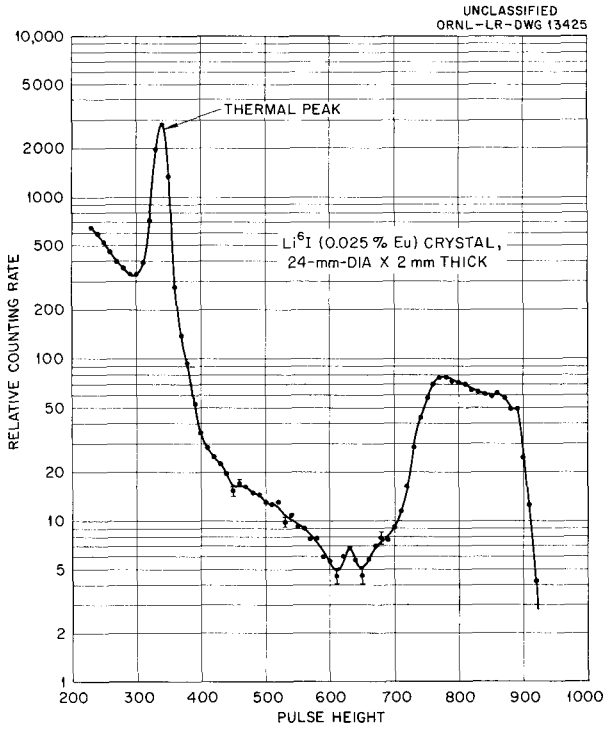

Fig. 48.5. Scintillation Response of an Li^6I (0.025% Eu) Crystal (24-mm-dia × 2-mm-thick) to 5.79-Mev Neutrons.

since gamma rays interact with the electrons of the crystal, the gamma-ray response of both crystals should be the same. The Li^7 pulse-height spectrum, however, will not demonstrate a direct effect from fast neutrons. Taking the difference between the Li^6 and the Li^7 pulse-height spectra should then subtract out the gamma-ray contribution. There are, of course, other neutron events in Li^6 and Li^7 which must be considered, such as inelastic scattering, radiative capture, and other charged-particle reactions. Inelastic scattering and radiative capture give rise to relatively low-energy gamma rays which will fall below the thermal-neutron peak and thus be eliminated. Charged-particle reactions such as (n,p) and (n,d) are endothermic and occur with small cross sections;[4] they will be observed only for neutrons above about 8 Mev. At the present time, this scheme of monitoring the gamma-ray background appears to be feasible. It will be necessary to

[4]G. M. Frye, Jr., *Phys. Rev.* 93, 1086 (1954).

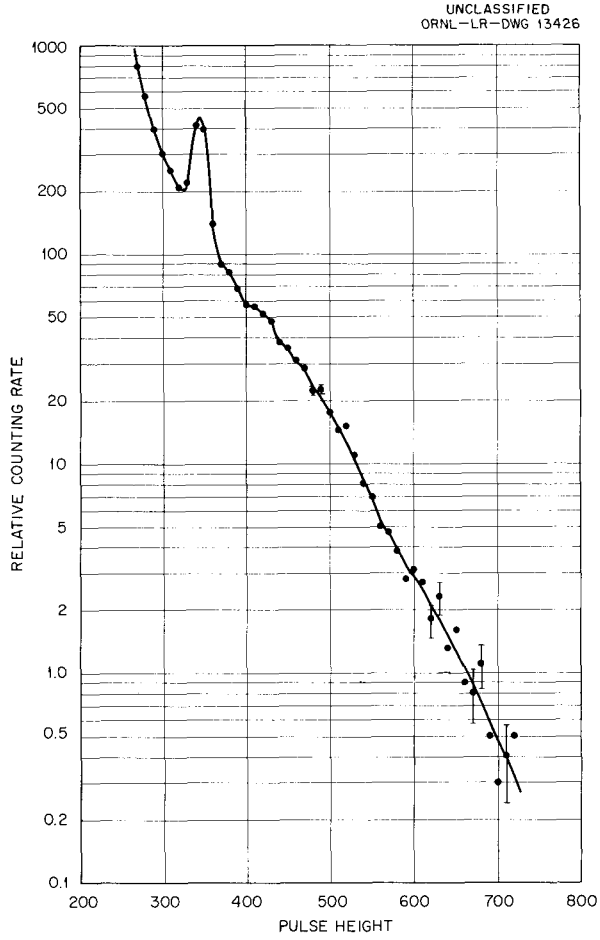

Fig. 48.6. Scintillation Response of an Li^7I (0.046% Eu) Crystal (24-mm-dia × 8-mm-thick) to 5.79-Mev Neutrons.

examine the response of the crystals to high-energy gamma rays and neutrons in greater detail, however, before this technique can be adopted.

The pulse-height spectrum from 14.9-Mev neutrons on $Li^6I(Eu)$ is shown in Fig. 48.7. Two qualitative differences between this spectrum and the spectra at lower energies are observed. First, the fast-neutron peak has a nearly Gaussian shape with a full-width at half-maximum of about 9%. Second, the continuum is quite large compared with the 14.9-Mev neutron peak and rises sharply to a plateau just below the (n,α) peak. In the case of 14.9-Mev neutrons, competing reactions may contribute to the background. This does not necessarily mean, however, that neutrons in the 1- to 8-Mev region of the fission spectrum will be obscured by the background from the higher-energy

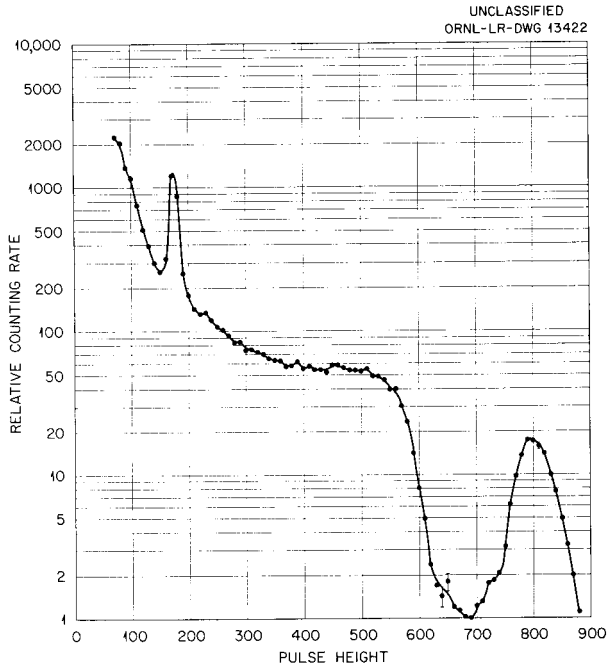

Fig. 48.7. Scintillation Response of an Li^6I (0.025% Eu) Crystal (24-mm-dia × 2-mm-thick) to 14.9-Mev Neutrons.

component; the fission spectrum falls off rapidly in energy, so that the continuum from high-energy neutrons will still be small.

Figure 48.8 shows a plot of pulse height vs total energy released for the Li^6I (0.025% Eu) crystal. The data are plotted as full-width of the peak at half-maximum. It is seen that the mid-points of the peaks can be joined by a straight line, indicating that the relationship is essentially linear throughout the range of interest.

Measurements of fast-neutron pulse-height spectra have been carried out on other crystals of LiI(Eu) with various concentrations of europium activator and Li^6 isotope. The spectra observed have all been basically similar to those shown in Figs. 48.3, 48.4, 48.5, and 48.7. Pulse-height spectra from fast neutrons on a 10-mm-thick crystal of LiI (0.1% Eu), with the natural concentration of Li^6, have been reported previously.[5]

Another variable which can affect the scintillation properties of a crystal is its temperature. In order to examine the effect of varying the

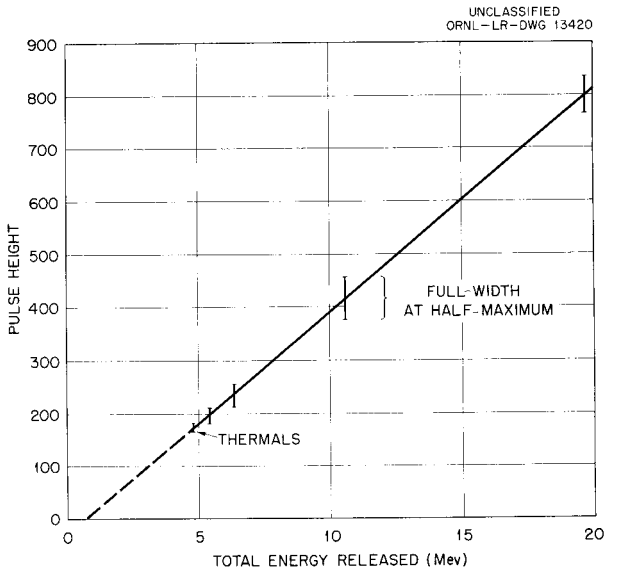

Fig. 48.8. Pulse Height vs Total Energy Released for an Li^6I (0.025% Eu) Crystal (2-mm-thick).

temperature, pulse-height spectra from 5.3-Mev neutrons on Li^6I(Eu) have been recorded at several temperatures. The apparatus used for cooling the crystals is shown schematically in Fig. 48.9; the design of this equipment was dictated by the fact that conventional photomultipliers do not function below about −140°C. With the scheme shown here the photocathode is maintained near room temperature, while the crystal temperature is continuously variable down to −196°C. The crystal temperature, which is measured by a copper-constantan thermocouple, is set by adjusting the flow rate of the cooling gas.

Two effects are observed upon cooling the crystals. First, the scintillation efficiency increases with decreasing temperature. The thermal-neutron pulse height as a function of temperature, for a normal LiI (0.1% Eu) crystal, is shown in Fig. 48.10. Second, the fast-neutron peak assumes a nearly Gaussian shape at about −140°C, with a marked improvement in resolution. This behavior is shown as a function of temperature for two different crystals in Figs. 48.11 and 48.12. The resolution indicated in these spectra is somewhat deceptive, in that it is the full-width at half-maximum divided by the pulse height of the maximum, following the usual convention. From the standpoint of neutron energy, however, the

[5] J. H. Neiler *et al.*, *Phys. Semiann. Prog. Rep. Sept. 10, 1954*, ORNL-1798, p 32.

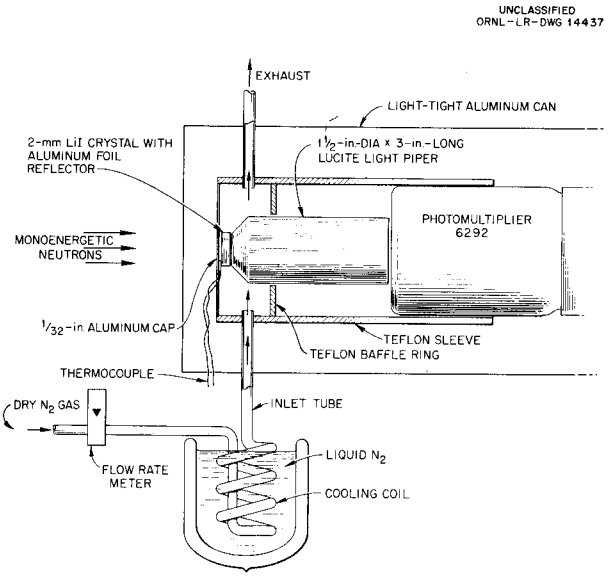

Fig. 48.9. Schematic Diagram of Cooling Apparatus.

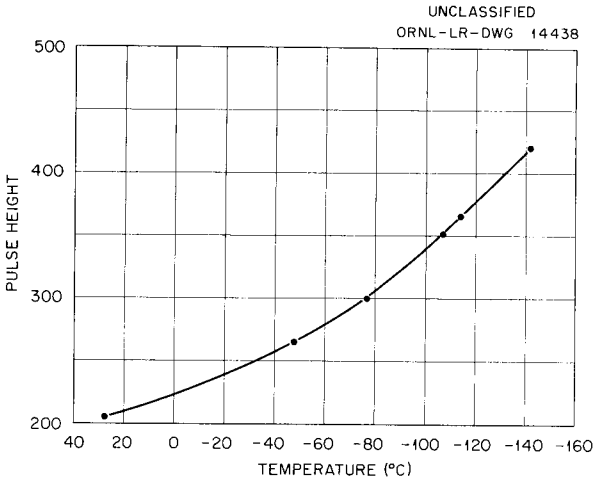

Fig. 48.10. Thermal-Neutron Pulse Height as a Function of Temperature for a Normal LiI (0.1% Eu) Crystal.

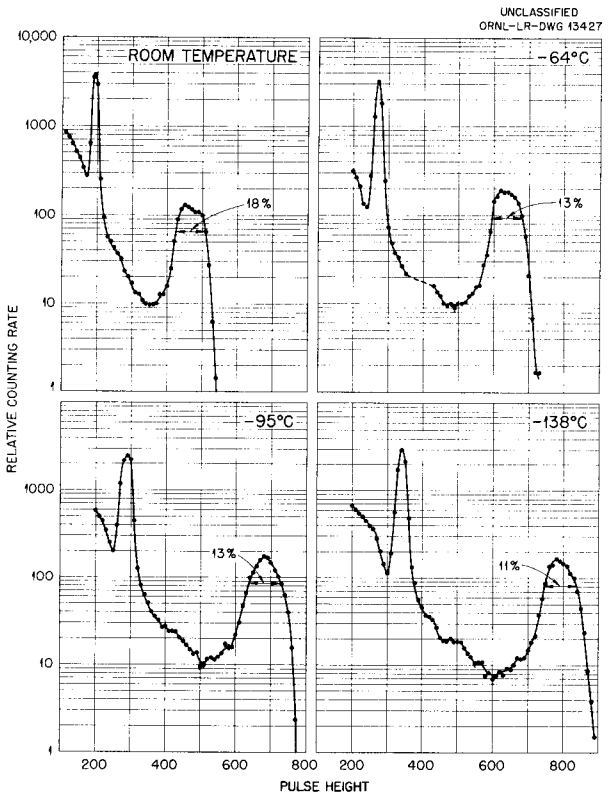

Fig. 48.11. Scintillation Response of an Li^6I (0.025% Eu) Crystal (24-mm-dia × 2-mm-thick) to 5.3-Mev Neutrons for Various Temperatures.

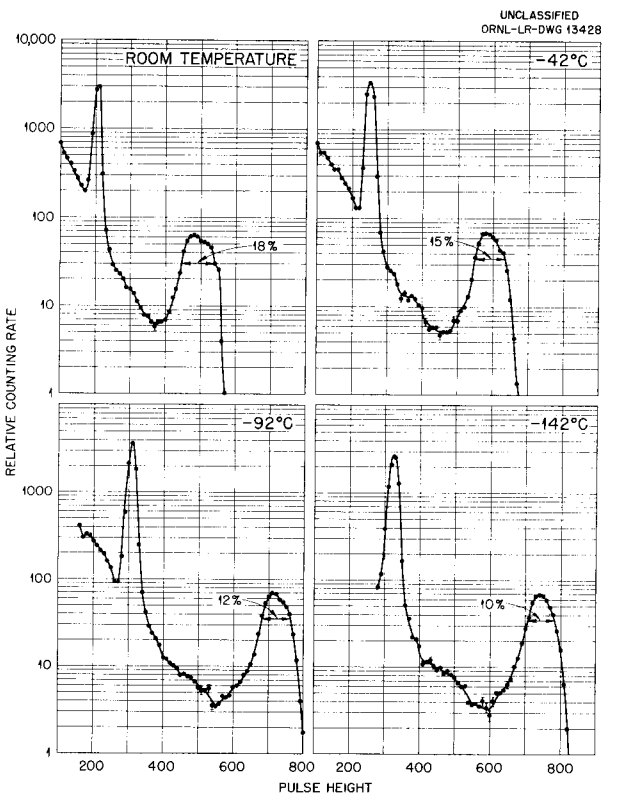

Fig. 48.12. Scintillation Response of an Li^6I (0.06% Eu) Crystal (24-mm-dia × 2-mm-thick) to 5.3-Mev Neutrons for Various Temperatures.

zero of energy occurs at the position of the thermal-neutron peak, so that the *neutron energy* resolution is greater than that shown. For example, the neutron energy resolution at −142°C (Fig. 48.12) is 17.7%. Only one experiment has been carried out at temperatures lower than −142°C, using the Li^6I (0.06% Eu) crystal. The pulse-height spectrum at −196°C, from 5.3-Mev neutrons, was similar to that observed at −142°C (Fig. 48.12). The continuous background in Figs. 48.11 and 48.12 is from the gas target.

The considerable improvement in fast-neutron response observed in these crystals upon cooling has provided the motivation for a continued study of pulse-height spectra at low temperatures. A new cooling apparatus is being constructed to replace that shown in Fig. 48.9, since the gas flow requires almost constant attention to maintain a steady temperature. It is hoped that it will be possible to eliminate the long light pipe, separating the crystal from the photomultiplier, by the use of special photomultipliers which will operate at liquid-nitrogen temperatures. As soon as these experimental details are worked out, it will be of immediate interest to examine fast-neutron pulse-height spectra, at various temperatures, for neutrons throughout the energy region from 1 to 15 Mev.

49. INVESTIGATION OF THE HORNYAK BUTTON AS A FAST-NEUTRON DOSIMETER

F. J. Muckenthaler

The Hurst-type fast-neutron dosimeters which are now being used for fast-neutron dose measurements at the ORNL Shielding Facilities are limited by several features. They cannot be operated in some of the gamma-ray fields maintained in shielding experiments, and they do not possess sufficient sensitivity for some of the measurements required at the Tower Shielding Facility. Perhaps the largest problem is operational, since frequent instrument breakdowns occur under the adverse conditions encountered.

For some time efforts have been devoted toward the development of a possible new dosimeter using a Hornyak button[1] as a detector. The button itself is a homogeneous mixture of fine Lucite (70 parts by weight) and ZnS powder (0.4 to 50 parts by weight) pressed into 2-in.-dia cylinders of various thicknesses and heat-treated at 375°F for several hours. This is encased in a light reflector and mounted on a phototube. The neutrons impinging upon the crystal collide with the protons present, and the recoiling protons excite the ZnS centers. These, in turn, emit photons whose wavelengths lie within the sensitive region of the photomultiplier tube. The pulses from the phototube are fed through a preamplifier and an A-1 amplifier including a pulse-height selector and then into a scaler or 20-channel analyzer. The button is calibrated in the same manner as the dosimeter, using a Po-Be neutron source of known intensity.

The success of the button as a dosimeter and its usefulness in shielding measurements depend on several things. Its range of neutron detection should lie from near 100 kev energy to as high as 15 Mev. It should be capable of weighting each individual proton recoil within the crystal; that is, it should do within the crystal what the integrator does for the Hurst-type dosimeter. The crystal should be small so that the point of detection is well known. It should, in general, be an isotropic detector. Along with these qualities, it should be capable of working in a high gamma-ray background, biasing out any effect the gamma rays may have. Too, the sensitivity of the detector to temperature change should be negligible. The detection efficiency should also be equal to or greater than the presently used dosimeter. Not all these requirements have been met by the Hornyak button, but data to date are encouraging.

The range of a 4-Mev proton in such a button is about 35 μ. If ZnS particles of about 25 μ in diameter are used, the light output per recoil proton would be expected to vary from zero to near maximum. Since the range of an equivalent energy electron is much greater, only a small part of the energy will be released in the scintillating component, so that the pulse due to the electron should be much less. Thus it should be possible to bias out the gamma-ray-produced electron pulses and still count a large portion of the neutrons. Biasing out the effects of gamma rays on the Hornyak button can be done in several ways. One method is to run the neutron-pulse-height-setting (PHS) curve both for a Po-Be neutron source and for the unknown neutron source, and then to set the bias where these two curves become parallel. This must be done where the gamma-ray field is greatest. If the strength of the gamma-ray field is approximately known ahead of time, the button may be set up in the same manner as is done for the dosimeter. This means that a Co^{60} gamma-ray source should be placed so that the field surrounding the button is known. If operation is to be in a 1-r/hr field maximum, the gain of the system and the high voltage are adjusted so that, when a bias of 6 v is used, the scaler will record about 25 to 35 counts/min. If the gamma-ray background is to be 100 r/hr, the over-all gain of the system is merely changed so that the same 25 to 35 counts/min are obtained.

The data in Fig. 49.1 show the response of Hornyak buttons (70 parts Lucite, 4 parts ZnS) of various thicknesses to a Po-Be neutron source. The source was kept at a fixed distance from the photocathode surface, and the thickness of the button was varied to determine the optimum response. As the button became thinner, more and more of the light which was originally absorbed in the upper part of the crystal was reflected back down through the crystal and into the phototube. Thus, there was a shift to larger pulses, and the

[1] W. F. Hornyak, *Rev. Sci. Instr.* **23**, 264 (1952).

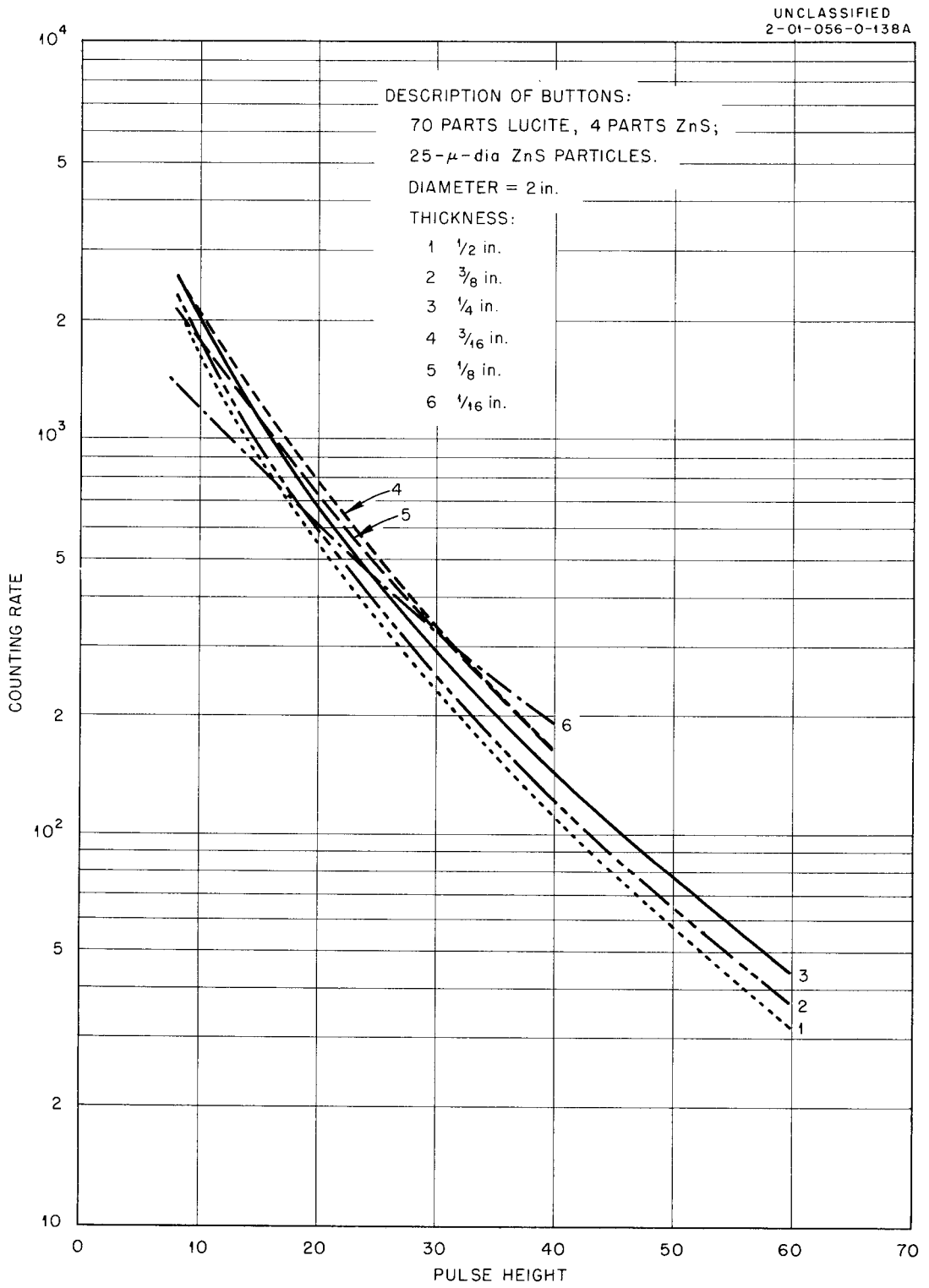

Fig. 49.1. Response of Various Hornyak Buttons to a Po-Be Neutron Source.

curves changed in slope. This increase in counting rate at larger pulse-height settings would continue until the crystal became so thin that the increase in light output failed to compensate for the decrease in the number of proton recoils.

Figure 49.2 shows the effect of placing the Hornyak button in an intense gamma-ray field. When the detector was placed in a 100-r/hr Co^{60} gamma-ray field, its response to a Po-Be neutron source for pulse-height settings lower than 40 was affected by the field. If the field had not been present, the neutron curves in Fig. 49.2 would follow the dotted lines (gain 8 and gain 16 indicate the amplification of the pulses). Thus for such a setup, the counts due to the gamma rays could be biased out by taking data at a pulse-height setting

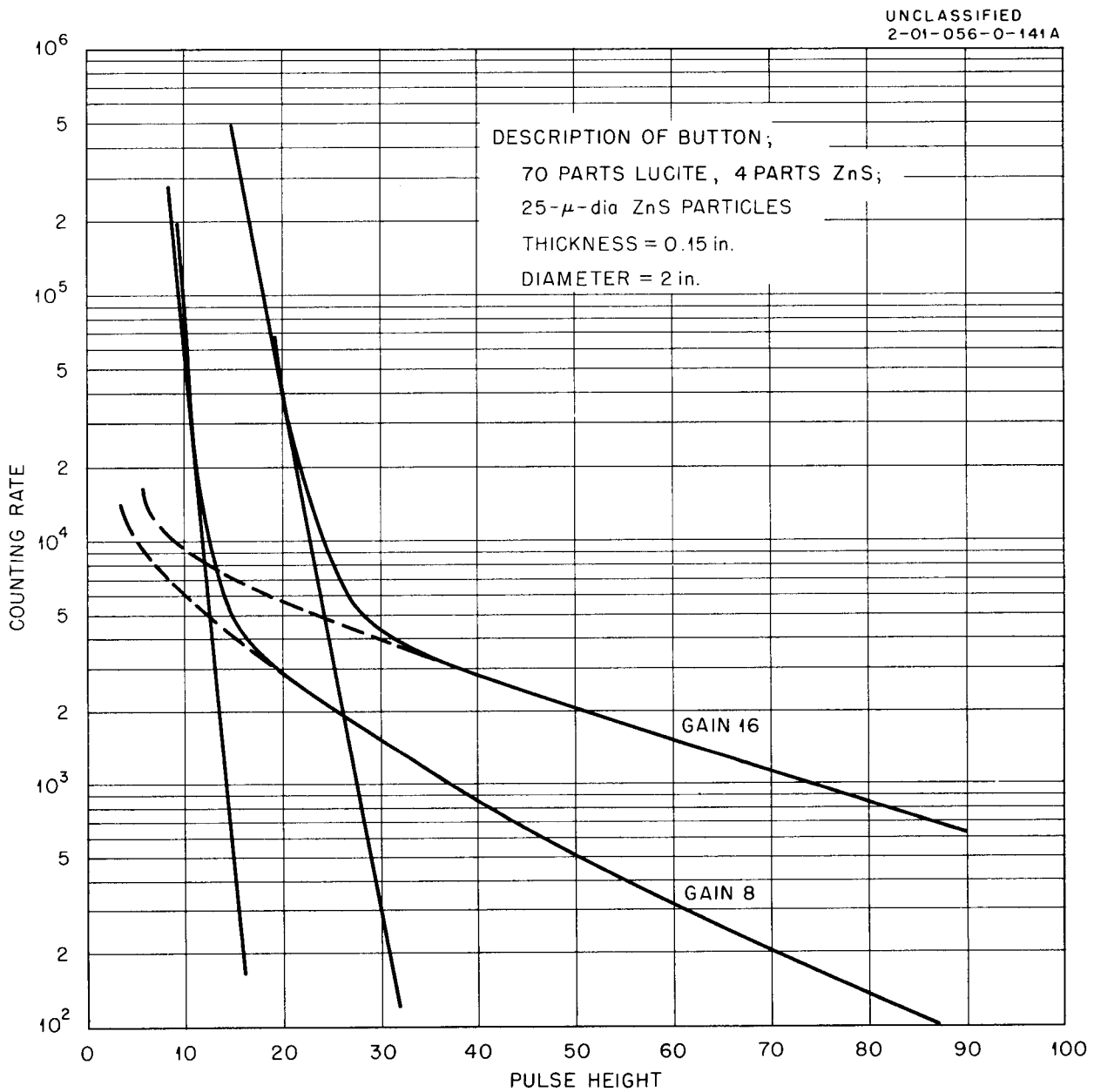

Fig. 49.2. Response of Hornyak Button to a Po-Be Neutron Source in the Presence of a 100-r/hr Co^{60} Gamma-Ray Field.

of 40 or greater. (The two straight curves at the left of Fig. 49.2 are typical gamma-ray plots.)

Measurements made with the same button placed in water near the Tower Shielding Reactor are shown for three reactor power levels in Fig. 49.3. Since the three curves are parallel above a pulse-height setting of 50, it can be seen that the Hornyak button could be used to count only neutrons, once the gamma-ray pulses are biased out. It should be noted from the curves, however, that an increase in power by a factor of 10 (i.e., from 100 to 1000 w) does not mean that the usable counting rate will be increased by the same factor, since the gamma rays also increase. For example, to count only neutrons, a pulse-height setting of 30 would be adequate for a 100-w power level, but

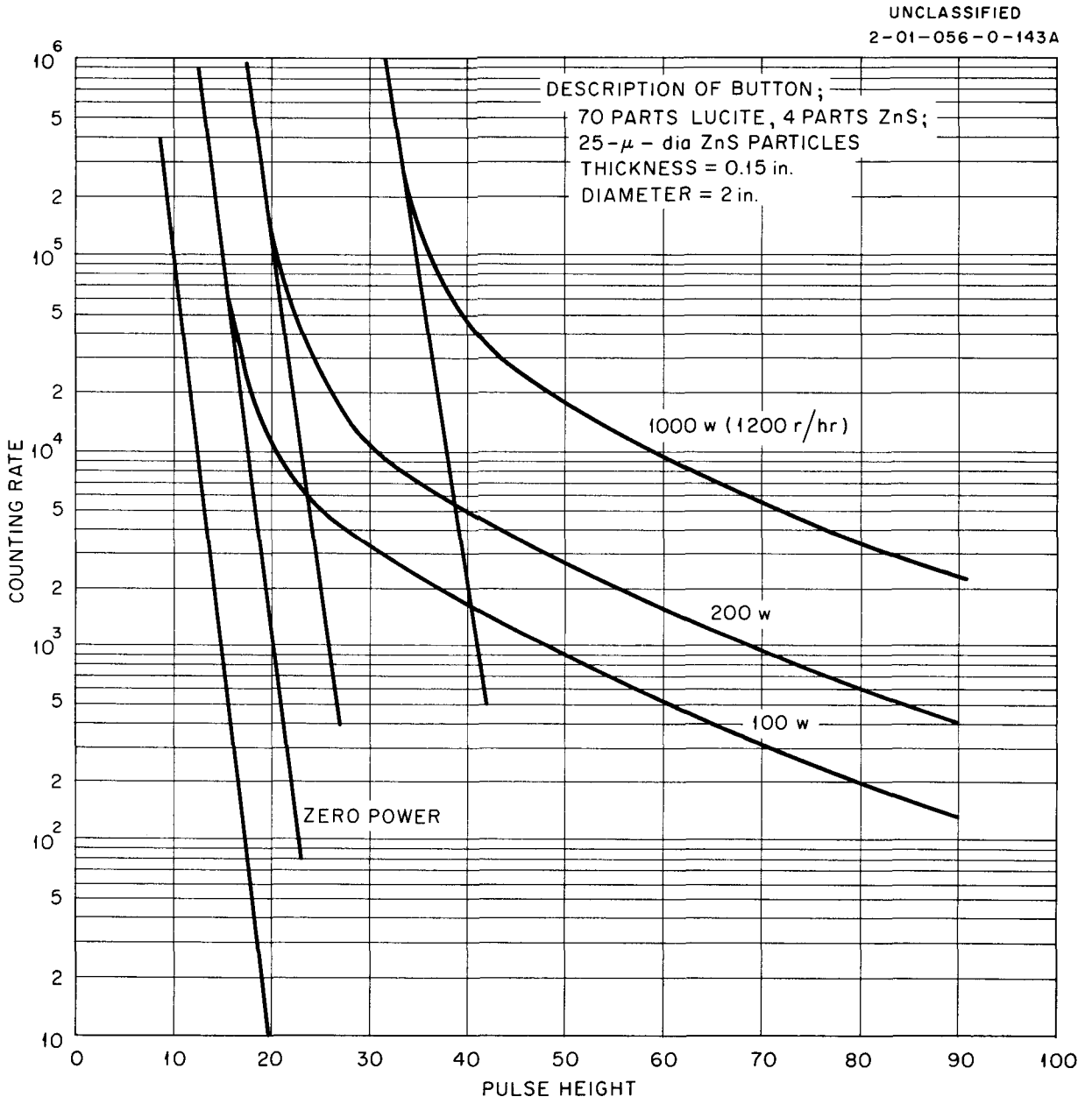

Fig. 49.3. Response of Hornyak Button for Various Power Levels of the TSR.

it must be increased to 50 for a 1000-w power level. Thus the increase in usable counting rate for this particular setup is about a factor of 5.

Measurements were made by the Bulk Shielding Facility group with both the Hurst-type dosimeter and a Hornyak button in the water surrounding the Bulk Shielding Reactor (Fig. 49.4). A 3-in.-thick lead shield which was held at a constant distance from the detectors on the reactor side reduced the gamma-ray flux to less than 1 r/hr. For these measurements the detectors were used in conjunction with an A-1 amplifier and a 20-channel analyzer. The four Hornyak button curves in Fig. 49.4 are all from the same run, but they are plotted as a function of a lower limit on the pulse-height selector. One hundred twenty channels on the analyzer compares with a coverage of 100 v on the pulse-height selector. The data at each point on curve 1 is the sum total of counts obtained between channels 6 and 43 at that particular water thickness. Curve 2 gives the counts between channels 10 and 43, etc. Since the curves remain parallel with this variation in the pulse-height selector setting, it is assumed that gamma rays were not contributing to the counting rate even at the lower settings. From this data it can be seen that the sensitivity of this particular button and phototube combination is less than that of the dosimeter but that the curves from the two detectors are parallel.

The effect of varying the temperature of the detector and the phototube was investigated (Fig. 49.5), using a Po-Be neutron source. Curve 1 represents the change in counting rate when only the Hornyak button temperature was changed (effected by inserting a 4-in. length of Lucite light piper between the detector and phototube). The change in counting rate was less than 4% over a range of 40°C. Curve 2 shows what happened when both the phototube and Hornyak button temperatures were varied; the sudden change in slope at the upper end of the temperature range is due to change in the photocathode surface. In this case the counting rate varied about 17% over a range of 40°C.

Attempts have been made to optimize the neutron response of the Hornyak button by varying both the concentration of ZnS within the crystal and the ZnS particle size. The standard 70 parts by weight of Lucite was combined with 0.4, 2, 4, 7, 10.5, and 20 parts by weight of ZnS particles 25 μ in diameter. Of these, the maximum counting rate for neutrons was obtained with 20 parts of ZnS. Actually, the difference in counting rates between concentrations of 20 and 4 parts of ZnS was small, particularly in the lower pulse-height region, where operation is desirable. As mentioned previously, the thinner crystals gave a higher counting rate when a Po-Be source was placed about 25 cm from the face of the crystal.

Variations in the concentration of 3- to 5-μ-dia ZnS particles (0.4 and 4 parts by weight) were also investigated. It was hoped that by decreasing the ZnS particle size the slope of the PHS curve for the Po-Be neutrons would be much less. This would be advantageous because it would allow operation at a higher pulse-height setting with little loss in counting rate. As can be seen in Fig. 49.6 the change is not large but is in the right direction. Along with this process of trying to improve the neutron detecting efficiency through the use of small-size particles, it was hoped that just the opposite effect would take place regarding gamma rays. Figure 49.6 also shows what happens in that respect. The over-all electronic gain for the system was increased by a factor of about 3 in order to bring the neutron response of the button using 3- to 5-μ-dia ZnS particles (4 parts by weight) equal to that of the button using 25-μ-dia particles at a particular pulse-height setting. In doing this, the gamma-ray response was increased to such an extent that it would be necessary to operate at about twice the previous pulse-height setting in order to obtain a counting rate independent of gamma rays. The over-all gain was increased again to bring the response of the button using 3- to 5-μ-dia particles (0.4 parts by weight) equal to the response of each of the other two buttons at a common point. With the smaller concentration of ZnS the number of smaller pulses increases, and at the same time there is a decrease in large pulses.

Probably the best procedure for determining the dosimetry capabilities of the Hornyak button is to compare it directly with the Hurst-type dosimeter, using monoenergetic neutrons. This has been done for several button compositions, particle sizes, and thicknesses. The source of the monoenergetic neutrons was the ORNL 3-Mev Van de Graaff. The neutron energies were obtained by using protons

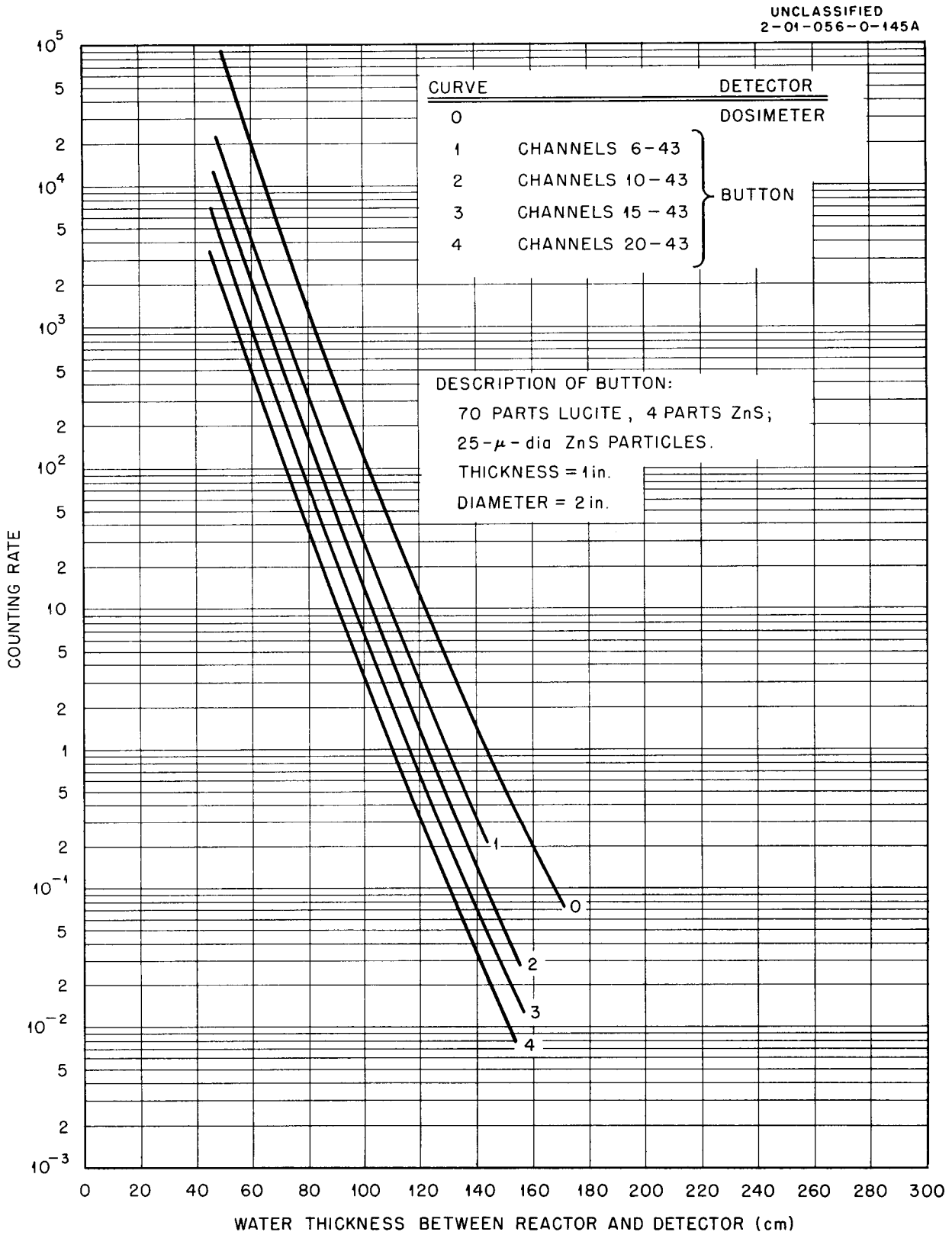

Fig. 49.4. Response of Hurst-Type Dosimeter and Hornyak Button at Various Distances from the BSR.

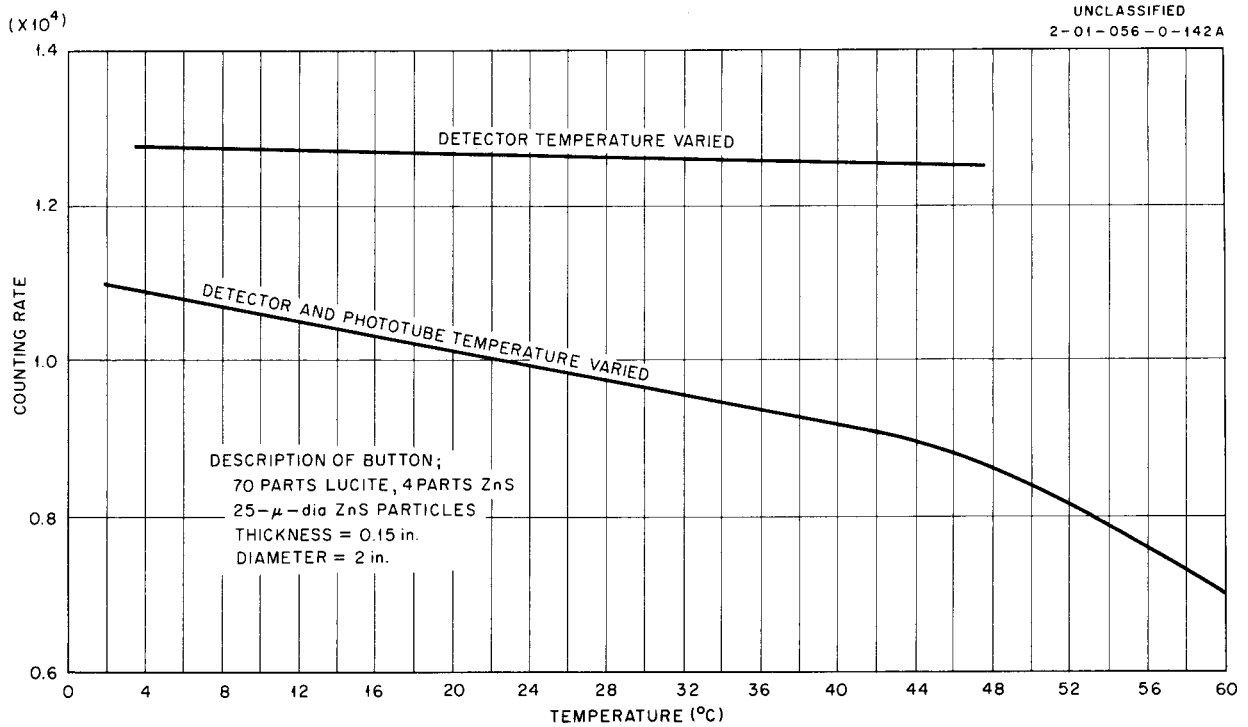

Fig. 49.5. Response of Hornyak Button to a Po-Be Neutron Source as a Function of Temperature.

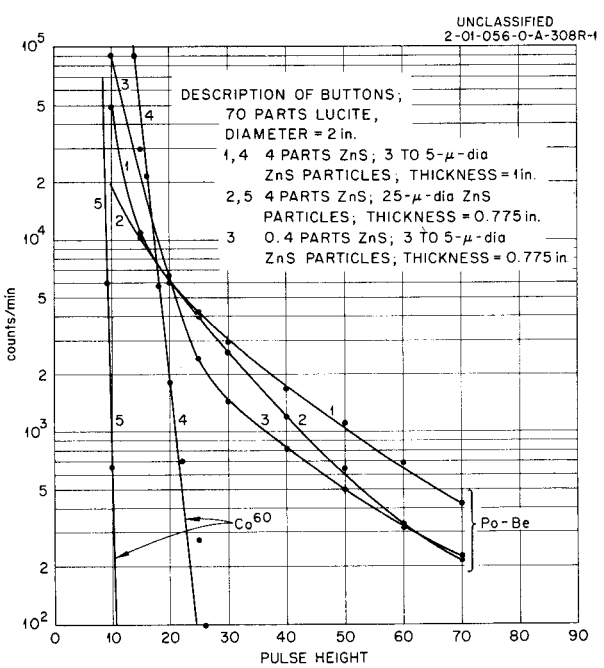

Fig. 49.6. Response of Various Hornyak Buttons to Po-Be and Co^{60} Sources.

on tritium, deuterons on deuterons, and deuterons on tritium. The three ranges of resulting energies thus covered were approximately 100 kev to 1.5 Mev, 2.5 to 5.5 Mev, and 14 to 17 Mev. With the exception of a few runs, both the button and the dosimeter were placed at an angle of 15 deg with the generator beam, thus ensuring that both counters saw the same intensity and neutrons of the same energy. For the 2.5- and 14-Mev neutrons, it was necessary to move the counter to an angle of 90 deg with the generator beam. For any individual set of runs the distance between center of detection and source remained the same.

Both the dosimeter and the Hornyak button were set up such that a bias of 6 v was used with an over-all gain that gave 30 counts/min when they were placed in a 1-r/hr gamma-ray field. The pulses from the Hornyak button were fed into a 20-channel analyzer, and those from the dosimeter were fed into a 20-channel analyzer and an integrator. Four buttons of the following compositions and thicknesses were used: (1) 25-μ-dia ZnS particles (4 parts by weight), 0.750-in. thick; (2) 25-μ-dia ZnS particles (4 parts by weight),

0.150-in. thick; (3) 25-μ-dia ZnS particles (4 parts by weight), 1-in. thick, $\frac{1}{8}$-in. Lucite rods inserted in the crystal; and (4) 3- to 5-μ-dia Zns particles (4 parts by weight), 1-in. thick. In order to eliminate any error due to counting time or beam intensity, both counters were run at the same time for the same amount of beam current. The ratios of the dose rate measured by the dosimeter to the dose rate measured by buttons 1 and 4 are shown in Fig. 49.7 as a function of neutron energy. For button 1 the ratio is quite high at low energies, approaching 1 near 1.5 Mev. Above this energy the ratio is near 1. For button 4 the ratio is much smaller at the low energies, approaching 1 at less than 1 Mev. For button 3 the curve (not shown) was essentially the same as for button 1. With button 2 (results not shown) the ratio at energies <1 Mev dropped to that shown here for button 4 but approached 1 Mev in the same manner as did button 1.

A check was made on the efficiency of the 750-mil-thick Hornyak button by using 25-μ-dia ZnS particles (4 parts by weight). For a neutron energy of 0.165 Mev it is about 0.001% efficient; at 0.5 Mev about 0.02%; and at 1.5 Mev about 0.216%. The dosimeter at this last energy is about 2% efficient. The calculations are based on the number of neutrons passing through the counter, determined from the beam current, differential cross section, and number of atoms of gas in the target.

Other runs on the Van de Graaff were made by using only the p,t reaction. Three of the buttons used contained 25-μ-dia ZnS particles, 4, 20, and 50 parts by weight. A button containing 3- to 5-μ-dia particles had 4 parts ZnS by weight. During these tests the thickness of the buttons was varied in an attempt to find some combination that would reduce the dose ratio at the lower energies. The results, plotted in Figs. 49.8, 49.9, and 49.10, are the dose rate ratios as a function of proton energy. Since these are preliminary data, no attempt was made to calculate the neutron energies. It can be noticed that as the thickness of the crystal decreased, the ratio at the lower energy improved. At about a 20-mil thickness the point of diminishing returns appears to have been reached.

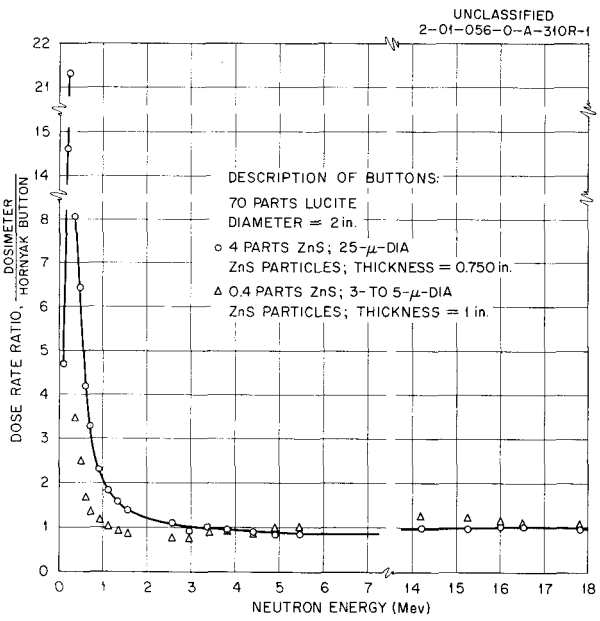

Fig. 49.7. Ratio of Dose Rate Response of the Dosimeter to the Response of Two Hornyak Buttons to a Po-Be Source.

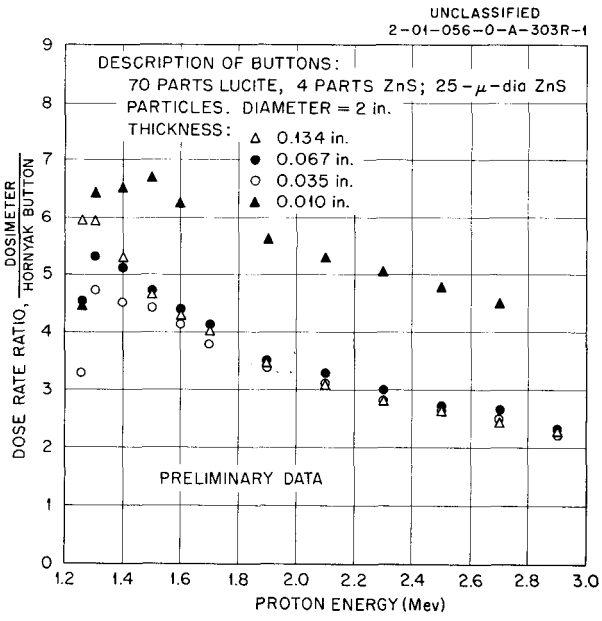

Fig. 49.8. Ratio of Dose Rate Response of the Dosimeter to the Response of Various Hornyak Buttons to Neutrons from the p,t Reaction (Van de Graaff Generator).

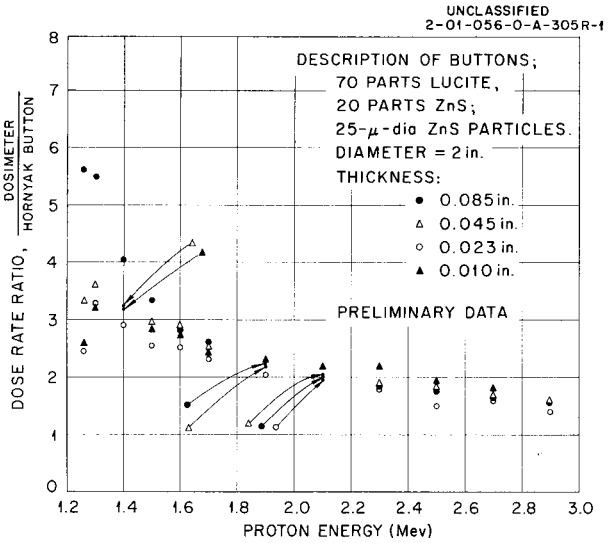

Fig. 49.9. Ratio of Dose Rate Response of the Dosimeter to the Response of Various Hornyak Buttons to Neutrons from the p,t Reaction (Van de Graaff Generator).

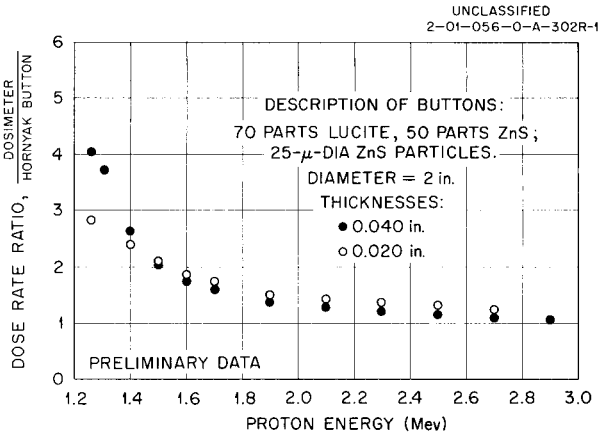

Fig. 49.10. Ratio of Dose Rate Response of the Dosimeter to the Response of Various Hornyak Buttons to Neutrons from the p,t Reaction (Van de Graaff Generator).

The best curves from each of Figs. 49.8, 49.9, and 49.10 are plotted in Fig. 49.11, which shows that as the concentration of ZnS was increased, more low-energy neutrons were observed. The present information does not give a full optimization of all components involved. The data do seem to indicate a need for larger ZnS concentrations in the crystal and optimum crystal thickness. No check has been made regarding response to gamma rays at these higher concentrations. More work is needed in regard to both the 25-μ-dia and the 3- to 5-μ-dia particle crystals.

It should be mentioned that, in addition to the 2-in.-dia buttons, several 5-in.-dia buttons mounted on 5-in.-dia photomultiplier tubes have been used for low-intensity neutron measurements.

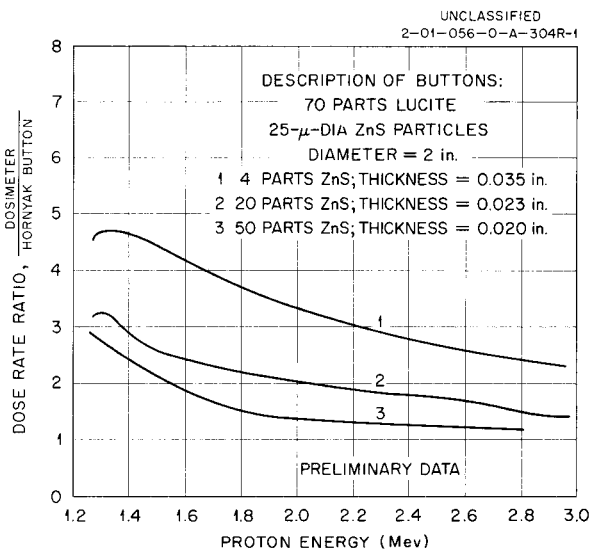

Fig. 49.11. Ratio of Dose Rate Response of the Dosimeter to the Response of Various Hornyak Buttons to Neutrons from the p,t Reaction (Van de Graaff Generator).

50. INSTRUMENTATION FOR A GAMMA-RAY SPECTROMETER

T. A. Love R. W. Peelle
W. Zobel

The development of instrumentation is an essential part of the program for measuring the energy spectrum of short-lived fission-product gamma rays (see "Time and Energy Spectra of Fission-Product Gamma Rays Measured at Short Times after Uranium Sample Irradiations," this report). The electronic instrumentation used with the multicrystal gamma-ray scintillation spectrometer at the Bulk Shielding Facility has been described previously.[1] Changes have now been incorporated in the instrumentation for the measurement of U^{235} foils immediately after their exposure in the ORNL Graphite Reactor. Modifications in the existing equipment and the new equipment which has been added to the system are described below.

Modifications in Existing Equipment

Figure 50.1 is a block diagram of the modified electronic equipment used with the multicrystal gamma-ray spectrometer.[2] Since the samples of U^{235} were irradiated at the ORNL Graphite Reactor and since the recording equipment was located approximately 500 ft from the reactor (in Building 3010), preamplifiers were required to drive cables of this length. Very short counting intervals were expected, and the amplifier and preamplifier had to be capable of reproducing high counting rates with small gain change. A DD2 amplifier[3] proved to be adequate for the counting rates involved, but the termination of the preamplifier at the detector end of the long cable was quite critical and had to be adjusted very carefully to avoid reflections. Since the DD2 amplifier will not properly drive a low impedance, a cathode follower circuit (Fig. 50.2) is used (in series with the DD2) to drive the two multichannel analyzers.

The fast pneumatic probe assembly[4] designed by E. C. Campbell[5] and already placed at hole 56 on the north face of the reactor was used to introduce the U^{235} sample into the flux. The sample, confined in a small nylon carrier or "rabbit," was simply blown by gas pressure through a tube into the region of high flux, where it was stopped. After bombardment it was blown out and stopped in front of the spectrometer collimator by a Viscaloid bumper. The sample had a transit time of approximately 0.3 sec each way. In order to determine the time the sample was in the flux, three photomultiplier tubes were placed along the pneumatic tube at 20-cm intervals starting at the face of the reactor. Measurements of the time that elapsed between these detectors permitted speed determinations, from which the transit times were calculated.

New Equipment

The experiment presented several timing problems: (1) the problem of selecting, with a considerable degree of accuracy and flexibility, the length of time a sample was to be bombarded; (2) the problem of selecting the length of time after bombardment at which observation of the spectrum was to begin; and (3) the problem of selecting the length of time the spectrum of gamma radiation was to be recorded.

Figure 50.3 is a block diagram of a sequence timer designed for the experiment by F. Glass.[6] Timing is controlled by a simple oscillator and three atomic scalers. Oscillations of 10, 2, and 1 cps may be chosen by a simple switching arrangement. Very short bombardment and waiting times are limited by the transit time of the sample in the pneumatic tube. With this limitation all times may be chosen in multiples of 2, 4, 8, 16, 32, and 64 times the period of the three available frequencies. All times are measured from the time

[1] T. A. Love, R. W. Peelle, and F. C. Maienschein, *Electronic Instrumentation for a Multiple-Crystal Gamma-Ray Scintillation Spectrometer*, ORNL-1929 (Oct. 3, 1955).

[2] F. C. Maienschein, *Multiple Crystal Gamma-Ray Spectrometer*, ORNL-1142 (April 14, 1952).

[3] E. Fairstein, *Rev. Sci. Instr.* 27, 475 (1956).

[4] E. C. Campbell and W. M. Good, *Phys. Rev.* 76, 195 (1949).

[5] Physics Division.

[6] Instrumentation and Controls Division.

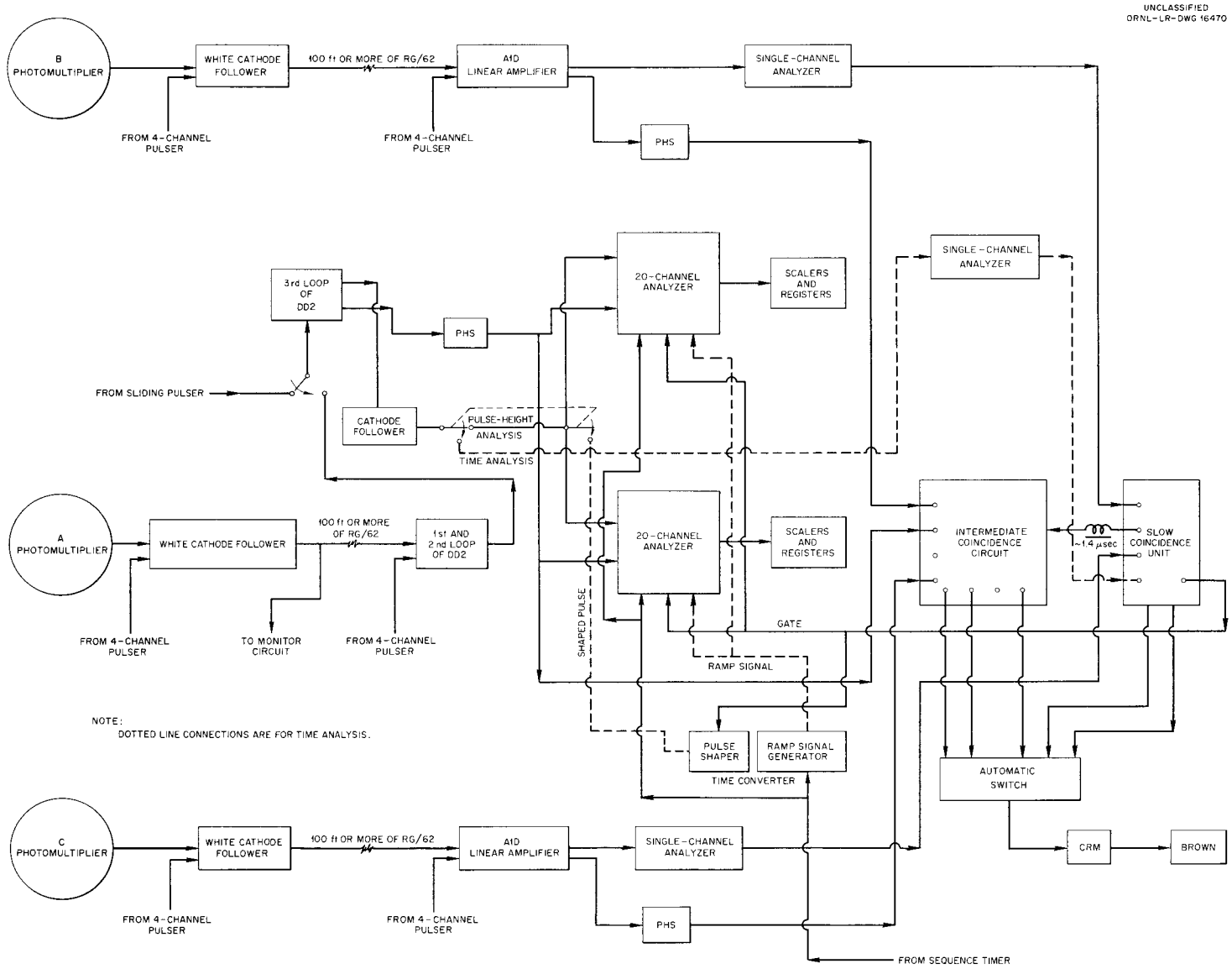

Fig. 50.1. Block Diagram of Modified Electronic Equipment Used with Multicrystal Gamma-Ray Spectrometer.

of the first cycle after the start-stop switch is thrown to start. The sequence of events after the times are chosen and the start-stop switch is thrown to "start" is as follows:

1. The sample is blown into the reactor.
2. After the chosen bombardment time the sample is blown out of the reactor and stopped in front of the collimator of the spectrometer. Immediately, the monitor gate, which allows an integral count to be taken for a time equal to 64 periods of the oscillator, is turned on.
3. At the time the recording of the spectrum is to begin, a gate signal is sent to the analyzer in Building 3010, which turns the analyzer on for the length of time chosen.

Any or all times may be extended indefinitely by simply biasing out the particular scaler or scalers

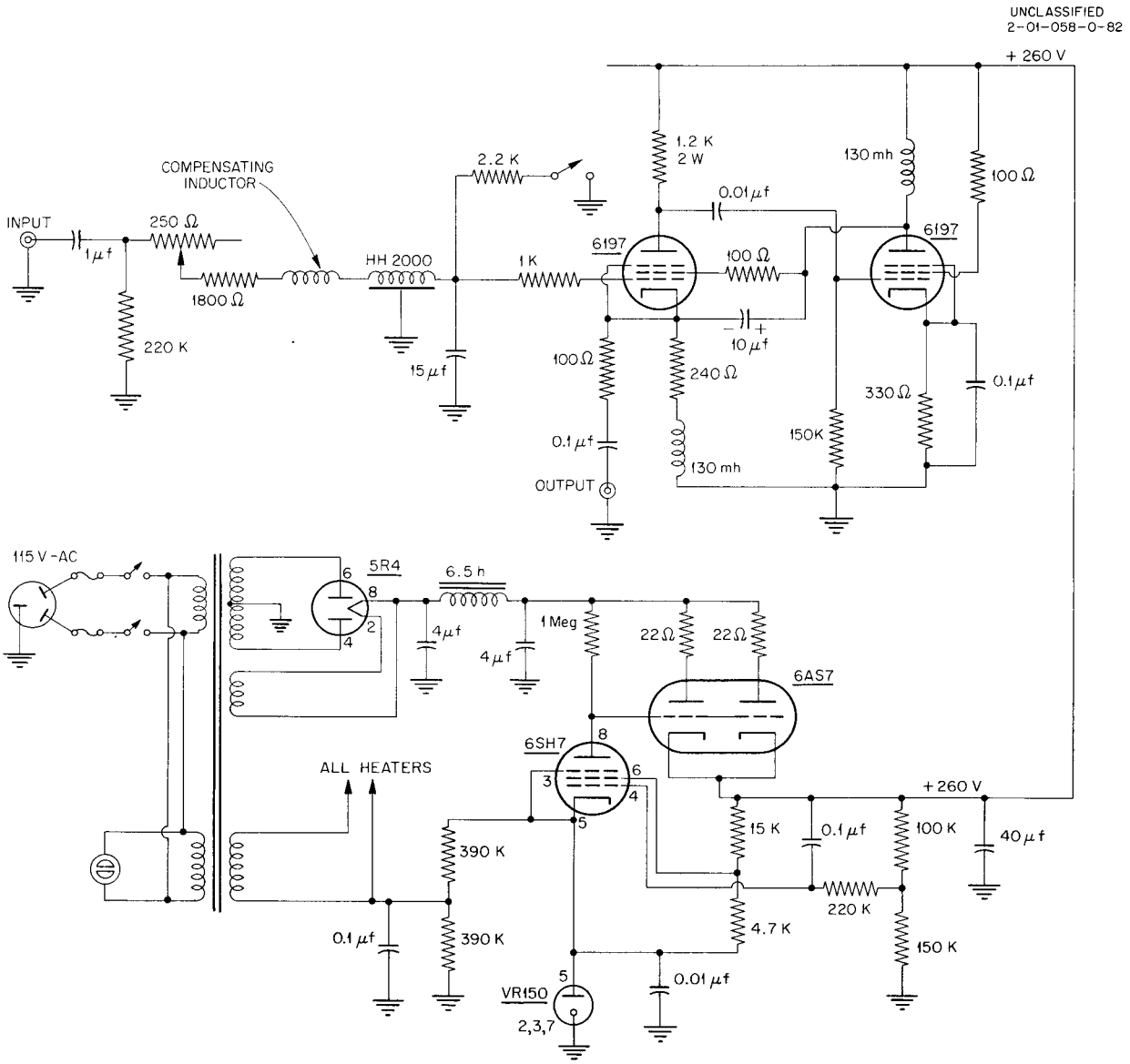

Fig. 50.2. Cathode Follower Circuit Used to Drive Two Multichannel Analyzers.

involved or by choosing manual operation. Oscillator frequency is monitored by a Berkley Universal counter-timer and is constant within 0.1%.

Since it would be valuable not only to know the spectrum of the fission-product gamma rays, but also to know the detailed time dependence of this spectrum, and since it was not practical to measure the complete time dependence of the detailed spectrum, measurements were made of the time dependence of relatively large energy groups within this spectrum. For these measurements a system was devised which required an additional single-channel analyzer and a unit (Fig. 50.4) to convert the multichannel analyzer from energy discrimination to time discrimination. The single-channel analyzer was used to select a particular energy group and, together with part of the time converter unit, to convert the pulses due to gamma rays in this group to pulses of uniform height and shape. The time converter varies the bias of the multichannel discriminator according to $1 - e^{-t/RC}$, where RC may be varied stepwise. The output pulses are then fed into and recorded by the multichannel analyzer in the usual way. Thus, since succeeding channels are recording during time intervals which increase according to $1 - e^{-t/RC}$, it is possible, by properly choosing RC equal to the mean radioactive life of the radiator, to obtain an equal number of counts in each channel.

The conversion bias circuit for energy analysis by two 20-channel analyzers is shown in Fig. 50.5. For time analysis this circuit is disconnected from the −87.5 v and from ground and connected to points B and A in the cathode circuit of the second half of V_3 of the time converter, as shown in Fig. 50.4. A "ramp" signal fed to the grid of the second half of V_3 raises the potential of the circuit in Fig. 50.5 exponentially with the time constant of the RC network in the grid of the second half of V_3 toward a constant potential determined

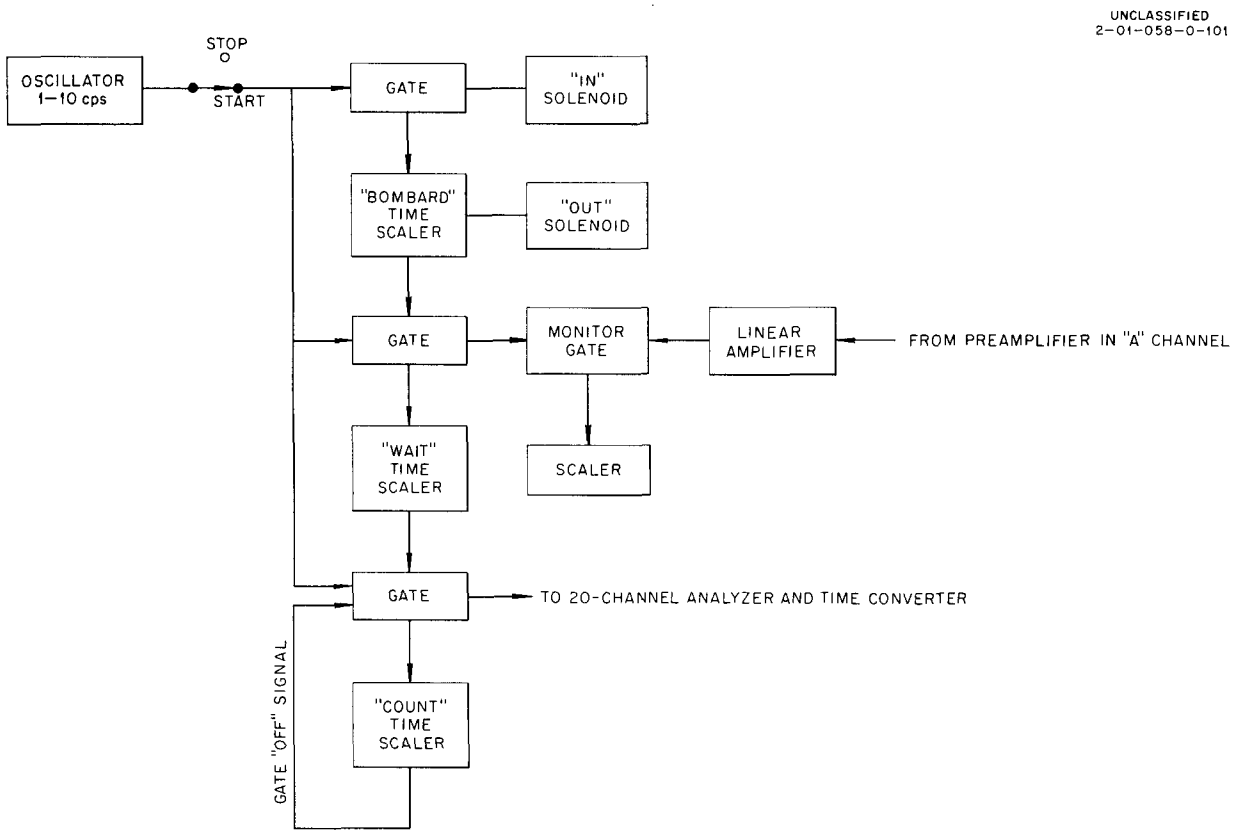

Fig. 50.3. Sequence Timer Block Diagram.

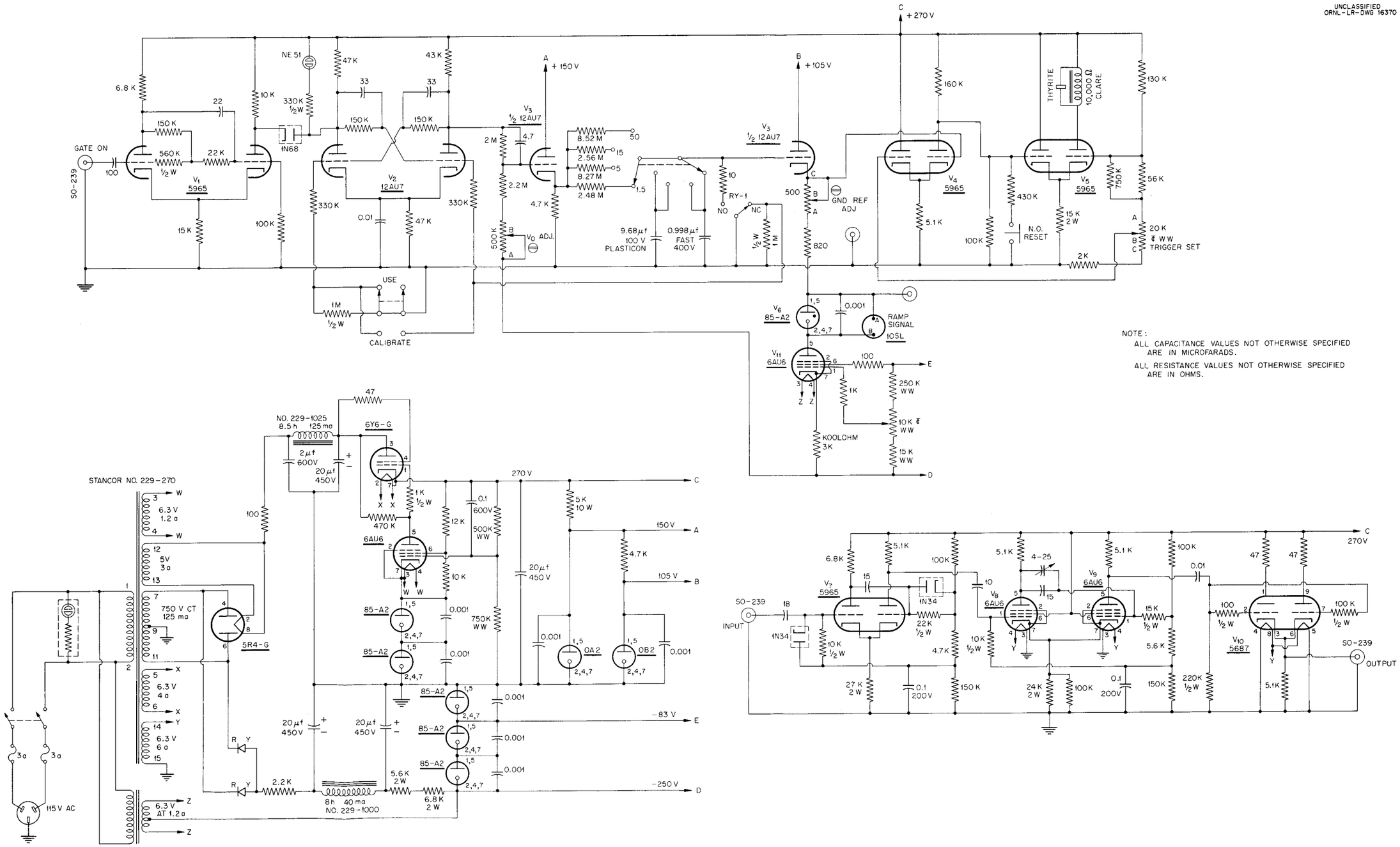

Fig. 50.4. Unit to Convert 20-Channel Analyzer to Time Analysis.

by the first half of V_3 and its circuitry. If a constant-frequency, constant-amplitude signal is fed into the input of the analyzer, a number of counts will be deposited in each channel, in turn, as the ramp rises. The number of counts in each channel will be proportional to the time interval of each channel, and the sum of all the counts up to a particular channel will represent the length of time from zero time to the time interval of the particular channel.

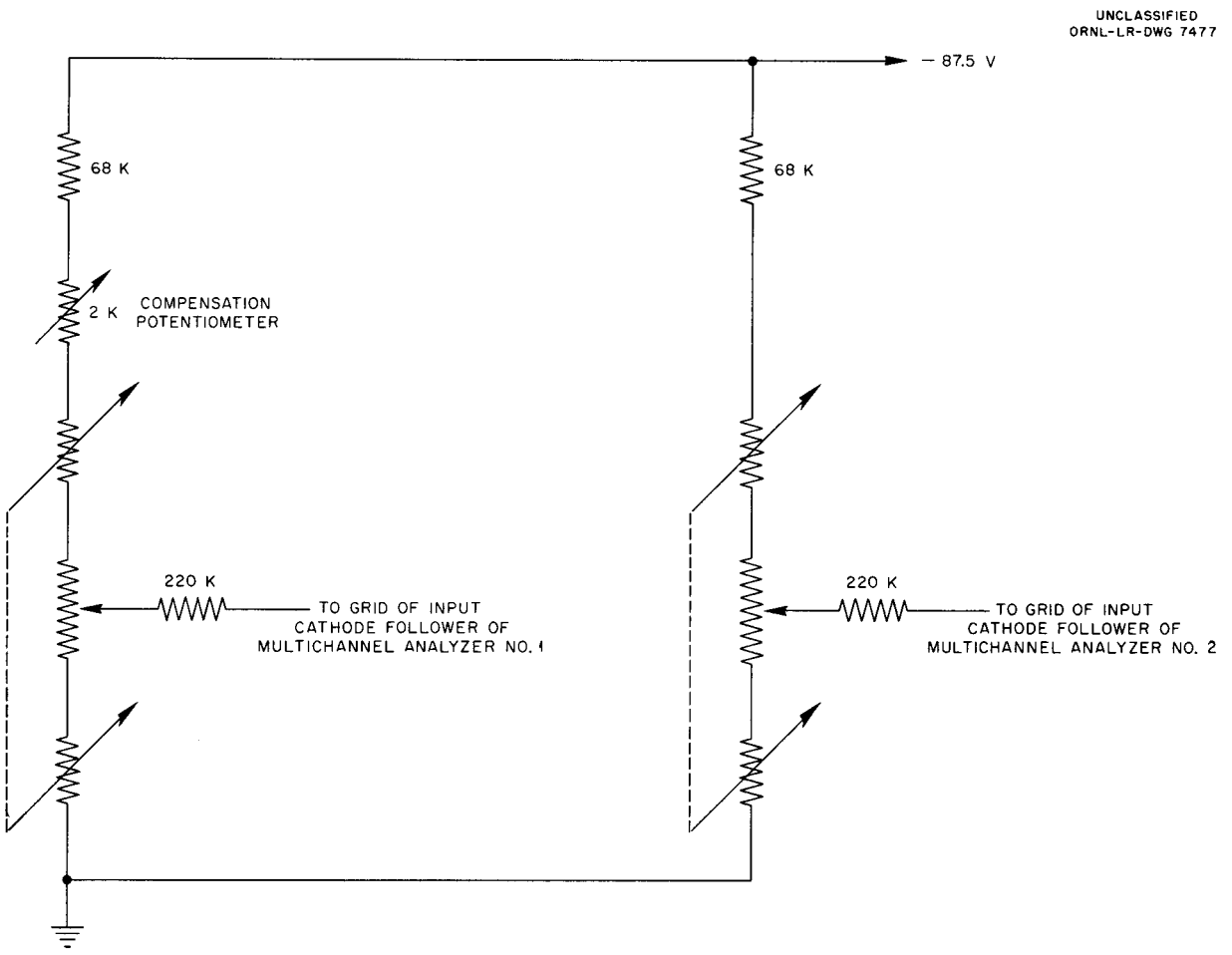

Fig. 50.5. Circuit Used to Tie Two 20-Channel Analyzers Together.

51. PULSE-HEIGHT DISTRIBUTION FROM AN NaI(Tl) CRYSTAL

C. D. Zerby

Sodium iodide crystals have been used extensively as gamma-ray spectrometers. The output of the photomultiplier tube attached to the crystal yields a pulse-height distribution which is related to the incident gamma-ray energy spectrum. However, analysis of the gamma-ray spectrum by use of the pulse-height distribution is complicated without calculations giving accurate relations between the two.

Analysis of a problem to calculate the relation between the incident gamma-ray energy spectra and the resulting pulse-height distribution has been started. The problem will be calculated on the Oracle – an automatic, electronic, digital, computing machine – using the Monte Carlo method.

The problem will be set up for crystals with the shape of a right circular cylinder, or a right circular cylinder with a truncated conical end corresponding to the large "total absorption" crystals now being produced. One source considered will be a point located on the axis of the crystal some distance from one end. An alternate source will be a monodirectional beam of a given diameter parallel to the axis which will be incident on the flat face of the crystal. The diameter of the beam need not be the same as the diameter of the crystal. If the crystal has a truncated end, that end will always face the radiation. The source can consist of as many as three different monoenergetic components in the proportions desired with maximum energy of 10 Mev.

The history of each sample photon incident on the crystal will be generated by established random methods. The energy deposited in the crystal resulting from photoelectric, pair production, and Compton interactions will be calculated at each photon collision and weighted according to the probability of occurrence. Losses from the crystal resulting from secondary bremsstrahlung and annihilation radiation will also be calculated by using the Monte Carlo method.

Results of the calculation will include the function $F(E,E')\ dE'$, which is the probability that a photon of initial energy E will deliver to the crystal an amount of energy between E' and $E' + dE'$ as the result of one or more collisions; the efficiency $K(E)$, which is the probability that an incident photon with energy E will have at least one interaction in the crystal; and the photofraction, which is the probability that an incident photon having at least one collision will finally be absorbed.

From data calculated for monoenergetic sources, the pulse-height distribution for a given spectrum can be obtained by superposition of results.

Part VII

PROJECT SHERWOOD

52. DIFFUSION OF IONS IN A PLASMA ACROSS A MAGNETIC FIELD

A. Simon

Some experiments at Berkeley by Bohm *et al.*[1] during the war had been interpreted as revealing an anomalously high diffusion rate of ions across a magnetic field (H). Bohm had shown that the measured rate was much faster (x700) than the rate which would be expected on the usual picture of ambipolar diffusion. To account for this presumed discrepancy he advanced a theory of enhanced diffusion across magnetic fields by means of plasma oscillations. The details of the theory have never been available. However, one prediction which is of great interest is that the diffusion coefficient should be proportional to $1/H$ rather than the more usual $1/H^2$. If the diffusion coefficient is really proportional to $1/H$, it would appear extremely difficult, if not impossible, to obtain a sufficiently long containment time of the plasma in a sensible system. On the other hand, if the classical $1/H^2$ law holds, the diffusion itself is no barrier to sufficient containment time.

An experimental investigation at ORNL[2] has revealed that the diffusion coefficient in an arc plasma actually varies as $1/H^2$. Theoretical considerations have also shown that the original supposition of Bohm, which was that a discrepancy existed between the measured and theoretical diffusion rate, was incorrect. Whenever the magnetic field lines end on a conducting surface, electron currents can flow in the direction of the field lines so as to maintain space charge neutrality in the plasma. This "shorting" effect[3] makes unnecessary the establishment of an "ambipolar" diffusion rate across the magnetic field. Instead, the ions are able to diffuse at their intrinsic rate, and this value results in agreement between the prediction of theory and the results of experiment. Thus, both the magnitude and magnetic field dependence of the diffusion coefficient may be understood on the basis of a classical collision-diffusion picture.

[1] D. Bohm *et al.*, *The Characteristics of Electrical Discharges in Magnetic Fields*, p 1, ed. by Guthrie and Wakerling, McGraw-Hill, New York, 1949.

[2] A. Simon and R. V. Neidigh, *Diffusion of Ions in a Plasma Across a Magnetic Field*, ORNL-1890 (Nov. 16, 1955).

[3] A. Simon, *Phys. Rev.* 98, 317 (1955).

53. DIFFUSION OF LIKE PARTICLES ACROSS A MAGNETIC FIELD

A. Simon

Many of the gross properties of a plasma may be obtained from the hydrodynamical (or macroscopic) equations of the plasma.[1] If an isotropic stress tensor is assumed, the force equation and Ohm's law take the form:

$$\nabla P = \vec{j} \times \vec{H} = \epsilon \vec{E} \quad , \tag{1}$$

$$\vec{E} + \frac{\vec{v} \times \vec{H}}{c} = \frac{\vec{j}}{\sigma} + \frac{\nabla P_i}{en} \quad , \tag{2}$$

where P is the gas pressure, H and E are the magnetic and electric field strengths, respectively, and j and ϵ are the current and the charge density in the plasma, respectively. The mass velocity of the plasma is denoted by $\vec{v}$, and the ion partial pressure by P_i. The conductivity is defined as

$$\sigma \cong \frac{ne^2}{mc\nu} \quad ,$$

where n is the density of electrons and ν is the collision frequency for electron-ion impact.

If it is assumed that the density gradient and electron field are in the x direction and that H is in the z direction, $\vec{j}$ may be eliminated from Eqs. 1 and 2. The result is

$$v_x = -\frac{c}{\sigma H^2} (\nabla P - \epsilon E) \quad . \tag{3}$$

[1] L. Spitzer, Jr., *Physics of Fully Ionized Gases* (in press), Interscience.

This has the usual form for diffusion, in that Fick's law is obeyed ($\nu \cong \nabla n$).

Unfortunately, this simple derivation fails for the case of a simple gas of charged particles, that is, a gas of one type of particle only. In this case, Eq. 2 no longer exists. Equation 1 is still valid; however, $\vec{v}$ and $\vec{j}$ are no longer independent and are related by

$$\vec{j} = \frac{\epsilon \vec{v}}{c} = \frac{ne\vec{v}}{c} . \tag{4}$$

As a result, Eq. 1 predicts no mass flow in the direction of ∇P.

The paradox may be resolved by extending Eq. 1 to include the effects of off-diagonal elements in the stress tensor. It is precisely these components which produce like-particle diffusion. The proper expression for the stress tensor has been given by Chapman and Cowling.[2] By substituting this expression in Eq. 1, the following result has been found:[3]

$$v_x = \frac{3}{8} \frac{r_0^4}{\tau} \frac{d}{dx} \left(\frac{1}{n} \frac{d^2 n}{dx^2} \right) , \tag{5}$$

where $r_0 = mvc/eH$, and $\tau = \lambda/v$ is the mean free time between collisions. Note that Fick's law is not obeyed and that the diffusion coefficient is proportional to $1/H^4$.

Equation 5 may be expected to give the proper form for the diffusion due to like-particle collisions even in a nonsimple gas. It has been shown by Kruskal[3] that the self-diffusion rate is usually smaller than that due to unlike particle collisions but may sometimes dominate.

[2] S. Chapman and T. G. Cowling, *The Mathematical Theory of Non-Uniform Gases*, p 338, University Press, Cambridge, England, 1952.

[3] M. Kruskal, private communication.

PAPERS PRESENTED AT SCIENTIFIC MEETINGS

International Conference on the Peaceful Uses of Atomic Energy, Geneva, Switzerland, August 8–20, 1955

A. D. Callihan, J. W. Morfitt, and J. T. Thomas (paper presented by A. D. Callihan), "Small Thermal Homogeneous Critical Assemblies."

National Industrial Conference Board, Fourth Annual Conference on Atomic Energy in Industry, New York, N.Y., October 26–28, 1955

E. P. Blizard, "Reactor Shielding Requirements for Mobile Application."

Nuclear Engineering and Science Congress and International Atomic Exposition, Cleveland, Ohio, December 12–16, 1955

E. P. Blizard, "Reactor Shielding."

J. T. Thomas, J. K. Fox, and A. D. Callihan (paper presented by J. T. Thomas), "A Direct Comparison of Some Nuclear Properties of U^{233} and U^{235}."

American Physical Society Meeting, New York, N.Y., January 30–February 3, 1956

G. deSaussure and E. Guth (paper presented by G. deSaussure), "Photo- and Electrodisintegration of C^{13}."

American Physical Society, 1956 Summer Meeting in the East, New Haven, Connecticut, June 21–23, 1956

R. B. Murray and J. Schenck (paper presented by R. B. Murray), "Scintillation Response of LiI(Eu) Crystals to Monoenergetic Fast Neutrons."